

# UNIVERSITÀ DEGLI STUDI DI NAPOLI FEDERICO II



D.I.I. - DIPARTIMENTO DI INGEGNERIA INDUSTRIALE

TESI DI DOTTORATO IN  
INGEGNERIA DEI SISTEMI MECCANICI

## **DEVELOPMENT OF A GRIP AND THERMODYNAMICS SENSITIVE TYRE/ROAD INTERACTION FORCES CHARACTERIZATION PROCEDURE EMPLOYED IN HIGH-PERFORMANCE VEHICLES SIMULATION**

RELATORE

PROF. ING. MICHELE RUSSO

DOTTORANDO

ING. FLAVIO FARRONI

COORDINATORE

PROF. ING. FABIO BOZZA

TUTOR AZIENDALE

ING. MARCO FAINELLO  
(FERRARI S.P.A.)

**XXVI CICLO**



*to the ones  
who believe in me*



## **Acknowledgments**

The work described in the following pages would not have been the same without the fundamental contribution of the people met during an extremely stimulating PhD path. In particular, a special thanks goes to professors Michele Russo and Francesco Timpone, leading and inspiring figures in research and in academic life, to Marco Fainello and Daniele Giordano from Ferrari S.p.A., for their being continuous source of innovative ideas, projects and challenges, to Vincenzo Ciaravola from Bridgestone T.C.E. and Francesco Massi from La.M.Co.S., for the priceless support provided during the activities carried out in collaboration and to Tommaso D'Avanzo from BMW, from whose friction model everything started.

Naples, March 25, 2014

Flavio Farroni



# **Table of Contents**

Notation.....	9
Introduction .....	13
1. The Tyre .....	15
1.1 Description and General Considerations	15
1.2 Historical Notes	17
1.3 Sidewall Markings	18
1.4 Mechanics of Tyres	20
1.4.1 Topology Notes	20
1.4.2 Lateral Interaction	21
1.4.3 Camber Thrust	23
1.4.4 Longitudinal Interaction	24
1.4.5 Interaction between Tangential Forces	27
2. TRICK tool - Tyre/Road Interaction Characterization & Knowledge .....	28
2.1 Introduction	28
2.2 Vehicle model	30
2.2.1 Basic hypotheses and reference system	30
2.2.2 Input channels	31
2.2.3 Input parameters	32
2.2.4 Test Procedure	35
2.2.5 Input processing, diagnostics and signal correction	36
2.2.6 Model equations	44
2.2.6.1 Vertical Forces	44
2.2.6.2 Lateral Forces	45
2.2.6.3 Longitudinal Forces	45
2.2.6.4 Tangential Forces in wheel reference system	47
2.2.6.5 Wheel Steering Angles	47
2.2.6.6 Wheel Absolute Velocities and Slip Indices	49
2.3 Forces estimation validation	50
2.4 Tangential Tyre/Road Interaction Characteristics - Results Analysis	52
2.4.1 General Notes	52
2.4.2 PLOT A & PLOT E: pure longitudinal interaction - front tyre	55
2.4.3 PLOT B & PLOT F: pure lateral interaction - front tyre	55
2.4.4 PLOT C & PLOT G: pure longitudinal interaction - rear tyre	56
2.4.5 PLOT D & PLOT H: pure lateral interaction - rear tyre	56
2.4.6 PLOT I: combined longitudinal interaction - front tyre	57
2.4.7 PLOT J: combined lateral interaction - front tyre	57
2.4.8 PLOT K: combined longitudinal interaction - rear tyre	57
2.4.9 PLOT L: combined lateral interaction - rear tyre	58
2.4.10 PLOT M & PLOT N: adherence ellipse - front tyre	59
2.4.11 PLOT O & PLOT P: adherence ellipse - rear tyre	59
2.4.12 Further Results	60
3. TRIP-ID tool - Tyre/Road Interaction Parameters Identification .....	61
3.1 Introduction	61
3.2 Similarity Curve and Combined Effect function	61
3.3 Classification and processing of experimental data	64
3.3.1 Input analysis	64
3.3.2 Identification Procedure - Pure Interaction	67
3.3.3 Identification Procedure - Combined Interaction	69
3.4 Results Analysis	70

3.4.1 Pure Interaction	70
3.4.2 Combined Interaction	72
3.5 Further Developments	73
3.5.1 An Alternative Identification Strategy - Pure Points Increasing	73
3.5.2 Temperature / Wear effects modelling in Pacejka formulation	74
4. TRT - Thermo Racing Tyre .....	77
4.1 Introduction	77
4.2 Tyre modelling and base hypotheses	77
4.3 Thermodynamic model	79
4.4 Friction power	80
4.5 Strain Energy Loss (SEL)	81
4.5.1 Introduction	81
4.5.2 The Test Bench	81
4.5.3 Tests Procedure	83
4.5.4 Normal Interaction Characteristic and Radial Stiffness	84
4.5.5 Hysteresis Cycles and Total Stiffness	84
4.6 Heat transfers modelling	87
4.7 Contact area calculation	89
4.8 The constitutive equations	92
4.9 Results and discussion	96
4.10 Further developments and implementations	99
4.10.1 TRT blown exhaust gas	99
4.10.1.1 Model Variations	99
4.10.1.2 Simulation Results	101
4.10.2 TRT Multi-Rib version	102
4.10.2.1 Model Variations	102
4.10.2.2 Simulation Results	103
4.11 Final Considerations	106
4.12 Appendix	107
5. GrETA - Grip Estimation for Tyre Analyses	112
5.1 Introduction	112
5.2 Model Definition And Basic Hypotheses	114
5.3 Material Characterization	116
5.4 Adhesion	120
5.4.1 Pin on Disk Tests	120
5.4.1.1 Introduction	120
5.4.1.2 Pin on Disk Experimental Test Bench	120
5.4.1.2 Results Analysis And Discussion	122
5.4.2 Adhesion Model	130
5.5 Hysteresis Model	131
5.6 Results And Validation	136
6. Tyre Models Integration.....	141
6.1 Introduction	141
6.2 TRICK & TRIP-ID	141
6.3 TRICK & TRT	147
6.4 TRIP-ID - TRT - GrETA	154
6.5 TRT - GrETA - Physical Interaction Model	156
Conclusions and Further Developments .....	157
References .....	159

**Notation**

<b>Symbol</b>	<b>Unit</b>	<b>Description</b>
$A_v$	[m <sup>2</sup> ]	vehicle master section
$A_0$	[m <sup>2</sup> ]	nominal tyre/road contact area
$A_{eff}$	[m <sup>2</sup> ]	effective tyre/road contact area
$C$		thermal model grid position coefficient
$C_\alpha$	[N/rad]	cornering stiffness
$C_\gamma$	[N/rad]	camber stiffness
$C_x$	[N/m]	braking stiffness
CG		centre of gravity
CR		thermal model partition coefficient
$C_x$	[-]	drag aerodynamic coefficient
$C_z$	[-]	downforce aerodynamic coefficient
DOF		degree of freedom
$E'$	[Pa]	rubber storage modulus
$E''$	[Pa]	rubber loss modulus
$E$	[Pa]	rubber complex dynamic modulus
$E_\infty$	[Pa]	glassy region dynamic modulus
$E_0$	[Pa]	rubbery region modulus
$F$	[N]	force
FP	[W/m <sup>2</sup> ]	friction power
$G$		MF (magic formula) combined function
$Gr$	[-]	Grashof number
$H$	[W/(m <sup>2</sup> K)]	heat transfer coefficient
$J_z$	[kg m <sup>2</sup> ]	vehicle moment of inertia about z axis
$I_w$	[kg m <sup>2</sup> ]	wheel moment of inertia about rotation axis
$K$		Kuznetsov adhesion parameter
$K_\phi$	[N/rad]	axle roll stiffness
$L$	[m]	characteristic length of the heat exchange surface
$L_a$	[m]	contact patch length
$M$	[Nm]	moment
$M_L$	[kg]	vehicle liquids mass (full tanks)
$M_w$	[kg]	total wheel mass
$N$	[m]	contact half length
NEC		number of tread elements in contact with road
$Nu$	[-]	Nusselt number
$Pr$	[-]	Prandtl number
$R_0$	[m]	tyre unloaded radius
$R_a$	[m]	roughness index
$R_c$	[m]	CG trajectory curvature radius
$R_r$	[m]	tyre rolling radius
$R_s$	[m]	curvature radius of asperity apex
SEL		strain energy loss
$T$	[K]	temperature
$T_\infty$	[K]	air temperature at an infinite distance

$T_g$	[K]	glassy transition temperature
$U$	[m/s]	vehicle CG longitudinal velocity
$V$	[m/s]	vehicle CG lateral velocity
$V$	[m/s]	sliding velocity
$V_x$	[m/s]	wheel longitudinal speed
$V_y$	[m/s]	wheel lateral speed
$V_i$	[m <sup>3</sup> ]	i-th node thermal model elementary volume
$VEL$	[m/s]	measured longitudinal speed
$VL$	[m/s]	measured lateral speed
$V_{TOT}$	[m <sup>3</sup> ]	total tread volume in contact with an asperity
$W$	[N]	axle static load
$W$	[m]	tread width
$W_{DISS}$	[W]	dissipated power
$a_x$	[m/s <sup>2</sup> ]	longitudinal acceleration
$a_y$	[m/s <sup>2</sup> ]	lateral acceleration
$a$	[m]	front wheelbase
$ack\%$	[-]	real/geometric maximum available ackermann angle
$b$	[m]	rear wheelbase
$C_{TEMP}$	[rad]	MF temperature shifting parameter
$c_v$	[J/(kg K)]	specific heat at constant volume
$c_p$	[J/(kg K)]	specific heat at constant pressure
$d$	[m]	roll centre height
$h$	[m]	vehicle CG height
$h_{EXH}$	[W/(m <sup>2</sup> K)]	convective heat transfer coefficient with exhaust gas
$h_{forc}$	[W/(m <sup>2</sup> K)]	external air forced convection coefficient
$h_{air}$	[W/(m <sup>2</sup> K)]	natural convection coefficient
$k_{air}$	[W/(m K)]	air thermal conductivity
$l$	[m]	wheelbase
$m$	[kg]	mass
$m_2$	[-]	track rms slope
$n$	[-]	viscoelastic dissipation parameter
$p$	[Pa]	pressure
$q$	[J/(m <sup>3</sup> )]	heat generated per unit of volume
$r$	[rad/s]	yaw rate
$slip_{xT}$	[%]	slip ratio in traction
$slip_{xB}$	[%]	slip ratio in braking
$slip_x$	[%]	generic slip ratio
$t$	[s]	time
$t_F$	[m]	front track
$t_R$	[m]	rear track
$t_p$	[m]	pneumatic trail
$\tan(\delta)$	[-]	tangent of the angle between storage and loss modulus
$v_c$	[m/s]	critical velocity
$v_x$	[m/s]	longitudinal sliding speed
$v_y$	[m/s]	lateral sliding speed
$x_c$		shifted MF ortho-slip variable
$x_s$		shifted MF slip variable
$\alpha$	[rad]	slip angle

$\alpha(T)$	[K]	WLF temperature shift
$\alpha_{AIR}$	[m <sup>2</sup> /s]	air thermal diffusivity
$\alpha_{ROAD}$	[m <sup>2</sup> /s]	road thermal diffusivity
$\beta$	[rad]	vehicle sideslip angle
$\gamma$	[rad]	camber angle
$\delta$	[rad]	nominal steering angle
$\varepsilon$	[-]	strain
$\zeta$	[rad]	effective wheel steering angle
$\lambda$	[m]	roughness wavelength
$\lambda_x$	[rad]	sensor installation angle in xz plane
$\lambda_y$	[rad]	sensor installation angle in yz plane
$\lambda_T$	[-]	MF temperature scaling factor
$\mu$	[-]	friction coefficient or friction function
$\mu_{air}$	[kg/(m s)]	air dynamic viscosity
$\nu$	[m <sup>2</sup> /s]	air kinematic viscosity
$\nu_p$	[-]	Poisson's ratio
$\omega$	[rad/s]	stress angular frequency
$\Omega$	[rad]	angular speed
$\rho$	[kg/m <sup>3</sup> ]	density
$\sigma$	[Pa]	stress
$\tau$	[Pa]	shear stress
$\tau_s$	[-]	nominal steering ratio
$\tau_{s,0}$	[Pa]	interfacial shear strength
$\chi$	[rad]	toe angle
$\psi$	[rad]	yaw angle

## Indices

0	undeformed, static or nominal value
F	front
R	rear
air	air
r	road
x	in x direction
y	in y direction
z	in z direction



## Introduction

The most powerful engine, the most sophisticated aerodynamic devices, the most complex control systems won't be never able to improve vehicle performances if the forces exchanged with the road won't be maximized by a proper employment and knowledge of tyres.

The vehicle interface with the soil is constituted by the sum of small surfaces, wide about as one of our palms, in which tyre/road interaction forces are exchanged. It results then clear how the optimization of tyre behaviour could represent a key-factor in the definition of the best setup of the whole vehicle [1][2]: from a handling point of view, suspensions main role is to make the tyre work in order to improve contact patch exploitation in the widest motion conditions range [3][4]; aerodynamic appendices and active wings are developed with the aim to increase the loads acting at tyre/ground interface, and consequently, braking and traction longitudinal forces and lateral roadholding [5]; safety and stability control devices usually modulate the activation of the braking system in order to act on tyre dynamics, obtaining reductions in stopping distance, optimizing handling and driveability performances and increasing the driver's response effectiveness to unexpected changes in motion conditions [6][7].

The fundamental role that in the last years tyres have played in motorsport and in automotive industry and the growing need to reproduce with a high level of detail the phenomena concerning with vehicle dynamics have given a strong impulse to the research in the field of vehicle systems analysis and modelling [8][9][10][11].

The activities described in the present PhD thesis concern with the study and the investigation of tyre/road interaction phenomena, with particular interest to their modelling in real-time simulation environments. They have been developed thanks to the precious support of the skilled and stimulating academic environment of Industrial Engineering Department of the University of Naples Federico II and of companies (Ferrari GT and Bridgestone Europe), motorsport teams (Ferrari GES and HT Mirage) and research institutes (LaMCoS) that can be doubtless considered as the excellence in everything concerns with automotive research, development, production and performance seeking fields.

Nowadays everyone playing a role in automotive sector is looking for the optimal solution to model and understand tyres behaviour both in experimental and simulation environments. The studies carried out and the developed tools allow to follow a new approach in tyre characterization and vehicle simulation procedures, enabling the complete reproduction of the dynamic response of a tyre and of its frictional and thermodynamic behaviour simply by means of specific track sessions and of few laboratory measurements, representing the bridge between a robust and widespread approach, like Pacejka's one [12], and a totally physical modelling, that satisfies predictive requests and the need of a deeper knowledge about complex phenomena.

After some brief notes about the basics of tyre characteristics and dynamics, the single developed models and procedures will be presented, highlighting their features, describing the path followed for the realization and discussing results and possible applications fields; the final product is composed by the following **four tools**, that can cooperate constituting a multitude of solutions, reported in the final chapter:

- **TRICK (Tyre/Road Interaction Characterization & Knowledge):**  
basically composed by a vehicle model able to process experimental signals acquired from vehicle CAN bus and from sideslip angle estimation additional instrumentation, providing a sort of "virtual telemetry", based on the acquired signals time history and containing force and slip estimations useful to provide tyre interaction characteristics.
- **TRIP-ID (Tyre/Road Interaction Parameters Identification):**  
provides an innovative procedure to identify the Pacejka coefficients starting from the experimental tests carried out measuring global vehicle data during outdoor track sessions. The procedure collects and processes the data provided by TRICK, allowing to eliminate the outlier points, to discriminate among the different tyre wear and thermal phenomena, taking into account the combined slip condition and the effects of vertical load and camber angle on the global grip.
- **TRT (Thermo Racing Tyre):**  
an analytical-physical thermal tyre model developed with the aim to predict the temperature with a high degree of accuracy, able to simulate the high-frequency thermal dynamics characterizing high performance systems. The model is able to estimate the temperature distribution even of the deepest tyre layers, usually not easily measurable on-line, to predict the effects that fast temperature variations induce in visco-elastic materials behaviour, and to take into account the dissipative phenomena related to the tyre deformations.
- **GrETA (Grip Estimation for Tyre Analyses):**  
a tyre/road friction physical model, developed to respond to the needs of motorsport racing teams and tyre manufacturing companies, able to provide an effective calculation of the power dissipated by road asperities indented in tyre tread and taking into account the phenomena involved with adhesive friction, expressed by means of an original formulation whose parameters are identified thanks to dedicated experimental tests.

# 1. The tyre

## 1.1 Description and General Considerations

The tyre is an under pressure, inextensible and deformable casing, made of composite material of polymeric matrix (vulcanized rubber and additives such as carbon black and silica) with reinforcement plies of steel or synthetic fibres [1][13][14].

It has the shape of a solid of revolution (toroidal ring) with the function to bear statically and dynamically a given load, to transmit to the ground the longitudinal and lateral forces necessary to motion, to ensure the directionality of the vehicle enabling the steering and the insertion of it in the driver's desired trajectory, to perform both traction and braking force by means of adherence with the road surface, improve passenger comfort contributing to the vehicle suspension.

Currently, the most common tyre in automotive industry is the tubeless type, lacking of inner tube. The inner side of the tyre is constituted by a special rubber coating, highly airtight, called liner. The parts constituting a tubeless tyre are the followings (Fig. 1.1) [15]:

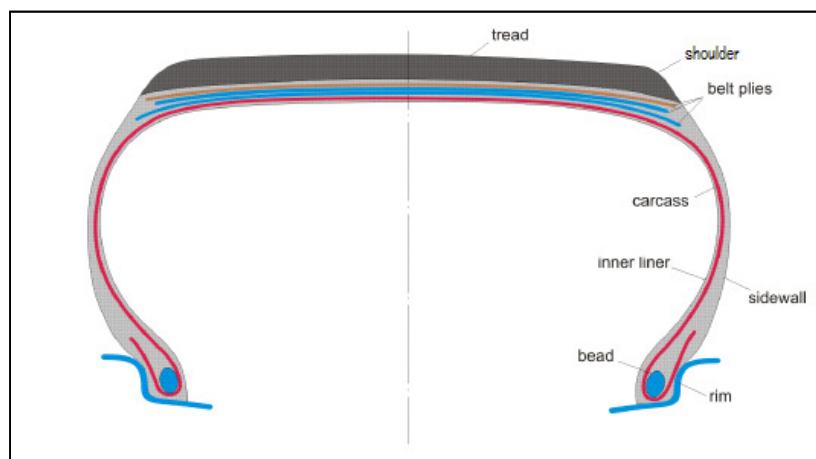


Fig. 1.1 - Tyre structure.

- **Tread:** consists of a rubber compound, commonly styrene-butadiene (SBR) copolymers [16], whose surface is crossed by a "pattern" able to ensure a good grip in both wet and dry conditions, as well as good characteristics of silent running. The pattern is composed by a particular arrangement of full (ribs) and void (grooves) volumes; the latter are designed to channel the water out and away ensuring a "dry" contact between rubber and soil.

- **Shoulder:** is the area including the tread lateral extreme edge and the beginning of the sidewall. A tyre needs to offer good heat dispersal and for this the shoulder section plays a crucial role.

- **Sidewall:** is the area between the shoulder and the bead bundle. It consists of a thin rubber layer, intended to protect the carcass plies against side impacts, such as the sidewalks edges. The sidewall helps to make tyre rigid and improves the ride quality; generally speaking, a high sidewall tyre is more comfortable than a low one as it is more flexible and hence able to better absorb the road unevennesses.

- **Bead**: tyre / rim coupling element; the core of a tyre's bead is made up of several individually rubber-coated steel wires formed into a hoop, that is then provided with a rubber apex. Bead function is to ensure that the tyre sits firmly on the rim, in order to prevent relative rotations. This coupling is particularly critical, considering that all the actions exchanged between tyre and road are transmitted to the vehicle via the bead / rim contact surface that has a very limited extension and therefore is subjected to high stress levels.
- **Inner liner**: is a thin, specially formulated compound placed on the inner surface of tubeless tyres to improve air retention by lowering permeation outwards through the tyre.
- **Belt plies**: restrict expansion of carcass plies, stabilizing the tread area and providing impact resistance. Varying the belt width and angles affects vehicle ride and handling characteristics. Alternate belt constructions with materials other than steel is also often utilized.
- **Carcass (or body plies)**: constitutes the resistant structure, mainly acting in normal interaction, composed of one or more layers of plies placed under the tread (or under belt plies in radial tyres). Every single ply is composed by a series of mutually parallel cords of very durable and at the same time flexible material, surrounded by the vulcanized rubber compound.

Each carcass ply extends from bead to bead, wrapping and transferring on them the stresses generated by inflation pressure and interaction forces. Body plies arrangement (Fig. 1.2) gives the name to the structure of the tyre: nowadays the most commonly employed structure is the radial one, in which the carcass is composed of one or more plies disposed through the meridian planes of the toroid. The radial carcass is made more stable by the belt annular reinforcing structure which runs below the tread. The belt plies have very small inclination angles, between  $5^\circ$  and  $10^\circ$  and absorb the shear stresses which arise in working conditions.

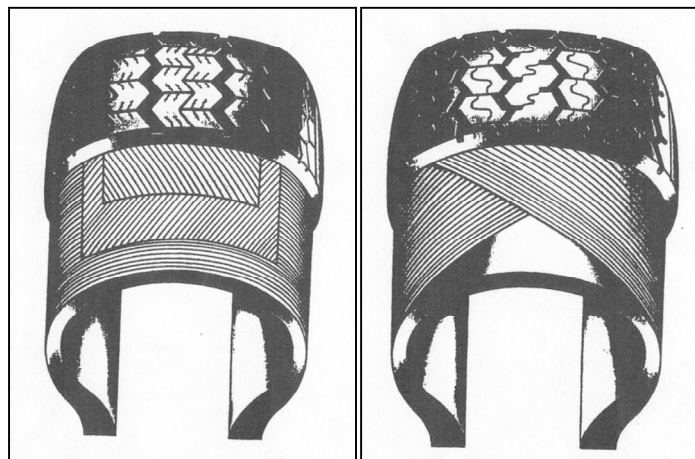


Fig. 1.2 - Radial (left) and diagonal or bias (right) tyre structure.

The other type of structure, still used in some applications for trucks, trailers and farm implements, is called diagonal or bias because the plies cross on the carcass being disposed according to proper inclinations respect to equatorial plane called "crown angles". Note that in these tyres there are not belt plies; therefore it is quite simple to recognize a radial tyre, being the sidewall plies fewer than the tread ones, for the presence in the latter of the belt reinforcements.

The advantages of radial are mainly due to the fact that the tread is independent from the carcass; consequently, the tangential stresses (absorbed by the belt plies) are decoupled from normal ones (absorbed by radial carcass plies), while in bias tyres all stresses decompose according to the crown angles. Furthermore the radial arrangement reduces fatigue and wear: being the sidewall thinner, the material is less subjected to hysteresis, occurring for shear between plies and generating heat to be dissipated.

Radial tyres are characterized by better grip, more stability and a higher braking efficiency, acting as safer than conventional ones; they also allow greater energetic saving (increased durability and fuel economy) and a greater level of comfort (more shock absorption) [1][2].

## 1.2 Historical Notes

In 1844 Goodyear invented the vulcanization process of natural rubber which consisted in manufacturing it in an environment saturated with sulphur under certain conditions of temperature and pressure. This technological step was essential for the subsequent evolution of the tyre, considering that natural rubber exhibits low yield strength and strongly varies its resistance with temperature. The vulcanization, through the sulphur bonds in the polymer chains, allows to natural rubber to increase its strength and its attitude to resist to deformation.

In 1846, Thomson patented an "air wheel": the first prototype of tyre. He had the idea to employ an air chamber in the wheels in order to both reduce the effort of the horses (the work was reduced by 40%) and to cushion noise and harshness. Despite the innovation, Thomson was not understood and his idea had no developments.

Only in 1888, Dunlop, in an attempt to build a tricycle for his son, began to study the wheels. He verified experimentally that between a solid rubber wheel and an hollow one filled with air, the latter bounced more; it was a proof of the excellent elastic behaviour of what would have become the first industrial manufactured tyre. Solid rubber is significantly visco-elastic, retrieving original shape after deformations with strong delay; moreover, being more insulating, cannot easily dissipate the heat generated by hysteresis, degrading consequently very quickly. On the contrary, the air contained in the hollow rubber accelerates the recovery after the deformation and the degradation is lower because the amount of rubber is reduced.

The huge commercial success of the Dunlop tyres was due to a cyclist who first used them and repeatedly won against his rivals who yet adopted solid rubber wheels.

The tyres were originally nailed to the rim; only after time the bead / rim coupling system was developed. Over the years the constructive structure has changed, bringing to the disappear of the inner tubes (which can still be found today for bicycles) and to the progressive diffusion of the radial plies arrangement. Even the colour has changed; initially the tyres were white because natural rubber is white, then the carbon black was added to composition to enhance performance under wear and fatigue and to prevent the action of ultraviolet rays. Finally, to further improve the mechanical properties, the silica and many other materials have been recently added, leading to very complex tyres, constituted by dozens of different compounds.

In the last few years, tyre makers have given a new shape to tyres, developing air-less prototypes. Michelin announced the Tweel in 2005 and presented it recently, while Bridgestone has shown his "Air Free Concept Tyre" at Tokyo Motor Show 2013. The prototypes don't use a traditional wheel hub assembly: a solid inner hub surrounded by polyurethane spokes arrayed in a pattern of wedges mounts to the axle. A shear band is

stretched across the spokes, forming the outer edge of the tyre (the part that comes in contact with the road). The tension of the shear band on the spokes and the strength of the spokes themselves replace the air pressure of a traditional tyre. The tread is then attached to the shear band [17]. It must still be understood if airless tyres will be able to substitute common pneumatic tyres, but they could represent an interesting solution for the advantages that they can offer as concerns punctures and damage resistance.

### 1.3 Sidewall Markings

Automobile tyres are described by an alphanumeric tyre code, which is generally moulded into the sidewall (Fig. 1.3). This code specifies the dimensions of the tyre and some of its key limitations, such as load-bearing ability and maximum speed. Sometimes the inner sidewall contains information not included on the outer sidewall, and vice versa.

The code has grown in complexity over the years, as is evident from the mix of metric and imperial units, and ad-hoc extensions to lettering and numbering schemes. New automotive tyres frequently have ratings for traction, tread wear and temperature resistance (collectively known as The Uniform Tyre Quality Grade (UTQG) ratings).

Most tyres sizes are given using the ISO Metric sizing system. However, some pickup trucks and SUVs use the Light Truck Numeric or Light Truck High Flotation system.

The ISO Metric tyre code consists of a string of letters and numbers, as follows:

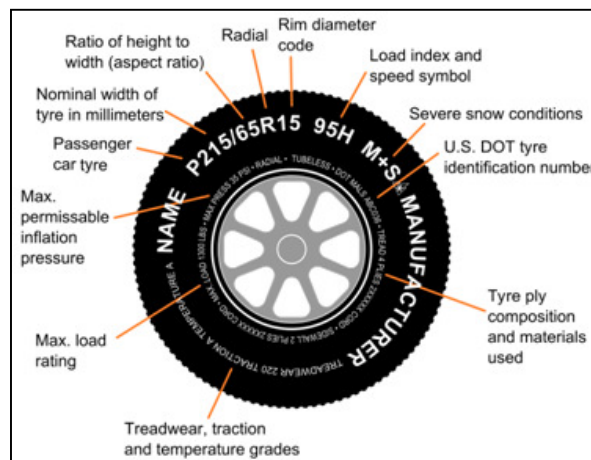


Fig. 1.3 - Tyre sidewall markings.

- An optional letter (or letters) indicating the intended use or vehicle class:
  - P: Passenger Car
  - LT: Light Truck
  - ST: Special Trailer
  - T: Temporary (restricted usage for "Space-Saver" spare wheels)

Use of the letter P indicates that the tyre is engineered to TRA standards and absence of a letter indicates that the tyre is engineered to ETRTO standards. In practice, the standards of the two organizations have evolved together and are fairly interchangeable, but not fully since the Load Index will be different for the same size tyre.

- 3 digit number: the "nominal section width" of the tyre in millimetres; the widest point from both outer edges (sidewall to sidewall). The tyre surface in contact with the road usually has smaller width.
- /: slash character for numbers separation.
- 2 or 3 digit number: the "aspect ratio" of the sidewall height as a percentage of the total width of the tyre. If the information is omitted, it is assumed to be 82% (if written, it should be like xxx/82). If the number is larger than 200, then this is the diameter of the entire tyre in millimetres.
- An optional letter indicating construction of the tyre carcass:
  - B: bias belt
  - D: diagonal
  - R: radial
  - if omitted, then it is a cross ply tyre.
- 1 or 2 digit number: diameter in inches of the rim that the tyres are designed to fit.

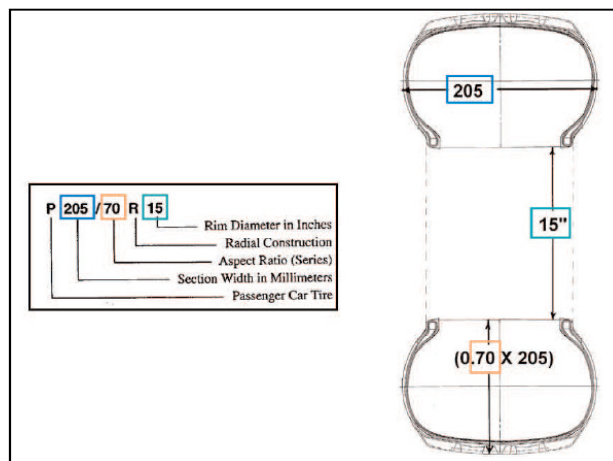


Fig. 1.4 - Tyre size graphic explanation.

- 2 or 3 digit number: load index [18]; some light truck tyres are approved for "dual use", that is they can be run in pairs next to each other. If so, separate load indices will be specified for single and dual usage. Tyres without this designation for dual usage are unsafe to use as such.
- 1 or 2 digit/letter combo: speed rating [18].
- Additional marks: the most common are the followings:
  - M+S or M&S: mud and snow; a tyre that meets the Rubber Manufacturers Association (RMA) and Rubber Association of Canada (RAC) all-season tyre definition. These are all-weather tyres, with self-cleaning tread and above-average traction in muddy or very light snowy conditions, and at low ambient temperatures. Spike tyres have an additional letter, "E" (M+SE).
  - M+T or M&T: mud and terrain; designed to perform in mud or on other terrain that requires additional traction such as on rocks, in deeper snow, and in loose gravel.
  - SFI or Inner: Side Facing Inwards; inside of asymmetric tyres.
  - SFO or Outer: Side Facing Outwards; outside of asymmetric tyres.
  - TWI: Tread Wear Indicator; a device, such as a triangle, located where the tread meets the sidewall. It indicates the location of the raised wear bars in between the tyre tread channels.

- LL: Light Load; tyres for light usage and loads.
- SL: Standard Load; tyre for normal usage and loads.
- XL: eXtra Load; a tyre that allows a higher inflation pressure than a Standard Load tyre, which increases the tyre's maximum load.
- RF: Reinforced - for Euro metric tyres - the term means the same thing as 'Extra Load'.
- Arrows: some tread designs are "directional", and designed to perform better when driven in a specific direction (clockwise or counter-clockwise). Such tyres have an arrow showing which way the tyre should rotate when the vehicle is moving forwards. It is important not to put a "clockwise" tyre on the left hand side of the car or a "counter-clockwise" tyre on the right side.
- DOT code: all tyres for use in the USA have the DOT code, as required by the Department of Transportation (DOT). It specifies the company, factory, mould, batch, and date of production (two digits for week of the year plus two digits for year). JATMA, the Japanese Automotive Tyre Manufacturers Association recommends that all tyres be inspected at five years and that all the ones manufactured more than ten years before be replaced.

## 1.4 Mechanics of Tyres

### 1.4.1 Topology Notes

Tyres are generally required to fulfil the following functions:

- to support the weight of the vehicle;
- to cushion the vehicle over surface irregularities;
- to provide sufficient traction for driving and braking;
- to provide adequate steering control and direction stability.

The study of the mechanics of tyres therefore is of fundamental importance to the understanding of the performance and characteristics of ground vehicles. To describe the behaviour of a tyre and the forces and moments acting on it, it is necessary to define an axis system that serves as a reference for the definition of various parameters. One of the commonly used axis systems recommended by the ISO8855 standard and shown in Fig. 1.5 [19]. The origin of the axis system is the centre of tyre contact (CTC), x axis is the intersection of the wheel plane and the ground plane with a positive direction forward, z axis is perpendicular to the ground plane with a positive direction upward and y axis is in the ground plane, and its direction is chosen to make the axis system orthogonal and right hand. There are three forces and three moments acting on the tyre from the ground: tractive force (or longitudinal force)  $F_x$  is the component in the x direction of the resultant force exerted on the tyre by the road, lateral force  $F_y$  is the component in the y direction, and normal force  $F_z$  is the component in the z direction. "Overturning moment"  $M_x$  is the moment about the x axis exerted on the tyre by the road, "rolling resistance" moment  $M_y$  is the moment about the y axis, and "aligning torque"  $M_z$  is the moment about the z axis.

With this axis system, many performance parameters of the tyre can be conveniently defined; for instance, the longitudinal shift of the centre of normal pressure is determined by the ratio of the rolling resistance moment to the normal load, the lateral shift of the centre of normal pressure is defined by the ratio of the overturning moment to the normal load and the integration of longitudinal shear stresses over the entire contact patch represents the tractive or braking force.

There are two important angles associated with a rolling tyre: "slip angle" and "camber angle": slip angle  $\alpha$  is the angle from the x axis to the velocity vector of the centre of tyre contact, about the z axis; camber angle  $\gamma$  is the angle formed between the xz plane and the wheel plane. Lateral interaction forces at the tyre/ground interface are a function of both the slip angle and the camber angle.

In the following, brief notes about lateral and longitudinal tyre dynamics will be provided; for more detailed analyses the consultation of the wide available bibliography is suggested [8][9][10][12].

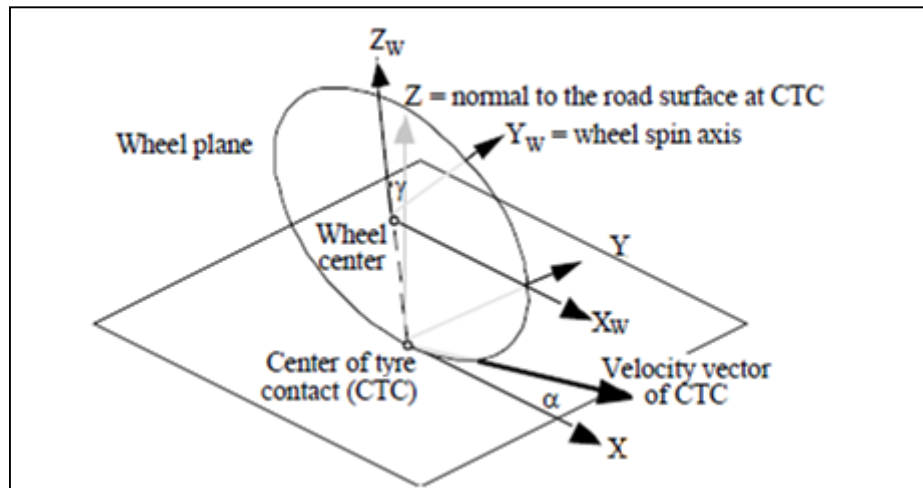


Fig. 1.5 - ISO wheel reference system.

#### 1.4.2 Lateral Interaction

When a tyre is not subject to any force perpendicular to the wheel plane, it will move along this last; if a side force  $F_s$  is applied to a wheel, a lateral force will be developed at the contact patch, and the tyre will move along a path at an angle equal to the slip angle  $\alpha$  with the wheel plane, mainly due to the lateral elasticity of the tyre, as shown in Fig. 1.6.

The lateral force developed at the tyre/ground contact patch is usually called cornering force  $F_{y\alpha}$  when the camber angle of the wheel is zero; the relationship between the cornering force and the slip angle is of fundamental importance to the directional control and stability of road vehicles. When the tyre is moving at a uniform speed, the side force  $F_s$  applied at the wheel centre and the cornering force  $F_{y\alpha}$  developed in the ground plane are usually not collinear: at small slip angles, the cornering force in the ground plane is normally behind the applied side force, giving rise to a torque which tends to align the wheel plane with the direction of motion. This torque is called the "aligning" or "self-aligning torque", and it is one of the restoring moments which help the steered tyre return to the original position after performing a curving manoeuvre. The distance  $t_p$  between the side force and the cornering force is called the "pneumatic trail", and the product of the cornering force and the pneumatic trail determines the self-aligning torque.

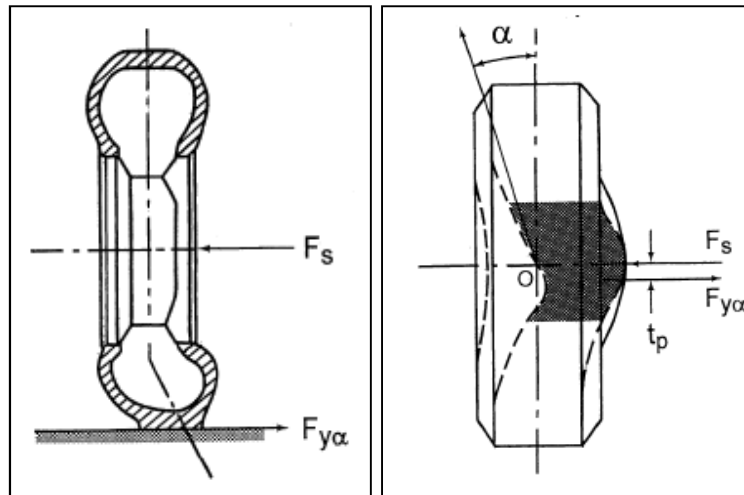


Fig. 1.6 - Tyre cornering behaviour and definition of slip angle  $\alpha$ .

The relationships between the slip angle and the cornering force of various types of tyre under a variety of working conditions have been investigated extensively. Typical plots of the cornering force as a function of the slip angle show that for slip angles below a certain value the cornering force is approximately proportional to the slip angle. Beyond that, the cornering force increases at a lower rate with an increase of the slip angle, and it reaches a maximum value where the tyre begins sliding laterally. For passenger car tyres, the maximum cornering force may occur at a slip angle about three times higher than for racing car tyres (characterized by definitely higher values of lateral stiffness).

A number of factors affect the cornering behaviour of tyres, as for example the normal load: it can be seen that for a given slip angle, the cornering force generally increases with an increase of the normal load. However, the relationship between the cornering force and the normal load is nonlinear (Fig. 1.7); it means that the transfer of load from the inside to the outside tyre during a turning manoeuvre will reduce the total cornering force that a pair of tyres can perform, making so possible to act on the under/oversteering behaviour of the whole vehicle modifying the value of the roll stiffness, able to manage the load transfers [8][20].

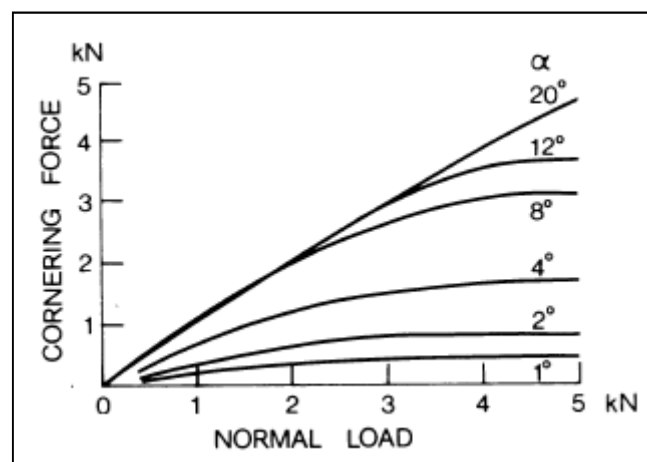


Fig. 1.7 - Effect of normal load on the cornering characteristics of a tyre.

To provide a measure for comparing the cornering behaviour of different tyres, a parameter called "cornering stiffness"  $C_\alpha$  is used. It is a very important parameter in determining the linear range behaviour of vehicles, the area in which most driving is done and is defined as the derivative of the cornering force  $F_{y\alpha}$  with respect to slip angle  $\alpha$  evaluated at zero slip angle:

$$C_\alpha = \left. \frac{\partial F_{y\alpha}}{\partial \alpha} \right|_{\alpha=0} \quad (1.1)$$

The cornering stiffness generally increases with load, but the rate of increase declines as load increases. The peak of the lateral force curve occurs at higher and higher slip angles as the normal force increases. However, if a pseudo coefficient of friction is computed by dividing the peak value of  $F_y$  at each load by the load itself, one discovers that the frictional capability of the tyre declines with increasing load. Thus, high performance vehicles on a dry road will exhibit their maximum cornering ability using large tyres operating at relatively light loads. Inflation pressure usually has a moderate effect on the cornering properties of a tyre, but in general, cornering stiffness increases with an increase of the inflation pressure.

### 1.4.3 Camber Thrust

Camber causes a lateral force usually referred to as "camber thrust"  $F_{y\gamma}$ , and the development of this thrust may be explained in the following way: a free-rolling tyre with a camber angle would revolve about point O, as shown in figure 1.8; however, the cambered tyre in a vehicle is constrained to move in a straight line, developing therefore a lateral force in the direction of the camber in the ground plane. It has been shown that the camber thrust is approximately one fifth the value of the cornering force obtained from an equivalent slip angle for a bias-ply tyre and somewhat less for a radial-ply tyre.

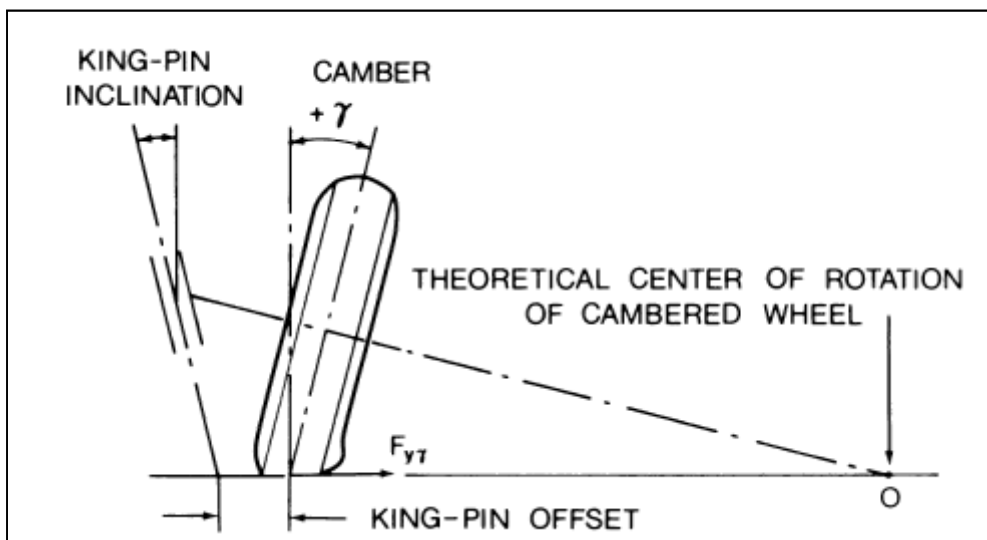


Fig. 1.8 - Behaviour of a cambered tyre.

To provide a measure for comparing the camber characteristics of different tyres, a parameter called "camber stiffness" is often used; it is defined as the derivative of the camber thrust with respect to the camber angle evaluated at zero camber angle:

$$C_{\gamma} = \left. \frac{\partial F_{y\gamma}}{\partial \gamma} \right|_{\gamma=0} \quad (1.2)$$

Similarly to the cornering stiffness, normal load and inflation pressure have an influence on the camber stiffness. It has been calculated that for truck tyres, the value of the camber stiffness is approximately one tenth to one fifth of that of the cornering stiffness under similar operating conditions.

The total lateral force of a cambered tyre operating at a certain slip angle is the sum of the cornering force  $F_{y\alpha}$  and the camber thrust  $F_{y\gamma}$ :

$$F_y = F_{y\alpha} \pm F_{y\gamma} \quad (1.3)$$

If the cornering force and the camber thrust are in the same direction, the positive sign should be used in the above equation. For small slip and camber angles, the relationship between the cornering force and the slip angle and the one between the camber thrust and the camber angle are essentially linear; the total lateral force of a cambered tyre at a slip angle can, therefore, be determined by:

$$F_y = C_{\alpha}\alpha \pm C_{\gamma}\gamma \quad (1.4)$$

As discussed previously, the lateral forces due to slip angle and camber angle produce a torque, but the component due to slip angle, however, is usually much greater and mainly responsible of the aligning torque acting on tyres in ordinary driving conditions.

#### 1.4.4 Longitudinal Interaction

When a driving torque is applied to a tyre, a tractive force is developed at the tyre/ground contact patch, as shown in Fig. 1.9. At the same time, the tyre tread zone in front of and within the contact patch is subjected to compression and a shear deformation of the sidewall is also developed.

As tread elements are compressed before entering the contact region, the distance that the tyre travels when subject to a driving torque will be less than that in free rolling. This phenomenon is usually referred to as longitudinal slip.

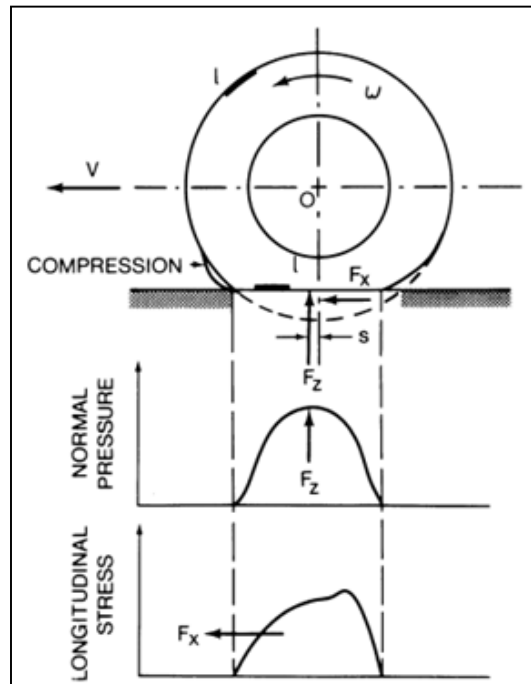


Fig. 1.9 - Behaviour of a tyre under the action of a driving torque.

Tyre longitudinal slip, when a driving torque is applied, is usually defined by:

$$slip_{xT} = \frac{\Omega R_r - V_x}{\Omega R_r} \cdot 100\% \quad (1.5)$$

where  $V_x$  is the longitudinal linear speed of the tyre centre,  $\Omega$  is the tyre angular speed and  $R_r$  is the rolling radius of the free-rolling tyre. When a driving torque is applied,  $R_r\Omega$  is greater than  $V_x$  and a positive value for  $slip_{xT}$  results; if a tyre is rotating at a certain angular speed but the linear speed of its centre is zero, then in accordance with equation 1.5, the longitudinal slip will be 100%. This is often observed on an icy surface, where the driven tyres are spinning at high angular speeds, while the vehicle does not move forward.

As the tractive force developed by a tyre is proportional to the applied wheel torque under steady-state conditions, slip is a function of tractive effort. Generally speaking, at first the wheel torque and tractive force increase linearly with slip because, initially, slip is mainly due to elastic deformation of the tread. A further increase of wheel torque and tractive force results in part of the tread sliding on the ground, that explains why the relationship between the tractive force and the slip is notoriously nonlinear.

Based on available experimental data, the maximum tractive force of a tyre on hard surfaces is usually reached somewhere between 15 and 20% slip. Any further increase of slip beyond that results in an unstable condition, with the tractive effort falling rapidly from the peak value to the pure sliding value.

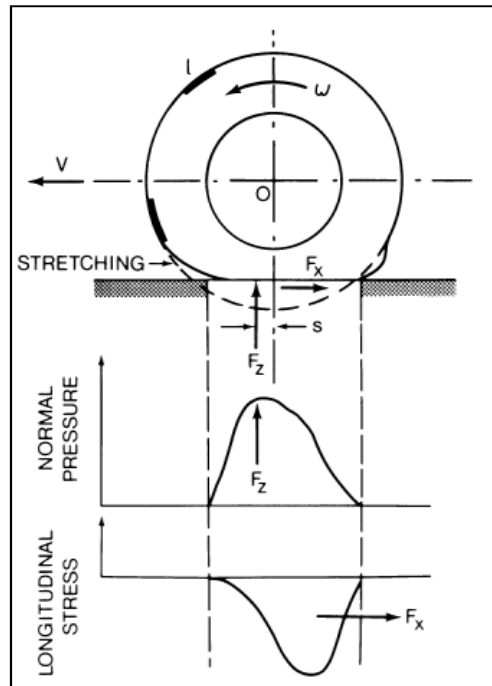


Fig. 1.10 - Behaviour of a tyre under the action of a braking torque.

When a braking torque is applied to the tyre, a stretching of the tread elements occurs prior to entering the contact area, as shown in figure 1.10, in contrast with the compression effect described for a driven tyre. The distance that the tyre travels when a braking torque is applied, therefore, will be greater than that in free rolling and  $slip_{xB}$  is the index usually employed to quantify the skid of the tyre:

$$slip_{xB} = \frac{V_x - \Omega R_r}{V_x} \cdot 100\% \quad (1.6)$$

For a locked wheel, the angular speed is zero, whereas the linear speed of the tyre centre is not zero; under this condition, the skid is denoted 100%.

Both in traction and in braking manoeuvres the contact patch can be split in two different parts: a first one, considered in adherence, in which tangential force is proportional to tread deformation along x direction; a second one, where sliding between tread and ground takes place, linked to normal pressure distribution and dynamic friction coefficient. If no sliding takes place on the contact patch, the relationship between the longitudinal force and the slip can be considered as linear:

$$F_x = C_x slip_x \quad (1.7)$$

in which  $slip_x$  is equal to  $slip_{xT}$  in traction phases and to  $slip_{xB}$  in braking ones and  $C_x$  is tyre longitudinal stiffness, often called "braking stiffness", even in traction phases:

$$C_x = \left. \frac{\partial F_x}{\partial slip_x} \right|_{slip_x=0} \quad (1.8)$$

### 1.4.5 Interaction between Tangential Forces

In the discussion about the cornering behaviour of tyres, the effect of the longitudinal force has not been considered. However, quite often both the side force and the longitudinal force are present, such as braking in a turn. In general, tractive (or braking) effort will reduce the cornering force that can be generated for a given slip angle; the cornering force decreases gradually with an increase of the tractive or braking effort. At low values of tractive (or braking) effort, the decrease in the cornering force is mainly caused by the reduction of the cornering stiffness of the tyre. A further increase of the tractive (or braking) force results in a pronounced decrease of the cornering force for a given slip angle. This is due to the mobilization of the available local adhesion by the tractive (or braking) effort, which reduces the amount of adhesion available in the lateral direction.

It is interesting to point out that if an envelope around each family of curves of figure 1.11 is drawn, a curve approximately semi-elliptical in shape may be obtained. This enveloping curve is often referred to as the friction ellipse.

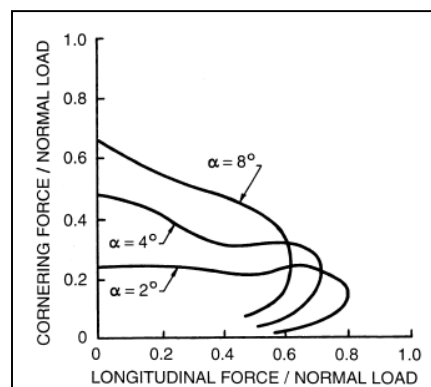


Fig. 1.11 - Effect of longitudinal force on the cornering characteristics of tyres.

The friction ellipse concept is based on the assumption that the tyre may slide on the ground in any direction if the resultant of the longitudinal force (either tractive or braking) and lateral (cornering) force reaches the maximum value defined by the coefficient of friction and by the normal load on the tyre. However, the longitudinal and lateral force components may not exceed their respective maximum values  $F_{x\max}$  and  $F_{y\max}$ , as shown in Fig. 1.12.  $F_{x\max}$  and  $F_{y\max}$  can be identified from measured tyre data and constitute respectively the major and minor axis of the friction ellipse.

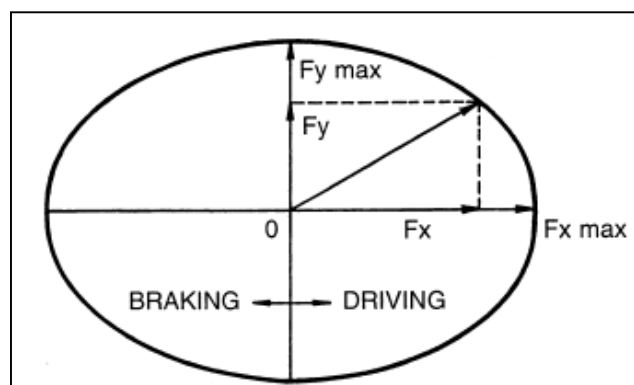


Fig. 1.12 - The friction ellipse concept relating the maximum available cornering force to a given longitudinal force.

## **2. TRICK tool - Tyre/Road Interaction Characterization & Knowledge**

### **2.1 Introduction**

The themes discussed in the previous chapter highlight how the development of a procedure able to estimate tyre forces and slip indices during outdoor test sessions can represent a crucial task for many actors playing a role in automotive industry, such as vehicle manufacturers, vehicle dynamics engineers and tyre production companies.

The main aims for which such kind of tool can be employed are:

- tyre characterization without test bench availability: complete and detailed studies of tyres in a wide range of working conditions are commonly carried out by means of complex, bulky and expensive test benches; the proposed procedure allows to employ the vehicle as a moving lab, easily applying experimental and processing techniques.
- real thermal and frictional tyre characterization: tyre test rigs bring unavoidably to adoption of expedients useful to analyse tyres under controlled conditions, but that sometimes result to be quite far from reality; an example can be the employment of sliding flat belts, able to keep the tyre in rolling, but very different from real road as concerns roughness characteristics, stiffness and thermal conductivity. The possibility to test tyres under real working conditions allows to take into account the real effect of frictional and thermal phenomena, usually neglected or misestimated.
- tyre testing session results analysis: testing departments often employ the opinion of specialized drivers as unique tyre performance evaluation instrument; this essential subjective phase could be supported by a pure objective tool, able to provide an immediate comparison among the different tested tyres.
- race and test performances analysis: tyres directly influence the vehicle performances; consequently, a detailed analysis of the tangential interaction characteristics and of the effects that tyres generate on the whole vehicle behaviour can provide useful suggestions about the direction in which the performance improvement strategies should move.
- tyre models parameters identification: with the availability of a wide data set, eventually acquired by means of dedicated track sessions, it is possible to predict the behaviour of tyres in all its possible working configurations; it allows to identify physical [21][22][23] and empirical [12][24] tyre models parameters, tuning their output in order to fit the experimental ones.

The tool described in the following paragraphs, developed by the Mechanics and Energetics group of Industrial Engineering Department of University of Naples Federico II in collaboration with Ferrari S.p.A<sup>1</sup>. GT department, has been named TRICK: Tyre/Road Interaction Characterization & Knowledge. It is basically composed by a vehicle model able to process experimental signals acquired from vehicle CAN bus and from sideslip angle estimation additional instrumentation (DATRON<sup>2</sup>) providing a sort

---

<sup>1</sup> For industrial confidentiality agreements, plots, diagrams and data will be provided as normalized respect to maximum reported value.

<sup>2</sup> Also commercialized as Correvit, it is a Non-Contact Optical Sensor designed for direct, slip-free measurement of longitudinal and transversal vehicle dynamics (<http://www.corrsys-datron.com/>). An example of application is provided in [25].

of "virtual telemetry", based on the acquired signals time history and stored in a MATLAB matrix variable "DATA" structured as follows:

nr.	Channel	U.O.M.	Description
1	Time	[s]	time
2	Distance	[m]	run distance from the start of acquisition
3	Speed	[km/h]	vehicle absolute speed
4	WheelSpeed_LF	[rpm]	left front wheel angular speed
5	WheelSpeed_RF	[rpm]	right front wheel angular speed
6	WheelSpeed_LR	[rpm]	left rear wheel angular speed
7	WheelSpeed_RR	[rpm]	right rear wheel angular speed
8	LongSlidingSpeed_LF	[m/s]	left front wheel longitudinal sliding speed
9	LatSlidingSpeed_LF	[m/s]	left front wheel lateral sliding speed
10	LongSlidingSpeed_RF	[m/s]	right front wheel longitudinal sliding speed
11	LatSlidingSpeed_RF	[m/s]	right front wheel lateral sliding speed
12	LongSlidingSpeed_LR	[m/s]	left rear wheel longitudinal sliding speed
13	LatSlidingSpeed_LR	[m/s]	left rear wheel lateral sliding speed
14	LongSlidingSpeed_RR	[m/s]	right rear wheel longitudinal sliding speed
15	LatSlidingSpeed_RR	[m/s]	right rear wheel lateral sliding speed
16	RollingRadiusF	[m]	front tyre effective rolling radius
17	RollingRadiusR	[m]	rear tyre effective rolling radius
18	Fz_LF	[N]	left front tyre vertical force
19	Fx_LF	[N]	left front tyre longitudinal force
20	Fy_LF	[N]	left front tyre lateral force
21	Fz_RF	[N]	right front tyre vertical force
22	Fx_RF	[N]	right front tyre longitudinal force
23	Fy_RF	[N]	right front tyre lateral force
24	Fz_LR	[N]	left rear tyre vertical force
25	Fx_LR	[N]	left rear tyre longitudinal force
26	Fy_LR	[N]	left rear tyre lateral force
27	Fz_RR	[N]	right rear tyre vertical force
28	Fx_RR	[N]	right rear tyre longitudinal force
29	Fy_RR	[N]	right rear tyre lateral force
30	Camber_LF	[deg]	left front wheel camber angle
31	Camber_RF	[deg]	right front wheel camber angle
32	Camber_LR	[deg]	left rear wheel camber angle
33	Camber_RR	[deg]	right rear wheel camber angle
34	SurfTemp_LF	[Celsius]	left front tyre measured surface temperature
35	SurfTemp_RF	[Celsius]	right front tyre measured surface temperature
36	SurfTemp_LR	[Celsius]	left rear tyre measured surface temperature
37	SurfTemp_RR	[Celsius]	right rear tyre measured surface temperature
38	Delta	[deg]	driver steering angle
39	Ay	[g]	vehicle lateral acceleration
40	LongSlip_FL	[%]	left front tyre slip ratio
41	LongSlip_FR	[%]	right front tyre slip ratio

42	LongSlip_RL	[%]	left rear tyre slip ratio
43	LongSlip_RR	[%]	right rear tyre slip ratio
44	SlipAngle_FL	[deg]	left front tyre slip angle
45	SlipAngle_FR	[deg]	right front tyre slip angle
46	SlipAngle_RL	[deg]	left rear tyre slip angle
47	SlipAngle_RR	[deg]	right rear tyre slip angle
48	RollRes_LF	[N]	left front tyre rolling resistance force
49	RollRes_RF	[N]	right front tyre rolling resistance force
50	RollRes_LR	[N]	left rear tyre rolling resistance force
51	RollRes_RR	[N]	right rear tyre rolling resistance force
52	Ax	[g]	vehicle longitudinal acceleration
53	Yaw Rate	[deg/s]	vehicle yaw rate
54	Beta	[deg]	vehicle sideslip angle
55	U	[m/s]	vehicle longitudinal velocity
56	V	[m/s]	vehicle lateral velocity

Table 2.1 - Structure of the "virtual telemetry" DATA matrix.

## 2.2 Vehicle model

### 2.2.1 Basic hypotheses and reference system

The vehicle has been modelled using an 8 degree of freedom (DOF) quadricycle model. In particular:

- 3 DOF refer to in plane vehicle body motions (longitudinal, lateral and yaw motions)
- 4 DOF to wheel rotations
- 1 DOF to the steering angle

Moreover, suspensions and steering system kinematics and compliances have been modelled by means of lookup tables based on multibody simulation data, allowing to take into account roll angle, front and rear wheels toe and camber variations as a function of vehicle longitudinal and lateral accelerations.

A wide and detailed description of vehicle characteristics, such as drag ( $C_x$ ) and downforce ( $C_z$ ) aerodynamic coefficients, tyres rolling resistance parameters and ackermann steering coefficients, gives the possibility to model dynamic effects commonly neglected because of their intrinsic complexity, but essential in an interaction characterization activity.

To describe the vehicle motions two coordinate systems have been introduced: one earth-fixed ( $X' ; Y'$ ), the other ( $x ; y$ ) integral to the vehicle as shown in Fig. 2.1. With reference to the same figure,  $v$  is the centre of gravity (CG) absolute velocity referred to the earth-fixed axis system and  $U$  (longitudinal velocity) and  $V$  (lateral velocity) are its components in the vehicle axis system;  $r$  is the yaw rate evaluated in the earth fixed system,  $\beta$  is the vehicle sideslip angle,  $F_{x_i}$  and  $F_{y_i}$  are respectively longitudinal and lateral components of the tyre-road interaction forces. The front and rear wheel tracks are indicated with  $t_F$  and  $t_R$ , while the distances from front and rear axle to the centre of gravity are represented by  $a$  and  $b$ , respectively. The steer angle of the front tyres is denoted by  $\delta$ , while the rear tyres are supposed non-steering.

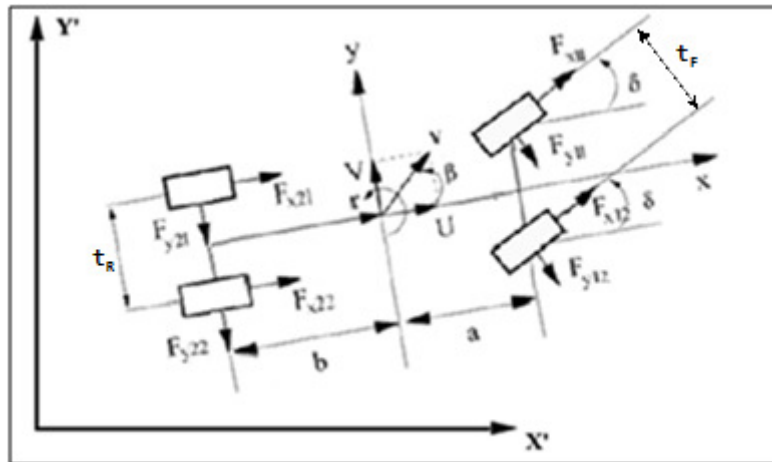


Fig. 2.1 - Coordinate systems.

As concerns tyre/road tangential forces, they are considered as acting from the tyres on the ground. Vertical loads, for reasons of coherence with ISO reference system [19], employed in Pacejka tyre models, are in ordinary conditions of tyre in contact with road, minor than 0. Camber and toe angles are considered in ISO reference system.

### 2.2.2 Input channels

TRICK tool, by means of a specifically developed GUI (graphical user interface), loads and processes input channels exported from the acquiring system (DEWESOFT) as MATLAB variables (files \*.mat), properly named as follows (Fig. 2.2):

<input type="checkbox"/>	Data1_BETA
<input type="checkbox"/>	Data1_LWS_Angle
<input type="checkbox"/>	Data1_LatAcceleration
<input type="checkbox"/>	Data1_LongAcceleration
<input type="checkbox"/>	Data1_Time
<input type="checkbox"/>	Data1_VEL
<input type="checkbox"/>	Data1_VL
<input type="checkbox"/>	Data1_VRD_LH__Wheel_Speed_Left
<input type="checkbox"/>	Data1_VRD_LV__Wheel_Speed_Left
<input type="checkbox"/>	Data1_VRD_RH__Wheel_Speed_Right
<input type="checkbox"/>	Data1_VRD_RV__Wheel_Speed_Right
<input type="checkbox"/>	Data1_YawRate

Fig. 2.2 - TRICK Input Channels.

Channels contents are:

- Data1\_BETA: vehicle sideslip Angle - Datron output [rad]
- Data1\_LWS\_Angle: driver's steering angle - CAN bus<sup>3</sup> output [rad]
- Data1\_LatAcceleration: vehicle lateral acceleration - CAN bus output [m/s<sup>2</sup>]
- Data1\_LongAcceleration: vehicle longitudinal acceleration - CAN bus output [m/s<sup>2</sup>]

<sup>3</sup> Controller Area Network bus, a vehicle bus standard designed to allow microcontrollers and devices to communicate with each other within a vehicle without a host computer.

- Data1\_Time: [s]
- Data1\_VEL: vehicle longitudinal velocity - Datron output [m/s]
- Data1\_VL: vehicle lateral velocity - Datron output [m/s]
- Data1\_VRD\_LH<sup>4</sup>\_\_Wheel\_Speed\_Left: rear left wheel speed - CAN bus output [m/s]
- Data1\_VRD\_LV<sup>5</sup>\_\_Wheel\_Speed\_Left: front left wheel speed - CAN bus output [m/s]
- Data1\_VRD\_RH\_\_Wheel\_Speed\_Righ: rear right wheel speed - CAN bus output [m/s]
- Data1\_VRD\_RV\_\_Wheel\_Speed\_Righ: front right wheel speed - CAN bus output [m/s]
- Data1\_YawRate: CAN bus output [rad/s]

Notice that wheel speeds are expressed in [m/s] because their CAN signal is equal to angular speed, measured by phonic wheel, multiplied by effective rolling radius, manually set in vehicle control unit during its initialization.

Even if the tool has been developed enabling reference system variations and offsets corrections, input channels would be preferably acquired and processed according with reference system shown in figure 2.3; measured accelerations refer to inertial ones, wheel speeds are positive for rotations able to make the vehicle move with positive longitudinal velocity.

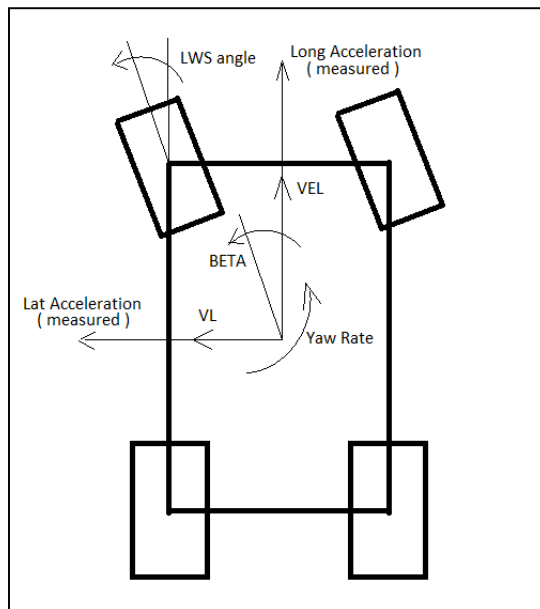


Fig. 2.3 - TRICK input channels reference system.

### 2.2.3 Input parameters

A reliable vehicle description is essential for a correct TRICK employment; in table 2.2 the necessary parameters and characterization data are reported:

Vehicle Data	Variable Name	U.O.M.
Front Tyre Sidewall Markings		
Rear Tyre Sidewall Markings		
Front Tyre Unloaded Radius	R0 <sub>F</sub>	[m]

4 From german, Hinterachse: rear axle.

5 From german, Vorderachse: front axle.

Rear Tyre Unloaded Radius	$R_{0R}$	[m]
Front Tyre Effective Rolling Radius	$R_{rF}$	[m]
Rear Tyre Effective Rolling Radius	$R_{rR}$	[m]
Dry Vehicle Mass	$m$	[kg]
Liquids Mass - Full Tanks	$M_L$	[kg]
Front Wheel + Tyre Mass	$M_{WF}$	[kg]
Rear Wheel + Tyre Mass	$M_{WR}$	[kg]
Vehicle Moment of Inertia about z-axis	$J_z$	[kg m <sup>2</sup> ]
Front Wheel Moment of Inertia about rotation axis	$I_{WF}$	[kg m <sup>2</sup> ]
Rear Wheel Moment of Inertia about rotation axis	$I_{WR}$	[kg m <sup>2</sup> ]
Wheelbase	$l$	[m]
Front Wheelbase	$a$	[m]
Rear Wheelbase	$b$	[m]
Front Track	$t_F$	[m]
Rear Track	$t_R$	[m]
Centre of Gravity Height	$h$	[m]
Front Axle Roll Stiffness	$K_{\Phi F}$	[N/rad]
Rear Axle Roll Stiffness	$K_{\Phi R}$	[N/rad]
Nominal Steering Ratio	$\tau_s$	[-]
Vehicle Master Section	$A_v$	[m <sup>2</sup> ]
Cx	$C_x$	[-]
Cz Front	$C_{zF}$	[-]
Cz Rear	$C_{zR}$	[-]
Roll Centre Height (at Centre of Gravity abscissa)	$d$	[m]
Static Camber Angle Front	$\gamma_{0F}$	[rad]
Static Camber Angle Rear	$\gamma_{0R}$	[rad]
Static Toe Angle Front	$\chi_{0F}$	[rad]
Static Toe Angle Rear	$\chi_{0R}$	[rad]
Real / Geometric maximum available Ackermann Angle	$ack\%$	[-]
Datron distances from CG (x, y, z)	$b_x, b_y, b_z$	[m, m, m]
<b>Rolling Resistance Curves</b>		
<b>Elasto-Kinematic Suspensions Characterization</b>		
<b>Axle Compliances Characterization</b>		

Table 2.2 - Vehicle characterization necessary data.

As concerns last three points, data can be provided by means of numeric charts, obtained from Multibody simulations or dedicated test sessions, reporting the following signals:

- for Rolling Resistance Curves (Fig. 2.4):
  - Wheel Vertical Load
  - Vehicle Speed
  - Rolling Resistance Force
- for Elasto-Kinematic Suspensions Characterization (Fig. 2.5 and 2.6):

- Lateral Acceleration
- Wheels Camber Angle
- Wheels Toe Angle
- for Axle Compliances Characterization (Fig. 2.7):
  - Axle Lateral Force
  - Steering Angle Variation

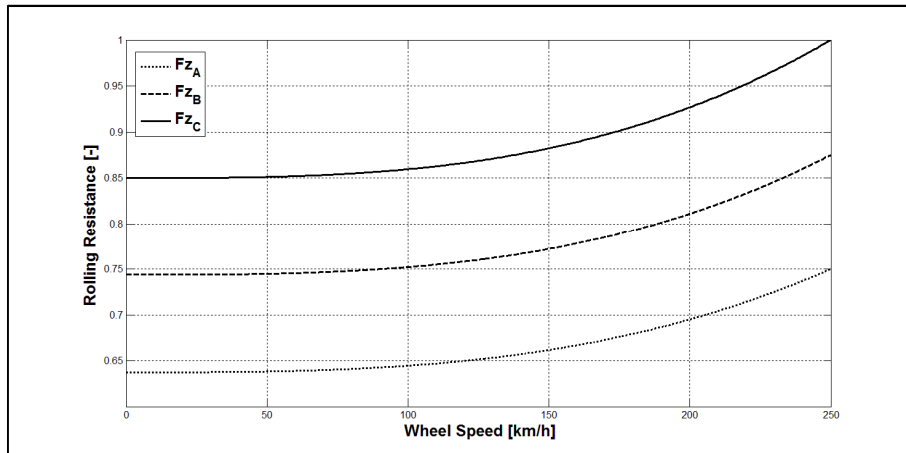


Fig. 2.4 - Rolling resistance curves at three different vertical loads ( $F_{zA} < F_{zB} < F_{zC}$ ).

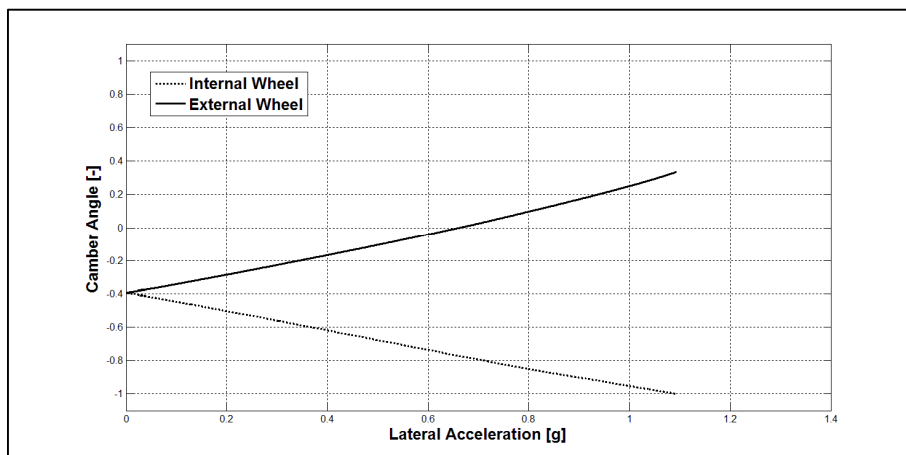


Fig. 2.5 - Camber angle at increasing lateral acceleration - ISO reference system.

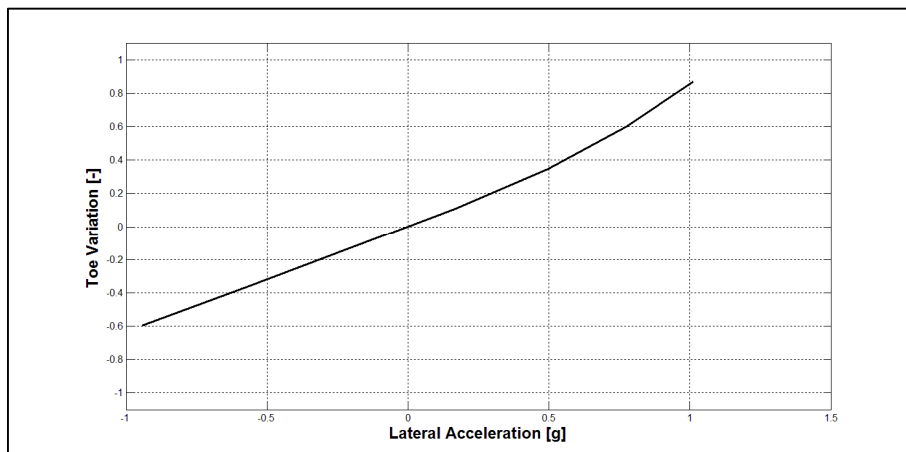


Fig. 2.6 - Toe angle at increasing lateral acceleration - ISO reference system.

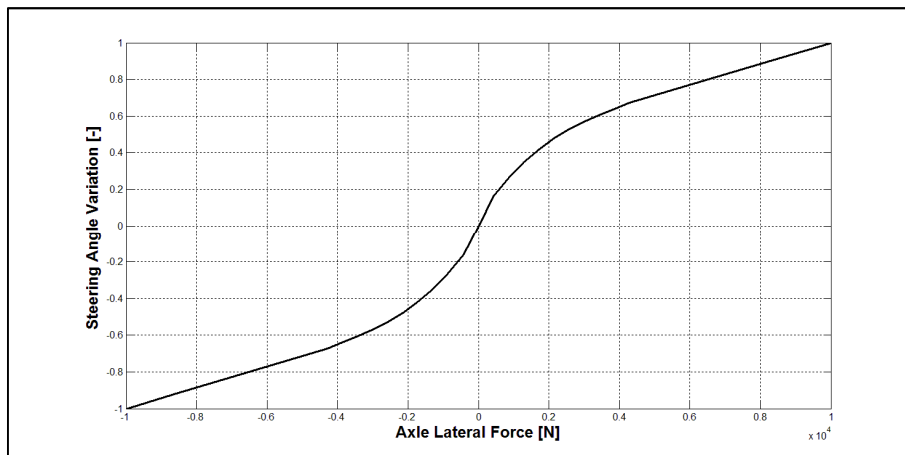


Fig. 2.7 - Steering angle variation

### 2.2.4 Test Procedure

Data useful to identify tyre interactions have to be acquired during dedicated track test sessions; the aim of the test routine reported in table 2.3 is to investigate tyre behaviour in the widest possible working conditions range. In particular, it is important to focus on manoeuvres that highlight the different tyre road interactions:

- pure longitudinal:
  - global sliding start on straight road
  - wheel blocking brake manoeuvre on straight road
- pure lateral:
  - curves performed at null longitudinal forces (different from power-off manoeuvres; traction must be present and able to contrast rolling resistances, making the tyre work in pure rolling conditions). Performing this kind of manoeuvre at as high as possible slip angles provides very useful indications about the shape of the lateral interaction characteristic and about the non-linear behaviour of the whole tyre.
- combined longitudinal and lateral:
  - track laps, run at different speeds and driving styles; in particular, it is important to remember that the main goal is to keep tyre at high exertion levels, adopting a driving style characterized by high sliding and sideslip angle values (electronic controls deactivation could help an expert driver to reach tyre limits and to explore a wider working range, experiencing the phases of incipient instability, in which tyre exhibits a strongly non-linear behaviour).

In order to analyse performances degradation caused by wear, tyres should start the test in brand-new conditions; DATRON employment, because of its optical working principle, is limited to dry tracks; a substitutive solution can be provided by sideslip angle estimation observers [26] or virtual sensors [27], but their full reliability still remains to be evaluated.

Manoeuvre Description	Aim
3 seconds standing vehicle	offset postprocessing correction
3 seconds in straight road at 50Km/h 3 seconds in straight road at 100Km/h	offset postprocessing correction

global sliding start on straight road	pure longitudinal
slow driving	tyres cooling
global sliding start on straight road	pure longitudinal
slow driving	tyres cooling
wheel blocking brake manoeuvre on straight road from 100km/h	pure longitudinal
slow driving	tyres cooling
wheel blocking brake manoeuvre on straight road from 100km/h	pure longitudinal
slow driving	tyres cooling
2 laps - curves in pure rolling	pure lateral - low tyre temperature
2 laps - medium speed	tyres heating
2 laps - high speed	optimal grip temperature - overheating
slow driving	tyres cooling
2 laps - low speed	linear tyre behaviour
2 laps - curves in pure rolling	pure lateral - low tyre temperature
2 laps - medium speed	tyres heating
2 laps - high speed	optimal grip temperature - overheating
slow driving	tyres cooling
2 laps - high lateral	maximum lateral exertion - nonlinear tyre behaviour
2 laps - high speed	wear effects

Table 2.3 - Tyre tests track procedure.

Observing test procedure, it is possible to notice how it has been defined in order to collect data at different tyre temperature and wear conditions. In chapter 6 analyses of this kind of data (Fig. 2.35) and models tuning and validation results obtained with them will be shown and discussed.

### 2.2.5 Input processing, diagnostics and signal correction

Acquired data, because of measurement noise, electromagnetic disturbances and high frequency vibrations, often contain information not directly linked with the phenomena involved in vehicle dynamics field. For this reason, a preliminary essential operation is a filtering of the channels that have to be processed. A Butterworth filter, employed in MATLAB command "filtfilt" [28], has been chosen; it has been designed in order to be a third order, 5 Hz low-pass filter, with a Nyquist normalizing frequency depending on sample rate, commonly equal to 50 or 100 Hz.

As an example, for a lateral acceleration signal the comparison between pre and post filtering data is the following (Fig. 2.8):

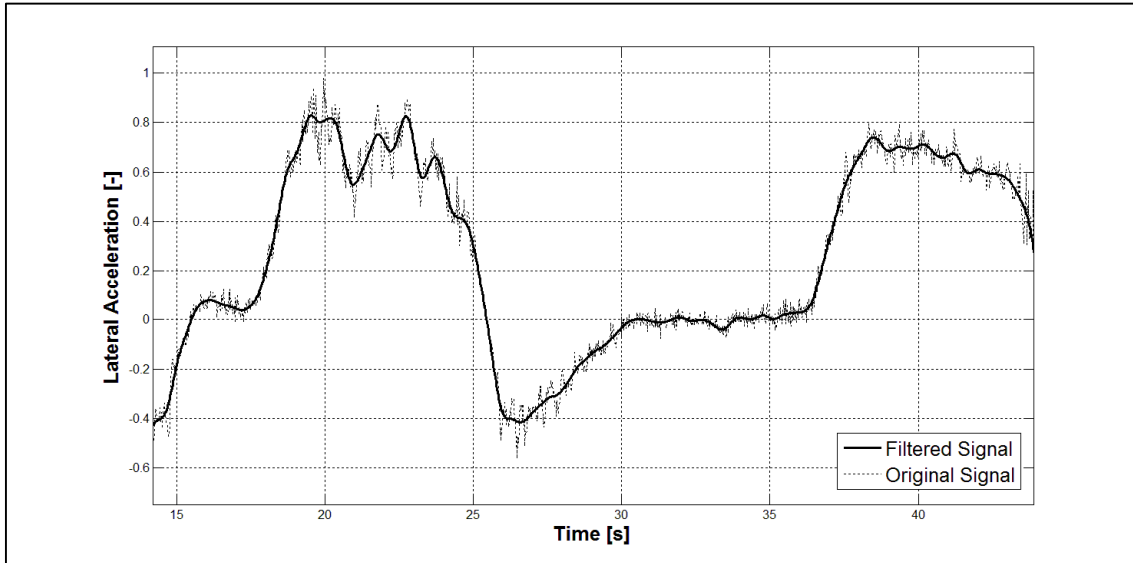


Fig. 2.8 - Effect of filtering on lateral acceleration acquired signal.

Vehicle onboard instrumentation is unavoidably installed with misalignments between its own reference system and the vehicle one; for this reason it is possible that, for example, if the tri-axial accelerometer is not exactly localized in the vehicle centre of gravity or its principal axes are not perfectly parallel to the vehicle ones, a certain amount of gravitational acceleration could be measured as longitudinal or lateral acceleration, making the following operations affected by miscalculations. Detecting such kind of error sources is fundamental to have a robust and reliable starting dataset.

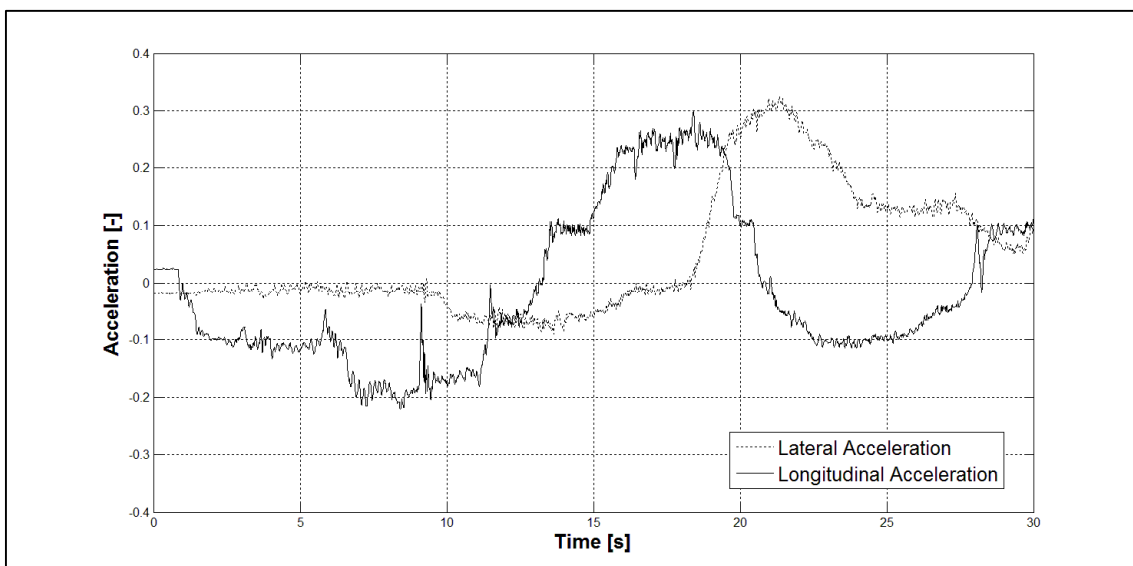


Fig. 2.9 - Longitudinal and lateral acceleration acquired signals.  
Initial offsets are clearly noticeable.

The starting 0.84 s of the accelerations time-history shown in figure 2.9 refer to vehicle null velocity conditions; it is possible to notice that during this phase, accelerations mean values  $a_{x0}$  and  $a_{y0}$  are different from zero and this could be caused by a not proper sensor installation.

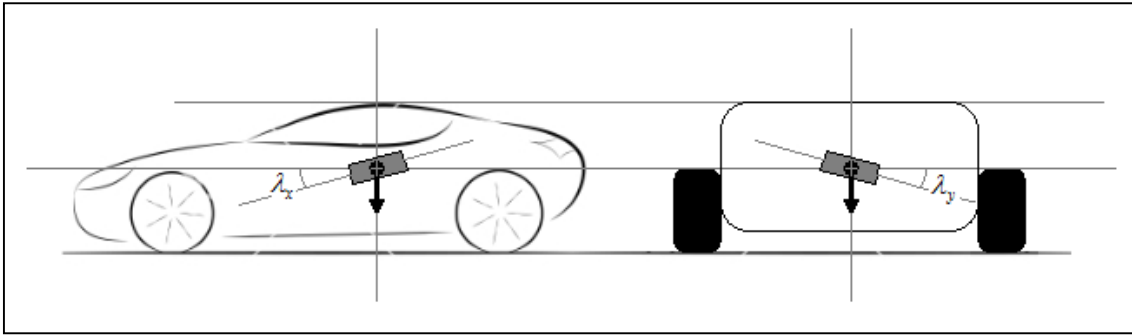


Fig. 2.10 - Accelerometer inclination angles in xz and yz planes.

Accelerometer inclination angles (Fig. 2.10),  $\lambda_x$  in xz plane and  $\lambda_y$  in yz plane, can be estimated as follows:

$$\begin{aligned}\lambda_x &= \sin^{-1}\left(\frac{a_{x0}}{g}\right) \\ \lambda_y &= \sin^{-1}\left(\frac{a_{y0}}{g}\right)\end{aligned}\quad (2.1)$$

consequently, in the hypothesis of horizontal road, the accelerations measured values can be corrected taking into account of the installation inclination angles:

$$\begin{aligned}a_x &= \frac{\text{Data1\_LongAcceleration} - a_{x0}}{\cos(\lambda_x)} \\ a_y &= \frac{\text{Data1\_LatAcceleration} - a_{y0}}{\cos(\lambda_y)}\end{aligned}\quad (2.2)$$

To ensure offsets correction data availability, the first step of the test procedure consists in 3 seconds at standing vehicle. Further signal corrections are possible by means of data collected during this step: wheel rotation speeds are supposed to be null at standing vehicle; otherwise, they can be nullified manually subtracting offset values.

Second test procedure step consists in 3 seconds in straight road; this kind of test allows to detect the presence of further offsets in steering, yaw rate and DATRON sensors. During straight motion, steering angle and yaw rate must be equal to zero; otherwise, they also can be nullified subtracting offset values. As concerns DATRON measurements, they can be affected by error if instrument axes are not parallel to vehicle ones; defining  $\lambda_D$  DATRON inclination angle in xy plane, it can be estimated, referring to figure 2.11, by means of longitudinal VELO and lateral VLO velocity measured mean values in straight stationary manoeuvres:

$$\lambda_D = \tan^{-1}\left(\frac{VLO}{VELO}\right)\quad (2.3)$$

It allows to correct DATRON measurements as follows:

$$\begin{bmatrix} VEL \\ VL \end{bmatrix} = \begin{bmatrix} \cos(\lambda_D) & \sin(\lambda_D) \\ -\sin(\lambda_D) & \cos(\lambda_D) \end{bmatrix} \begin{bmatrix} Data1\_VEL \\ Data1\_VL \end{bmatrix} \quad (2.4)$$

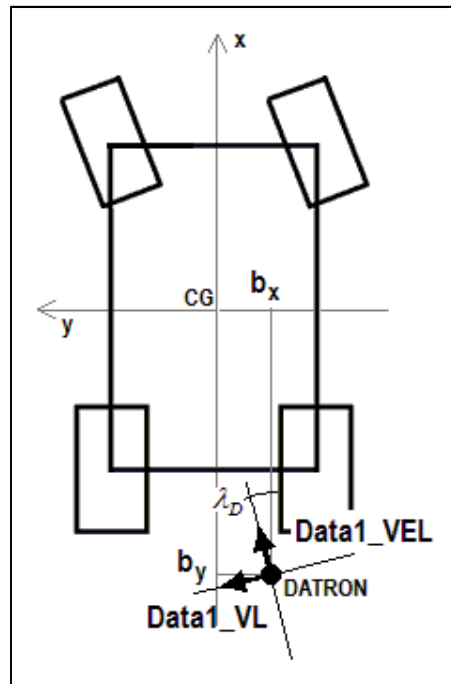


Fig. 2.11 - DATRON inclination angle in xy plane.

Sensors output can be affected not only by errors that can be treated as constant signal offsets, due to incorrect installation, but also by an eventual progressive measurement degradation to consider as a signal gain that has to be estimated and corrected. As concerns yaw rate, an effective method to solve the problem can be based on the fact that at the end of each track lap, yaw angle in the absolute system (X'; Y') must be equal to  $\pm 2\pi$  (depending from track drive direction), in the realistic hypothesis that the vehicle crosses the end lap line in  $U \gg V$  conditions.

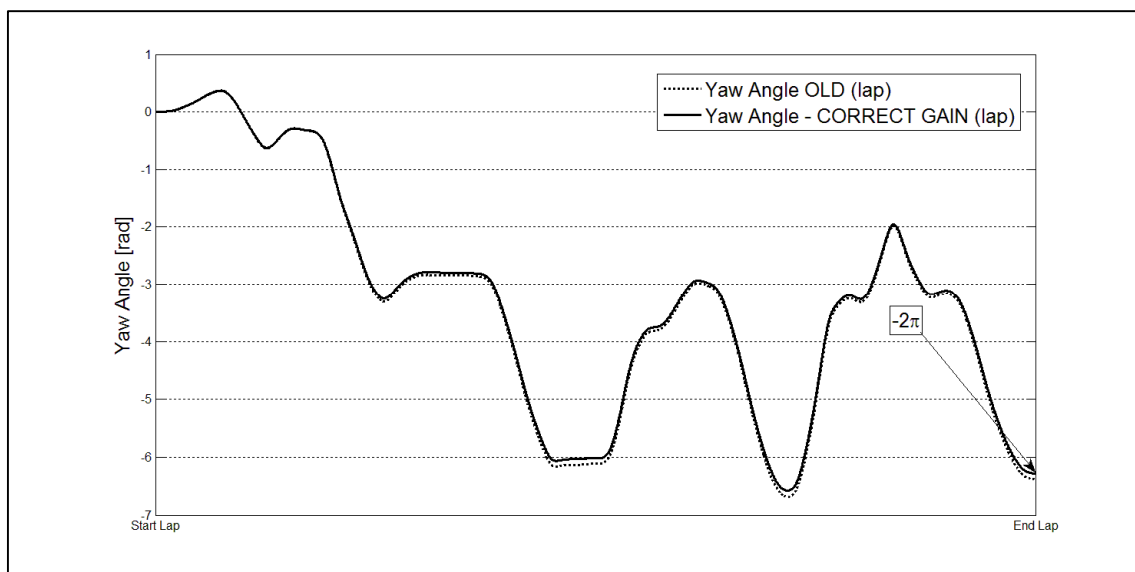


Fig. 2.12 - Yaw angle before and after lap correction.

Isolating a lap, it is possible, integrating yaw rate signal, to rebuilt yaw angle time-history; last yaw angle value  $\psi_{END}$ , that should be equal to  $\pm 2\pi$ , gives information about yaw rate signal time deviation that has to be corrected<sup>6</sup>. Corrective factor  $K_r$  can be estimated as:

$$K_r = \text{sign}(\psi_{END}) \frac{\psi_{END}}{2\pi} \quad (2.5)$$

and by means of it, yaw rate signal to employ in the procedure becomes (Fig. 2.12):

$$r = \dot{\psi} = \frac{\text{Data1\_YawRate}}{K_r} \quad (2.6)$$

As noticeable from figure 2.11, DATRON is not mounted in the neighbourhood of centre of gravity; it is commonly installed in proximity of an axle by means of a rigid removable structure, that makes it move integral with vehicle. In order to employ DATRON to know vehicle speed it is necessary to elaborate its measurements taking into account of distances from centre of gravity and of yaw rate effect. Once made yaw rate signal more reliable, rigid body kinematics equations allow to determine CG velocity in the following way:

$$\begin{aligned} U &= VEL + rb_y \\ V &= VL + rb_x \end{aligned} \quad (2.7)$$

in which  $b_x$  and  $b_y$  are the DATRON coordinates in the vehicle coordinates system. It is important that during vehicle instrumentation these coordinates are carefully measured, because a wrong vehicle CG velocity calculation can easily cause sideslip angle and tyres slip angles misestimation.

Once determined CG velocity components, it is possible to deperate also longitudinal and lateral acceleration signals from their time deviation (gain correction already operated on yaw rate signal), and in some way, from road inclination effects, basing on information deducted by DATRON measurements.

As concerns longitudinal acceleration, it is possible to compare the measured value with the derivative of CG longitudinal velocity (Fig 2.13); multiple linear regression ("regress" MATLAB command [29]) between the two signals allows to identify the gain value, to employ as correcting factor, that optimises the correspondence (Fig. 2.14).

---

<sup>6</sup> The described yaw rate correction method can be applied only in case the track does not have crossing points (bridges or underpasses, like in Fiorano or Suzuka tracks), because in such cases  $\psi_{END}$  is equal to zero.

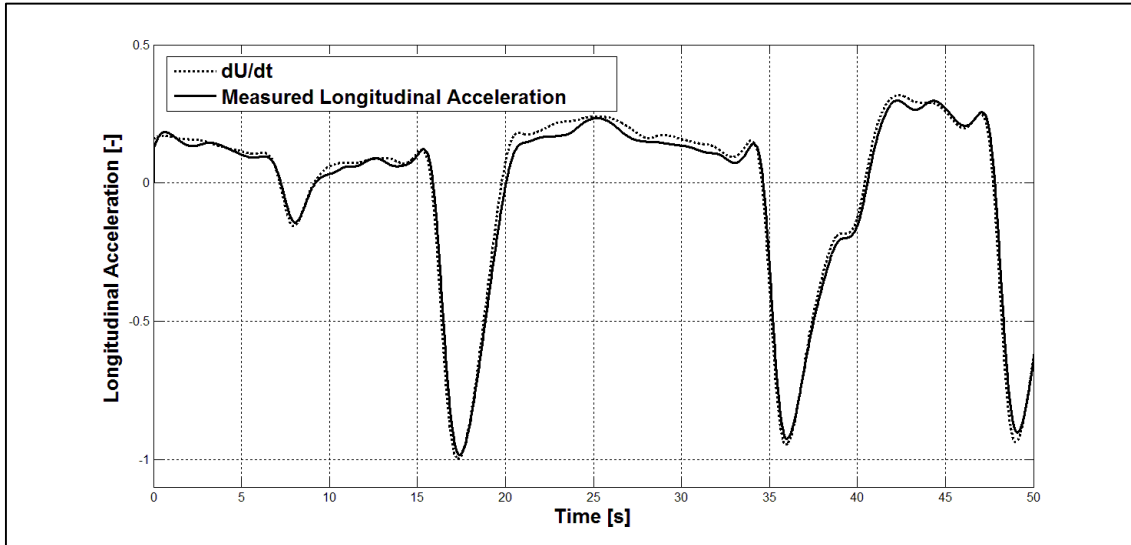


Fig. 2.13 - Comparison between longitudinal acceleration measured by accelerometer and DATRON longitudinal speed derivative.

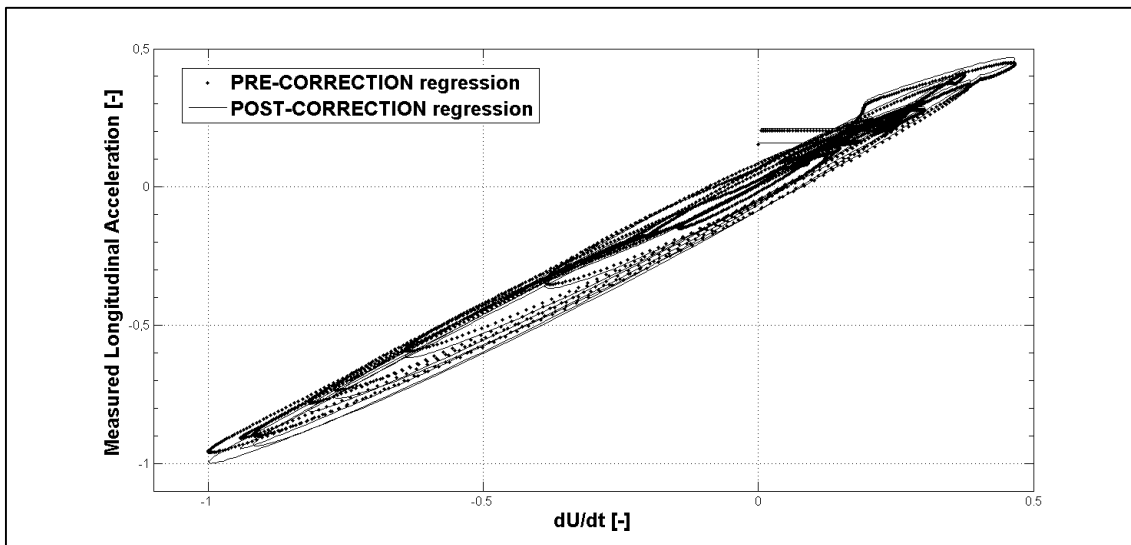


Fig. 2.14 - Result of the correction procedure operated by means of the regression between longitudinal acceleration measured by accelerometer and DATRON longitudinal speed derivative.

In analogous way, it is possible to "scale" lateral acceleration measured signal, on the basis of equation:

$$a_y = Ur + \dot{V} \quad (2.8)$$

In this case it is firstly very important to provide a clean lateral velocity signal, that, as a rough DATRON output, is heavily affected by noise and vibrations. Figure 2.15a shows the difference between  $V$  signal processed with a too light filter and the same signal obtained after proper filtering design. The consequences of the derivative operation are shown in Fig 2.15b, that highlights how an incorrect data filtering can cause a dramatic lost of useful information, making the following procedure useless. The comparison between the quantities linked by equation (2.8) is reported in figure 2.16; it appears clear that, although the main part of lateral acceleration is constituted by the

product between yaw rate and longitudinal velocity, lateral velocity derivative provides a fundamental contribution in lateral transients phases (for example, between 73 and 76 seconds).

Linear regression between the signals shown in figure 2.17 leads to the results reported in figure 2.18; because of the good accordance between the compared signals, the regression line angular coefficient is already very close to 1 (error is lower than 2%), making the correction less evident than in figure 2.14.

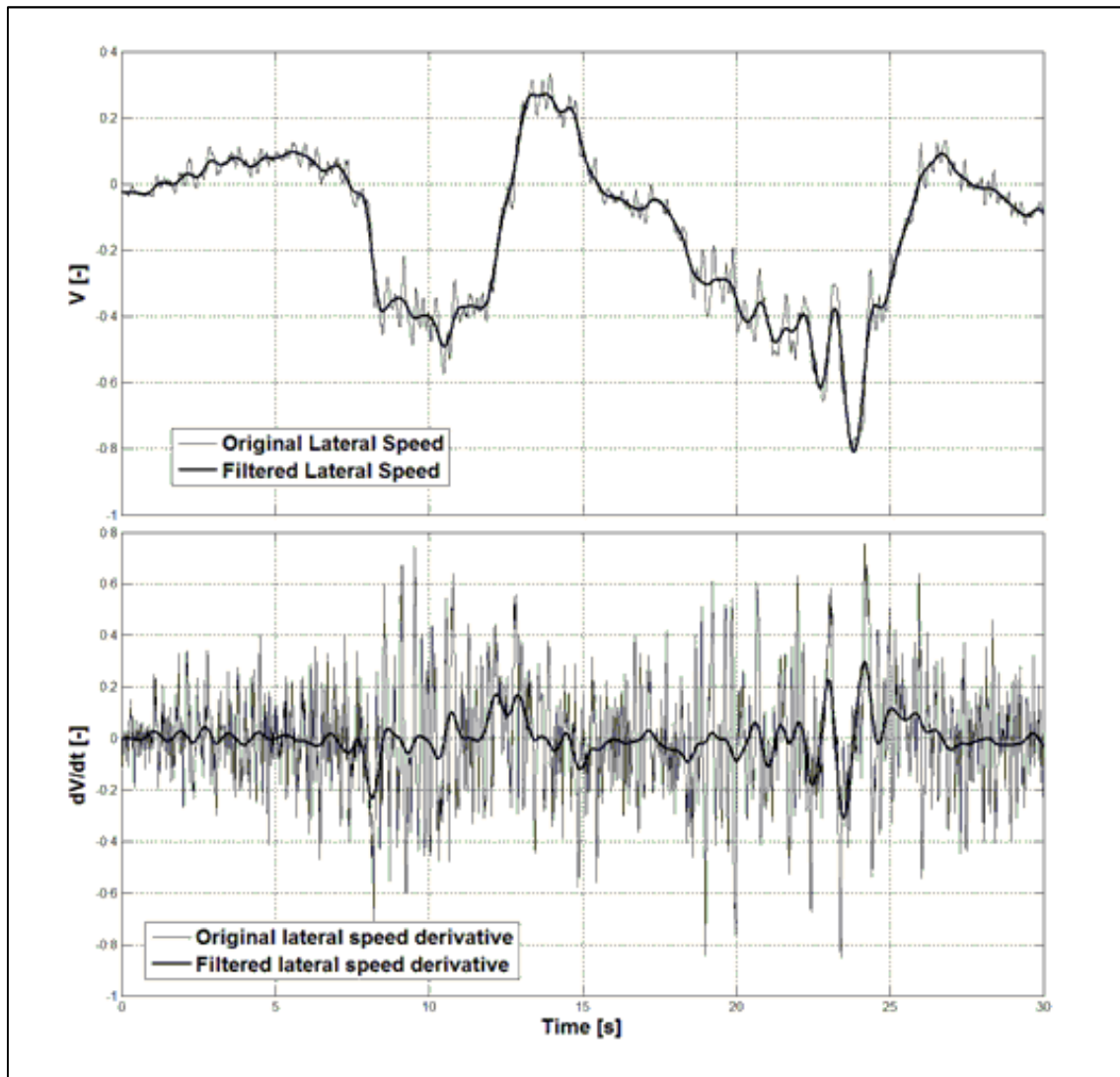


Fig. 2.15a - Comparison between filtered and non-filtered lateral speed signal.

Fig. 2.15b - Comparison between the derivative of filtered and non-filtered lateral speed signal.

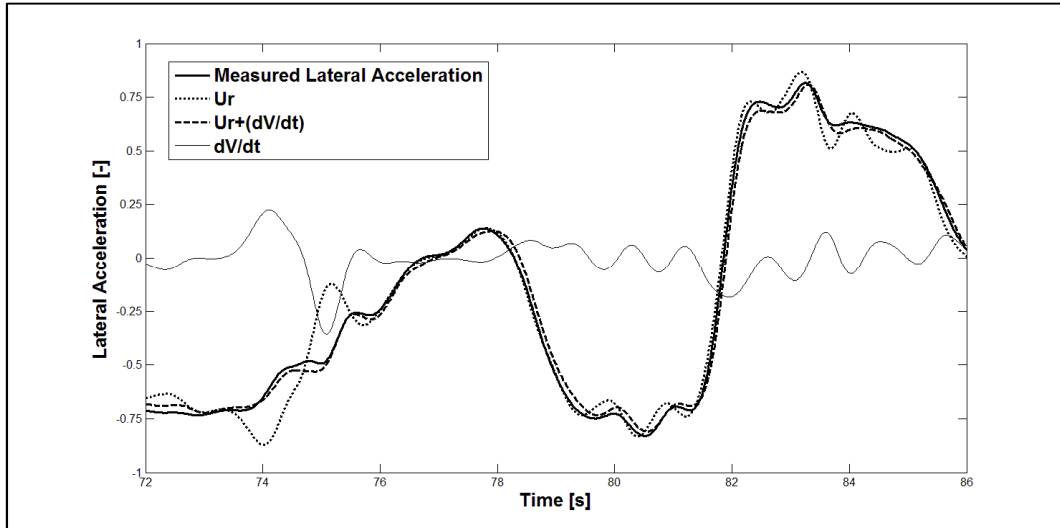


Fig. 2.16 - Decomposition of lateral acceleration signal in its different components.

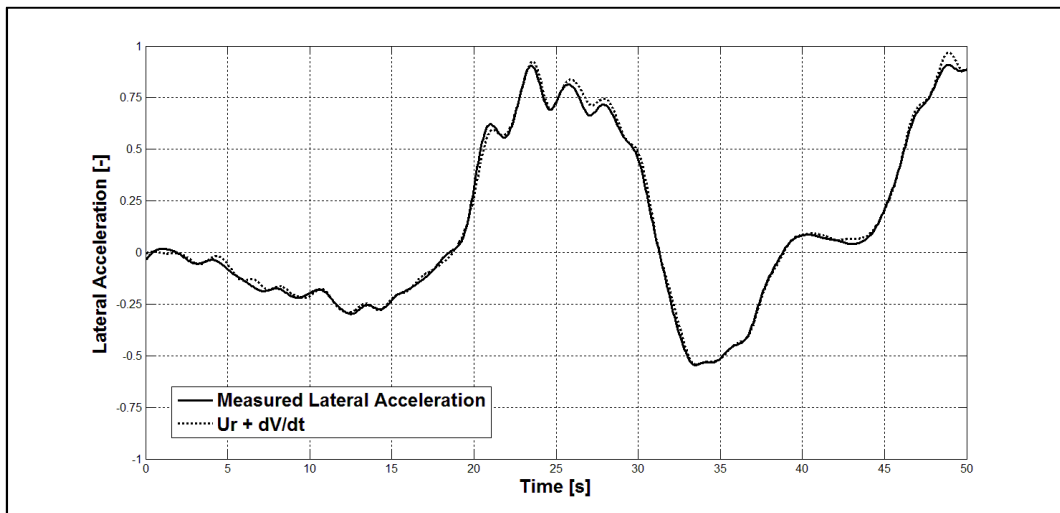


Fig. 2.17 - Comparison between lateral acceleration measured by accelerometer and DATRON lateral speed derivative.

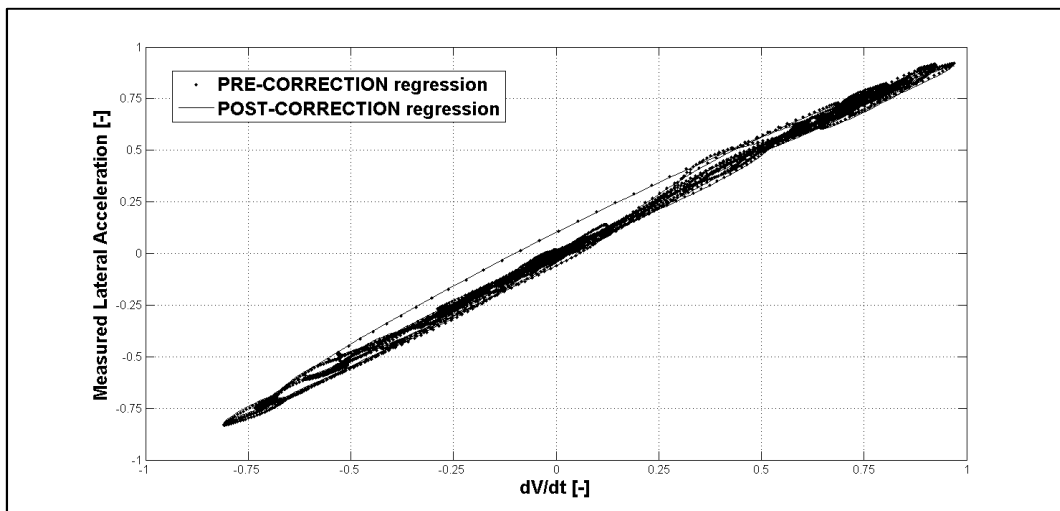


Fig. 2.18 - Result of the correction procedure operated by means of the regression between lateral acceleration measured by accelerometer and DATRON lateral speed derivative.

The measured accelerations comparison with velocity derivatives and the regression method allow to bypass the common road inclination and roll angle estimation procedures<sup>7-8</sup>, that allow to depurate accelerations from their gravitational component.

## 2.2.6 Model equations

### 2.2.6.1 Vertical Forces

In motion conditions characterized by null steering angle and constant vehicle speed ( $d(U+V)/dt=0$ ), vertical loads acting on axles are the so called "static loads"  $W_F$  and  $W_R$ , that, in absence of significant aerodynamic interactions, only depend on centre of gravity position:

$$\begin{aligned} W_F &= \frac{mgb}{l} \\ W_R &= \frac{mga}{l} \end{aligned} \quad (2.9)$$

Longitudinal load transfers are linked to longitudinal acceleration signal ( $a_x$ ) and, for longitudinal equilibrium equations [8], they are:

$$\Delta F_{z_{LONG}} = \left( \frac{mha_x}{l} \right) \quad (2.10)$$

Lateral load transfers are linked with lateral acceleration signal ( $a_y$ ) and, for lateral equilibrium equations [8], are:

$$\begin{aligned} \Delta F_{z_{LAT-F}} &= \frac{K_{\Phi F}}{(K_{\Phi F} + K_{\Phi R})} \left( \frac{ma_y(h-d)}{t_F} \right) \\ \Delta F_{z_{LAT-R}} &= \frac{K_{\Phi R}}{(K_{\Phi F} + K_{\Phi R})} \left( \frac{ma_y(h-d)}{t_R} \right) \end{aligned} \quad (2.11)$$

Vertical aerodynamic interactions (air density  $\rho = 1.2 \text{ kg/m}^3$ ) can be expressed as:

$$aerodown_F = \frac{1}{2} \rho A_v U^2 C_{z_F} \quad (2.12)$$

---

<sup>7</sup> Longitudinal road inclination is commonly calculated as  $\sin^{-1} \left( \frac{a_x - \frac{dU}{dt}}{g} \right)$ .

<sup>8</sup> Road banking can be calculated as the difference between measured roll angle (available if the vehicle is equipped with a gyroscope) and vehicle roll-rate times lateral acceleration.

$$aerodown_R = \frac{1}{2} \rho A_v U^2 C_{z_R}$$

Wheel vertical loads result equal to:

$$\begin{aligned} F_{z_{LF}} &= -\left( \frac{W_F}{2} + \Delta F_{z_{LONG}} + \Delta F_{z_{LAT-F}} + \frac{aerodown_F}{2} \right) \\ F_{z_{RF}} &= -\left( \frac{W_F}{2} + \Delta F_{z_{LONG}} - \Delta F_{z_{LAT-F}} + \frac{aerodown_F}{2} \right) \\ F_{z_{LR}} &= -\left( \frac{W_R}{2} - \Delta F_{z_{LONG}} + \Delta F_{z_{LAT-R}} + \frac{aerodown_R}{2} \right) \\ F_{z_{RR}} &= -\left( \frac{W_R}{2} - \Delta F_{z_{LONG}} - \Delta F_{z_{LAT-R}} + \frac{aerodown_R}{2} \right) \end{aligned} \quad (2.13)$$

### 2.2.6.2 Lateral Forces

In a vehicle integral reference system, axle lateral forces, respecting vehicle lateral dynamic equilibrium, can be calculated after a yaw rate derivative operation ( $dr/dt$ ) resolving the following equations system:

$$\begin{cases} F_{y_F} = (ma_y - F_{y_R}) \\ F_{y_R} = \frac{maa_y + J_z(dr/dt)}{l} \end{cases} \quad (2.14)$$

Basing on the experimental results obtained in the track testing sessions, it is possible to hypothesize that in a quite wide range of working conditions the distribution of axle lateral forces on the two sides can be considered proportional to the same axle vertical forces distribution:

$$\begin{aligned} \bar{F}_{y_{LF}} &= F_{y_F} \left( \frac{F_{z_{LF}}}{F_{z_{LF}} + F_{z_{RF}}} \right) \\ \bar{F}_{y_{RF}} &= F_{y_F} \left( \frac{F_{z_{RF}}}{F_{z_{LF}} + F_{z_{RF}}} \right) \\ \bar{F}_{y_{LR}} &= F_{y_R} \left( \frac{F_{z_{LR}}}{F_{z_{LR}} + F_{z_{RR}}} \right) \\ \bar{F}_{y_{RR}} &= F_{y_R} \left( \frac{F_{z_{RR}}}{F_{z_{LR}} + F_{z_{RR}}} \right) \end{aligned} \quad (2.15)$$

### 2.2.6.3 Longitudinal Forces

Under the same hypotheses it is possible to consider vehicle longitudinal dynamic equilibrium to estimate longitudinal interaction forces. Differently from lateral forces

calculation, wheels inertial effects, aerodynamic drag and tyre rolling resistances contributions must be considered.

For the well known aerodynamics equations, drag resistance force is expressed by:

$$aerodrag = \frac{1}{2} \rho A U^2 C_x \quad (2.16)$$

Rolling resistance forces "rollres", already considered as acting at ground level, can be determined as a function of vertical load and wheel speed by means of vehicle characterization data previously listed (figure 2.4).

Defining  $i$  and  $j$  indices as respectively referred to axle (front or rear) and to side (left or right), wheel rotation inertial resistant contribution, reported on the ground, is:

$$F_{WIR}^{ij} = \frac{I w_i \frac{d\Omega_{ij}}{dt}}{R r_i} \quad (2.17)$$

For a rear wheel drive vehicle and hypothesizing again the distribution of tangential forces proportional to the vertical forces distribution,  $F_x$  forces can be estimated as follows:

- for deceleration manoeuvres (measured  $a_x > 0$ )

$$\begin{aligned} \bar{F}_{x_{LF}} &= \left[ (m a_x - aerodrag) \left( \frac{F_{z_{LF}}}{\sum_{ij} F_{z_{ij}}} \right) + F_{WIR}^{LF} \right] + rollres_{LF} \\ \bar{F}_{x_{RF}} &= \left[ (m a_x - aerodrag) \left( \frac{F_{z_{RF}}}{\sum_{ij} F_{z_{ij}}} \right) + F_{WIR}^{RF} \right] + rollres_{RF} \\ \bar{F}_{x_{LR}} &= \left[ (m a_x - aerodrag) \left( \frac{F_{z_{LR}}}{\sum_{ij} F_{z_{ij}}} \right) + F_{WIR}^{LR} \right] + rollres_{LR} \\ \bar{F}_{x_{RR}} &= \left[ (m a_x - aerodrag) \left( \frac{F_{z_{RR}}}{\sum_{ij} F_{z_{ij}}} \right) + F_{WIR}^{RR} \right] + rollres_{RR} \end{aligned} \quad (2.18)$$

- for acceleration manoeuvres (measured  $a_x < 0$ )

$$\begin{aligned} \bar{F}_{x_{LF}} &= F_{WIR}^{LF} + rollres_{LF} \\ \bar{F}_{x_{RF}} &= F_{WIR}^{RF} + rollres_{RF} \end{aligned} \quad (2.19)$$

$$\bar{F}x_{LR} = \left[ (ma_x - aerodrag - (rollres_{LF} + rollres_{RF})) \left( \frac{Fz_{LR}}{Fz_{LR} + Fz_{RR}} \right) + F_{WIR}LR \right] + rollres_l$$

$$\bar{F}x_{RR} = \left[ (ma_x - aerodrag - (rollres_{LF} + rollres_{RF})) \left( \frac{Fz_{RR}}{Fz_{LR} + Fz_{RR}} \right) + F_{WIR}RR \right] + rollres_r$$

It is interesting to notice how the different contributions act differently in dependence of the kind of interaction considered:

- drag is a resistant force for vehicle motion in traction manoeuvres, so it has to be contrasted by rear driving wheels; during braking, drag gives an advantageous contribution to the speed reduction, so the braking tyres have to perform longitudinal forces lower in modulus than the ones that they would have performed in absence of drag.
- wheel rotation inertial resistant contribution is always positive but its sign is intrinsic in the performed manoeuvre.
- front tyres rolling resistances, being not contrasted by front tyres (not driving), become external causes of resistance for rear tyres, that in traction manoeuvres have to overcome also them.

Summarizing, longitudinal tyres interactions can be considered as the sum of the forces regarding the tyres, and consequently, as rolling resistances plus the external efforts that tyres have to face in order to perform the driver's requests.

#### 2.2.6.4 Tangential Forces in wheel reference system

By means of a proper rotation matrix, it is possible to move the estimated tangential forces from vehicle integral reference system to a wheel integral one:

$$\begin{bmatrix} Fx_{ij} \\ Fy_{ij} \end{bmatrix} = \begin{bmatrix} \cos(\zeta_{ij}) & -\sin(\zeta_{ij}) \\ \sin(\zeta_{ij}) & \cos(\zeta_{ij}) \end{bmatrix} \begin{bmatrix} \bar{F}x_{ij} \\ \bar{F}y_{ij} \end{bmatrix} \quad (2.20)$$

It is useful because slip ratio and slip angle are expressed in such coordinates system, and to plot forces as a function of them, all the variables need to be expressed according with an unique reference. Angle  $\zeta$  has to be considered as the steering angle of the (i-th, j-th) wheel and in the following paragraphs it will be explained how it can be determined taking into account suspension and steering structure and compliances.

#### 2.2.6.5 Wheel Steering Angles

Supposing a front wheel steering vehicle, nominal steering angle is equal to:

$$\delta = \frac{Data1\_LWS\_Angle}{\tau_s} \quad (2.21)$$

Adding Ackermann effect [8][10], by means of the following equations, the kinematic steering can be modelled (rear axle is still supposed non-steering) as:

$$\begin{cases} \delta_{INTERNALWHEEL} = \delta + \Delta\delta \\ \delta_{EXTERNALWHEEL} = \delta - \Delta\delta \end{cases}$$

$$\Delta\delta = \Delta Ack_{100\%} \frac{1}{2} ack\% \quad (2.22)$$

$$\Delta Ack_{100\%} = \tan^{-1} \left( \frac{l}{R_c - \frac{t_F}{2}} \right) - \tan^{-1} \left( \frac{l}{R_c + \frac{t_F}{2}} \right)$$

in which  $R_c$  is CG trajectory curvature radius:

$$R_c = \frac{l}{\tan(\delta)} \quad (2.23)$$

Toe angle, thanks to static toe value (expressed in ISO reference system - regardless of the choice of coordinate systems, inward steer is positive) and to toe variation ( $\Delta\chi$ ) data (Fig. 2.6), can be evaluated for each corner as a function of lateral acceleration as:

$$\begin{aligned} \chi_{LF} &= -\chi_{0F} \pm \Delta\chi_F \\ \chi_{RF} &= +\chi_{0F} \mp \Delta\chi_F \\ \chi_{LR} &= -\chi_{0R} \pm \Delta\chi_R \\ \chi_{RR} &= +\chi_{0R} \mp \Delta\chi_R \end{aligned} \quad (2.24)$$

Additional steering angles  $\chi_c$  due to axle compliances (Fig. 2.7), whose effect is closely connected to self-alignment moment (lateral forces acting on the axle make the front wheels steer in opposition to driver steering request), have been modelled by means of a two-parameters function:

$$\begin{aligned} \chi_{C-F} &= K_{1F} (Fy_{LF} + Fy_{RF})^{K_{2F}} \\ \chi_{C-R} &= K_{1R} (Fy_{LR} + Fy_{RR})^{K_{2R}} \end{aligned} \quad (2.25)$$

Accounting for all the cited contributions to steering, supposing a right curving manoeuvre (external LEFT wheel - internal RIGHT wheel), effective steering angles are:

$$\begin{aligned} \zeta_{LF} &= (\delta - \Delta\delta) + \chi_{LF} + \chi_{C-F} \\ \zeta_{RF} &= (\delta + \Delta\delta) + \chi_{RF} + \chi_{C-F} \\ \zeta_{LR} &= \chi_{LR} + \chi_{C-R} \\ \zeta_{RR} &= \chi_{RR} + \chi_{C-R} \end{aligned} \quad (2.26)$$

### 2.2.6.6 Wheel Absolute Velocities and Slip Indices

Rigid body kinematics equations already employed for CG velocity calculation [8] can be used to determine wheels absolute velocity components (in vehicle-integral reference system), considered at wheel hub:

$$\begin{cases} V_{x_{ABS-LF}} = U - r \frac{t_F}{2} \\ V_{y_{ABS-LF}} = V + ra \end{cases}
 \begin{cases} V_{x_{ABS-RF}} = U + r \frac{t_F}{2} \\ V_{y_{ABS-RF}} = V + ra \end{cases}
 \begin{cases} V_{x_{ABS-LR}} = U - r \frac{t_R}{2} \\ V_{y_{ABS-LR}} = V - rb \end{cases}
 \begin{cases} V_{x_{ABS-RR}} = U + r \frac{t_R}{2} \\ V_{y_{ABS-RR}} = V - rb \end{cases}
 \quad (2.27)$$

In order to calculate slip ratio and slip angle for each tyre, it is necessary to express the wheel velocity in the wheel-integral reference system:

$$\begin{bmatrix} V_{x_{ij}} \\ V_{y_{ij}} \end{bmatrix} = \begin{bmatrix} \cos(\zeta_{ij}) & \sin(\zeta_{ij}) \\ -\sin(\zeta_{ij}) & \cos(\zeta_{ij}) \end{bmatrix} \begin{bmatrix} V_{x_{ABS-ij}} \\ V_{y_{ABS-ij}} \end{bmatrix} \quad (2.28)$$

Once calculated wheels angular speed in the following way:

$$\begin{aligned}
 \Omega_{LF} &= \frac{Data1\_VRD\_LV \text{ \_\_\_ } Wheel\_Speed\_Left}{R_{rF}} \\
 \Omega_{RF} &= \frac{Data1\_VRD\_RV \text{ \_\_\_ } Wheel\_Speed\_Righ}{R_{rF}} \\
 \Omega_{LR} &= \frac{Data1\_VRD\_LH \text{ \_\_\_ } Wheel\_Speed\_Left}{R_{rR}} \\
 \Omega_{RR} &= \frac{Data1\_VRD\_RH \text{ \_\_\_ } Wheel\_Speed\_Righ}{R_{rR}}
 \end{aligned} \quad (2.29)$$

slip ratio, variable in a range  $[-\infty, 1]$  ( $-\infty$  for global sliding traction manoeuvres, 1 for full blocking braking manoeuvres), is:

$$s_{ij} = \frac{V_{x_{ij}} - \Omega_{ij} R_j}{V_{x_{ij}}} \quad (2.30)$$

while slip angle is calculated as:

$$\alpha_{ij} = -\tan^{-1}\left(\frac{Vy_{ij}}{Vx_{ij}}\right) \quad (2.31)$$

### 2.3 Forces estimation validation

With the aim to test and validate the developed tool a specific experimental session on a high performance rear wheel drive vehicle has been planned, whose results will be analysed and discussed in the paragraph. As already said, for industrial confidentiality agreements, plots, diagrams and data will be provided as normalized.

An immediate comparison, able to test the procedure reliability, can be offered by interaction forces measurements by dynamometric wheels instrumentation. Such kind of device provides forces values strongly influenced by the mass of the measurement instruments, that can be easily taken into account, and by road irregularities.

Figure 2.19 shows, in the first plot, the comparison between the sum of the measured tyre vertical forces and of the estimated ones; in the second plot, vehicle speed is reported. Dynamometric wheels output appears very noisy, mainly because of road unevenness, but the dependence from vehicle speed is clearly highlighted (tested vehicle has a strong aerodynamic-oriented design). TRICK vertical forces estimation results coherent with measured data, being the downforce modelled thanks to the introduction of the  $C_z$  parameters.

The comparisons between estimated and measured axle forces are reported in the following figures (Fig. 2.20), highlighting again that provided estimations are in good agreement with test results.

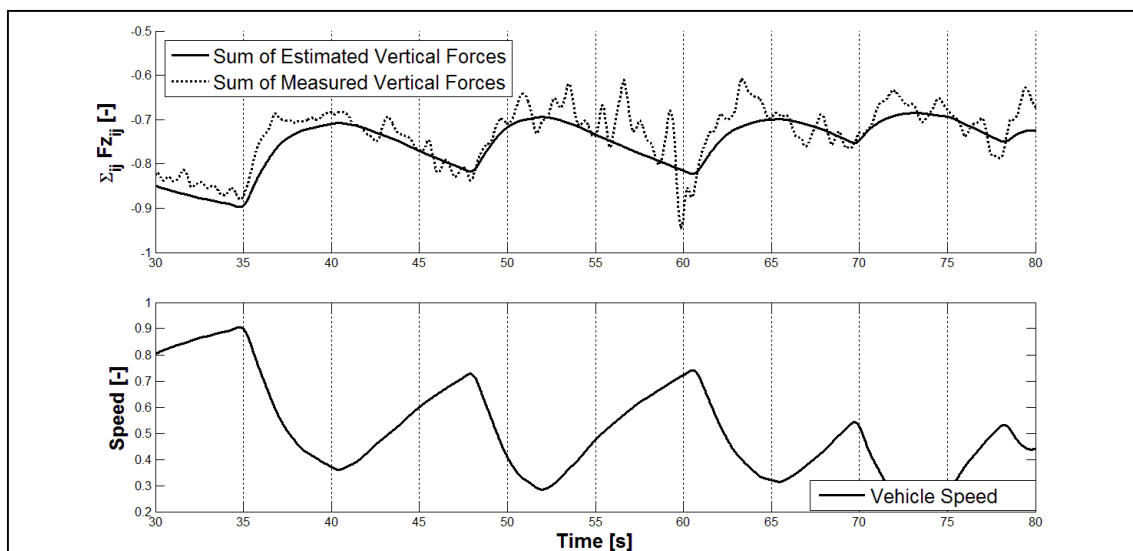


Fig. 2.19 - Comparison of sum of measured and calculated tyre vertical forces with measured vehicle speed profile.

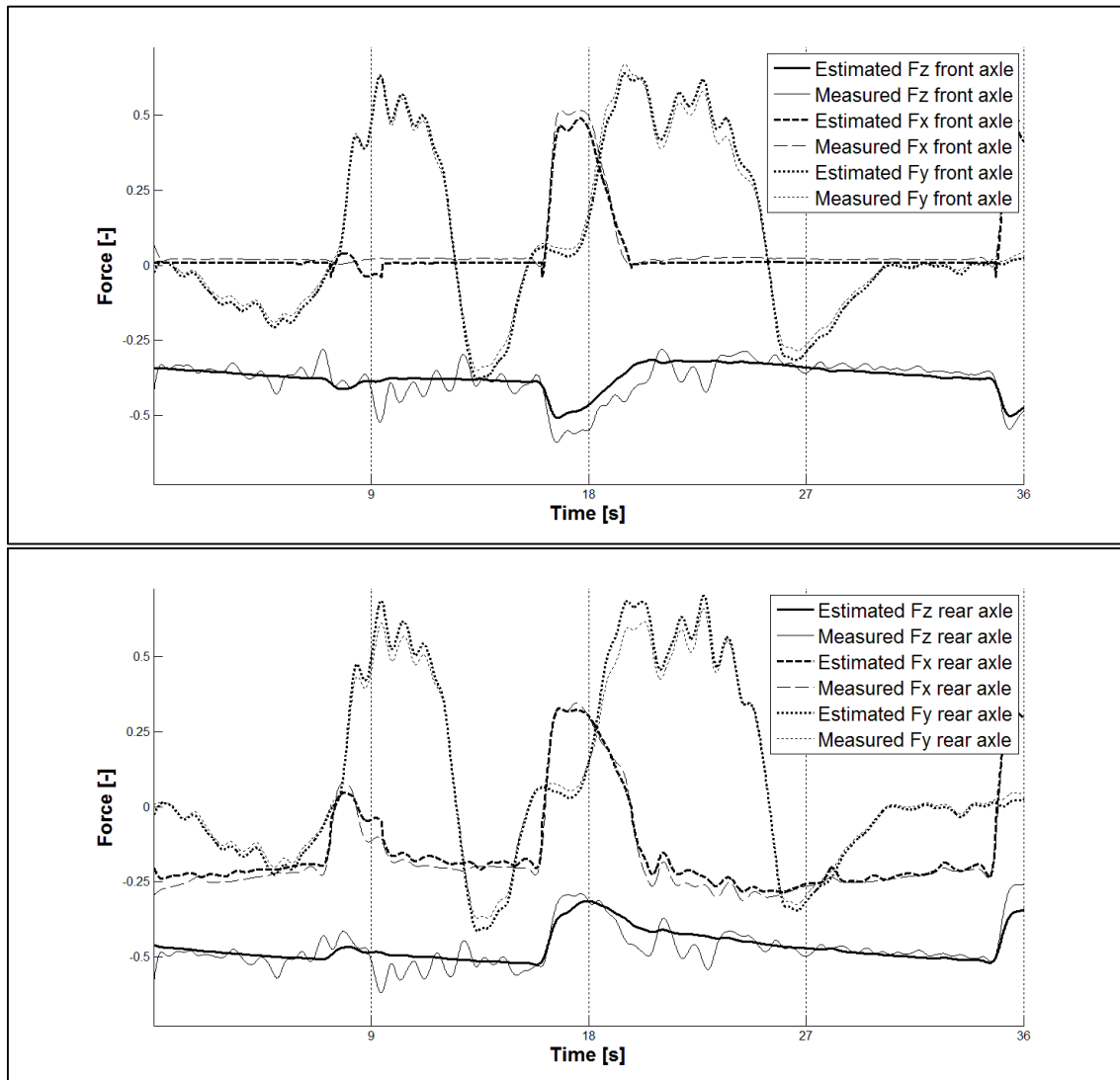


Fig. 2.20a - Comparison between measured and calculated front axle forces.

Fig. 2.20b - Comparison between measured and calculated rear axle forces.

As concerns the forces acting on each single corner, figures 2.21 report the trends relative to left side tyres, about which the following considerations can be done:

- Measured vertical forces, as already said, are affected by fluctuations mainly due to road irregularities, that model cannot obviously reproduce.
- Longitudinal front measurements show, after braking phases, low negative force values, meaning traction wheel states (unexpected in a rear wheel drive vehicle). This could be due to non-optimal wheel angular acceleration calculations, whose causes have to be better investigated.
- Lateral forces are in some cases lightly overestimated, because of the proportional trend between vertical and lateral forces, that leads to neglect contact patch, and consequently tangential forces, saturation effects. Despite that, the estimation can be considered satisfying (RMS error < 5%).
- The forces global trends are in good agreement with the expected ones.

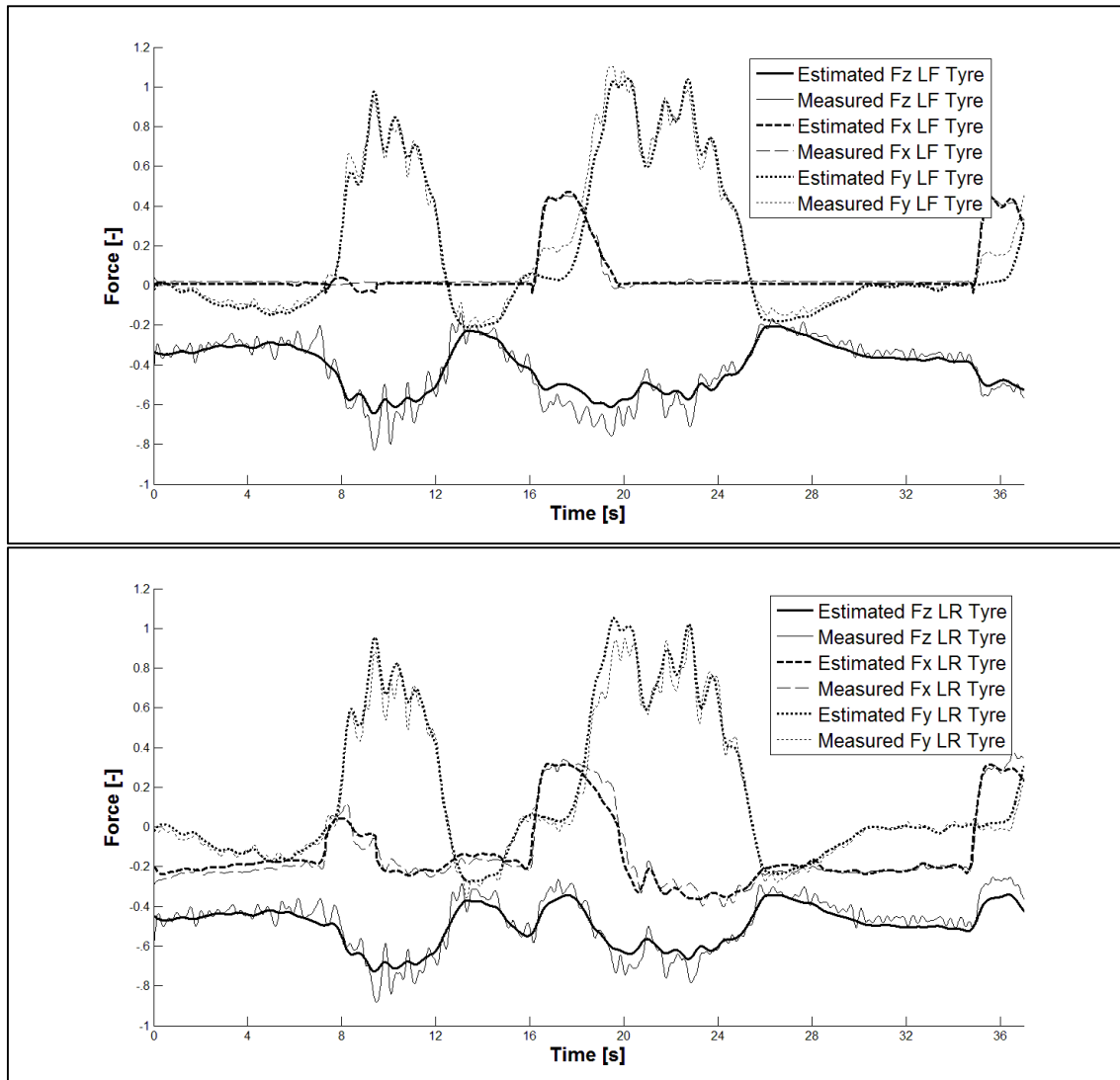


Fig. 2.21a - Comparison between measured and calculated front tyre interaction forces.

Fig. 2.21b - Comparison between measured and calculated rear tyre interaction forces.

## 2.4 Tangential Tyre/Road Interaction Characteristics - Results Analysis

### 2.4.1 General Notes

The main output of the TRICK procedure is the plot of the pure and combined tyre/road tangential interaction characteristics. The defined standard plot set is composed by:

- PLOT A:  $F_x/F_z$  vs slip ratio - pure interaction<sup>9</sup> - front tyre (Fig. 2.25a)
- PLOT B:  $F_y/F_z$  vs slip angle - pure interaction<sup>10</sup> - front tyre (Fig. 2.26a)
- PLOT C:  $F_x/F_z$  vs slip ratio - pure interaction - rear tyre (Fig. 2.27a)
- PLOT D:  $F_y/F_z$  vs slip angle - pure interaction - rear tyre (Fig. 2.28a)

<sup>9</sup> Pure longitudinal interaction points have been selected considering the working conditions characterized by slip angle lower than 0.1deg (0.0017 rad).

<sup>10</sup> Pure lateral interaction points have been selected considering the working conditions characterized by slip ratio lower than 0.001 (0.1%).

- PLOT E: Fx vs slip ratio - pure interaction - front tyre (Fig. 2.25b)
  - PLOT F: Fy vs slip angle - pure interaction - front tyre (Fig. 2.26b)
  - PLOT G: Fx vs slip ratio - pure interaction - rear tyre (Fig. 2.27b)
  - PLOT H: Fy vs slip angle - pure interaction - rear tyre (Fig. 2.28b)
  - PLOT I: Fx/Fz vs slip ratio - combined interaction - front tyre (Fig. 2.29)
  - PLOT J: Fy/Fz vs slip angle - combined interaction - front tyre (Fig. 2.30)
  - PLOT K: Fx/Fz vs slip ratio - combined interaction - rear tyre (Fig. 2.31)
  - PLOT L: Fy/Fz vs slip angle - combined interaction - rear tyre (Fig. 2.32)
  - PLOT M: Fy/Fz vs Fx/Fz - isoslipratio tyre adherence ellipse - front tyre (Fig. 2.33a)
  - PLOT N: Fy/Fz vs Fx/Fz - isoslipangle tyre adherence ellipse - front tyre (Fig. 2.33b)
  - PLOT O: Fy/Fz vs Fx/Fz - isoslipratio tyre adherence ellipse - rear tyre (Fig. 2.34a)
  - PLOT P: Fy/Fz vs Fx/Fz - isoslipangle tyre adherence ellipse - rear tyre (Fig. 2.34b)
- in the following subparagraphs the plots will be shown and discussed, for a rear wheel drive sport vehicle.

Plot settings, adjustable by means of a dedicated panel, have been arranged in order to provide pure interaction data points coloured from blue to red for increasing vertical load (Fig. 2.22), according with the following Fz ranges:

[-750, -2250[ [-2250, -3750[ [-3750, -5250[ [-5250, -6750[ [-6750, -8250] N

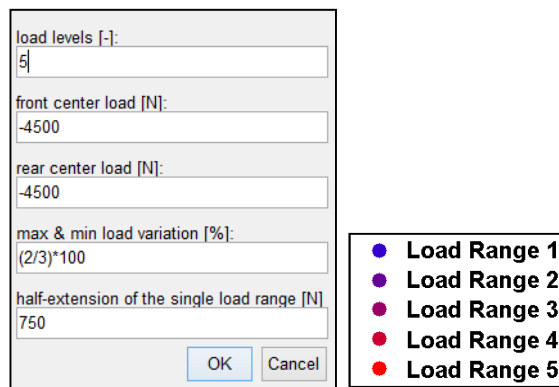


Fig. 2.22 - Plot panel settings and load colours legend.

Combined interaction and adherence ellipses data points have been plotted coloured from red to blue for increasing "antagonist" slip index (slip angle for longitudinal combined, slip ratio for lateral combined - Fig. 2.23), according with the following ranges:

FOR LONGITUDINAL COMBINED INTERACTION:

slip angle = [0, 2.5[ [2.5, 5[ [5, 7.5[ [7.5, +∞[ deg

FOR LATERAL COMBINED INTERACTION:

slip ratio = [0, 2.5[ [2.5, 5[ [5, 7.5[ [7.5, +∞[ %

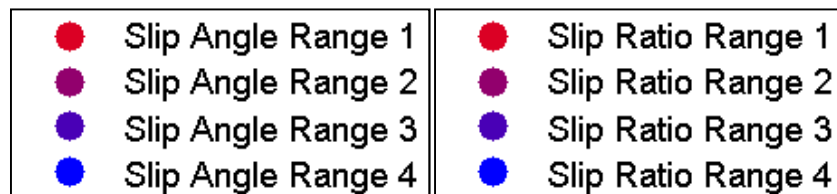


Fig. 2.23 - Slip angle and slip ratio colours legend.

Common track lap acquisitions do not contain a sufficient number of working points able to characterize pure interaction; for this reason, some of the manoeuvres described in the test procedure paragraph have been planned with the aim to collect as many as possible usually missing pure data. Figure 2.24 shows for a rear tyre, at purely qualitative aim, the differences between normal (top plots) and specifically performed (bottom plots) track laps, for longitudinal (left plots - different x-scales) and lateral (right plots) interactions.

Longitudinal plots demonstrate that global sliding starting manoeuvres, properly performed, are able to completely describe the shape of the traction half of the interaction curve, highlighting the expected peak and the following decreasing trend (in the circular frame). As concerns the braking half, despite the dedicated manoeuvres, the shape is not fully sketched because of ABS intervention (points cloud in the square frame), that for an optimal tyre characterization should be off.

Lateral specific tests enable the investigation of the nonlinear tyre working zone, providing fundamental information about lateral roadholding at the limit and allowing to describe the shape of the interaction curve at high slip angles (in the hexagons). This trend is the main factor able to transmit to the driver the feelings that allow to control the vehicle as close as possible to the threshold between lateral stability and instability, and, if properly modelled, can be the crucial step to achieve a satisfying driving simulation experience.

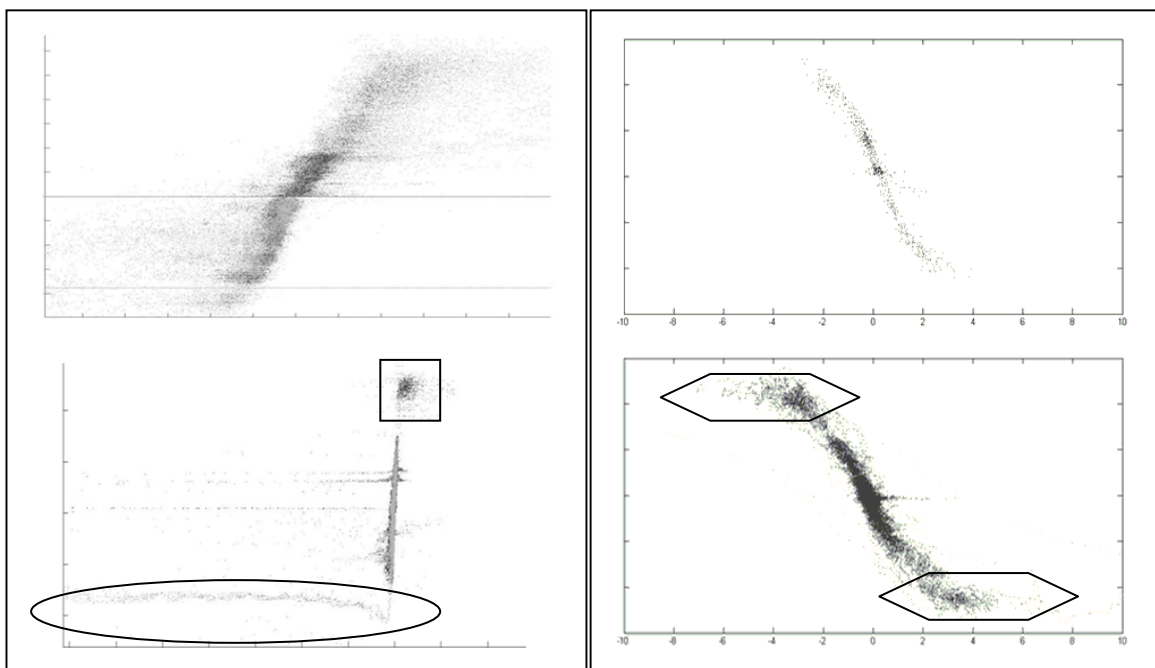


Fig. 2.24a - Comparison between common (top plot) and specifically performed laps (table 2.3 - bottom plot) longitudinal interaction tyre curve. x-axis scales are different. In the square, a braking points cloud, due to ABS. In the oval, a well sketched trend of the traction zone.  
Fig. 2.24b - Comparison between common (top plot) and specifically performed laps (table 2.3 - bottom plot) lateral interaction tyre curve. x-axis scales are different. In the hexagons, zones of limit lateral roadholding, absent in the top plot.

### 2.4.2 PLOT A & PLOT E: pure longitudinal interaction - front tyre

Coherently with the expected front tyre longitudinal interactions, for a rear wheel drive vehicle, the plots highlight the presence of points characterizing only braking or free rolling conditions (slip ratio > 0). The forces sign inversion, in this and in the following figures, is due to the negative sign of vertical loads in the adopted reference system.

Acquired data and estimated forces allow a good understanding of the curve shape, making maximum grip value identification possible. Load effect is not clearly deductible because of the probably excessive width of each load range.

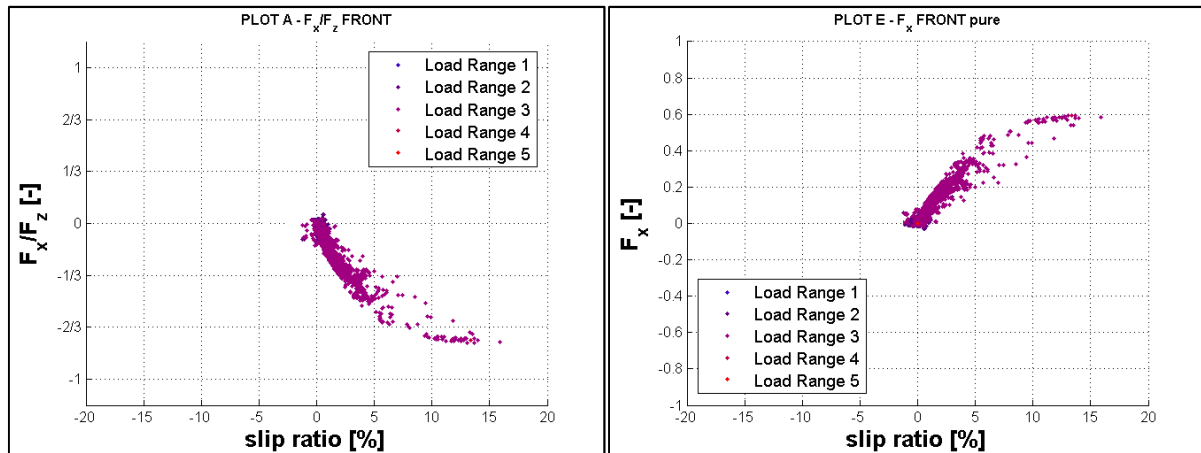


Fig. 2.25a - Plot A.

Fig. 2.25b - Plot E.

### 2.4.3 PLOT B & PLOT F: pure lateral interaction - front tyre

Being front axle in null longitudinal force conditions (neglecting rolling resistance contribution) during all vehicle traction phases, lateral pure interaction results easy to be characterized. The big amount of available points allows to have a clear overview of the main variables effect on tyre behaviour. Grip vs vertical load decreasing, cornering stiffness vs vertical load increasing and global shape trend can be deeply analysed, obtaining useful information for tyre knowledge and model parameters identification.

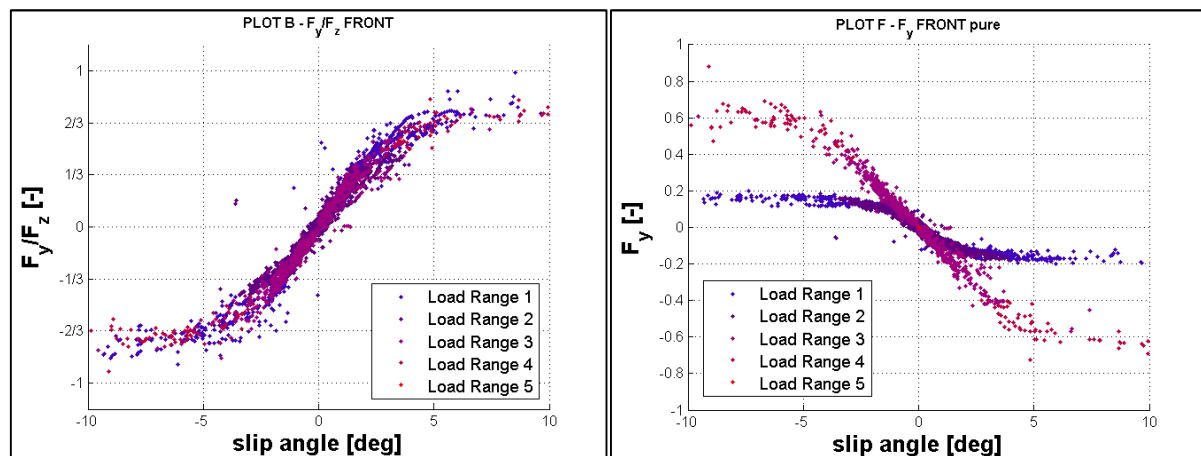


Fig. 2.26a - Plot B.

Fig. 2.26b - Plot F.

### 2.4.4 PLOT C & PLOT G: pure longitudinal interaction - rear tyre

Interaction characteristic curve is well sketched for rear tyres, even if it seems that maximum possible longitudinal grip in traction phases has not been fully exploited by driver. The thickness of the points cloud could be due to slip ratio misestimations connected with the fact that tyre radius variation as a function of wheel vertical load has been neglected.

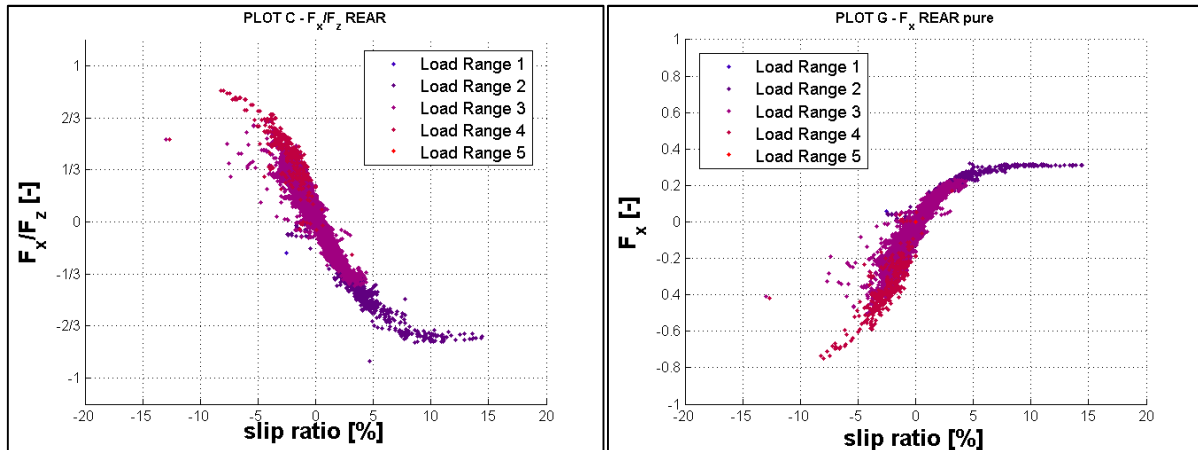


Fig. 2.27a - Plot C.  
 Fig. 2.27b - Plot G.

### 2.4.5 PLOT D & PLOT H: pure lateral interaction - rear tyre

Being rear tyre the driving one, lateral pure curves, if compared with front tyre ones, are constituted by a lower number of points. Despite that, it is possible to clearly notice higher grip and cornering stiffness for rear tyres (rear tyre width is 20% higher than front one) and to evaluate the influence of load on tyre behaviour.

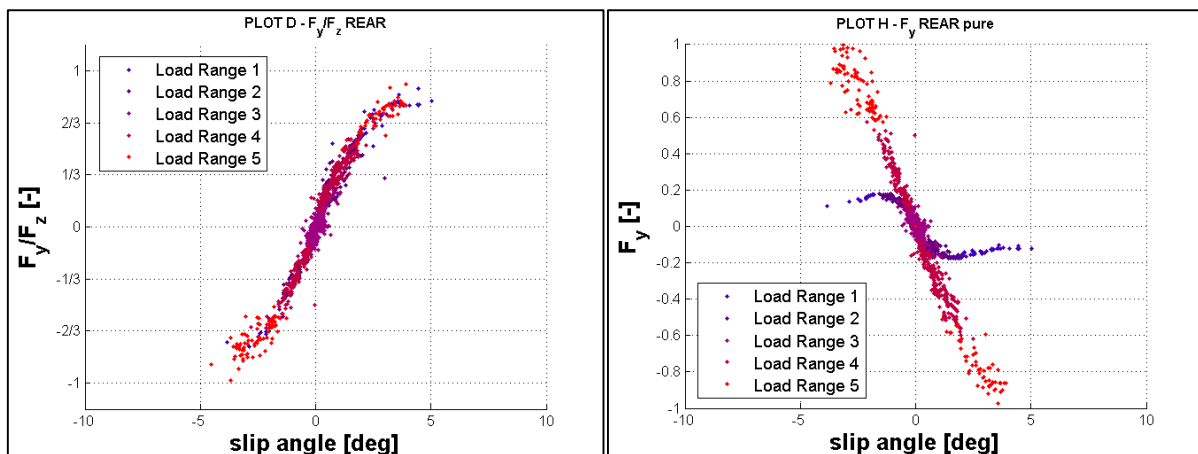


Fig. 2.28a - Plot D.  
 Fig. 2.28b - Plot H.

### 2.4.6 PLOT I: combined longitudinal interaction - front tyre

Slip angle increasing acts on combined longitudinal interaction, as expected, causing a force decrease. Not enough can be said about the variation of slip ratio value corresponding to force maximum at different slip angles. The curves are again too thick, because of slip ratio probable misestimation.

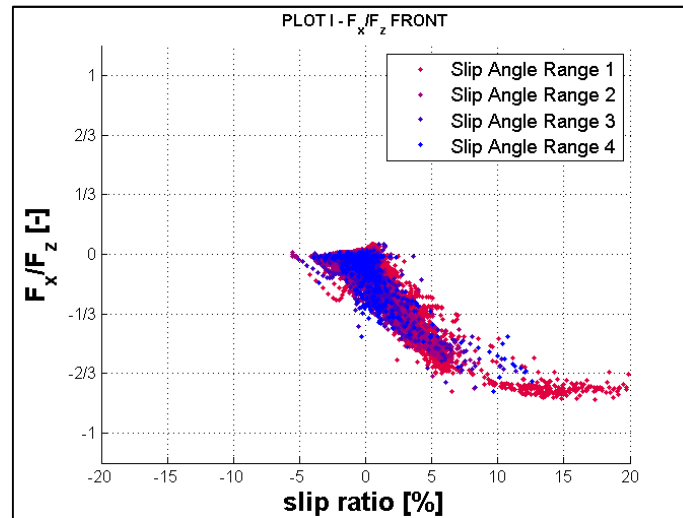


Fig. 2.29 - Plot I.

### 2.4.7 PLOT J: combined lateral interaction - front tyre

As for pure interaction, front lateral curves are very useful to deduct essential information about tyre dynamics. By means of the great number of useful points it is possible to have a clear idea of curves trend, of force maximum value localization and of slip ratio effect, that in the examined case causes a sharp decrease of lateral force and cornering stiffness.

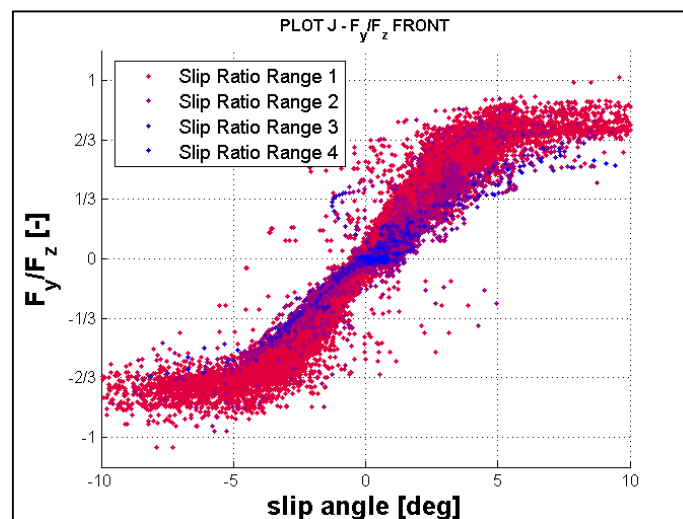


Fig. 2.30 - Plot J.

### 2.4.8 PLOT K: combined longitudinal interaction - rear tyre

In analogous way to pure case, longitudinal rear interaction estimation is affected by quite high uncertainty level, mainly due to slip ratio difficult calculation. Moreover,

braking grip values result to be higher than expected because during manoeuvres characterized by high load transfers, an eventual tyre vertical force underestimation causes a grip overestimation. Information about slip angle effect are satisfying, making traction force decrease estimation possible.

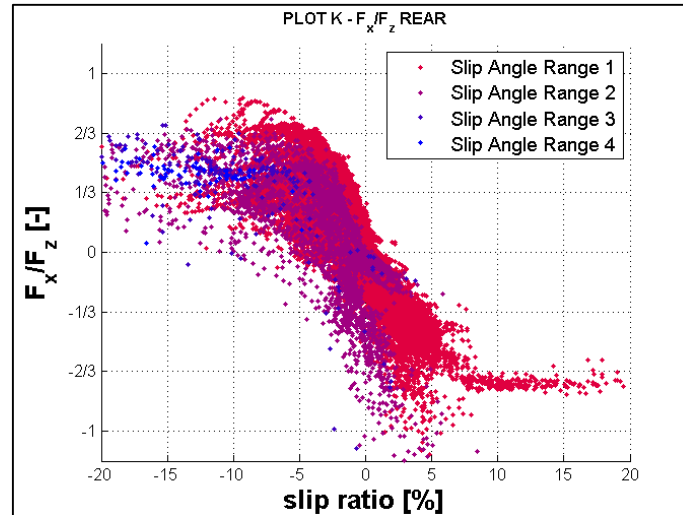


Fig. 2.31 - Plot K.

#### 2.4.9 PLOT L: combined lateral interaction - rear tyre

Also rear combined lateral interaction, as front one, allows a good comprehension of the effect that slip ratio increase has on lateral axle stiffness and roadholding. Differently from front case, curves trend after maximum grip point is less easy to determine, because driving the tyres in such working points means to exceed rear axle limit roadholding, leading the whole vehicle to instability conditions.

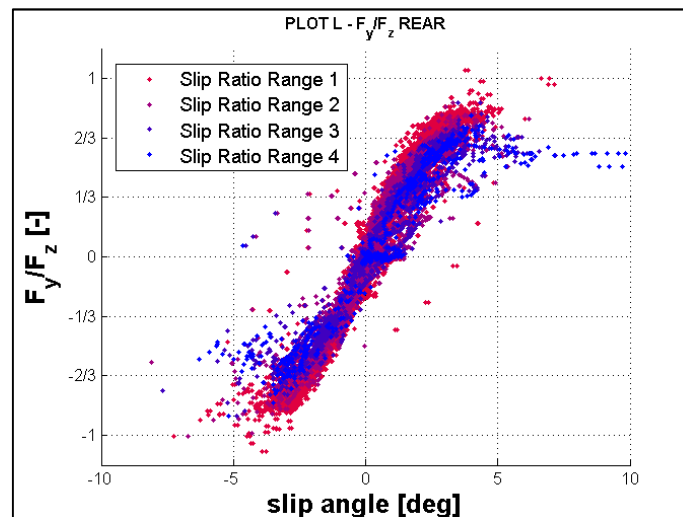


Fig. 2.32 - Plot L.

### 2.4.10 PLOT M & PLOT N: adherence ellipse - front tyre

One of the most common and intuitive instruments to evaluate tyre performances is the so called "adherence ellipse", obtained plotting tyre lateral grip as a function of longitudinal one. The characteristic elliptic shape (or half-elliptic, for not driving wheels) in which points are arranged in this kind of diagram gives it its name.

The points have been coloured in different ways, depending from slip ratio (Fig. 2.33a) or from slip angle (2.33b). These plots will offer direct comparison between the result of tyre models parameters identification procedure and experimentally acquired data.

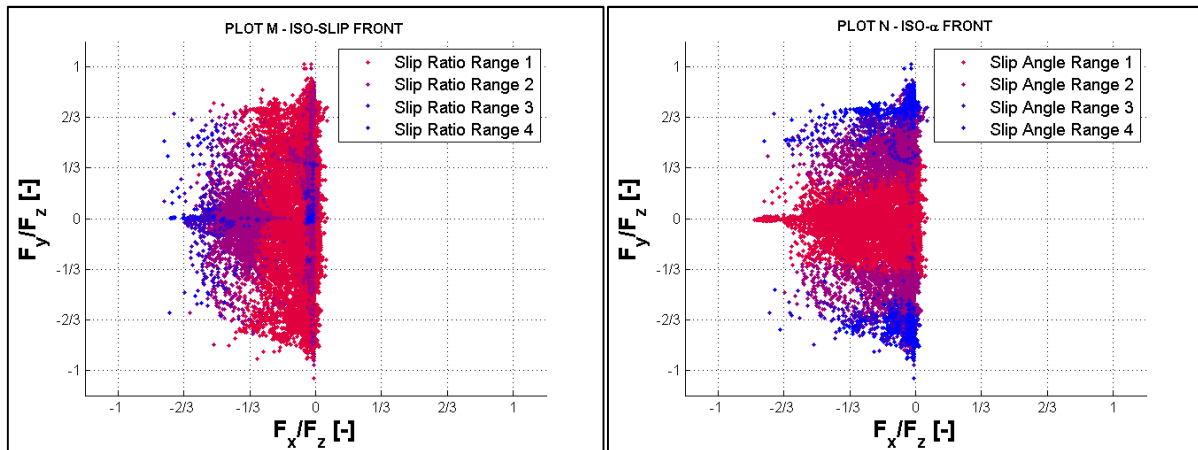


Fig. 2.33a - Plot M.

Fig. 2.33b - Plot N.

### 2.4.11 PLOT O & PLOT P: adherence ellipse - rear tyre

Rear adherence ellipses give a direct feedback as concerns tyres maximum exploitable grip, observable in pure longitudinal (horizontal axis of the ellipse) and pure lateral (vertical axis of the ellipse) conditions. The unexpected appendices of points external to ellipse, related to lateral braking manoeuvres, are due to longitudinal braking grip over already discussed in 2.4.9.

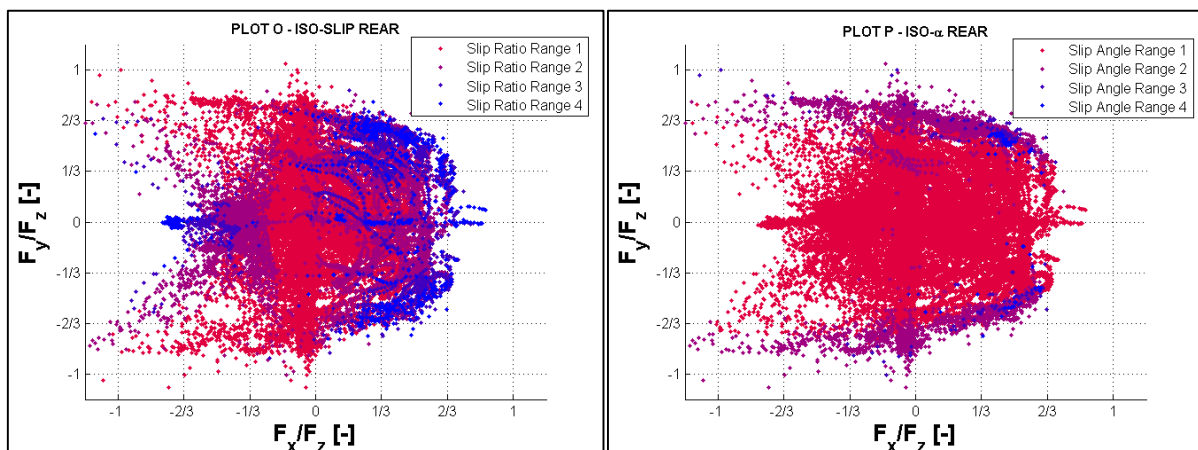


Fig. 2.34a - Plot O.

Fig. 2.34b - Plot P.

#### 2.4.12 Further Results

Temperature measurements and thermal model outputs (chapter 4) can be usefully employed to study tyre friction / temperature mutual influences. The following figure (Fig. 2.35) gives experimental confirmation of the expected theoretical phenomena: high temperature (red points - estimated tyre bulk temperature  $> 55\text{ }^{\circ}\text{C}$ ) acts increasing grip and reducing cornering stiffness respect to values observed at low temperature (blue points). These results can be employed to tune tyre grip and thermal models and, coupled with rubber visco-elastic characterizations and with thermal conductivity identification, to configure a vehicle setup able to optimise tyre performances (chapter 6).

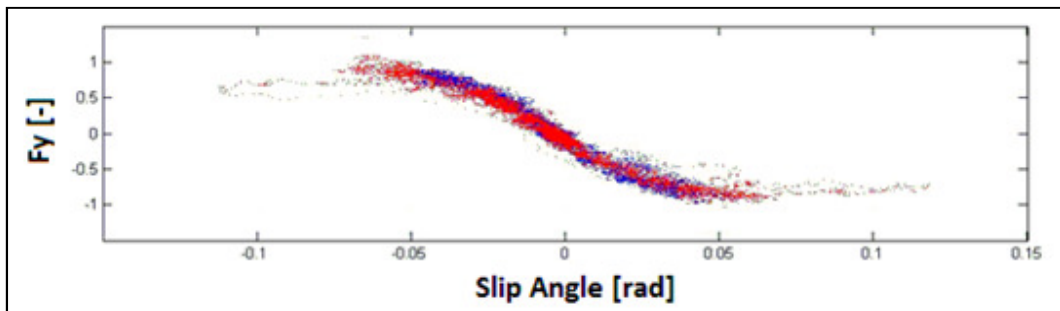


Fig. 2.35 - Temperature effect on tyre lateral interaction characteristic. Red points, relative to hot conditions (tyre bulk temperature  $> 55\text{ }^{\circ}\text{C}$ ), describe a curve characterized by higher grip and lower cornering stiffness respect to the cold one, in good agreement with expected results.

### **3. Trip-ID Tool - Tyre/Road Interaction Parameters Identification**

#### **3.1 Introduction**

One of the most diffused tyre/road interaction models, widely employed in simulation applications, is the Pacejka's Magic Formula (MF) [12][30]. It is a semi-empirical interpolation model able to fit full scale test data, characterized by a large number of coefficients, often called micro-parameters, grouped basing on physical considerations in order to create specific functions, called macro-parameters.

MF model coefficients provided by tyre manufacturers are generally not fully representative of the behaviour of tyres in contact with road. This is due to the testing conditions employed to identify model coefficients; tests are usually performed on a specific rolling bench or on a flat-trac<sup>11</sup>, that keep the tyre in contact with a steel or an abrasive paper covered belt.

The impossibility to test the tyres under real working conditions causes unavoidable approximation errors, mainly due to differences in thermal exchanges and wear phenomena between tyre/belt and real tyre/road contact. Therefore it is commonly necessary to modify the MF coefficients in order to improve the bench data correlation and to be able to validate vehicle models with data coming from experimental tests.

The aim of the developed tool, called TRIP-ID (Tyre/Road Interaction Parameters Identification), is to provide an innovative procedure to identify the Pacejka coefficients basing on the experimental tests carried out measuring global vehicle data during outdoor track sessions. The procedure collects and processes the data provided by TRICK tool (chapter 2), allowing to eliminate the outlier points, to discriminate wear and thermal phenomena, taking into account the combined slip condition and the effects of vertical load and camber angle on the global grip.

The innovative approach proposed can be useful to reproduce in real time simulation applications the feedback that high performances tyres give to sport vehicle drivers, whose interest and skills are focused on keeping them in the optimal thermal range. The coupling of a properly modified MF model with a thermal and with a friction model can provide a reliable simulation and analysis instrument for drivers, carmakers and tyre producers.

#### **3.2 Similarity Curve and Combined Effect function**

The Pacejka Magic Formula formulation is analogous both for pure longitudinal and lateral interaction and can be simply described using the following expression:

$$\begin{aligned} F_0 &= D \sin\{C \arctan[Bx_s - E(Bx_s - \arctan Bx_s)]\} + S_v \\ x_s &= X_s + S_h \end{aligned} \quad (3.1)$$

for which the adjective "pure" is used to indicate that the sliding velocity lies exclusively in the yz ISO plane [19] (in the case of pure side slip) or in the xz ISO plane (in the case

---

<sup>11</sup> Tyre testing system, commercialised by MTS Systems Corporation. It applies forces and motions to a tyre running on a continuous flat belt.

of pure longitudinal slip). In case of longitudinal interaction the variable  $X_s$  is the longitudinal slip ratio, while in case of lateral interaction it is the lateral; the output is the tangential force in pure interaction conditions. Sub-functions B, C, D, E,  $S_v$ ,  $S_h$ , called macro-parameters, are polynomial or exponential functions variable with the vertical load  $F_z$  and the camber angle  $\gamma$ , consequently able to make the model sensitive to these effects. Macro-parameters can be linked with physical quantities, assuming a graphical meaning in the forces plots (Fig. 3.1): B is linked to the braking stiffness, C represents the shape of the function, D the peak value, E fixes the maximum position and  $S_h$ ,  $S_v$  are the shifts from the Cartesian axes centre.

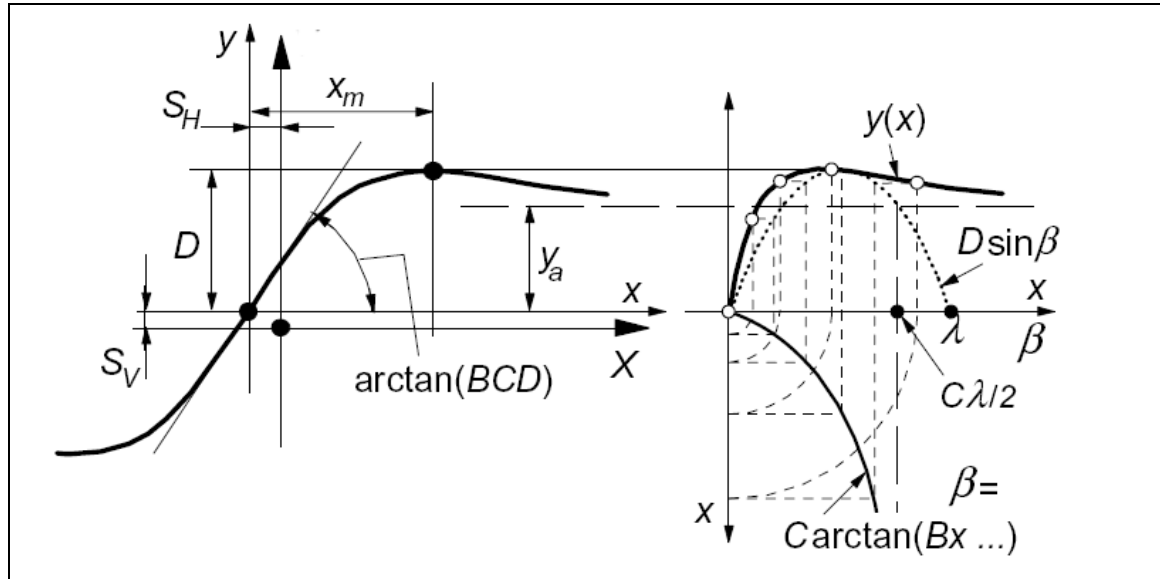


Fig. 3.1 - Magic Formula macro-parameters graphical meaning.

Equation (3.1) is not fully representative of the possible tangential interactions, because conditions in which the sliding velocity has simultaneously components in yz and xz plane can occur (combined tangential interactions). In this case the pure forces can be converted in the combined ones by multiplying the G combined function [12]:

$$G = \frac{\cos \left[ C_c \arctan \left\{ B_c x_c - E_c \left( B_c x_c - \arctan (B_c x_c) \right) \right\} \right]}{\cos \left[ C_c \arctan \left[ B_c S_{hc} - E_c \left( B_c S_{hc} - \arctan (B_c S_{hc}) \right) \right] \right]} \quad (3.2)$$

Sub-functions  $B_c$ ,  $C_c$ ,  $E_c$ ,  $S_{hc}$  contain the combined interaction micro-coefficients and depend on camber angle and vertical load variations.  $x_c$  variable, renamed in the following "ortho-slip", is lateral slip for longitudinal combined forces expression and slip ratio for lateral ones.

The Pacejka micro-coefficients identification cannot be developed as a simple function-fitting procedure, because it would not ensure a proper response of the formula in all the operating conditions. Unlike brush models, magic formula expression and parameters do not have direct physical meaning, not being obtained from an analytical closed form solution; in some way, a physical meaning can be found, linking the effects that parameters variations induce in the curves shape in analogous way to some physical variable experimentally known effects.

A first important step forward would be the possibility to recognize if the numerical values of the micro coefficients calculated by a regression algorithm are plausible or not. The new approach focuses mainly on the idea to find out a physical meaning for the coefficients and for the sub-functions of the equation and to consequently impose constraints to them in the identification algorithm.

In the first step some sub-functions are extracted from the model so that the complex structure of explicit Pacejka's formulation (where macro-coefficients do not appear) can be resumed as:

$$F(x_s, x_c, F_z, \gamma) = G(x_s, x_c, F_z, \gamma) * [\mu(x_s, F_z, \gamma) * F_z * f_0(x_s, F_z, \gamma) + F_z * S_v(x_s, F_z, \gamma)] \quad (3.3)$$

Dividing by  $F_z$ :

$$f(x_s, x_c, F_z, \gamma) = G(x_s, x_c, F_z, \gamma) * [\mu(x_s, F_z, \gamma) * f_0(x_s, F_z, \gamma) + S_v(x_s, F_z, \gamma)] \quad (3.4)$$

and assuming the quantity:

$$f_\mu(x_s, F_z, \gamma) = [\mu(x_s, F_z, \gamma) * f_0(x_s, F_z, \gamma) + S_v(x_s, F_z, \gamma)] \quad (3.5)$$

the equation becomes:

$$f(x_s, x_c, F_z, \gamma) = G(x_s, x_c, F_z, \gamma) * f_\mu(x_s, F_z, \gamma) \quad (3.6)$$

in which

- $F$  is the generic tangential interaction (longitudinal or lateral) [N]
- $\mu$  is the grip function [-], equal to  $D$  macro-parameter
- $f_0$  is the pure interaction normalized shape function [-]
- $f_\mu$  is the normalized pure interaction [-]
- $f$  is the "similarity curve" [-]

It is possible to identify in the previous sub-functions a particular physical meaning:

- $f$ , the so called "Similarity Curve", contains the pure interaction shape (inside  $f_0$ ) and the information about tyre maximum grip (inside  $D$ ), braking and cornering stiffness (BCD), etc, that are in turn expressed as a function of  $F_z$  and  $\gamma$ .
- $G$  multiplies the pure interaction to take into account the combined effect of interaction reducing the available adherence in the considered interaction direction, as discussed in chapter 1. It can be also called "Combined Effect" function and depends on asphalt roughness, grip anisotropy distribution and on the tyre stiffness components.

The clear distinction of Combined Effect and Similarity Curve functions is important for the development of the identification procedure, because it allows to separate in dedicated object functions the coefficients with different physical meaning in order to drive the identification towards a rational distinction of the different physical phenomena.

### 3.3 Classification and processing of experimental data

#### 3.3.1 Input analysis

The 56 channels matrix DATA provided by TRICK tool (chapter 2) works as an input for the identification procedure. The big amount of available data needs to be classified with the aim to separate the effects linked with the different events that occurred during the acquired track session, making to the single coefficient possible to vary inside a limited range, assuming the numerical value that enables the optimal reproduction of the effects to which they are destined inside Pacejka's formulation.

In the following figures the grip vs slip angle for the front lateral interaction are shown in non-dimensional plots for industrial confidentiality agreements; the experimental session has been carried out employing a high performance rear wheel drive sport vehicle. The front axle has been preferred for the discussion because its tyres are, for a rear wheel drive vehicle, more often in pure lateral interaction conditions than the rear axle ones; it allows to plot more clearly the experimental interaction curves, highlighting their variations at the different tyre working conditions.

It can be observed that the similarity curves for front tyre points measured in conditions of lateral interaction have a shape very similar to the expected theoretical characteristic curve (Fig. 3.2). The peak value of the similarity curves is the available grip and the thickness of the points cloud is due to load, camber, temperature and wear effects that cannot be split and separately analyzed if the whole session points are plotted together.

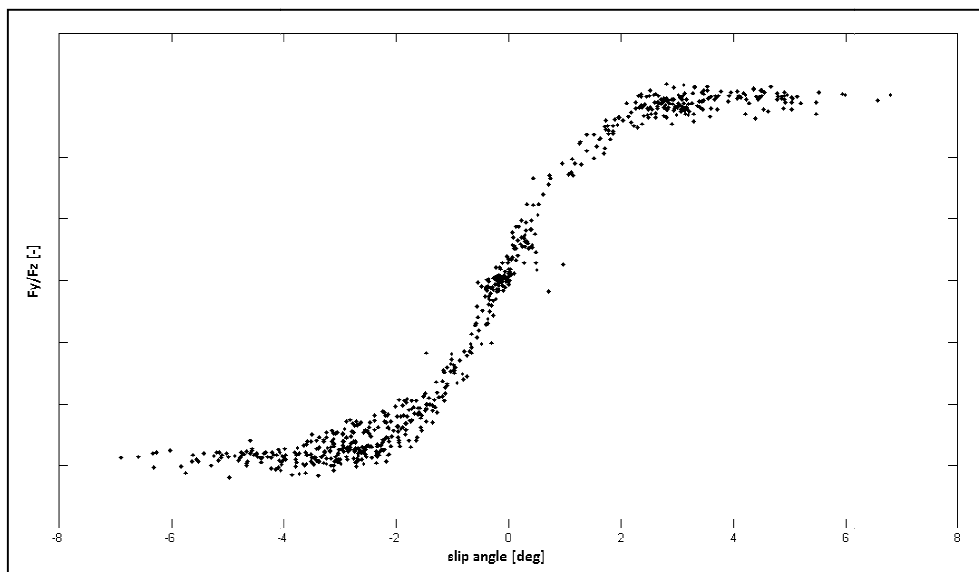


Fig. 3.2 - Front tyre lateral experimental points.

The procedure has been designed in order to be able to arrange the experimental points basing on the type of effect that has to be investigated and whose reproduction the coefficients identification must be driven to. As an example, focusing on thermal effect thanks to a specific test session and to a double experimental/predictive procedure better explained in chapter 6, it is possible to highlight the variations induced by temperature in the points cloud shape (Fig. 3.3); each differently coloured family of point can be then employed to study further effects like camber and load.

This kind of graph allows to easily identify outliers: all the points outside the expected s-shaped cloud can be discarded by means of specific algorithms [29], eliminating possible sources of misidentifications.

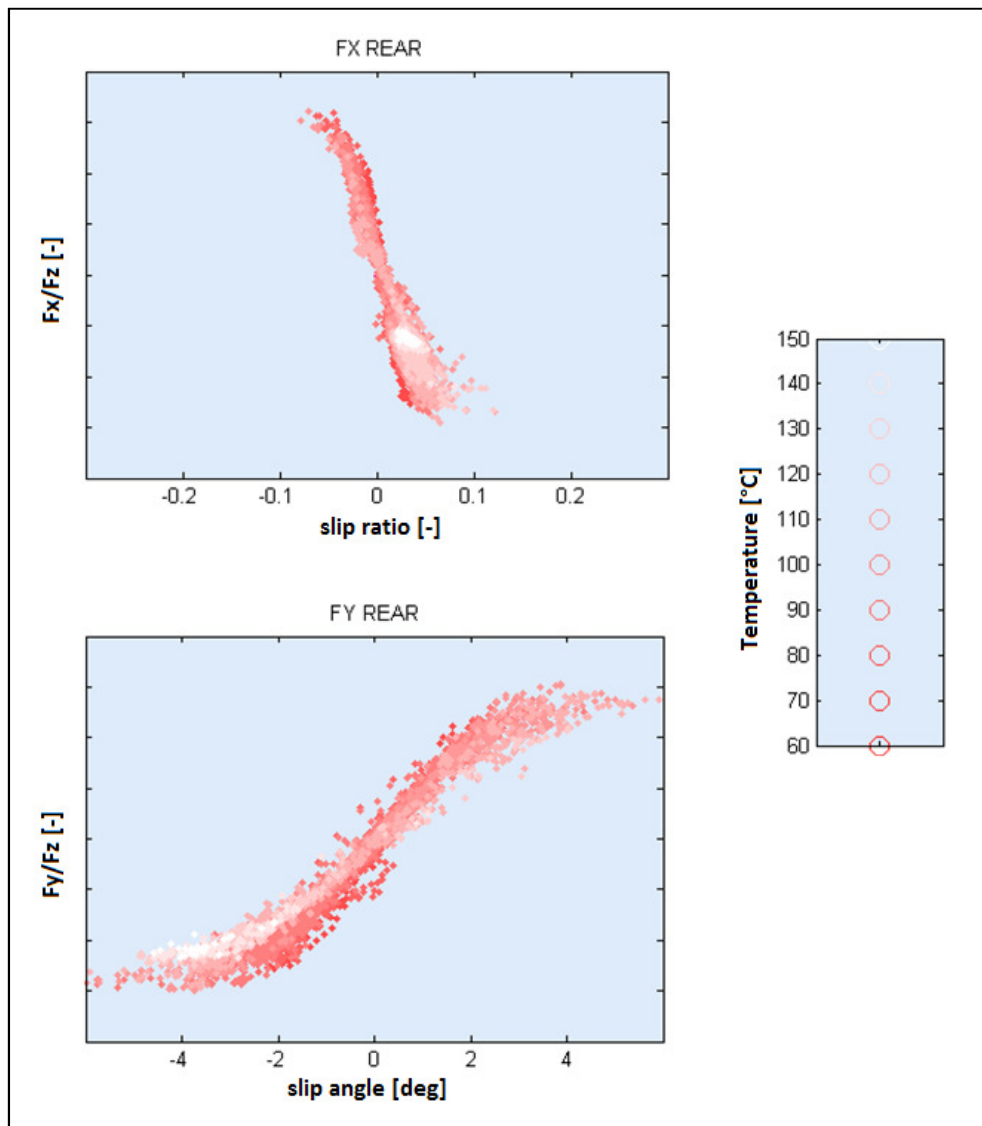


Fig 3.3 - Temperature effect analysis for rear sport tyre.

Observing the experimental similarity curve for the rear lateral case (Fig. 3.4), the shape of the points cloud does not appear well outlined as for the front case (Fig. 3.2), because of the effect of the combined interaction. Being rear axle characterized by traction and braking phases, rear tyres are often interested by both longitudinal and lateral slip at the same time. The vertical thickness of the points cloud is due to the decrease of available grip in lateral direction when a part of it is employed in the longitudinal direction for traction or braking and to the effect of tread temperature and wear on tyre grip.

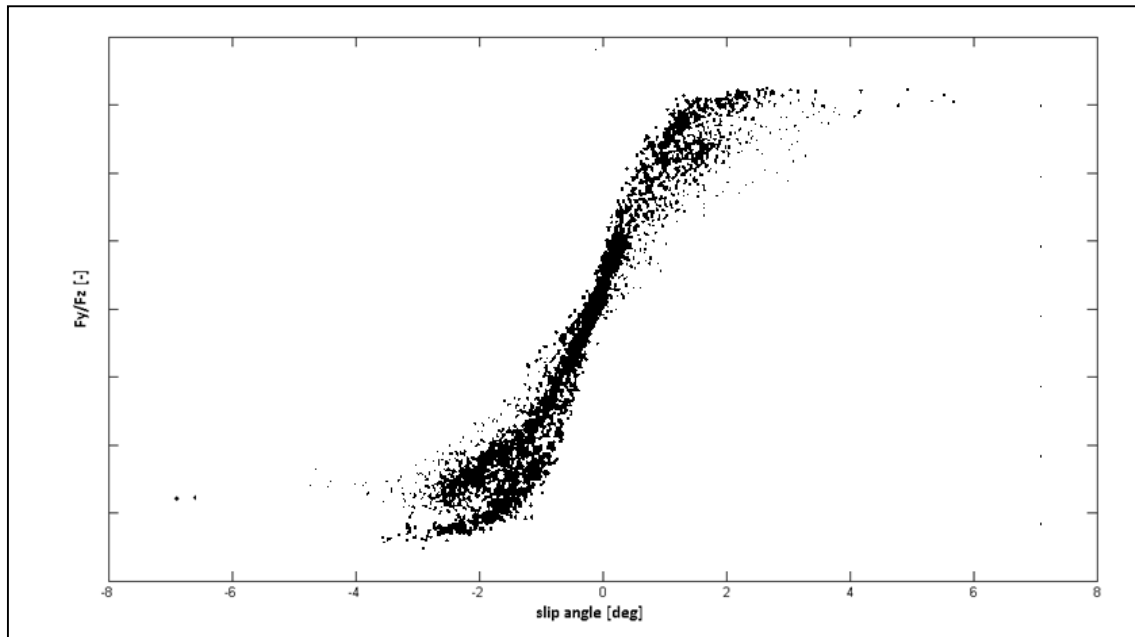


Fig. 3.4 - Rear tyre lateral experimental points.

A more detailed analysis can help to understand more clearly how the adherence can be split between lateral and longitudinal direction and consequently to estimate the decreasing trend of the bell-shaped G function. In figure 3.5 the points cloud relative to longitudinal interaction for a rear tyre is reported; the similarity graph shows a decreasing grip trend at slip angle increase, further confirmation of grip splitting theory along x and y directions. These data have been acquired during a normal race session; such kind of event is commonly sufficient to provide all possible conditions of combined slip useful to identify this effect.

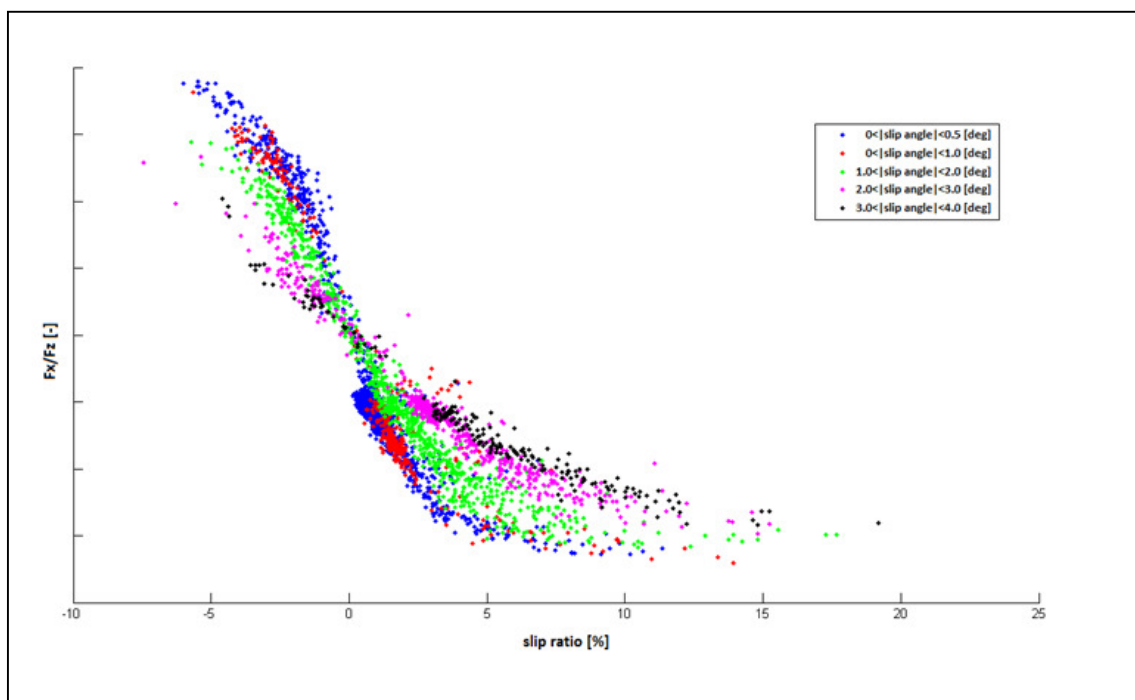


Fig. 3.5 - Experimental verification of combined effect on longitudinal interaction curve.

### 3.3.2 Identification Procedure - Pure Interaction

The first step of the procedure is the selection of the pure interaction conditions (working points characterized by longitudinal or lateral slip  $\approx 0$ , indicated by blue points in figure 3.5) that allow to identify  $f_\mu$  function coefficients. To this aim, DATA matrix points (chapter 2) have to be screened sample by sample in order to select the ones characterized by slip values contained inside a user-defined range. To wider ranges will obviously correspond a larger number of "pure points" but a less accurate identification; the optimal trade-off is an interesting theme further discussed in the following.

In a second phase, the coefficients of the combined effect function  $G$  will be identified in order to make the latter able to fit the remaining acquired nonzero-slip points scaling the  $f_\mu$  function already identified.

The regression algorithm, based on a constrained nonlinear optimization procedure [31][32], calculates the pure micro-coefficients  $X_{pmc}$  vector that minimizes the  $F_{OBJp}$  function, defined as the norm of an error vector  $ERRp$ , whose length is equal to the number of time samples constituting the starting dataset (DATA matrix):

$$\begin{aligned} [ERRp] &= [f_\mu(X_{pmc}, x_s(t), F_z(t), \gamma(t))] - [F_{DATA}(t)] \\ F_{OBJp} &= \text{norm}[ERRp] \end{aligned} \quad (3.7)$$

In equation (3.7),  $t$  is time and  $F_{DATA}$  is the vector employed for fitting, containing the temporal sequence of the measured (ore, more correctly, estimated by means of TRICK) interaction force values.

In simpler words, pure interaction identification procedure acts feeding Pacejka pure formulation with real acquired input values and comparing the consequent calculated output force with the "real" force value estimated under the same working conditions, looking for the micro-coefficients set able to minimize the difference between the two forces.

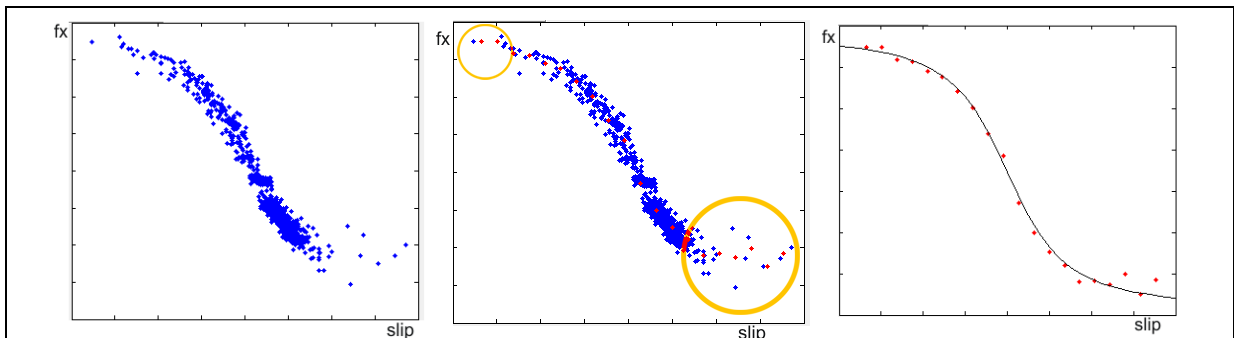


Fig. 3.6 - Effect of "mean function" on an inhomogeneous data set.

Having a large number of acquired points available, it is usually unavoidable that their distribution can be inhomogeneous; it could represent a problem for the identification procedure because the zones characterized by a higher number of points would have a greater weight and error vector norm minimization would be affected by it. For this reason a "mean function" has been adopted, consisting in:

- selection of points characterized by similar values (i.e. included in consecutive ranges of user-defined extension) of vertical load and camber angle (in figure 3.6a points belonging to a single range are reported);
- arrangement of the points of each range in sub-ranges based on slip ratio (or slip angle, for lateral interaction);
- calculation of the mean value of the points belonging to each sub-range (Fig. 3.6b).

In this way the  $F_{DATA}$  value that will be considered for each point will be the one provided by the "mean function"; points belonging to the same sub-range will be moreover considered only one time, providing an iso-weight tyre interaction characteristic, that will be identified by the algorithm (Fig. 3.6c).

Being the procedure based on a function minimization of "constrained" type, a great attention must be paid to the starting value of the parameters and on the extension of the range inside which they can vary. The minimization iterative algorithm commonly stops when a relative minimum for the objective function is found; in order to increase the possibility that the minimum found is also an absolute one, that means the optimal possible solution, it is firstly necessary that optimal values belong to the variation ranges, and that the starting set is already close enough to the optimal one.

The analysis of Pacejka formulation allows to define proper parameters variation ranges according to physical considerations; starting from the original Magic Formula in pure case (Eq. (3.1)), it is possible to analyze  $\mu$  function, aimed to model friction coefficient variations, that can be obtained from the D macro-parameter as  $\mu = D/F_z$ :

$$\begin{aligned} \mu_i &= (pD_{i1} + pD_{i2} \cdot dfz)(1 - pD_{i3} \cdot (\sin \gamma)^2) \\ dfz &= \frac{F_z - F_{z0}}{F_{z0}} \end{aligned} \quad (3.8)$$

in which index i is x for longitudinal interaction and y for lateral one and  $F_{z0}$  is a reference vertical load [12]. Neglecting camber effect, it is noticeable that the formulation describes a strongly nonlinear phenomenon like friction between viscoelastic materials and rough surfaces by means of a linear function; trying to give a general overview to the grip trend as a function of vertical load (see chapter 5 for further details), it can be said that, in particular for sport tyres, it is commonly decreasing because of the saturation effect that concerns with less than proportional contact area increase respect to vertical load [33]. It is moreover interesting to observe that:

$$\text{for } F_z = F_{z0} \rightarrow \mu_i = pD_{i1} \quad (3.9)$$

The previous considerations allow to set starting points and ranges of grip parameters in order to drive their identification following a physical approach;  $pD_{i1}$ , equal to available limit grip at reference vertical load, can be determined by means of specific experimental tests or analyzing acquired data, providing robust and easy starting value and variation range definition.  $pD_{i2}$ , even if not able to describe nonlinear functionalities, can be hypothesized negative for the discussed reasons, reducing sensitively its variation range.

For what concerns braking and cornering stiffness, they are described by macro-parameter K, that, differently from grip function, introduces the nonlinear effect:

$$K_i = B_i C_i D_i = F_z (pK_{i1} + pK_{i2} \cdot dfz) \cdot \exp(pK_{i3} \cdot dfz) \quad (3.10)$$

It is well known in literature [1][2] and experimentally observable [34] that tyre stiffness increases with vertical load; for this reason a constraint can be applied to micro-parameter  $pK_{i2}$ :

$$pK_{i2} \geq 0 \quad (3.11)$$

and in analogous way to equation (3.9), parameter  $pK_{i1}$  can be determined considering that:

$$\text{for } F_z = F_{z0} \rightarrow \frac{K_i}{F_{z0}} = pK_{i1} \quad (3.12)$$

Other hypotheses about physical constraints can be made analyzing available data for every specific case, in particular about shape coefficients ( $C_i$  macro-parameter); in the proposed case-study greater attention has been paid to grip and stiffness, that can be considered the causes of the main effects observable in tyre dynamics in average working conditions. Secondary effects can be modelled making the procedure work also without too strict constraints, leaving the variation ranges equal to the ones proposed by Pacejka himself.

### 3.3.3 Identification Procedure - Combined Interaction

Once identified  $f_\mu$  function parameters, it is possible to step forward to combined effect processing. G identification objective function is structured as follows:

$$\begin{aligned} [ERRc] &= [G(X_{cmc}, x_s(t), x_c(t), F_z(t), \gamma(t)) \cdot f_\mu(x_s(t), F_z(t), \gamma(t))] - [F_{DATA}(t)] \\ F_{Objc} &= \text{norm}[ERRc] \end{aligned} \quad (3.13)$$

The developed regression algorithm works with the aim to minimize  $F_{Objc}$  acting similarly to the pure interaction case, varying the values of the elements of the combined effect micro-coefficients vector  $X_{cmc}$ . For longitudinal case,  $f_\mu$  function and  $F_{DATA}$  values will be relative to longitudinal interactions; lateral case will employ lateral interactions data.

Also in this case a "mean function" has been adopted, different from the previous one for a preliminary selection criteria that allows to arrange points inside ortho-slip ranges, providing the results highlighted in figure 3.5 by different colours.

Points selected for G function identification show a friction and generalized stiffness trend (Fig. 3.7 and 3.8) in good agreement with the expected theoretical ones (Fig. 3.9).

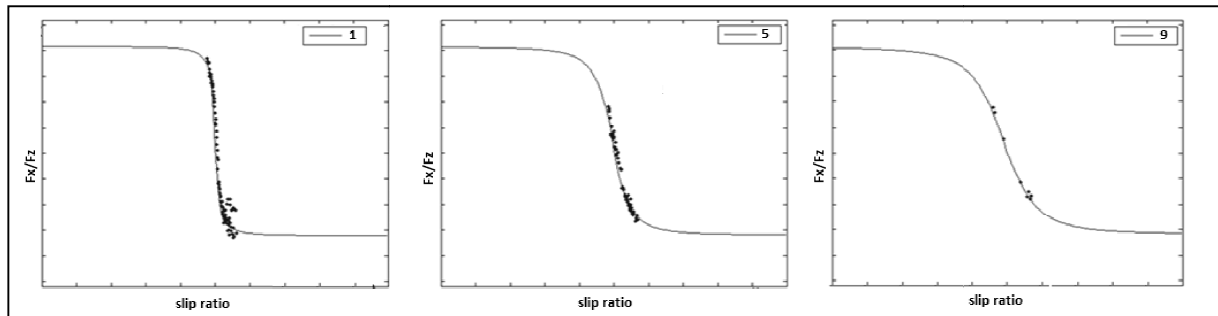


Fig. 3.7 - Comparison between identified curves and experimental points for combined longitudinal interaction at increasing slip angle (expressed in degrees in the boxes).

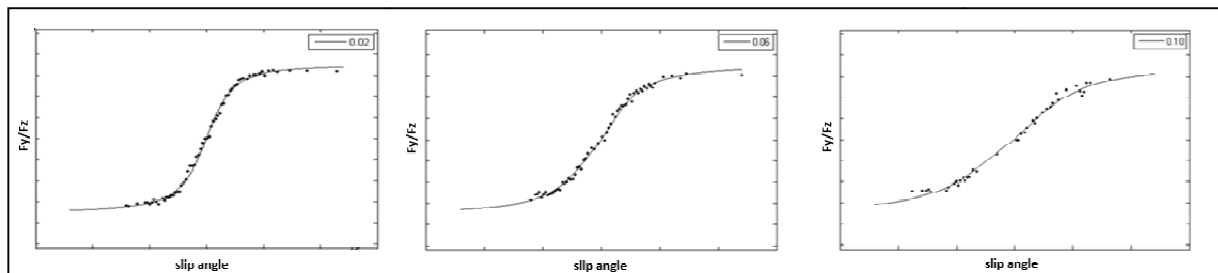


Fig. 3.8 - Comparison between identified curves and experimental points for combined lateral interaction at increasing slip ratio (expressed in nondimensional form in the boxes).

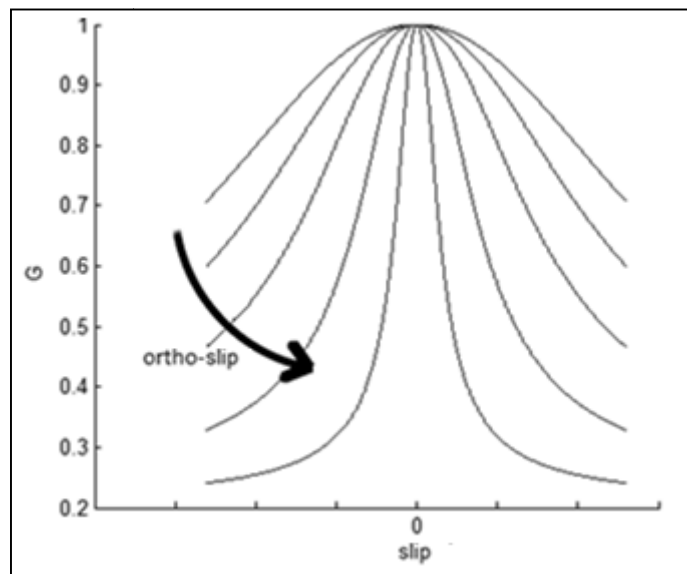


Fig. 3.9 - Theoretical trend of G function as a function of slip and ortho-slip.

### 3.4 Results Analysis

#### 3.4.1 Pure Interaction

In the following plots the results of pure interaction coefficients identification are presented and discussed; the lines are Pacejka Magic Formula output and they have been compared with the experimental points obtained by TRICK procedure shown in paragraph 2.4 (plots E-H).

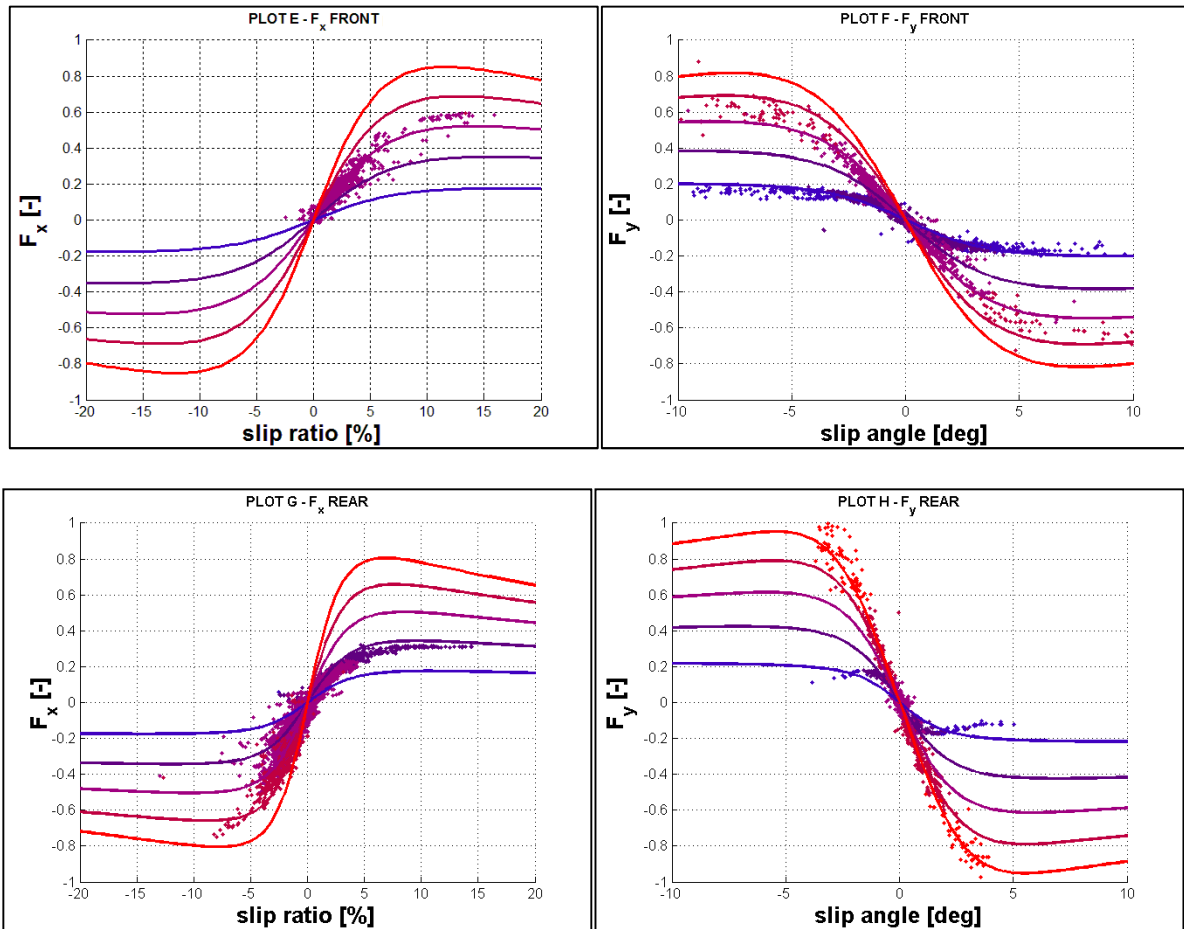


Fig. 3.10 - Plot E F G H - Comparison between identified pure interaction curves and respective experimental points.

In figure 3.10 to different colours correspond different load levels, reported in paragraph 2.4; a Pacejka parameters set provided by the tyre-maker has been employed as starting point and in figure 3.11 the iterative evolution that pure identification process has had from it can be observed in a time-based plot. The discontinuities are due to the selection of the pure conditions, that cuts away many points from the time history.

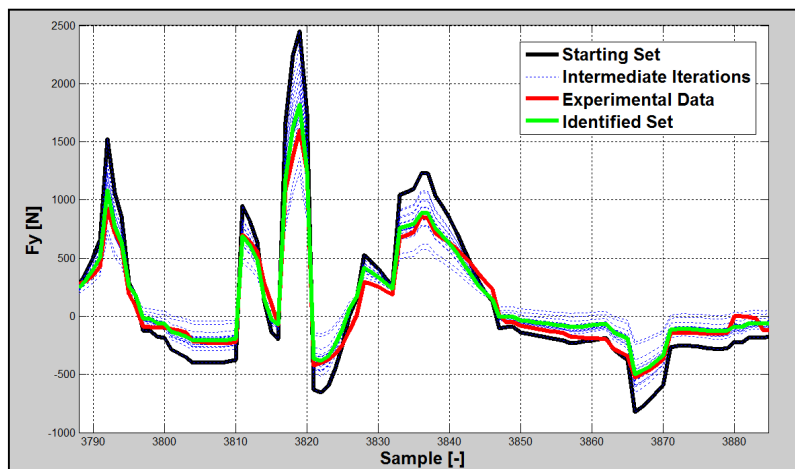


Fig. 3.11 - Evolution of the iterative procedure from the starting set to the final identified one.

### 3.4.2 Combined Interaction

From the pure interaction set shown in paragraph 3.4.1 and from the starting set provided by the tyre-maker, combined interaction function has been identified; the results of the procedure are reported in the following. Vertical loads acting on the tyres are equal to static ones, about 3500N at front and 4500N at rear.; slip and ortho-slip increasing step has been defined in 2.4.1.

Please note that, as already said, plots have been reported in non-dimensional form because of industrial confidentiality agreement.

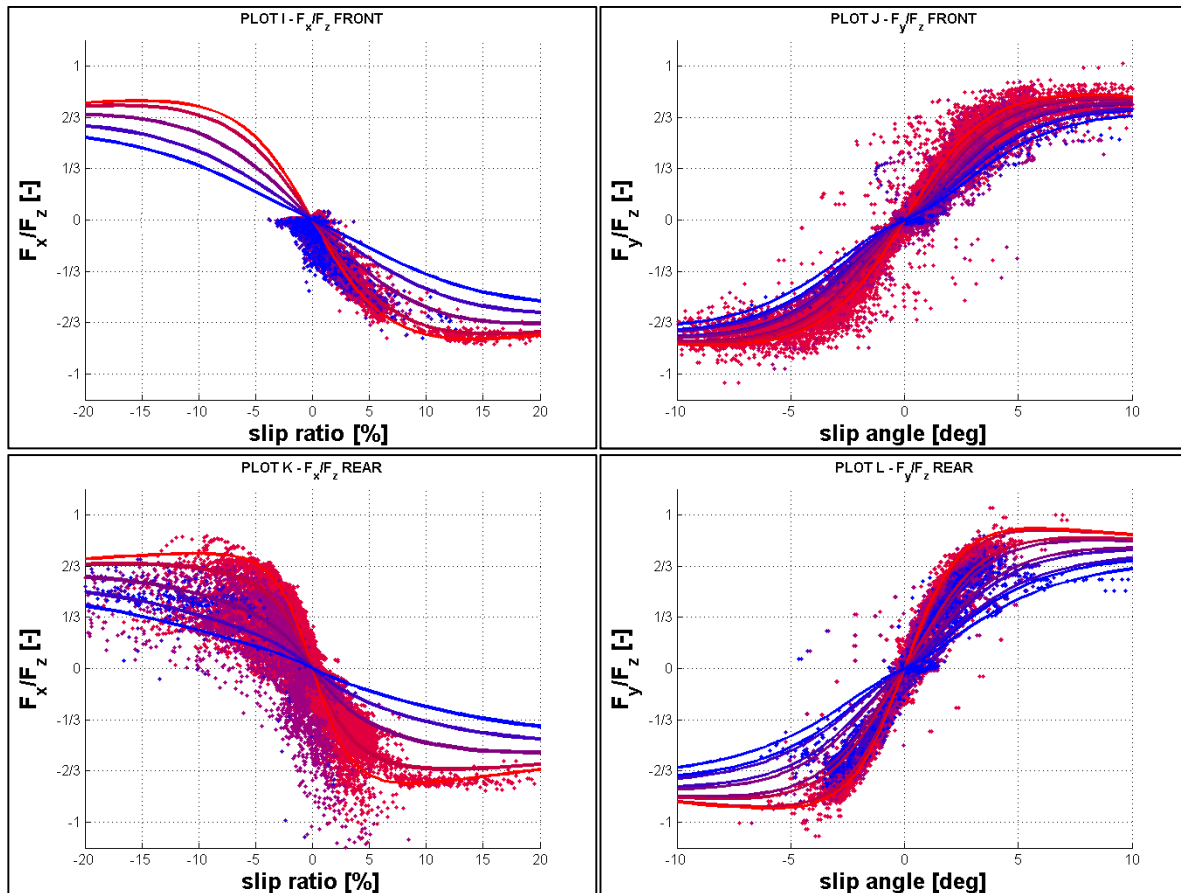


Fig. 3.12 - Plot I J K L - Comparison between identified combined interaction curves and respective experimental points.

As noticed in 2.4, combined longitudinal results are affected by error because of slip ratio misestimations. Their identification has been possible adding further constraints, consisting in null horizontal and vertical shifts. The employment of a proper starting set and a reliable pure interaction set identification has allowed to obtain good results, in particular for what concerns nonlinear zones characterized by a small or no number of points useful for identification.

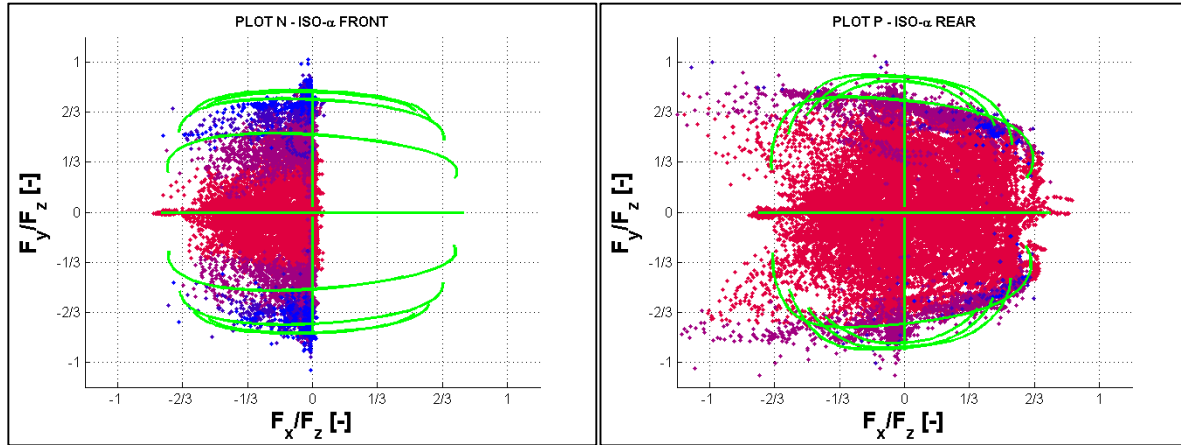


Fig. 3.13 - Plot N P - Comparison between identified iso- $\alpha$  ellipses and respective experimental points.

Adherence ellipses have been reported in figure 3.13 with different colours to make the comparison clearer. It can be noticed that iso-slip angle lines follow the profiles sketched by the points of the same colour, reproducing the expected phenomena, like the decreasing lateral force trend from the braking to the traction zone [1][12].

### 3.5 Further Developments

#### 3.5.1 An Alternative Identification Strategy - Pure Points Increasing

As stated in chapter 2, a complete tyre characterization (and its consequential parameters identification) is possible only if a satisfying number of points, representative of a working conditions range as wide as possible, is available.

In case of data acquired during not specific test sessions such requirement is not often respected, bringing to lack of fundamental information; a typical case is represented by too few points relative to pure interaction conditions, that result to be quite rare in usual driving manoeuvres (longitudinal pure conditions are characteristic of tyre states employing null slip angles, while lateral pure interaction is performed at null slip ratio, that represents a very particular and hardly reproducible condition during track sessions if not expressly requested).

An alternative method to increase the number of pure points useful for the identification procedure consists in the employment of the combined function: the coefficients of G function are commonly provided by tyre-makers together with the full Pacejka parameters set; their evaluation is in general less sensitive to road roughness and temperature variations, making it more robust than the pure function  $f_{\mu}$ . For this reason, following a "reverse" procedure it is possible, knowing the combined experimental force values  $F_{DATA}$  in each acquired instant  $t$  and the combined Pacejka G function value under the same input conditions  $(x_s(t), x_c(t), F_z(t), \gamma(t))$ , to obtain "virtual" pure experimental points  $F_{DATA-P}$ , that can be employed to identify pure interaction parameters.

$$F_{DATA-P}(x_s(t), F_z(t), \gamma(t)) = G(x_s(t), x_c(t), F_z(t), \gamma(t))^{-1} * F_{DATA}(t) \quad (3.14)$$

In figure 3.14 the result of the described method on the pure rear longitudinal interaction characteristic is reported; it is possible to notice that the number of points, rather unsatisfying at the beginning, is definitely increased, allowing to clearly distinguish braking and traction phases and to have a larger amount of available points able to feed a consistent identification procedure.

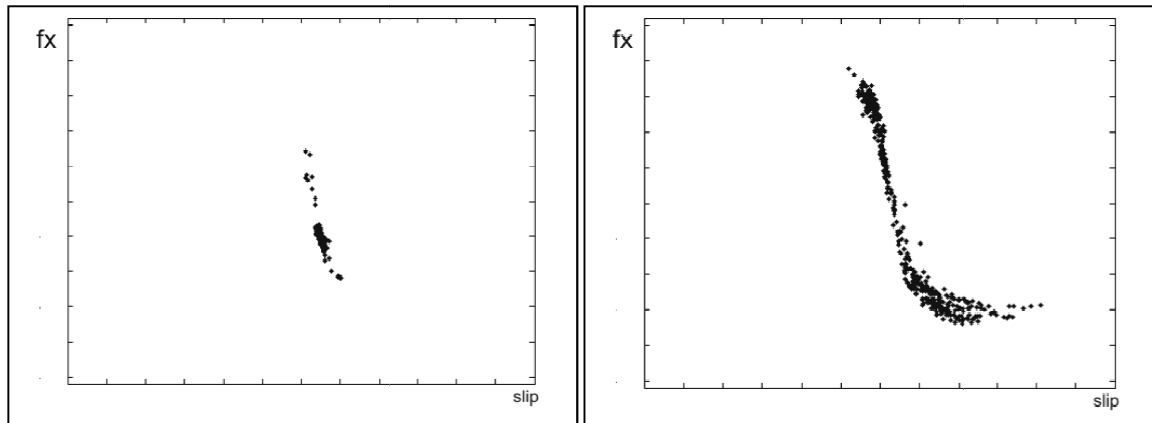


Fig. 3.14 - Results of the procedure developed to increase the number of pure interaction points.

### 3.5.2 Temperature / Wear effects modelling in Pacejka formulation

Tyre/road friction coefficient is highly influenced by working temperature (it will be deeply discussed in the following chapter), showing a dependence commonly described by a bell-shaped curve. In racing and sport tyres, such trend is particularly evident and depending on the employed tread compound the curves are characterized by different peak and respective temperature values.

In general, sport tyres are characterized by an optimal thermal working range: low working range compounds (LWR), often called "soft", offer their optimal performances at lower temperatures than high working range ones (HWR), commonly defined "hard" (Fig. 3.15) and, maximizing hysteretic and adhesive grip components thanks to their lower dynamic modulus (see chapter 5), are able to reach higher friction level.

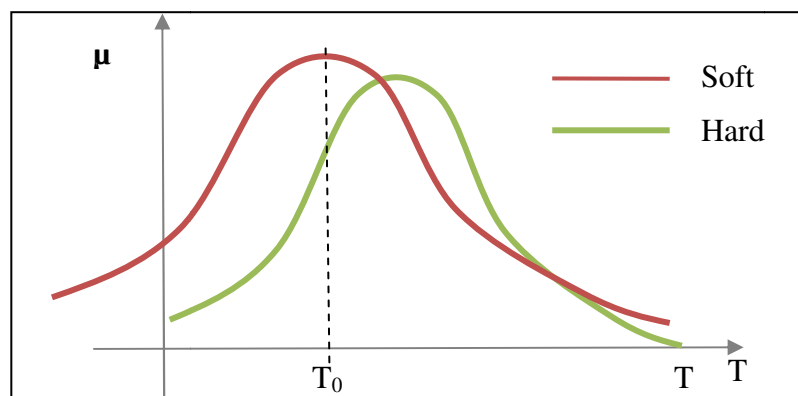


Fig. 3.15 - Theoretical friction vs temperature trend for LWR (soft) and HWR (hard) compounds.

In the Pacejka formulation the grip dependence with temperature is not taken into account, but data analysis and driver feelings strongly highlight how fundamental

such functionality is. Thermal effects are clearly noticeable observing the shape of the similarity curve at different temperatures (Fig. 3.3) and can be summarized with a stiffness decrease at increasing temperature and with a grip maximization inside its optimal thermal range.

The possibility to include the temperature effect inside Pacejka formulation could represent a key feature in order to model in driving simulations and in vehicle dynamics analyses an effect that results absolutely not negligible; a method studied to achieve the result consists in the employment of a specific scaling factor inside G function, generating a variation in the analytic structure the less invasive as possible.

Considering the longitudinal formulation (but the procedure can be applied for the lateral one exactly in the same way), indicating slip ratio with  $slip_x$  and slip angle with  $\alpha$  and imposing micro-parameter  $r_{Hx1}$  (and consequently  $S_{Hx\alpha}$ ) equal to zero:

$$G_x = \cos \left[ C_{x\alpha} \arctan \left\{ B_{x\alpha} \alpha - E_{x\alpha} \left( B_{x\alpha} \alpha - \arctan ( B_{x\alpha} \alpha ) \right) \right\} \right] \quad (3.15)$$

in which  $B_{x\alpha}$  is equal to the classical Pacejka macro-parameter multiplied by the additional scaling factor  $\lambda_T$ :

$$B_{x\alpha} = r_{Bx1} \cos(\arctan(r_{Bx2} slip_x)) \lambda_{x\alpha} \lambda_T \quad (3.16)$$

$r_{Hx1}$  is imposed equal to zero with the aim to prevent the hill function from translating vertically, with the consequence to ensure that the peak value is unitary. The scaling factor  $\lambda_T$  is structured as follows, having unitary maximum value and decreasing linearly when the difference  $(T-T_0)$  increases:

$$\lambda_T = \frac{1}{\alpha} \left( \alpha + c_{TEMP} \left| \frac{T - T_0}{T_0} \right| \right) \quad (3.17)$$

in which T is actual tyre temperature,  $T_0$  is optimal one, determined experimentally or by means of a grip model (chapter 5) and  $c_{TEMP}$  is a parameter that needs to be identified together with  $T_0$  and that is linked with the width of the bell curve that describes grip performance decreasing.

Being introduced inside combined interaction formulation, temperature dependence works similarly to ortho-slip, making the scaling bell shaped curve translate along slip axis as shown in figure 3.16.

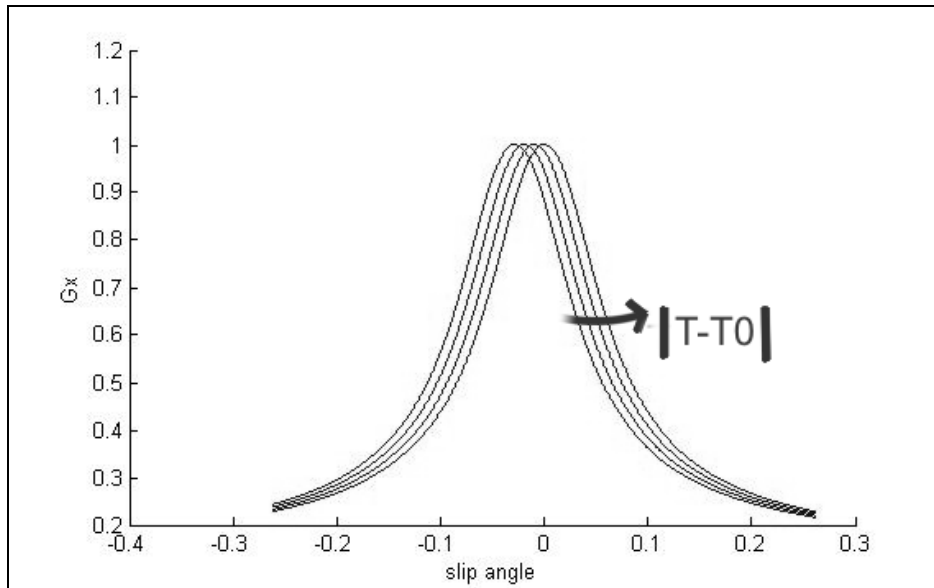


Fig. 3.16 - Scheme of the temperature effect modelled inside Pacejka formulation with the proposed method.

A detailed picture of the peak zone with reference to temperature is provided in figure 3.17; it is possible to notice that function maximum possible value is one and that, tuning properly the function parameters, the experimental or modelled link between grip and temperature can be reproduced, with the consequence that the resulting Pacejka model is able to take into account the desired phenomena. Further details about the possibilities that the described procedure opens will be discussed in detail in chapter 6, together with the analysis techniques derived from the developed models cooperation.

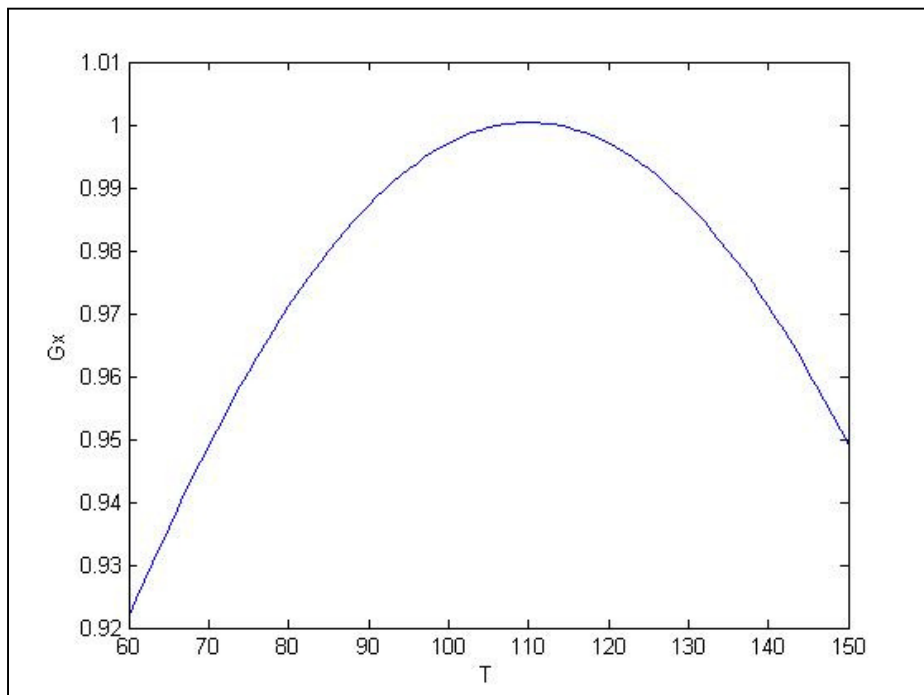


Fig. 3.17 - Peak of the  $G$  vs Temperature bell shaped curve.

## **4. TRT - Thermo Racing Tyre**

### **4.1 Introduction**

In automobile racing world, where reaching the limit is the standard and the time advantage in an extremely short time period is a determining factor for the outcome, predicting in advance the behaviour of the vehicle system in different conditions is a pressing need. Moreover, new regulations limits to the track test sessions made the "virtual experimentation" fundamental in the development of new solutions.

Through the wheels, the vehicle exchanges forces with the track [12][21] which depend on the structure of the tyres [35] and on their adherence, strongly influenced by temperature [36][37]. Theoretical and experimental studies, aimed to predict temperature distribution in steady state pure rolling conditions, useful to evaluate its effects on energetic dissipation phenomena, are quite diffused in literature [38][39]. Less widespread are analyses conducted in transient conditions involving tyre temperature effects on vehicle dynamics. A thermal tyre model for racing vehicles, in addition to predict the temperature with a high degree of accuracy, must be able to simulate the high-frequency dynamics characterizing this kind of systems. Furthermore, the model has to be able to estimate the temperature distribution even of the deepest tyre layers, usually not easily measurable on-line; it must predict the effects that fast temperature variations induce in visco-elastic materials behaviour, and it must take into account the dissipative phenomena related to the tyre deformations.

With the aim to understand the above phenomena and to evaluate the influence of the physical variables on the thermal behaviour of the tyre, an analytical-physical model has been developed and called Thermo Racing Tyre (TRT).

At present time there are not physical models available in literature able to describe the thermal behaviour of the tyres in a sufficiently detailed way to meet the needs of a racing company. The TRT model may be considered as an evolution of the ThermoTyre model [40] that allows to determine in a simplified way the surface temperature of such system, neglecting the heat produced by cyclic deformations and not considering the structure of the different layers.

The above mentioned limitations of ThermoTyre have been removed in the implementation of TRT, that results in an accurate physical model useful for the thermal analysis of the tyre and characterized by predictive attitudes since it is based on physical parameters known from literature or measurable by specific tests [41].

### **4.2 Tyre modelling and base hypotheses**

The tyre is considered as unrolled in the circumferential direction (and then parallelepiped-shaped), lacking of sidewalls and grooves (so the tyre is modelled as slick), discretized by means of a grid, whose nodes represent the points in which the temperature will be determined instant by instant (Fig. 4.1).

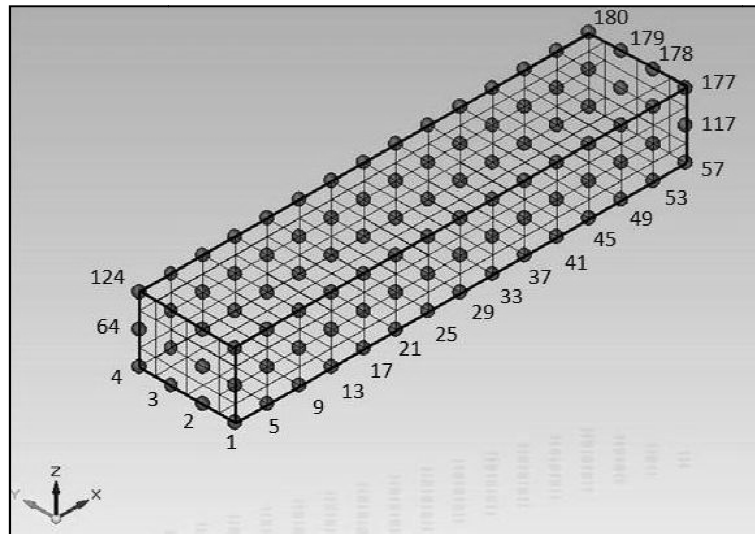


Fig. 4.1 – Discretization of the tyre.

The parallelepiped is constituted by three layers in the radial direction  $z$ , which will be hereinafter indicated as surface (outer surface of the tyre), bulk (intermediate layer), and inner liner (inner surface).

The number of nodes of the grid is given by the product ( $\text{numx} \cdot \text{numy} \cdot \text{numz}$ ) where  $\text{numx}$  represents the number of nodes along the  $x$  direction,  $\text{numy}$  the number of nodes along the  $y$  direction and  $\text{numz}$  is the number of nodes along the  $z$  direction. Nodes enumeration has been carried out starting from the first layer in contact with the road, proceeding transversely. Each layer is subdivided in 15 elements in the longitudinal direction and 4 elements in the transversal direction, so the entire tyre results discretized in 180 elements (but clearly the discretization can be modified).

The chosen Cartesian reference system has its origin in the node 1;  $x$ -axis is oriented in the circumferential direction of the tyre enrolled in a plane,  $y$ -axis is oriented in the direction of its width, and finally  $z$ -axis is oriented in the thickness direction; the positive direction is defined in all the three cases by the increasing numbering of the nodes. Along the radial direction, i.e. along  $z$ , two zones of homogeneous material are identified: the first one (thickness =  $\Delta z_1$ ), localized between surface and bulk nodes, correspondent to the tread; the second one (thickness =  $\Delta z_2$ ) to the tyre carcass.

Tread is mainly constituted by visco-elastic vulcanized polymers and fillers, while carcass includes also reinforcements.

Each one of them is characterized by the following physical parameters, accounting for the material composition:

- density  $\rho$
- Specific heat  $c$
- Thermal conductivity  $K$

and for the last two quantities it has been taken into account their variability with temperature.

To the generic  $i$ -th node a parallelepiped volume was associated, equal to

$$V_i = \Delta x \cdot \Delta y \cdot \Delta Z_{m,i} \quad (4.1)$$

in which  $\Delta x$  and  $\Delta y$  are respectively the dimensions along the directions  $x$  and  $y$ , while the quantity  $\Delta Z_{m,i}$  represents the dimension along the  $z$ -direction of the  $i$ -th layer defined so that once multiplied the obtained volume  $V_i$  by the density, the mass results equal to the expected one for each single element.

Each node will then have a mass  $m_i$  expressed as follows:

$$m_i = C \cdot V_i \cdot \rho \quad (4.2)$$

where the  $C$  coefficient depends on the position in the grid. Indeed, from figure 4.1 it is easy to notice that the volumes associated to the external nodes (e.g. node 1) are characterized to be parallelepiped-shaped, having sides in the direction  $y$  and  $z$  respectively equal to  $\Delta Y/2$  and to  $\Delta Z_{m,i}/2$ . Therefore, in this case, the coefficient  $C$  will be equal to  $1/4$ . With the aim to characterize the coefficients  $C$  for each kind of node, the following list is proposed:

- $C = 1/4$  for a node of the first layer, external in the transversal direction
- $C = 1/2$  for a node of the first layer, internal in the transversal direction
- $C = 1/2$  for a node of the bulk layer, external in the transversal direction
- $C = 1$  for a node of the bulk layer, internal in the transversal direction
- $C = 1/4$  for a node of the inner liner, external in the transversal direction
- $C = 1/2$  for a node of the inner liner, internal in the transversal direction

With the aim of modelling heat flows and tyre layers temperatures, the following assumptions have been adopted:

- Road is isotropic and homogeneous in all its characteristics, without irregularities, schematized as a geometric plane, whose surface temperature is known and equal to  $T_s$
- It is assumed that the contact area is rectangular in shape, characterized by width  $W$  equal to the width of the tread, and length  $L_a$  depending on the radial stiffness of the tyre and on the normal load. The assumption of rectangular shape of the contact area is realistic in the case of sport tyres, characterized by high width values.
- Camber angle is assumed equal to zero
- During rolling it is assumed that the tyre keeps the deformed configuration, and consequently contact patch extension, reached under the application of the static load.
- The tyre is also assumed motionless, in a Lagrangian approach, with variable boundary conditions
- The radiation heat transfer mechanism is neglected.

### 4.3 Thermodynamic model

The developed thermodynamic tyre model is based on the use of the diffusion equation of Fourier applied to a three-dimensional domain.

The complexity of the phenomena under study and the degree of accuracy required have made that it becomes necessary to take into account the dependence of the thermodynamic quantities and in particular of the thermal conductivity on the temperature.

Furthermore, the non-homogeneity of the tyre has made it necessary to consider the variation of the above parameters also along the thickness.

Therefore, the Fourier equation takes the following formulation [42]:

$$\frac{\partial T}{\partial t} = \frac{\dot{q}_G}{\rho \cdot c_v} + \frac{1}{\rho \cdot c_v} \cdot \left( \frac{\partial^2 k(z, T) \cdot T}{\partial x^2} + \frac{\partial^2 k(z, T) \cdot T}{\partial y^2} + \frac{\partial^2 k(z, T) \cdot T}{\partial z^2} \right) \quad (4.3)$$

Writing the balance equations for each generic node needs the modelling of heat generation and of heat exchanges with the external environment.

For the tyre system, the heat is generated in two different ways: for friction phenomena arising at the interface with the asphalt and because of stress - deformation cycles to which the entire mass is subjected during the exercise.

#### 4.4 Friction power

The first heat generation mechanism is connected with the thermal power produced at tyre-road interface because of interaction; in particular, it is due to the tangential stresses that, in the sliding zone of the contact patch [1], do work dissipated in heat. This power is called "friction power" and will be indicated in the following with FP. In the balance equations writing, FP can be associated directly to the nodes involved in the contact with the ground.

Since the lack in local variables availability, FP is calculated as referred to global values of force and sliding velocity, assumed to be equal in the whole contact patch:

$$FP = \frac{F_x \cdot v_x + F_y \cdot v_y}{A} \quad [W/m^2] \quad (4.4)$$

A part of this thermal power is transferred to the tyre and the remaining to the asphalt. This is taken into account by means of a partition coefficient CR.

To determine the partition coefficient, the following expression can be used [43]:

$$CR = \frac{k_t}{k_r} \cdot \sqrt{\frac{\alpha_r}{\alpha_t}} \quad (4.5)$$

in which thermal diffusivity  $\alpha$  can be expressed as  $\alpha = \frac{k}{\rho \cdot c_v}$ .

Considering the following road properties:

$$k_r = 0.55 \left[ \frac{W}{m \cdot K} \right] \quad (4.6)$$

$$\rho_r = 2200 \left[ \frac{Kg}{m^3} \right] \quad (4.7)$$

$$c_{v_r} = 920 \left[ \frac{J}{Kg \cdot K} \right] \quad (4.8)$$

and the properties of the SBR (Styrene and Butadiene mixture used for the production of passenger tyres), available in literature [44][45], the resulting calculated value of CR is about 0.55, which means that the 55% of the generated power is directed to the tyre.

Since the model takes into account the variability of the thermal conductivity of rubber with the temperature, also the CR coefficient will be a function of the calculated temperature; this results in a variation between 0.5 and 0.8.

Since  $F_x$  and  $F_y$  are global forces between tyre and road, and not known the contribution of each node to these interaction forces, heat generated by means of friction power mechanism transferred to the tyre has been equally distributed to all the nodes in contact with the ground. The model allows not uniform local heat distributions as soon as local stresses and velocities distributions are known.

## 4.5 Strain Energy Loss (SEL)

### 4.5.1 Introduction

The energy dissipated by the tyre as a result of cyclic deformations is called Strain Energy Loss (SEL). This dissipation is due to a superposition of several phenomena: intra-ply friction, friction inside plies, nonlinear visco-elastic behaviour of all rubbery components.

The cyclic deformations to which the system is subject occur with a frequency corresponding to the tyre rotational speed. During the rolling, in fact, portions of tyre, entering continuously in the contact area, are submitted to deformations which cause energy loss and then heat dissipation.

In the model the amount of heat generated by deformation (SEL) is estimated through experimental tests carried out deforming cyclically the tyre in three directions (radial, longitudinal and lateral) [34]. These tests are conducted on a proper test bench and a test plan, based on the range of interaction forces and frequencies at which tyre is usually stressed, has been developed.

### 4.5.2 The Test Bench

The tyre test rig is essentially composed by:

- A system for applying the vertical load to the tyre consisting of:
  - A manually actuated hydraulic press (Fig. 4.2 (1));
  - A fixed frame integral with the press fixed structure (Fig. 4.2 (2));
  - A vertically mobile frame (Fig. 4.2 (3)) in contact with a press actuator on which a universal quick flange (Fig. 1 (4)) to lock the wheel is mounted;
  - A system with manually variable weights (Fig. 4.2 (5)) to balance the weights of the mobile frame and the wheel so that the tyre has no initial vertical load;
  - Two linear guide rails (Fig. 4.2 (6)) placed along the vertical direction between the fixed and the mobile frame;
    - A system to apply the tangential load to the tyre, consisting of:
      - A linear actuator (Fig. 4.2 (7)) whose fixed part is integral with the press fixed frame;
      - A plate (Fig. 4.2 (8) and Fig. 4.4), on which the tyre is vertically loaded, which can be moved horizontally and is directly connected to the linear actuator;
      - A fixed plate (Fig. 4.2 (9) and Fig. 4.4) integral with the press fixed frame;
      - Two linear guide rails (Fig. 4.2 (10) and Fig. 4.4) placed along the tangential direction between the fixed and the mobile plate.

The test rig is also equipped with the following measurement instruments:

- A strain gauge load cell (Fig. 4.2 (11)) to measure the vertical load applied by the press;
- A draw-wire sensor (Fig. 4.2 (12)) to evaluate tyre deformation along the vertical direction;

- A quartz force sensor (Fig. 4.2 (13) and Fig. 4.4) to measure the horizontal load applied by the linear actuator;
- A position transducer with restoring spring (Fig. 4.2 (14) and Fig. 4.4) to evaluate tyre deformation along the horizontal direction.

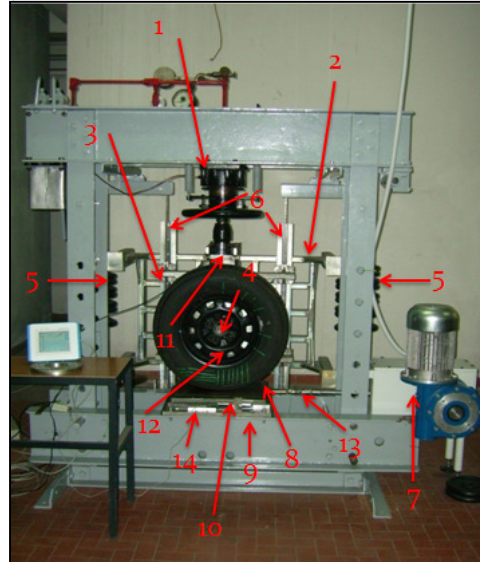


Fig. 4.2 - The test rig.

The horizontal linear actuator (Fig. 4.2 (7)) converts the rotary motion, imposed by an electric motor coupled to a gearbox with a transmission ratio equal to 20, into the alternative rectilinear motion of the mobile plate (Fig. 4.2 (8)). The actuator includes an innovative rotary crank mechanism in which the crank consists of a double eccentric as shown in figure 4.3.

The drive mechanism consists of three elements: a disc eccentrically fixed on the transmission shaft placed inside a second disc (collar) which is also eccentric, and finally a connecting rod, linked to the collar by a rolling bearing, which moves the plate by means of a bar.

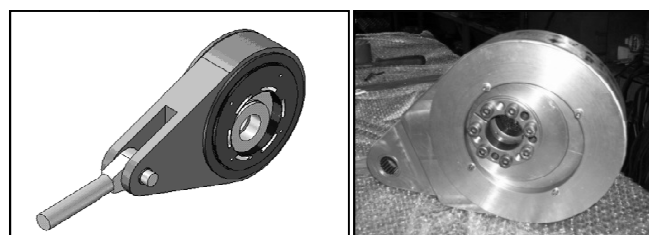


Fig. 4.3 - Crank-rod drive mechanism.

The offline relative rotation of the two eccentric elements provides the change of the crank radius, thus allowing the drive system to achieve different values of the movable plate stroke and different values of tyre strain amplitude; this operation should be done before starting each test campaign. The range of plate stroke can vary from 0 to 40 mm since each of the eccentric parts has an eccentricity of 10 mm.

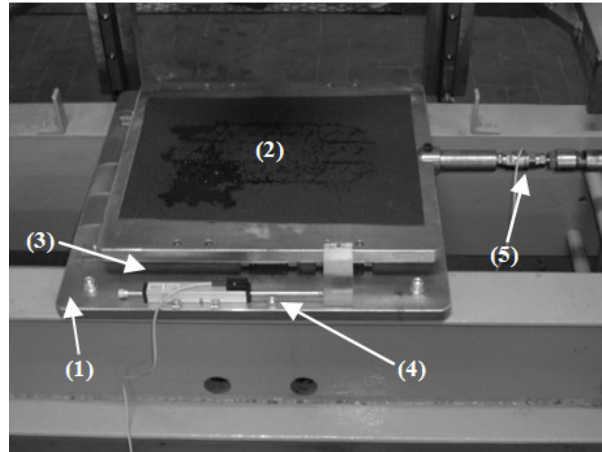


Fig. 4.4 - Test rig detail – (1) Frame; (2) Mobile plate; (3) Linear guide rail; (4) Longitudinal position transducer; (5) Load Cell.

The driving rod is fixed to the connecting rod on one side by flanges and bolts, the other side is articulated to the plate through a universal joint. The eccentric inner disc has been fixed on the transmission shaft through a self-centring friction device (sit-lock).

Alternative fixing systems of the universal quick flange on the vertically mobile frame, suitably inclined, allow to conduct tests with nonzero camber and/or toe angles.

#### 4.5.3 Tests Procedure

Opportune tests carried on the described test rig allow to determine the following mechanical characteristics of an automotive pneumatic tyre: the normal interaction characteristic, the radial stiffness, the total stiffness, the longitudinal and lateral hysteretic cycles and the consequent strain energy loss.

In particular, to this aim, two different test procedures have been developed: radial and horizontal tests. To execute these tests the tyre has been locked to the universal quick flange.

- Radial test

This kind of test consists in a quasi-static tyre radial compression; it is realized manually actuating the press while the horizontal movable plate is kept stopped, and it is conducted with different values of the inflation pressure. During this kind of test the vertical load and the corresponding strain are acquired, and consequently it is possible to determine the normal interaction characteristic and the radial stiffness.

- Horizontal test

To perform this kind of test, first of all, it is necessary to move the plate to one of the ends of its stroke. Then the tyre is positioned so that, for longitudinal tests, its midplane, orthogonal to its axis, contains the crank-rod mechanism axis; for lateral tests tyre axis must be in the same vertical plane that contains the crank-rod mechanism axis. Subsequently a prescribed vertical load is applied, greater than the one necessary to avoid tyre sliding. After this the linear actuator is activated with fixed values of its motion amplitude and frequency.

So all the available stroke is used to strain the tyre along a unique direction (unilateral test), as occurs usually during its working in pure tangential interaction conditions.

The linear actuator imposes the stroke and hence the tyre strain in the contact patch.

This kind of test can be conducted, for a fixed tyre, varying the inflation pressure, the vertical load, the stroke magnitude, the linear actuator motion frequency. At the end of this test it is possible to determine the total stiffness, the longitudinal and lateral hysteretic cycles.

#### 4.5.4 Normal Interaction Characteristic and Radial Stiffness

The radial tests, as said, allow to determine the normal interaction characteristic and the radial stiffness of a tyre. The first one is obtained measuring the vertical load applied to the tyre and its deformation along the same direction and representing the first as function of the second, while the radial stiffness is the discrete derivative of the normal interaction curve as a function of the vertical strain. This measure can be repeated varying the tyre radial direction unlocking the tyre, after having rotated it of a fixed angle, and locking it again to the universal quick flange (the radial stiffness should be the same along each radial direction considering the tyre axial symmetry). It is possible to see how the considered quantities vary with the inflation pressure. In figure 4.5 different normal interaction characteristics, obtained varying the inflation pressure, together with the relative mean values of the radial stiffness, for a Firestone 195/65 R 15 91T Tubeless pneumatic tyre, are reported.

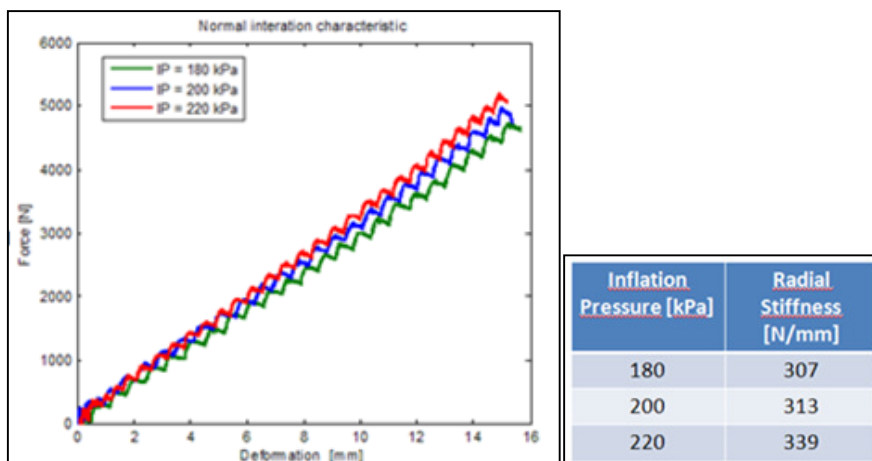


Fig. 4.5 - Normal interaction characteristic and radial stiffness.

As expected the tyre becomes more stiff in radial direction increasing the inflation pressure. Oscillations in the curves are due to the fact that vertical load is manually applied acting on the press; after each load increase, the tyre exhibits an elastic release, that causes the visible oscillations.

#### 4.5.5 Hysteresis Cycles and Total Stiffness

The horizontal tests allow to determine the tyre total stiffness and its hysteretic cycles. The total stiffness is the one involved in the tangential test due to the vertical load and the horizontal tyre strain. It is called “total” because it includes both a radial, an axial and a torsional contribution.

The tyre hysteresis cycles come out plotting the horizontal load as a function of the horizontal strain.

A test campaign has been conducted, on a predetermined tyre, varying the amplitude and the frequency of the linear actuator motion, the vertical load, the tyre inflation pressure and the toe angle. In particular the values adopted for the above

parameters are reported in table 4.1:

Amplitude of the linear actuator motion [mm]	9 - 18
Frequency of the linear actuator motion [Hz]	1 - 3 - 5
Vertical load [N]	5500 - 6000
Tyre inflating pressure [kPa]	160 - 200
Toe angle [°]	0 - 5

Table 4.1 - Test Parameters.

All the possible combinations have been tested and for each of them at least 5 cycles have been acquired.

The measured cycles showed irregularities due to backlash in the test rig, so, during the elaboration process the force-displacement diagrams have been “reconstructed” by means of a moving average based procedure in order to reduce these irregularities.

In figure 4.6 a measured hysteretic cycle is reported together with the correspondent reconstructed one.

Figure 4.7a, 4.7b and 4.8 show some results about the influence of actuator stroke, motion frequency and vertical load on hysteretic cycles shape and position. In all showed hysteresis cycles diagrams tyre inflation pressure is equal to 200 kPa and toe angle is equal to 0°.

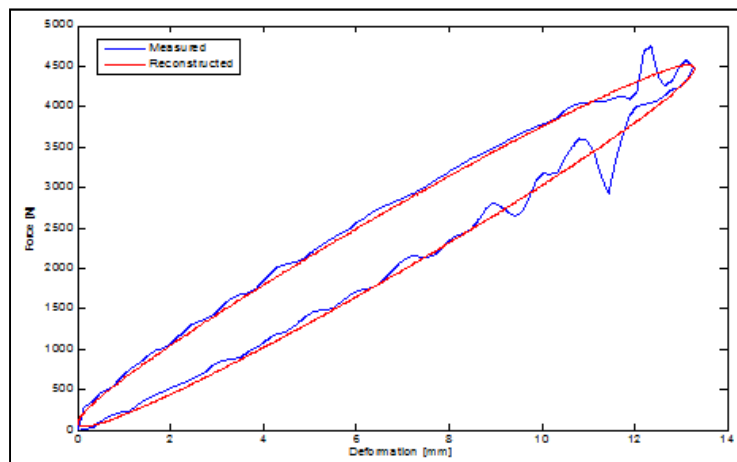


Fig. 4.6 - Measured and reconstructed hysteretic cycles - longitudinal test.

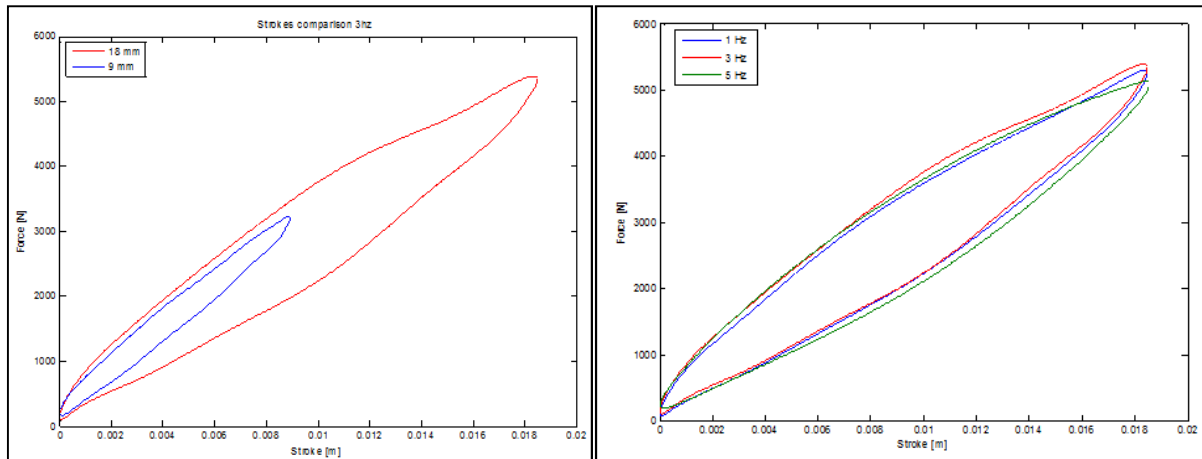


Fig. 4.7a - Longitudinal hysteresis cycles: Linear actuator stroke influence  
 Vertical load: 5500 N, Motion frequency: 3 Hz.

Fig. 4.7b - Longitudinal hysteresis cycles: Motion frequency influence  
 Vertical load: 5500 N, Actuator stroke: 18 mm.

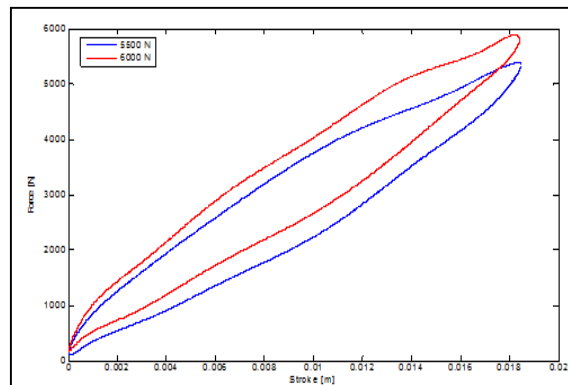


Fig. 4.8 - Longitudinal hysteresis cycles: Vertical load influence  
 Motion frequency: 1 Hz; Actuator stroke: 18 mm.

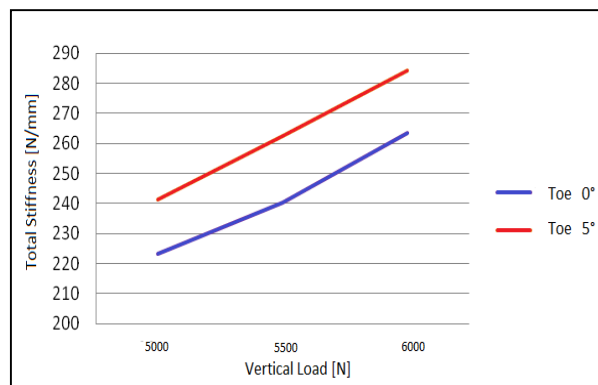


Fig. 4.9 - Toe angle influence on total stiffness  
 Motion frequency: 1 Hz; Actuator stroke: 18 mm.

As expected increasing the linear actuator stroke the energy loss (hysteresis cycles area) rapidly increases (Fig. 4.7a), while linear actuator motion frequency seems not influent on position and extension of cycles (Fig. 4.7b). As concerns the vertical load (Fig. 4.8) and toe angle (Fig. 4.9) they seem directly influent mainly on total stiffness (increasing the two parameters, increases this stiffness).

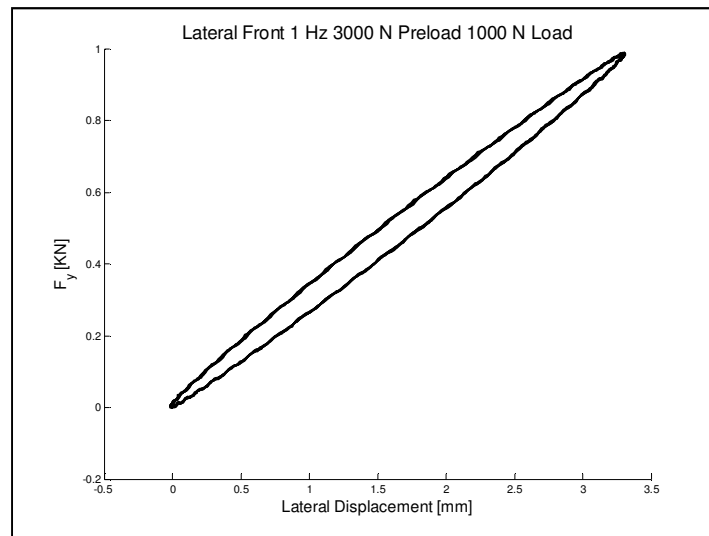


Fig. 4.10 – Normalized lateral hysteresis cycle for a front sport tyre.

For each testing parameters combination, the acquired and measured area of the hysteresis cycle is representative of the energy dissipated in the deformation cycle (Fig. 4.10). Estimated energies do not exactly coincide with the ones dissipated in the actual operative conditions, as the deformation mechanism is different; it is however possible to identify a correlation between them on the basis of coefficients estimated from real data telemetry.

Interpolating all the results obtained by means of the test plan, a specific analytic function has been identified; it expresses the SEL as a function of the parameters (amplitude of the interaction force components and applying frequency) on which it depends.

#### 4.6 Heat transfers modelling

As regards the heat exchange between the tyre and the external environment, it can be classified as follows:

- Heat exchange with the road (called “cooling to the ground”)
- Heat exchange with the outside air
- Heat exchange with the inflating gas

As said, the radiation mechanism of heat exchange is neglected. The same has to be said about the convective heat exchange with the external air along the surface of the sidewalls because the air flow is directed almost tangentially to them; for this reason the value of convective heat exchange coefficient is small. Moreover, being the rubber characterized by very low thermal conductivity, belt thermal dynamics do not influence significantly sidewall dynamics and vice versa

The phenomenon of thermal exchange with the asphalt has been modelled through Newton's formula [46], schematizing the whole phenomenon by means of an appropriate coefficient of heat exchange. The term for such exchanges, for the generic  $i$ -th node will be equal to:

$$H_c \cdot (T_r - T_i) \cdot \Delta X \cdot \Delta Y \quad (4.9)$$

The heat exchange with the outside air is described by the mechanism of forced convection, when there is relative motion between the car and the air, and by natural convection, when such motion is absent.

The determination of the convection coefficient  $h$ , both forced and natural, is based on the classical approach of the dimensionless analysis [35].

Considering the tyre invested by the air similarly to a cylinder invested transversely from an air flux, the forced convection coefficient is provided by the following formulation [42][47]:

$$h_{forc} = \frac{k_{air}}{L} \cdot \left[ 0.0239 \cdot \left( \frac{V_{air} \cdot L}{\nu} \right)^{0.805} \right] \quad (4.10)$$

in which,  $K_{air}$  is evaluated at an average temperature between the effective air one and outer tyre surface one.  $V_{air}$  is considered to be coincident with the forward speed of the vehicle (air speed is supposed to be zero); the values of  $h_{forc}$  calculated with the above approach are close to those obtained by means of CFD simulations [48].

The natural convection coefficient  $h_{air}$ , also obtained by the dimensionless analysis, can be expressed as:

$$h_{air} = \frac{Nu \cdot k_{air}}{L} \quad (4.11)$$

in which, for this case:

$$Nu = 0.53 \cdot Gr^{0.25} \cdot Pr^{0.25} \quad (4.12)$$

The last heat exchange, the convection with the inflating gas, can be expressed by means of a mechanism of natural convection, as the indoor air is considered stationary with respect to the tyre during rolling. In this case, by modelling the system as a horizontal cylinder coaxial with the inflating gas contained in a cavity, the heat exchange coefficient is:

$$h_{int} = \frac{k_{air}}{\delta_r} \cdot \left[ 0.40 \cdot \left( \frac{g \cdot \beta_T \cdot \delta^3 \cdot (T - T_\infty)}{\nu^2} \right)^{0.20} \cdot \left( \frac{\mu_{air} \cdot c_p}{k} \right)^{0.20} \right] \quad (4.13)$$

with  $\delta_r$  equal to the difference between effective rolling radius and rim radius.

#### 4.7 Contact area calculation

The size and the shape of the contact area are function of the vertical load acting on each wheel, of the inflation pressure and of camber and toe angles.

In the T.R.T. model the contact area is assumed to be rectangular in shape, as already said, with constant width  $W_a$ , equal to the tread width, and length  $L_a$ , variable with the above mentioned parameters, except the toe angle.

The extension of the patch depends on the number of nodes in contact with the road and it is calculated as:

$$A_0 = NEC \cdot \Delta x \cdot \Delta y \quad (4.14)$$

NEC is given by  $(NEC_x) \cdot (NEC_y)$ .

$NEC_x$  is the number of nodes in contact along x minus one, calculated as explained in the following and  $NEC_y$  is the number of nodes in contact with the road along y minus one, identified by the ratio between the width  $W_a$  of the tread and the lateral dimension  $\Delta y$  of the single element.

The area is indicated with  $A_0$  to emphasize that it is not variable during the simulation after having been calculated in pre-processing. The real number of nodes in contact is calculated from the effective area of contact  $A_{eff}$ , which is obtained by means of diagrams as the ones showed in figures 3 and 4, taking into account actual vertical load and inflating pressure:

$$NEC_{eff} = \frac{A_{eff}}{W_a \cdot \Delta x} \cdot NEC_y \quad (4.15)$$

in which for the amount  $\frac{A_{eff}}{W_a \cdot \Delta x}$ , representing the number of nodes in contact with the road in the x direction minus one, it is considered the nearest integer.

The effective area of contact has been obtained on the basis of the results provided by FEM simulations (Fig. 4.11 and 4.12<sup>12</sup>) and pressure sensitive sheets (described in paragraph 6.3), both for front and for rear tyre. The used tyre FE model was validated on measured static contact patch and on measured static and dynamic tyre profiles [49].

Below are shown the extensions of the effective contact area as a function of the vertical load and of the camber angle for a value of the inflation pressure equal to the one employed in usual working conditions.

Effective contact area values have been adimensionalized respect to a reference value for confidentiality reasons.

---

<sup>12</sup> In figures 4.11 and 4.12 camber values A, B, C, vertical load values  $Fz_A$ ,  $Fz_B$ ,  $Fz_C$  and inflating pressure values A, B, C are inside typical working ranges of the considered tyres. Their relative order is specified in figure captions and they are not explicitated for confidentiality reasons.

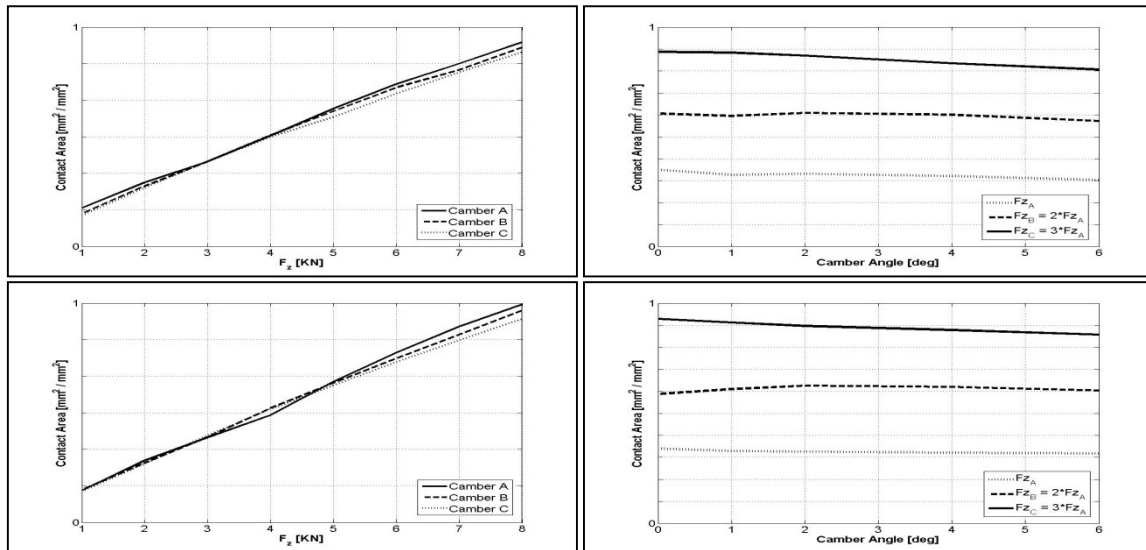


Fig. 4.11a - Contact area as a function of the vertical load for different camber angles - front tyre (Camber C > Camber B > Camber A).

Fig. 4.11b - Contact area as a function of the camber angle for different vertical loads - front tyre ( $F_{zA}$ ,  $F_{zB}=2F_{zA}$ ,  $F_{zC}=3F_{zA}$ ).

Fig. 4.11c - Contact area as a function of the vertical load for different camber angles - rear tyre (Camber C > Camber B > Camber A).

Fig. 4.11d - Contact area as a function of the camber angle for different vertical loads - rear tyre ( $F_{zA}$ ,  $F_{zB}=2F_{zA}$ ,  $F_{zC}=3F_{zA}$ ).

In the figures below it is possible to observe the influence of inflating pressure variations on the contact area.

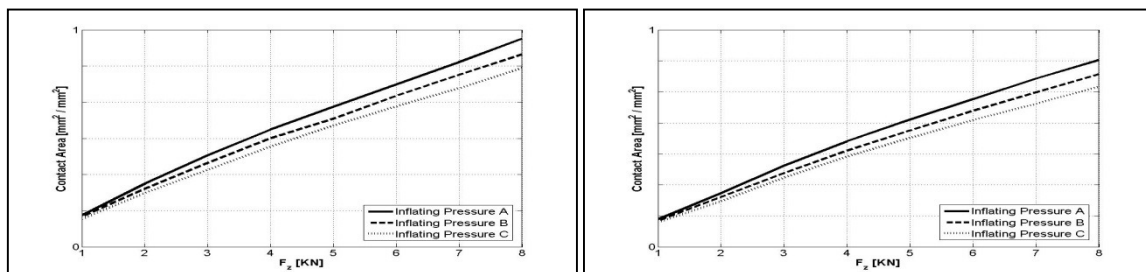


Fig. 4.12a - Contact area as a function of the vertical load for different values of the inflation pressure - front tyre (Press. C > Press. B > Press. A).

Fig. 4.12b - Contact area as a function of the vertical load for different values of the inflation pressure - rear tyre (Press. C > Press. B > Press. A).

The obtained analytical expressions have been optimized around the average value of camber angle assumed by each axle in typical working conditions and they are of the type:

$$A_{eff} = [f(F_z, \gamma, p_i)] \cdot groove\ factor \quad (4.16)$$

In which groove factor is a coefficient taking into account the presence or not of grooves on the tread and represents the ratio between the effective area of a grooved tyre and a of slick one with the same nominal dimensions. By definition, then, this coefficient assumes unitary value in the case of a slick tyre.

Then, considering that in steady state conditions the variations of the inflation pressure are small and that camber angle does not have a great influence on the size of the contact area, for simplicity, these dependencies have been neglected. As a result, it is possible to consider an expression, optimized on internal pressure typical values at medium values of speed and camber, of the type:

$$A_{eff} = [f(F_z)] \cdot groove\ factor \quad (4.17)$$

As said, in order to avoid excessive computational loads, the number of nodes in contact has been considered constant during a simulation. So for its determination the average normal load acting on the single wheel has been considered. This average normal load is determined considering the dynamic behaviour of the car, taking into account longitudinal and lateral load transfers and aerodynamics downforce. Therefore, it results:

$$NEC_x = \frac{A_{eff} [f(F_{z,average})] \cdot groove\ factor}{W_a \cdot \Delta x} \quad (4.18)$$

To take into account the variation of the contact area extension as a function of the normal instantaneous load in the model, the values of the coefficients characterizing the heat exchanges, depending on the variations of the size of the area (in particular  $H_c$  for what concerns the conductive exchange with the asphalt and  $h_{forc}$  for the remaining area of the surface) have to be scaled, having decided not to act directly on  $NEC_x$  and  $NEC_y$ .

Since heat exchanges are expressed by relations of the type:

$$\dot{Q} = h \cdot \Delta T \cdot A \quad (4.19)$$

the effect of the contact patch variations can be transferred to the heat transfer coefficients by means of factors which are proportional to the ratio between the extension of the effective area with respect to the static one.

The equations of heat exchange become, therefore, the following:

$$\dot{Q} = C_1 \cdot H_c \cdot (T_r - T) \cdot A_0 \quad (4.20)$$

$$\dot{Q} = C_2 \cdot h_{forc} \cdot (T_\infty - T) \cdot A_{conv} \quad (4.21)$$

where:

$$C_1 = \frac{A_{eff}}{A_0} \quad (4.22)$$

$$C_2 = 1 + \frac{(1 - k_1) \cdot A_0}{A_{conv}} \quad (4.23)$$

$$A_{conv} = A_{tot} - A_0 \quad (4.24)$$

#### 4.8 The constitutive equations

On the basis of the previous considerations it is possible to write the power balance equations, based on heat transfers, for each elementary mass associated to each node. These equations are different for each node, depending on its position in the grid.

The conductivity between the surface and the bulk layers is indicated with  $k_1$ , while with  $k_2$  is indicated the conductivity associated to the exchange between the bulk and the inner liner layers.

An image depicting the control volume associated with the node 2 (surface layer) is reported below. The image shows the thermal powers exchanged in all directions respectively for the two cases: road contact (Fig. 4.13) and contact with the external air (Fig. 4.14).

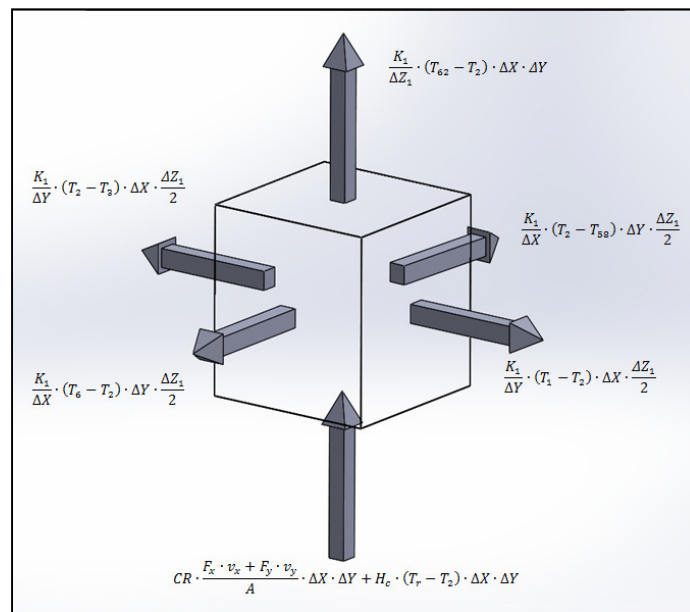


Fig. 4.13 - Control volume associated with the node 2, assumed in contact with the road.

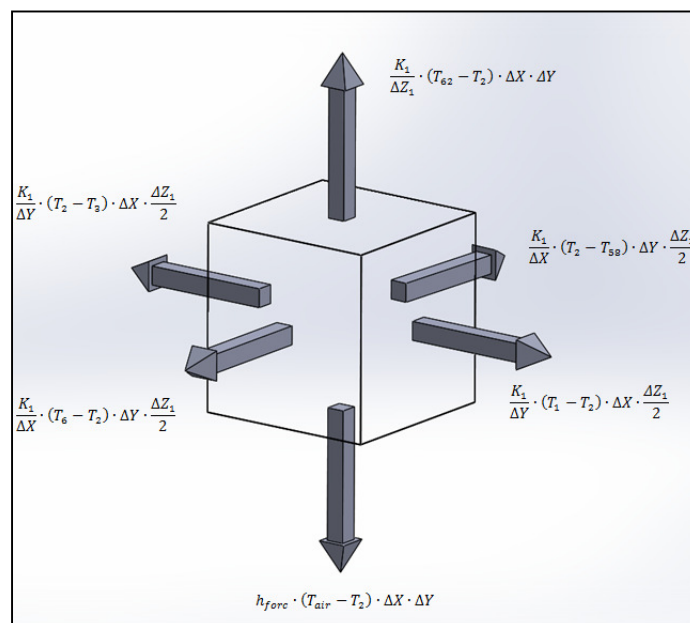


Fig. 4.14 - Control volume associated with the node 2, assumed in contact with the external air.

As an example, the only heat balance equation for node 2 along the x direction is reported, recalling that, for the performed discretization, the nodes adjacent to 2 are 6 and 58:

$$\frac{k_1}{\Delta X} \cdot (T_6 - T_2) \cdot \Delta Y \cdot \frac{\Delta Z_1}{2} - \frac{k_1}{\Delta X} \cdot (T_2 - T_{58}) \cdot \Delta Y \cdot \frac{\Delta Z_1}{2} = m_2 \cdot c_{v1} \cdot \frac{\Delta T_2}{\Delta t} \quad (4.25)$$

Substituting the expression of the mass (4.2) (reminding that in this case  $C = 1/2$ ) leads to the equation:

$$\frac{\Delta T_2}{\Delta t} = \frac{1}{\rho \cdot c_{v1}} \cdot \left[ \frac{k_1}{\Delta X^2} \cdot T_6 - \frac{2 \cdot k_1}{\Delta X^2} \cdot T_2 + \frac{k_1}{\Delta X^2} \cdot T_{58} \right] \quad (4.26)$$

Taking into account the exchanges along all directions and all the possible heat generations, the equation of node 2 can be written (see Appendix):

- in the case of contact with the road:

$$\begin{aligned} \frac{\Delta T_2}{\Delta t} = \frac{1}{\rho \cdot c_{v1}} \cdot \left[ \frac{2 \cdot \dot{Q}_{SEL}}{\Delta X \cdot \Delta Y \cdot \Delta Z_1} + \left( -\frac{2 \cdot k_1}{\Delta X^2} - \frac{2 \cdot k_1}{\Delta Y^2} - \frac{2 \cdot k_1}{\Delta Z_1^2} - \frac{2 \cdot H_c}{\Delta Z_1} \right) \cdot T_2 + \frac{k_1}{\Delta Y^2} \cdot T_1 \right. \\ \left. + \frac{k_1}{\Delta Y^2} \cdot T_3 + \frac{k_1}{\Delta X^2} \cdot T_6 + \frac{k_1}{\Delta X^2} \cdot T_{58} + \frac{2 \cdot k_1}{\Delta Z_1^2} \cdot T_{62} + \frac{2 \cdot FP}{\Delta Z_1} + \frac{2 \cdot H_c}{\Delta Z_1} \right. \\ \left. \cdot T_r \right] \quad (4.27) \end{aligned}$$

- in the case of contact with external air:

$$\begin{aligned} \frac{\Delta T_2}{\Delta t} = \frac{1}{\rho \cdot c_{v1}} \cdot \left[ \frac{2 \cdot \dot{Q}_{SEL}}{\Delta X \cdot \Delta Y \cdot \Delta Z_1} + \left( -\frac{2 \cdot k_1}{\Delta X^2} - \frac{2 \cdot k_1}{\Delta Y^2} - \frac{2 \cdot k_1}{\Delta Z_1^2} - \frac{2 \cdot h_{forc}}{\Delta Z_1} \right) \cdot T_2 + \frac{k_1}{\Delta Y^2} \right. \\ \left. \cdot T_1 + \frac{k_1}{\Delta Y^2} \cdot T_3 + \frac{k_1}{\Delta X^2} \cdot T_6 + \frac{k_1}{\Delta X^2} \cdot T_{58} + \frac{2 \cdot k_1}{\Delta Z_1^2} \cdot T_{62} + \frac{2 \cdot h_{forc}}{\Delta Z_1} \cdot T_{air} \right] \quad (4.28) \end{aligned}$$

having denoted by  $\dot{Q}_{SEL}$  the power dissipated by cyclic deformation.

Note the presence, in the equation (4.27), of the generative term identified by FP and of the term identifying the cooling with the road (characterized by the presence of the  $H_c$  coefficient). On the other hand, in the equation (4.28) it is possible to notice the absence of the generative term and the presence of the term identifying the exchange with the outside air (characterized by the presence of the  $h_{forc}$  coefficient).

In the model the tyre has been considered motionless and the boundary conditions rotating around it to take into account the fact that elements belonging to the surface layer will be affected alternatively by the boundary conditions corresponding to the contact with the road and to the forced convective exchange with the external air.

The equations showed for node 2 are valid for all the nodes belonging to the surface layer, localized internally in lateral direction.

For a node still belonging to the surface layer, but external in lateral direction ( $C = 1/4$ ), for example node 1, the equations are (see Appendix):

- in the case of contact with the road:

$$\frac{\Delta T_1}{\Delta t} = \frac{1}{\rho \cdot c_{v1}} \cdot \left[ \frac{4 \cdot \dot{Q}_{SEL}}{\Delta X \cdot \Delta Y \cdot \Delta Z_1} + \left( -\frac{2 \cdot k_1}{\Delta X^2} - \frac{2 \cdot k_1}{\Delta Y^2} - \frac{2 \cdot k_1}{\Delta Z_1^2} - \frac{2 \cdot H_c}{\Delta Z_1} \right) \cdot T_1 + \frac{2 \cdot k_1}{\Delta Y^2} \cdot T_2 + \frac{k_1}{\Delta X^2} \cdot T_5 + \frac{k_1}{\Delta X^2} \cdot T_{57} + \frac{2 \cdot k_1}{\Delta Z_1^2} \cdot T_{61} + \frac{2 \cdot FP}{\Delta Z_1} + \frac{2 \cdot H_c}{\Delta Z_1} \cdot T_r \right] \quad (4.29)$$

- in the case of contact with external air:

$$\frac{\Delta T_1}{\Delta t} = \frac{1}{\rho \cdot c_{v1}} \cdot \left[ \frac{4 \cdot \dot{Q}_{SEL}}{\Delta X \cdot \Delta Y \cdot \Delta Z_1} + \left( -\frac{2 \cdot k_1}{\Delta X^2} - \frac{2 \cdot k_1}{\Delta Y^2} - \frac{2 \cdot k_1}{\Delta Z_1^2} - \frac{2 \cdot h_{forz}}{\Delta Z_1} \right) \cdot T_1 + \frac{2 \cdot k_1}{\Delta Y^2} \cdot T_2 + \frac{k_1}{\Delta X^2} \cdot T_5 + \frac{k_1}{\Delta X^2} \cdot T_{57} + \frac{2 \cdot k_1}{\Delta Z_1^2} \cdot T_{61} + \frac{2 \cdot h_{forc}}{\Delta Z_1} \cdot T_{air} \right] \quad (4.30)$$

The equation relating to the bulk layer, for an internal node in the lateral direction ( $C = 1$ ), e.g. node 62, is (see Appendix):

$$\frac{\Delta T_{62}}{\Delta t} = \frac{1}{\rho \cdot c_{v2}} \cdot \left[ \frac{\dot{Q}_{SEL}}{\Delta X \cdot \Delta Y \cdot \left( \frac{\Delta Z_1}{2} + \frac{\Delta Z_2}{2} \right)} + \left( -\frac{2 \cdot k_2}{\Delta X^2} - \frac{2 \cdot k_2}{\Delta Y^2} - \frac{k_2}{\Delta Z_2 \cdot \left( \frac{\Delta Z_1}{2} + \frac{\Delta Z_2}{2} \right)} - \frac{k_1}{\Delta Z_1 \cdot \left( \frac{\Delta Z_1}{2} + \frac{\Delta Z_2}{2} \right)} \right) \cdot T_{62} + \frac{k_2}{\Delta Y^2} \cdot T_{61} + \frac{k_2}{\Delta Y^2} \cdot T_{63} + \frac{k_2}{\Delta X^2} \cdot T_{66} + \frac{k_2}{\Delta X^2} \cdot T_{118} + \frac{k_2}{\Delta Z_2 \cdot \left( \frac{\Delta Z_1}{2} + \frac{\Delta Z_2}{2} \right)} \cdot T_{122} + \frac{k_1}{\Delta Z_1 \cdot \left( \frac{\Delta Z_1}{2} + \frac{\Delta Z_2}{2} \right)} \cdot T_2 \right] \quad (4.31)$$

Similarly, relatively to a bulk external node in the transverse direction, ( $C = 1/2$ ), it results (see Appendix):

$$\frac{\Delta T_{61}}{\Delta t} = \frac{1}{\rho \cdot c_{v2}} \cdot \left[ \frac{2 \cdot \dot{Q}_{SEL}}{\Delta X \cdot \Delta Y \cdot \left( \frac{\Delta Z_1}{2} + \frac{\Delta Z_2}{2} \right)} + \left( -\frac{2 \cdot k_2}{\Delta X^2} - \frac{2 \cdot k_2}{\Delta Y^2} - \frac{k_2}{\Delta Z_2 \cdot \left( \frac{\Delta Z_1}{2} + \frac{\Delta Z_2}{2} \right)} - \frac{k_1}{\Delta Z_1 \cdot \left( \frac{\Delta Z_1}{2} + \frac{\Delta Z_2}{2} \right)} \right) \cdot T_{61} + \frac{2 \cdot k_2}{\Delta Y^2} \cdot T_{62} + \frac{k_2}{\Delta X^2} \cdot T_{65} + \frac{k_2}{\Delta X^2} \cdot T_{117} + \frac{k_2}{\Delta Z_2 \cdot \left( \frac{\Delta Z_1}{2} + \frac{\Delta Z_2}{2} \right)} \cdot T_{121} + \frac{k_1}{\Delta Z_1 \cdot \left( \frac{\Delta Z_1}{2} + \frac{\Delta Z_2}{2} \right)} \cdot T_1 \right] \quad (4.32)$$

As concerns the innermost layer, the inner liner, the equation of exchange for an internal node in the transverse direction ( $C = 1/2$ ), eg 122, is (see Appendix):

$$\begin{aligned} \frac{\Delta T_{122}}{\Delta t} = \frac{1}{\rho \cdot c_{v2}} \cdot \left[ \frac{2 \cdot \dot{Q}_{SEL}}{\Delta X \cdot \Delta Y \cdot \Delta Z_2} + \left( -\frac{2 \cdot k_2}{\Delta X^2} - \frac{2 \cdot k_2}{\Delta Y^2} - \frac{2 \cdot k_2}{\Delta Z_2^2} - \frac{2 \cdot h_{int}}{\Delta Z_2} \right) \cdot T_{122} \right. \\ \left. + \frac{k_2}{\Delta Y^2} \cdot T_{121} + \frac{k_2}{\Delta Y^2} \cdot T_{123} + \frac{k_2}{\Delta X^2} \cdot T_{126} + \frac{k_2}{\Delta X^2} \cdot T_{158} + \frac{2 \cdot k_2}{\Delta Z_2^2} \cdot T_{62} \right. \\ \left. + \frac{2 \cdot h_{int}}{\Delta Z_2} \cdot T_{air\_int} \right] \end{aligned} \quad (4.33)$$

Finally, for an external node in the transverse direction belonging to the Inner liner ( $C = 1/4$ ), it is (see Appendix):

$$\begin{aligned} \frac{\Delta T_{121}}{\Delta t} = \frac{1}{\rho \cdot c_{v2}} \cdot \left[ \frac{4 \cdot \dot{Q}_{SEL}}{\Delta X \cdot \Delta Y \cdot \Delta Z_2} + \left( -\frac{2 \cdot k_2}{\Delta X^2} - \frac{2 \cdot k_2}{\Delta Y^2} - \frac{2 \cdot k_2}{\Delta Z_2^2} - \frac{2 \cdot h_{int}}{\Delta Z_2} \right) \cdot T_{121} \right. \\ \left. + \frac{2 \cdot k_2}{\Delta Y^2} \cdot T_{122} + \frac{k_2}{\Delta X^2} \cdot T_{125} + \frac{k_2}{\Delta X^2} \cdot T_{157} + \frac{2 \cdot k_2}{\Delta Z_2^2} \cdot T_{61} + \frac{2 \cdot h_{int}}{\Delta Z_2} \right. \\ \left. \cdot T_{air\_int} \right] \end{aligned} \quad (4.34)$$

In conclusion, the matrix equation at the basis of the model is:

$$\begin{pmatrix} \frac{\partial T_1}{\partial t} \\ \frac{\partial T_2}{\partial t} \\ \frac{\partial T_3}{\partial t} \\ \dots \\ \frac{\partial T_n}{\partial t} \end{pmatrix} = \begin{pmatrix} b_1 \\ b_2 \\ \dots \\ b_n \end{pmatrix} + \frac{1}{\rho \cdot c_v} \begin{pmatrix} a_{11} & \dots & a_{1n} \\ a_{21} & \dots & a_{2n} \\ \dots & \dots & \dots \\ \dots & \dots & \dots \\ a_{n1} & \dots & a_{nn} \end{pmatrix} \cdot \begin{pmatrix} T_1 \\ T_2 \\ \dots \\ T_n \end{pmatrix} \quad (4.35)$$

in which  $a_{ij}$  is the generic coefficient, relative to the energy balance equation of the node  $i$ , that multiplies the  $j$ -th node temperature, while  $b_i$  is the generic coefficient not multiplying nodes temperatures.

To properly operate in order to provide the tyre temperature distribution, the model requires the following input data: normal, longitudinal and lateral interaction tyre-road forces, longitudinal and lateral slip speeds, forward speed at the wheel centre,

air and road temperature. The structural characteristics and thermal properties of the tyre and the thermal conductivity of the track are also required.

Some of these data result from the measures of telemetry available for different circuits and are preliminary analyzed in order to check their reliability; others, such as in particular the ones related to structural and thermal characteristics of the tyre, are estimated on the basis of measurements and tests conducted on the tyres [41].

At the end of the model development, sensitivity analyses have been performed; it resulted that employed instruments, characterized by high accuracy, are able to guarantee low uncertainty levels that do not affect the goodness of model results.

In addition to surface, bulk and inner liner temperature distributions, the model also provides the thermal flows affecting the tyre, such as the flow due to the external air cooling, the one due to the cooling with the road, the one with the inflation air as well as the flows due to friction, hysteresis and exchanges between the different layers.

#### **4.9 Results and discussion**

The model needs an initial tuning phase to be carried out only once for each season, because of changes in car setup and tyres construction, aimed to the identification of the values of some scaling factors. This is done on the basis of the results obtained during pre-season testing, which commonly take place early in the year before the season starts. This phase also allows the direct experimental check of tyre thermal parameters.

Once developed through this operation it can be used in a predictive manner, known all inputs, with reference to the various operating conditions of the different circuits. The results obtained are in good agreement with the telemetry data.

This is clearly shown in the following figures which illustrate a comparison between the temperatures provided by the telemetry (measured by means of infrared sensors, pointing the middle line of the tyre) during a race and the results provided by the model in simulation. The signals show a certain periodicity because they refer to race laps.

Figure 4.15 in particular shows a comparison between the temperature of surface measured and simulated for all the four wheels. As can be seen the agreement between the model and telemetry is excellent.

With regard to the front wheels, the fragmentary telemetry data is due to the fact that when the steering angle exceeds a certain threshold, the temperature measurement is not trusted because the sensor detects temperature values corresponding to different zones of the tyre. Substantially when the steering wheel is over a certain value the reliability of the temperature signal is lost.

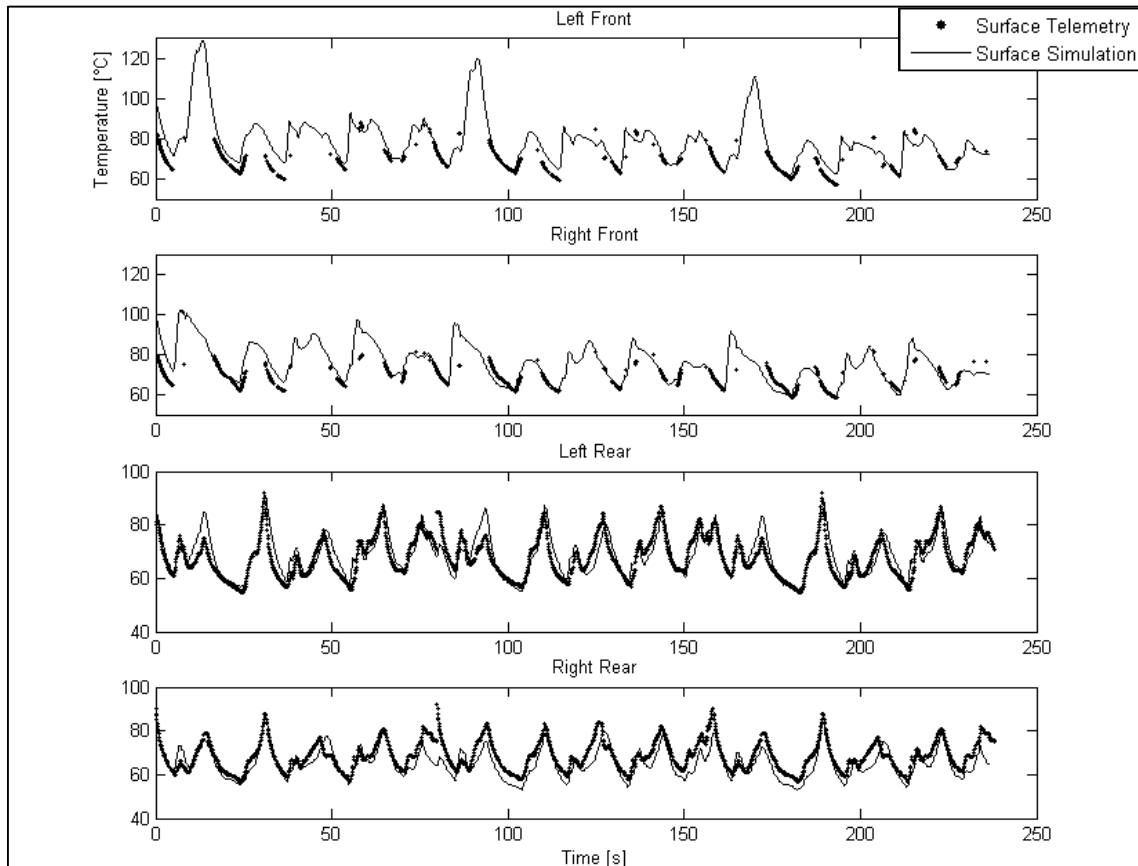


Fig. 4.15 - Comparison between measured and simulated surface temperatures both for rear and front tyres.

In the next figure, 4.16, the temperatures of the inner liner measured and those calculated with the model are reported. Also in this case, for all four wheels the agreement is excellent. In the figure are also reported bulk temperatures estimated by means of model simulations. For bulk temperatures no data are available from telemetry.

Proper time ranges have been selected to highlight thermal dynamics characteristic of each layer; in particular, as concerns bulk and inner liner (Fig. 4.16), temperature decreasing trend is due to a vehicle slowdown before a pit stop.

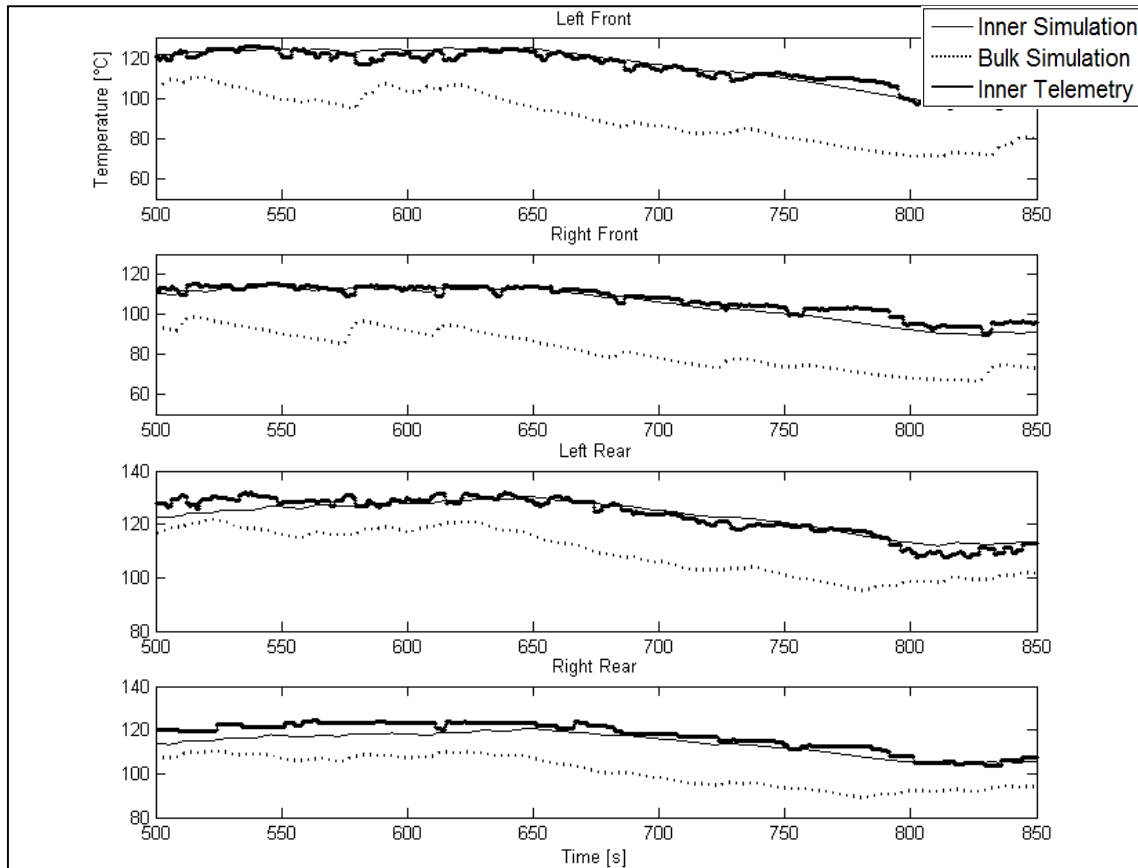


Fig. 4.16 - Bulk simulated temperature and comparison between measured and simulated inner liner temperatures both for rear and front tyres.

Finally in figure 4.17, with reference to a different circuit, the comparisons between the measured temperatures and those supplied by the model for all four wheels of the vehicle are reported.

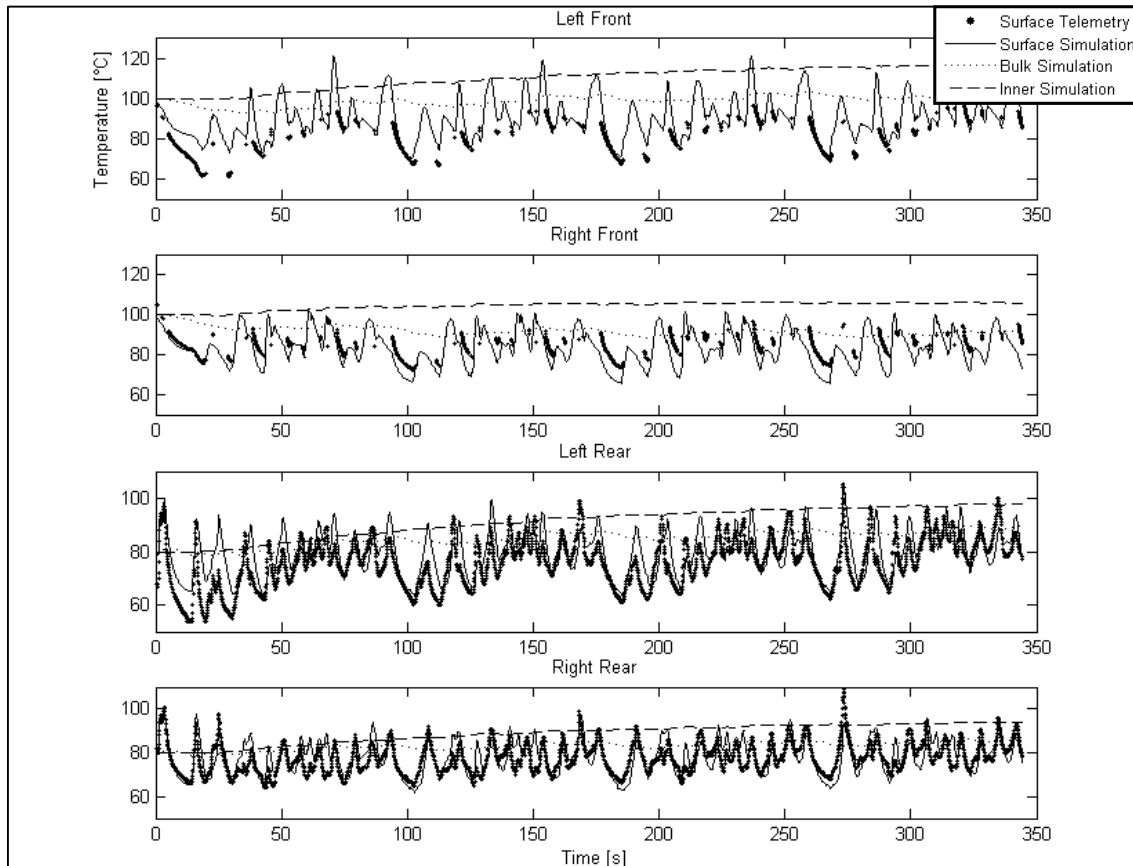


Fig. 4.17 - Another example of bulk and inner liner simulated temperature and comparison between measured and simulated surface temperatures both for rear and front tyres.

Even in this case, despite the fragmentary telemetry data of the front tyres surface temperature, the agreement between the telemetry data and those evaluated with the model is good.

## 4.10 Further developments and implementations

### 4.10.1 TRT blown exhaust gas

#### 4.10.1.1 Model Variations

One of the major technical innovations in recent Formula 1 seasons has been the introduction of special exhaust systems, called "Exhaust Blown Diffusers", which, employing the kinetic energy of such gases, are able to act on aerodynamic downforce increasing ground effect. Maximizing the vertical load acting on the wheel, in fact, it is possible to get a consequent improvement in terms of forces exchanged with the road.

The thermal contribution coming from the exhaust gases, depending on the aerodynamic solutions used, is directed to the rear of the car, eventually investing different areas of the tyres (Fig. 4.18). The ways in which the different solution can be adopted need to be studied in detail; if improperly canalized, heat flows risk to damage the tyre because of too high thermal stress levels; on the other hand, an appropriate strategy to employ the thermal additional source may represent a key factor for the management of the tyres in terms of optimization of the grip/temperature relationship.



Fig. 4.18 - Rear tyre heated by exhaust gas flow.

Starting from these considerations, it is evident the importance that a study able to take into account the extremely severe thermal conditions due to localized hot gas flows could have for racing teams. The phenomena have been modelled inside the TRT enabling the possibility to introduce an external localized thermal source. Being the followed approach of Lagrangian type, the tyre is considered as motionless and the boundary conditions move, varying by means of specific permutation matrices.

The "road contact" matrix is constituted by a  $\text{num} \times \text{numy}$  number of elements, characterized to be equal to 1 if relative to tyre surface points in contact with road and equal to 0 elsewhere. "Exhaust gases" matrix has the same dimensions, but elements equal to 1 are the ones that are considered to be invested by gas flow (Fig. 4.19).

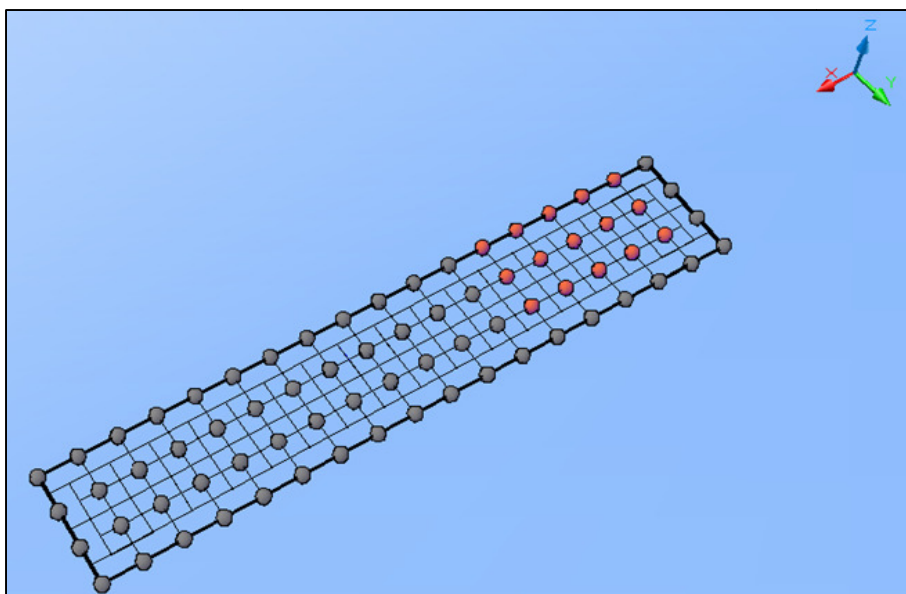


Fig. 4.19 - Surface layer mesh; in red, the nodes interested by exhaust gas flow.

Heating due to external sources acting on the surface layer is modelled again thanks to Newton's equation:

$$h_{EXH}(T_{GAS} - T_i)\Delta X \Delta Y \quad (4.36)$$

in which  $h_{EXH}$  is the convective heat transfer coefficient,  $T_{GAS}$  is gas unidirectional flow temperature, considered constant and  $T_i$  is  $i$ -th surface element temperature.

Referring to node 2, hypothesizing it interested by gas flow, balance equation (4.28) becomes:

$$\frac{\Delta T_2}{\Delta t} = \frac{1}{\rho \cdot c_{v1}} \cdot \left[ \frac{2 \cdot \dot{Q}_{SEL}}{\Delta X \cdot \Delta Y \cdot \Delta Z_1} + \left( -\frac{2 \cdot k_1}{\Delta X^2} - \frac{2 \cdot k_1}{\Delta Y^2} - \frac{2 \cdot k_1}{\Delta Z_1^2} - \frac{2 \cdot h_{EXH}}{\Delta Z_1} \right) \cdot T_2 + \frac{k_1}{\Delta Y^2} \cdot T_1 + \frac{k_1}{\Delta Y^2} \cdot T_3 \right. \\ \left. + \frac{k_1}{\Delta X^2} \cdot T_6 + \frac{k_1}{\Delta X^2} \cdot T_{58} + \frac{2 \cdot k_1}{\Delta Z_1^2} \cdot T_{62} + \frac{2 \cdot h_{EXH}}{\Delta Z_1} \cdot T_{GAS} \right] \quad (4.37)$$

#### 4.10.1.2 Simulation Results

T.R.T. model with the addition of the exhaust gases effect has been employed in order to obtain a quantitative analysis, although approximate, of the effect in terms of average temperatures of the hot flow on a portion of the tyre.

Simulations have been performed employing telemetry input related to measurements obtained during a race on a track characterized by not particularly stressing environmental conditions. Some simplifying assumptions have been taken, according to the instructions provided by the vehicle maker:

- Convective heat transfer coefficient  $h_{EXH}$  is constant and equal to 200 W/(m<sup>2</sup>K), equal to about twice the average value of the exchange coefficient with the air
- Temperature of the exhaust gas is uniform and constant during the simulation; basing on available data, a value of 300 °C has been chosen
- Tyre surface affected by the gas flow has been considered equal to about 23% of the total including 5 knots in the longitudinal direction and 3 in the side
- The heating induced by the impact of exhaust gases on the sidewall has been neglected

The results highlighted that the thermal variations induced by hot flows are absolutely not negligible; the difference in terms of mean layers temperature between the normal case and the exhaust gas one reaches several tens of degrees (Fig. 4.20)

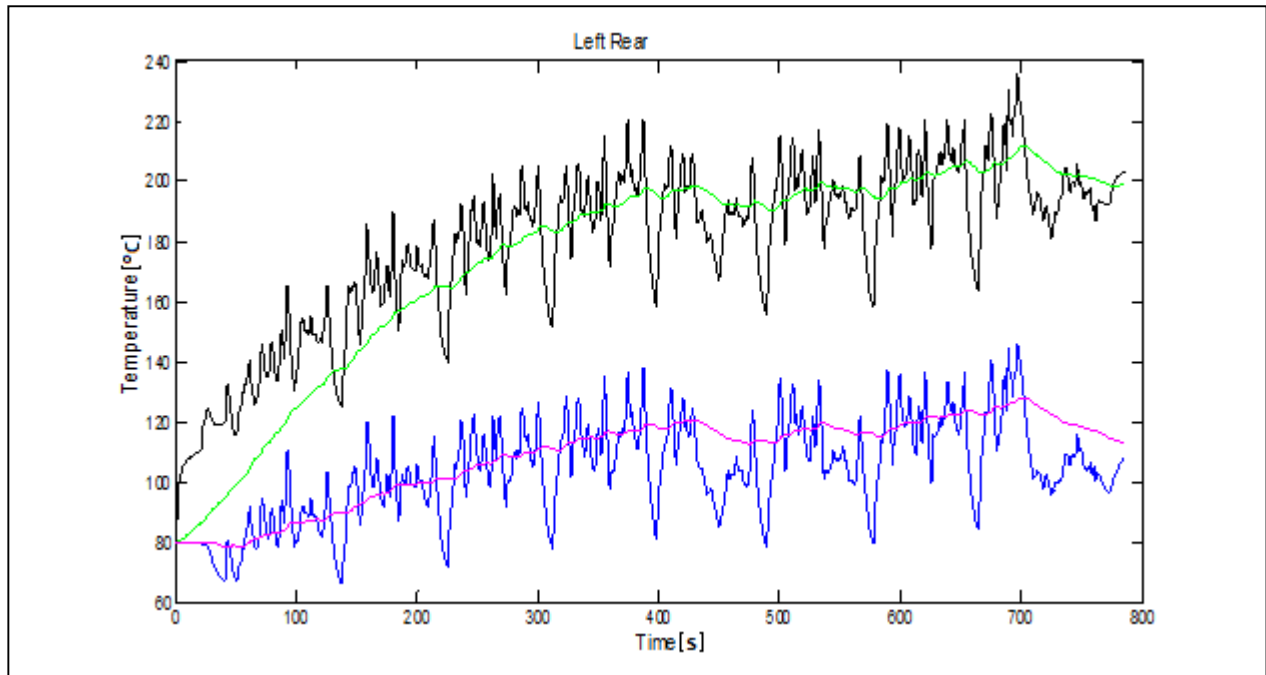


Fig 4.20 - left rear wheel TRT simulation output: comparison between normal thermal vehicle setup (blue = surface mean temperature, magenta = bulk mean temperature) and exhaust gas solution (black = surface mean temperature, green = bulk mean temperature).

The results, even if the analysis has been carried out with a first approximation method, fully highlight the effect of the added external heat source. As a partial conclusion for the discussed analysis, the tyre surface area interested by the flow should be reduced, because the thermal stress reached under the tested conditions would unavoidably bring the tyre to a too fast degradation and to average temperatures not able to maximize the grip.

In order to perform a more detailed analysis, a better estimation of heat exchange coefficient, of flow temperature expressed as a function of the distance from exhaust pipe tip, of the extension of the tyre area invested by gases and of the thermal exchanges with sidewalls should be provided.

Further developments of the described TRT version could be adapted to motorcycle tyres thermal dynamics, in which contact patch width is not the whole tread one, but is a portion of it and moves as a function of camber angle [50].

## 4.10.2 TRT Multi-Rib version

### 4.10.2.1 Model Variations

One of the main limits of the T.R.T. model is definitely due to the fact to be based on global quantities (in particular, the forces that are given as input to the model are the ones that the tyre globally exchanges with the road) that are not able to describe the inhomogeneous distribution of local variables inside the contact patch (for example, stresses and deformations due to camber thrust).

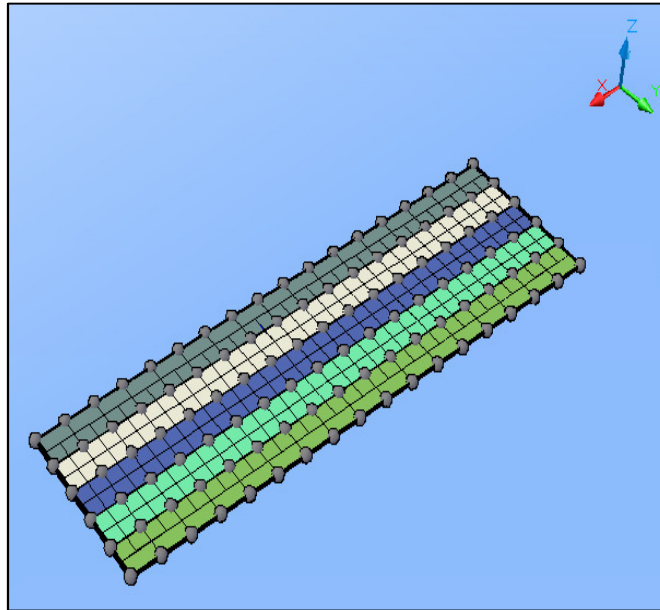


Fig. 4.21 - Tyre surface subdivided in five ribs.

In order to model actual phenomena, the model has been properly modified, making it compatible with inputs of a local type. Specifically tyre has been subdivided in ribs (Fig. 4.21), each one interested by a different friction power. In this way temperature gradients are generated in the  $y$  direction, between consecutive ribs operating under different conditions.

Ribs expedient allows to model effects linked with common tyre configurations, like nonzero camber angles or under/over inflation. At present, the model includes five ribs and consequently six knots in the lateral direction; it means that this version of TRT must be associated to a contact model, able to provide different local forces and sliding velocities, useful for each rib friction power calculation. At this aim, tests have been performed employing models discussed in [21] and [51].

Each rib is characterized by its specific CR, because each conductivity and thermal diffusivity depend on rib temperature. A node completely belonging to a single rib (as node 1) is characterized by FP value calculated on the base of forces and velocities assigned to the rib by the contact model; physical quantities relative to nodes localized between two consecutive ribs (as node 2) have been considered as the mean value of the ones assigned to the ribs.

#### 4.10.2.2 Simulation Results

Three different tests have been carried out:

- Decreasing FP along tread lateral direction (camber simulation, Fig. 4.22 and 4.23)
- Central rib (rib 3) interested by a three times higher FP than other ribs (over inflation test, Fig. 4.25 and 4.26)
- Lateral ribs (rib 1 and 5) interested by a three times higher FP than other ribs (under inflation test, Fig. 4.27 and 4.28)

The first test reproduces a situation obtainable performing laps with a wheels setup characterized by constant camber angles. It is a specific setup, surely not common in usual conditions, in which camber angle varies during the vehicle motion. Figures 4.22 and 4.23 show overheating in the side interested by higher pressure, due to the presence of nonzero camber angle values.

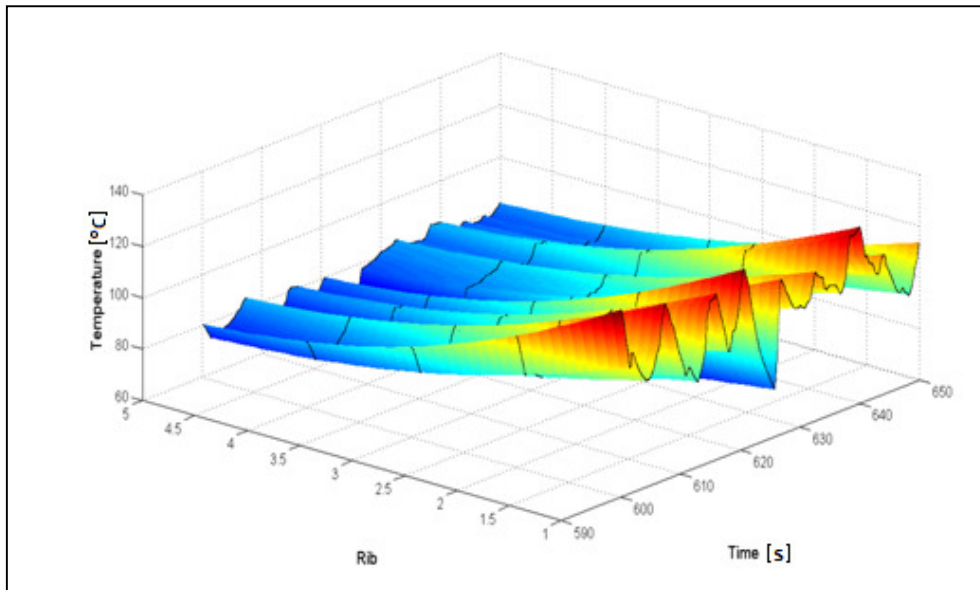


Fig. 4.22 - Results of test1: decreasing FP along tread lateral direction.

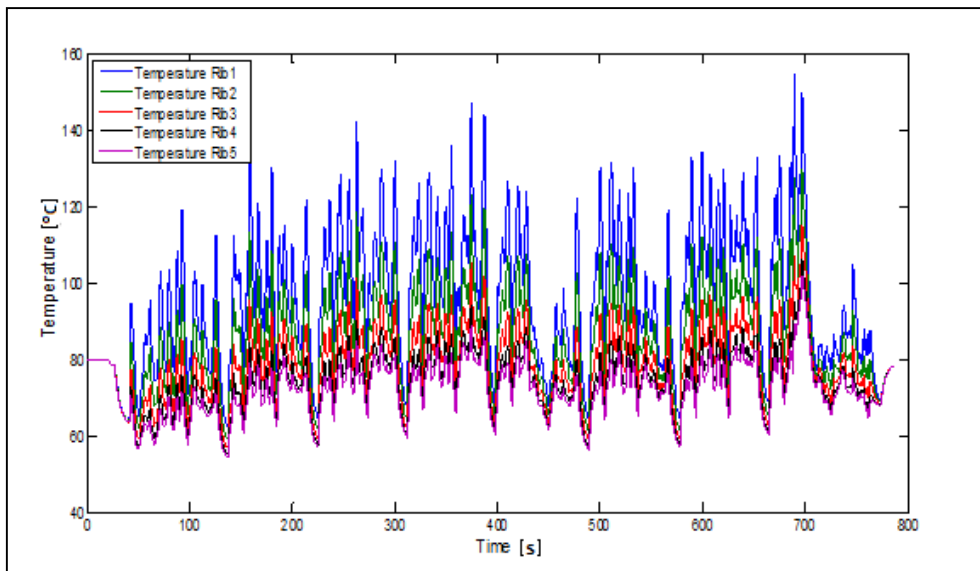
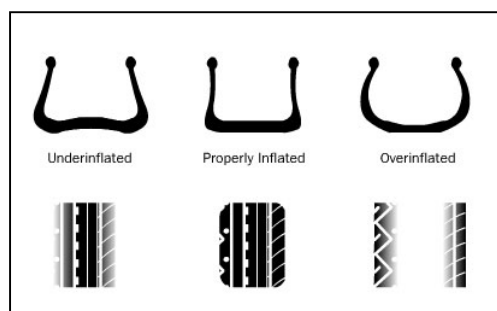


Fig. 4.23 - Results of test1: ribs temperature.

Test2 has been designed with the aim to reproduce phenomena concerning with tyre over inflation, that commonly generates high contact pressure distribution (and consequently higher tangential stresses) in the central zone of the tread (Fig. 4.24).



4.24 - Effects of tyre inflation on tread shape and wear.

A three times higher friction power has been assigned to the central rib (rib 3); this value is quantitatively excessive, but has been employed in order to highlight the qualitative effect of the overheating. The perfectly symmetric nature of the problem brings the symmetric ribs (2 and 4, 1 and 5) to the same thermal equilibrium conditions (as showed in figure 4.26).

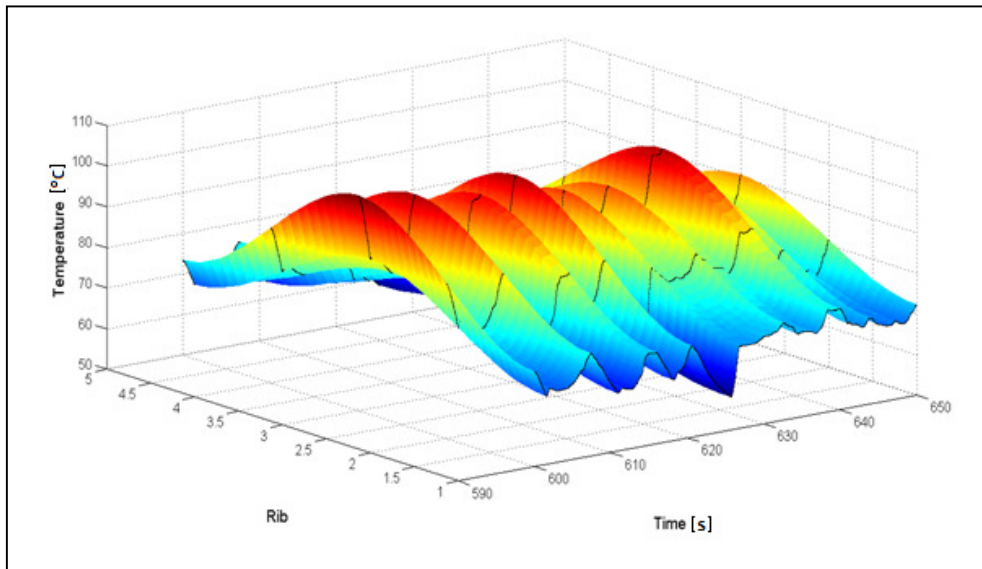


Fig. 4.24 - Results of test2: overheated central rib.

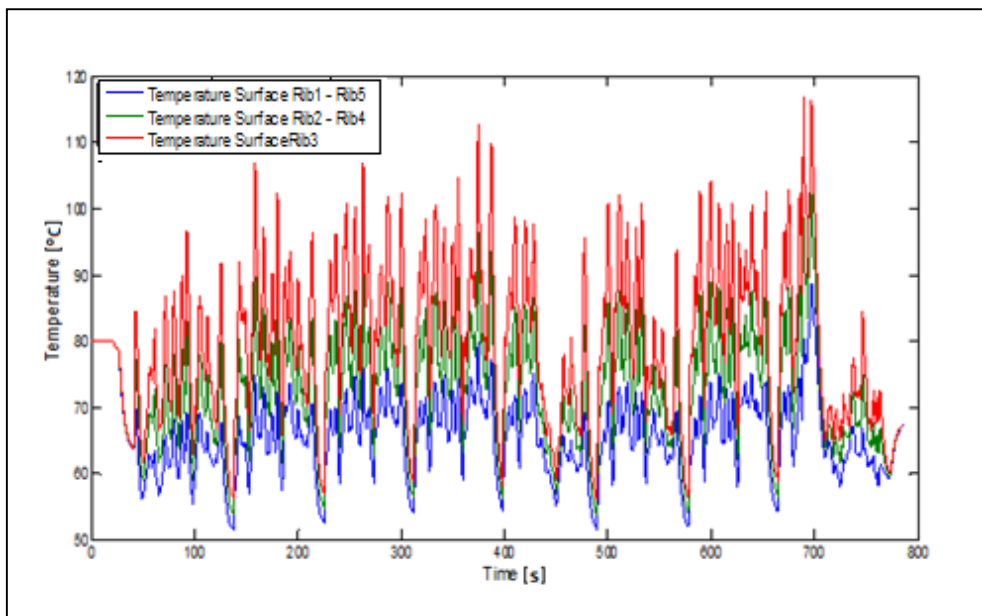


Fig. 4.25 - Results of test2: ribs temperature.

Test3 has been designed with the aim to reproduce phenomena concerning with tyre under inflation, that commonly generates high contact pressure distribution (and consequently higher tangential stresses) in the lateral zone of the tread (Fig. 4.24).

In analogous way to test2, a three times higher friction power has been assigned to the lateral ribs (ribs 1 and 5); this value is quantitatively excessive, but has been

employed in order to highlight the qualitative effect of the overheating. The perfectly symmetric nature of the problem brings the symmetric ribs (2 and 4, 1 and 5) to the same thermal equilibrium conditions (as showed in figure 4.28).

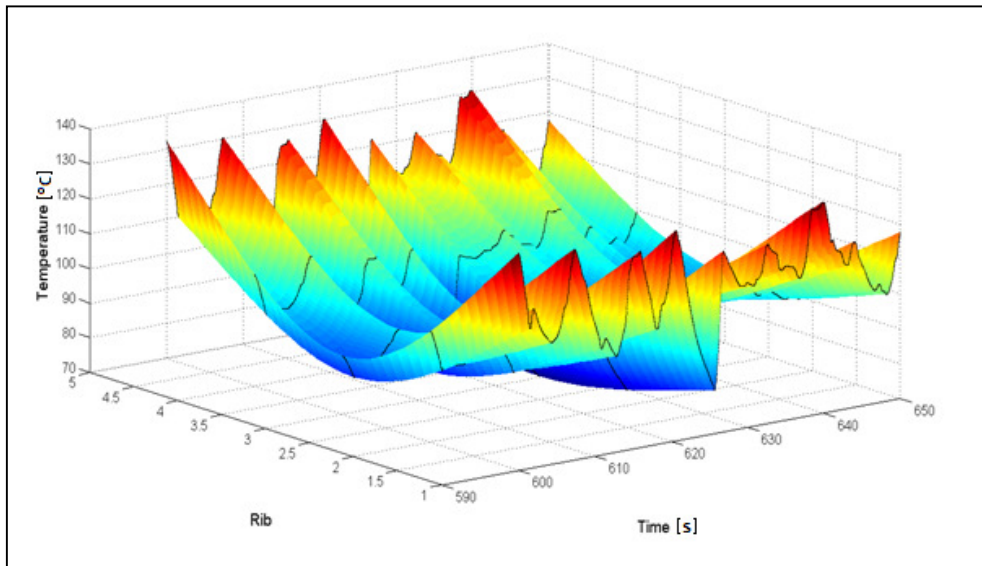


Fig. 4.26 - Results of test3: overheated lateral ribs.

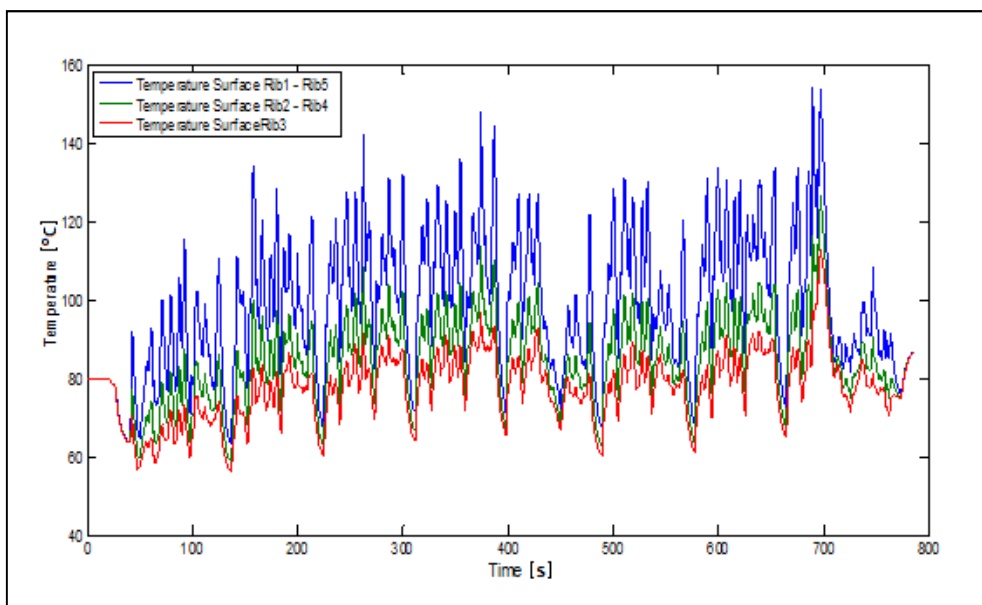


Fig. 4.27 - Results of test3: ribs temperature.

#### 4.11 Final Considerations

TRT model discussed in this chapter is an indispensable instrument to optimize vehicle performances since tyre surface temperatures as well as bulk ones have great influence on the tyre-track interaction. The interaction forces reach their maximum values only within a narrow temperature range, while decay significantly outside of it. The ability to predict the temperature distribution on the surface, and also inside the tyre in the different operating situations makes possible to ensure the optimum temperature to maximize the forces exchanged with the track.

Moreover, having the model the possibility to run in real time, it is suitable for applications on a driving simulator where it is necessary to reproduce the real operating conditions including the tyre temperatures.

The physical nature of the model, based on analytic equations containing known or measurable physical parameters, in addition to give to the model predictive attitudes, also allows an analysis of the influence of different parameters including the constructive characteristics and chemical-physical properties of the rubber. This is extremely useful in the design phase of the tyres, but also for the thermal/frictional analyses that will be discussed in the following chapters.

The knowledge of heat flows and hence their balance is another important instrument for the identification of optimum operating conditions in order to maximize tyre performances.

#### 4.12 Appendix

As an example, heat balance equation for node 2 along the x direction is reported, recalling that, for the performed discretization, the nodes adjacent to 2 are 6 and 58:

$$\frac{k_1}{\Delta X} \cdot (T_6 - T_2) \cdot \Delta Y \cdot \frac{\Delta Z_1}{2} - \frac{k_1}{\Delta X} \cdot (T_2 - T_{58}) \cdot \Delta Y \cdot \frac{\Delta Z_1}{2} = m_2 \cdot c_{v1} \cdot \frac{\Delta T_2}{\Delta t} \quad (4.25)$$

Substituting the expression of the mass (4.2) (reminding that in this case  $C = 1/2$ ) leads to the equation:

$$\frac{\Delta T_2}{\Delta t} = \frac{1}{\rho \cdot c_{v1}} \cdot \left[ \frac{k_1}{\Delta X^2} \cdot T_6 - \frac{2 \cdot k_1}{\Delta X^2} \cdot T_2 + \frac{k_1}{\Delta X^2} \cdot T_{58} \right] \quad (4.26)$$

Taking into account the exchanges along all directions and all the possible heat generations, the equation of node 2 can be written:

- in the case of contact with the road:

$$\begin{aligned} \dot{Q}_{SEL} + \frac{k_1}{\Delta X} \cdot (T_6 - T_2) \cdot \Delta Y \cdot \frac{\Delta Z_1}{2} - \frac{k_1}{\Delta X} \cdot (T_2 - T_{58}) \cdot \Delta Y \cdot \frac{\Delta Z_1}{2} + \frac{k_1}{\Delta Y} \cdot (T_1 - T_2) \\ \cdot \Delta X \cdot \frac{\Delta Z_1}{2} - \frac{k_1}{\Delta Y} \cdot (T_2 - T_3) \cdot \Delta X \cdot \frac{\Delta Z_1}{2} + \frac{k_1}{\Delta Z_1} \cdot (T_{62} - T_2) \cdot \Delta X \cdot \Delta Y \\ + CR \cdot \frac{F_x \cdot v_x + F_y \cdot v_y}{A} \cdot \Delta X \cdot \Delta Y + H_c \cdot (T_r - T_2) \cdot \Delta X \cdot \Delta Y \\ = m_2 \cdot c_{v1} \cdot \frac{\Delta T_2}{\Delta t} \end{aligned} \quad (4.26A)$$

- in the case of contact with external air:

$$\begin{aligned} \dot{Q}_{SEL} + \frac{k_1}{\Delta X} \cdot (T_6 - T_2) \cdot \Delta Y \cdot \frac{\Delta Z_1}{2} - \frac{k_1}{\Delta X} \cdot (T_2 - T_{58}) \cdot \Delta Y \cdot \frac{\Delta Z_1}{2} + \frac{k_1}{\Delta Y} \cdot (T_1 - T_2) \\ \cdot \Delta X \cdot \frac{\Delta Z_1}{2} - \frac{k_1}{\Delta Y} \cdot (T_2 - T_3) \cdot \Delta X \cdot \frac{\Delta Z_1}{2} + \frac{k_1}{\Delta Z_1} \cdot (T_{62} - T_2) \cdot \Delta X \cdot \Delta Y \quad (4.26B) \\ + h_{forc} \cdot (T_{air} - T_2) \cdot \Delta X \cdot \Delta Y = m_2 \cdot c_{v1} \cdot \frac{\Delta T_2}{\Delta t} \end{aligned}$$

having denoted by  $\dot{Q}_{SEL}$  the power dissipated by cyclic deformation.

Once developed, the two expressions lead respectively to:

- in the case of contact with the road:

$$\begin{aligned} \frac{\Delta T_2}{\Delta t} = \frac{1}{\rho \cdot c_{v1}} \cdot \left[ \frac{2 \cdot \dot{Q}_{SEL}}{\Delta X \cdot \Delta Y \cdot \Delta Z_1} + \left( -\frac{2 \cdot k_1}{\Delta X^2} - \frac{2 \cdot k_1}{\Delta Y^2} - \frac{2 \cdot k_1}{\Delta Z_1^2} - \frac{2 \cdot H_c}{\Delta Z_1} \right) \cdot T_2 + \frac{k_1}{\Delta Y^2} \cdot T_1 \right. \\ \left. + \frac{k_1}{\Delta Y^2} \cdot T_3 + \frac{k_1}{\Delta X^2} \cdot T_6 + \frac{k_1}{\Delta X^2} \cdot T_{58} + \frac{2 \cdot k_1}{\Delta Z_1^2} \cdot T_{62} + \frac{2 \cdot FP}{\Delta Z_1} + \frac{2 \cdot H_c}{\Delta Z_1} \right. \\ \left. \cdot T_r \right] \quad (4.27) \end{aligned}$$

- in the case of contact with external air:

$$\begin{aligned} \frac{\Delta T_2}{\Delta t} = \frac{1}{\rho \cdot c_{v1}} \cdot \left[ \frac{2 \cdot \dot{Q}_{SEL}}{\Delta X \cdot \Delta Y \cdot \Delta Z_1} + \left( -\frac{2 \cdot k_1}{\Delta X^2} - \frac{2 \cdot k_1}{\Delta Y^2} - \frac{2 \cdot k_1}{\Delta Z_1^2} - \frac{2 \cdot h_{forc}}{\Delta Z_1} \right) \cdot T_2 + \frac{k_1}{\Delta Y^2} \right. \\ \left. \cdot T_1 + \frac{k_1}{\Delta Y^2} \cdot T_3 + \frac{k_1}{\Delta X^2} \cdot T_6 + \frac{k_1}{\Delta X^2} \cdot T_{58} + \frac{2 \cdot k_1}{\Delta Z_1^2} \cdot T_{62} + \frac{2 \cdot h_{forc}}{\Delta Z_1} \cdot T_{air} \right] \quad (4.28) \end{aligned}$$

The equations showed for node 2 are valid for all the nodes belonging to the surface layer, localized internally in lateral direction.

For a node still belonging to the surface layer, but external in lateral direction ( $C = 1/4$ ), for example node 1, the complete equations are:

- in the case of contact with the road:

$$\begin{aligned} \dot{Q}_{SEL} + \frac{k_1}{\Delta X} \cdot (T_5 - T_1) \cdot \frac{\Delta Y}{2} \cdot \frac{\Delta Z_1}{2} - \frac{k_1}{\Delta X} \cdot (T_1 - T_{57}) \cdot \frac{\Delta Y}{2} \cdot \frac{\Delta Z_1}{2} + \frac{k_1}{\Delta Y} \cdot (T_2 - T_1) \\ \cdot \Delta X \cdot \frac{\Delta Z_1}{2} + \frac{k_1}{\Delta Z_1} \cdot (T_{61} - T_1) \cdot \Delta X \cdot \frac{\Delta Y}{2} + CR \cdot \frac{F_x \cdot v_x + F_y \cdot v_y}{A} \cdot \Delta X \quad (4.28A) \\ \cdot \frac{\Delta Y}{2} + H_c \cdot (T_r - T_1) \cdot \Delta X \cdot \frac{\Delta Y}{2} = m_1 \cdot c_{v1} \cdot \frac{\Delta T_1}{\Delta t} \end{aligned}$$

- in the case of contact with external air:

$$\begin{aligned}
\dot{Q}_{SEL} + \frac{k_1}{\Delta X} \cdot (T_5 - T_1) \cdot \frac{\Delta Y}{2} \cdot \frac{\Delta Z_1}{2} - \frac{k_1}{\Delta X} \cdot (T_1 - T_{57}) \cdot \frac{\Delta Y}{2} \cdot \frac{\Delta Z_1}{2} + \frac{k_1}{\Delta Y} \cdot (T_2 - T_1) \\
\cdot \Delta X \cdot \frac{\Delta Z_1}{2} + \frac{k_1}{\Delta Z_1} \cdot (T_{61} - T_1) \cdot \Delta X \cdot \frac{\Delta Y}{2} + h_{forc} \cdot (T_{air} - T_1) \cdot \Delta X \quad (4.28B) \\
\cdot \frac{\Delta Y}{2} = m_1 \cdot c_{v1} \cdot \frac{\Delta T_1}{\Delta t}
\end{aligned}$$

leading, respectively, to:

- for the first case:

$$\begin{aligned}
\frac{\Delta T_1}{\Delta t} = \frac{1}{\rho \cdot c_{v1}} \cdot \left[ \frac{4 \cdot \dot{Q}_{SEL}}{\Delta X \cdot \Delta Y \cdot \Delta Z_1} + \left( -\frac{2 \cdot k_1}{\Delta X^2} - \frac{2 \cdot k_1}{\Delta Y^2} - \frac{2 \cdot k_1}{\Delta Z_1^2} - \frac{2 \cdot H_c}{\Delta Z_1} \right) \cdot T_1 + \frac{2 \cdot k_1}{\Delta Y^2} \right. \\
\left. \cdot T_2 + \frac{k_1}{\Delta X^2} \cdot T_5 + \frac{k_1}{\Delta X^2} \cdot T_{57} + \frac{2 \cdot k_1}{\Delta Z_1^2} \cdot T_{61} + \frac{2 \cdot FP}{\Delta Z_1} + \frac{2 \cdot H_c}{\Delta Z_1} \cdot T_r \right] \quad (4.29)
\end{aligned}$$

- for the second case:

$$\begin{aligned}
\frac{\Delta T_1}{\Delta t} = \frac{1}{\rho \cdot c_{v1}} \cdot \left[ \frac{4 \cdot \dot{Q}_{SEL}}{\Delta X \cdot \Delta Y \cdot \Delta Z_1} + \left( -\frac{2 \cdot k_1}{\Delta X^2} - \frac{2 \cdot k_1}{\Delta Y^2} - \frac{2 \cdot k_1}{\Delta Z_1^2} - \frac{2 \cdot h_{forz}}{\Delta Z_1} \right) \cdot T_1 + \frac{2 \cdot k_1}{\Delta Y^2} \right. \\
\left. \cdot T_2 + \frac{k_1}{\Delta X^2} \cdot T_5 + \frac{k_1}{\Delta X^2} \cdot T_{57} + \frac{2 \cdot k_1}{\Delta Z_1^2} \cdot T_{61} + \frac{2 \cdot h_{forc}}{\Delta Z_1} \cdot T_{air} \right] \quad (4.30)
\end{aligned}$$

The equation relating to the bulk layer, for an internal node in the lateral direction ( $C = 1$ ), e.g. node 62, is:

$$\begin{aligned}
\dot{Q}_{SEL} + \frac{k_2}{\Delta X} \cdot (T_{66} - T_{62}) \cdot \Delta Y \cdot \left( \frac{\Delta Z_1}{2} + \frac{\Delta Z_2}{2} \right) - \frac{k_2}{\Delta X} \cdot (T_{62} - T_{118}) \cdot \Delta Y \\
\cdot \left( \frac{\Delta Z_1}{2} + \frac{\Delta Z_2}{2} \right) + \frac{k_2}{\Delta Y} \cdot (T_{61} - T_{62}) \cdot \Delta X \cdot \left( \frac{\Delta Z_1}{2} + \frac{\Delta Z_2}{2} \right) - \frac{k_2}{\Delta Y} \\
\cdot (T_{62} - T_{63}) \cdot \Delta X \cdot \left( \frac{\Delta Z_1}{2} + \frac{\Delta Z_2}{2} \right) + \frac{k_2}{\Delta Z_2} \cdot (T_{122} - T_{62}) \cdot \Delta X \cdot \Delta Y \\
- \frac{k_1}{\Delta Z_1} \cdot (T_{62} - T_2) \cdot \Delta X \cdot \Delta Y = m_{62} \cdot c_{v2} \cdot \frac{\Delta T_{62}}{\Delta t} \quad (4.30A)
\end{aligned}$$

Such expression, suitably developed, leads to:

$$\frac{\Delta T_{62}}{\Delta t} = \frac{1}{\rho \cdot c_{v2}} \cdot \left[ \frac{\dot{Q}_{SEL}}{\Delta X \cdot \Delta Y \cdot \left( \frac{\Delta Z_1}{2} + \frac{\Delta Z_2}{2} \right)} + \left( -\frac{2 \cdot k_2}{\Delta X^2} - \frac{2 \cdot k_2}{\Delta Y^2} - \frac{k_2}{\Delta Z_2 \cdot \left( \frac{\Delta Z_1}{2} + \frac{\Delta Z_2}{2} \right)} - \frac{k_1}{\Delta Z_1 \cdot \left( \frac{\Delta Z_1}{2} + \frac{\Delta Z_2}{2} \right)} \right) \cdot T_{62} + \frac{k_2}{\Delta Y^2} \cdot T_{61} + \frac{k_2}{\Delta Y^2} \cdot T_{63} + \frac{k_2}{\Delta X^2} \cdot T_{66} + \frac{k_2}{\Delta X^2} \cdot T_{118} + \frac{k_2}{\Delta Z_2 \cdot \left( \frac{\Delta Z_1}{2} + \frac{\Delta Z_2}{2} \right)} \cdot T_{122} + \frac{k_1}{\Delta Z_1 \cdot \left( \frac{\Delta Z_1}{2} + \frac{\Delta Z_2}{2} \right)} \cdot T_2 \right] \quad (4.31)$$

Similarly, relatively to a bulk external node in the transverse direction, ( $C = 1/2$ ), it results:

$$\begin{aligned} \dot{Q}_{SEL} + \frac{k_2}{\Delta X} \cdot (T_{65} - T_{61}) \cdot \frac{\Delta Y}{2} \cdot \left( \frac{\Delta Z_1}{2} + \frac{\Delta Z_2}{2} \right) - \frac{k_2}{\Delta X} \cdot (T_{61} - T_{117}) \cdot \frac{\Delta Y}{2} \\ \cdot \left( \frac{\Delta Z_1}{2} + \frac{\Delta Z_2}{2} \right) + \frac{k_2}{\Delta Y} \cdot (T_{62} - T_{61}) \cdot \Delta X \cdot \left( \frac{\Delta Z_1}{2} + \frac{\Delta Z_2}{2} \right) + \frac{k_2}{\Delta Z_2} \\ \cdot (T_{121} - T_{61}) \cdot \Delta X \cdot \frac{\Delta Y}{2} - \frac{k_1}{\Delta Z_1} \cdot (T_{61} - T_1) \cdot \Delta X \cdot \frac{\Delta Y}{2} \\ = m_{61} \cdot c_{v2} \cdot \frac{\Delta T_{61}}{\Delta t} \end{aligned} \quad (4.31A)$$

that becomes:

$$\frac{\Delta T_{61}}{\Delta t} = \frac{1}{\rho \cdot c_{v2}} \cdot \left[ \frac{2 \cdot \dot{Q}_{SEL}}{\Delta X \cdot \Delta Y \cdot \left( \frac{\Delta Z_1}{2} + \frac{\Delta Z_2}{2} \right)} + \left( -\frac{2 \cdot k_2}{\Delta X^2} - \frac{2 \cdot k_2}{\Delta Y^2} - \frac{k_2}{\Delta Z_2 \cdot \left( \frac{\Delta Z_1}{2} + \frac{\Delta Z_2}{2} \right)} - \frac{k_1}{\Delta Z_1 \cdot \left( \frac{\Delta Z_1}{2} + \frac{\Delta Z_2}{2} \right)} \right) \cdot T_{61} + \frac{2 \cdot k_2}{\Delta Y^2} \cdot T_{62} + \frac{k_2}{\Delta X^2} \cdot T_{65} + \frac{k_2}{\Delta X^2} \cdot T_{117} + \frac{k_2}{\Delta Z_2 \cdot \left( \frac{\Delta Z_1}{2} + \frac{\Delta Z_2}{2} \right)} \cdot T_{121} + \frac{k_1}{\Delta Z_1 \cdot \left( \frac{\Delta Z_1}{2} + \frac{\Delta Z_2}{2} \right)} \cdot T_1 \right] \quad (4.32)$$

As concerns the innermost layer, the inner liner, the equation of exchange for an internal node in the transverse direction ( $C = 1/2$ ), eg 122, is:

$$\begin{aligned}
\dot{Q}_{SEL} + \frac{k_2}{\Delta X} \cdot (T_{126} - T_{122}) \cdot \Delta Y \cdot \frac{\Delta Z_2}{2} - \frac{k_2}{\Delta X} \cdot (T_{122} - T_{158}) \cdot \Delta Y \cdot \frac{\Delta Z_2}{2} + \frac{k_2}{\Delta Y} \\
\cdot (T_{121} - T_{122}) \cdot \Delta X \cdot \frac{\Delta Z_2}{2} - \frac{k_2}{\Delta Y} \cdot (T_{122} - T_{123}) \cdot \Delta X \cdot \frac{\Delta Z_2}{2} + \frac{k_2}{\Delta Z_2} \\
\cdot (T_{62} - T_{122}) \cdot \Delta X \cdot \Delta Y + h_{int} \cdot (T_{air\_int} - T_{122}) \cdot \Delta X \cdot \Delta Y \\
= m_{122} \cdot c_{v2} \cdot \frac{\Delta T_{122}}{\Delta t}
\end{aligned} \quad (4.32A)$$

that simplified returns:

$$\begin{aligned}
\frac{\Delta T_{122}}{\Delta t} = \frac{1}{\rho \cdot c_{v2}} \cdot \left[ \frac{2 \cdot \dot{Q}_{SEL}}{\Delta X \cdot \Delta Y \cdot \Delta Z_2} + \left( -\frac{2 \cdot k_2}{\Delta X^2} - \frac{2 \cdot k_2}{\Delta Y^2} - \frac{2 \cdot k_2}{\Delta Z_2^2} - \frac{2 \cdot h_{int}}{\Delta Z_2} \right) \cdot T_{122} \right. \\
+ \frac{k_2}{\Delta Y^2} \cdot T_{121} + \frac{k_2}{\Delta Y^2} \cdot T_{123} + \frac{k_2}{\Delta X^2} \cdot T_{126} + \frac{k_2}{\Delta X^2} \cdot T_{158} + \frac{2 \cdot k_2}{\Delta Z_2^2} \cdot T_{62} \\
\left. + \frac{2 \cdot h_{int}}{\Delta Z_2} \cdot T_{air\_int} \right]
\end{aligned} \quad (4.33)$$

Finally, for an external node in the transverse direction belonging to the Inner liner ( $C = 1/4$ ), it is:

$$\begin{aligned}
\dot{Q}_{SEL} + \frac{k_2}{\Delta X} \cdot (T_{125} - T_{121}) \cdot \frac{\Delta Y}{2} \cdot \frac{\Delta Z_2}{2} - \frac{k_2}{\Delta X} \cdot (T_{121} - T_{157}) \cdot \frac{\Delta Y}{2} \cdot \frac{\Delta Z_2}{2} + \frac{k_2}{\Delta Y} \\
\cdot (T_{122} - T_{121}) \cdot \Delta X \cdot \frac{\Delta Z_2}{2} + \frac{k_2}{\Delta Z_2} \cdot (T_{61} - T_{121}) \cdot \Delta X \cdot \frac{\Delta Y}{2} + h_{int} \\
\cdot (T_{air\_int} - T_{121}) \cdot \Delta X \cdot \frac{\Delta Y}{2} = m_{121} \cdot c_{v2} \cdot \frac{\Delta T_{121}}{\Delta t}
\end{aligned} \quad (4.33A)$$

which, simplified, provides:

$$\begin{aligned}
\frac{\Delta T_{121}}{\Delta t} = \frac{1}{\rho \cdot c_{v2}} \cdot \left[ \frac{4 \cdot \dot{Q}_{SEL}}{\Delta X \cdot \Delta Y \cdot \Delta Z_2} + \left( -\frac{2 \cdot k_2}{\Delta X^2} - \frac{2 \cdot k_2}{\Delta Y^2} - \frac{2 \cdot k_2}{\Delta Z_2^2} - \frac{2 \cdot h_{int}}{\Delta Z_2} \right) \cdot T_{121} \right. \\
+ \frac{2 \cdot k_2}{\Delta Y^2} \cdot T_{122} + \frac{k_2}{\Delta X^2} \cdot T_{125} + \frac{k_2}{\Delta X^2} \cdot T_{157} + \frac{2 \cdot k_2}{\Delta Z_2^2} \cdot T_{61} + \frac{2 \cdot h_{int}}{\Delta Z_2} \\
\left. \cdot T_{air\_int} \right]
\end{aligned} \quad (4.34)$$

## **5. GrETA - Grip Estimation for Tyre Analyses**

### **5.1 Introduction**

Rubber frictional behaviour in tyre/road interaction is one of the main topics in a wide range of research fields. Knowledge about phenomena concerning with adherence is a key factor in the development of braking/traction and stability control systems adopted in automotive industry [52], such as in the study of innovative tyre structures and compounds, able to minimize braking distances, to preserve vehicle stability in panic situations and to guarantee optimal roadholding on wet/icy surfaces [53].

Moreover, the continuous drivers' seeking of the optimal grip for each different driving condition, makes the development of a physical grip model an essential instrument for a top-ranking racing team, in particular thanks to the definitely lower resources needed by simulations than by experimental tests carried out in order to acquire information about tyres behaviour. Rubber/asphalt friction, in fact, is influenced by a great number of variables and parameters, often hard to be controlled and measured [54]; macro and micro roughness of the bodies in contact, pressure arising at their interface, materials stiffness characteristics and their frequency and temperature dependence, relative motion direction and speed are only a small number of the factors that take part in a phenomenon involving contact mechanics, thermodynamics, polymers chemistry and, from a wider point of view, vehicle dynamics.

Since the ancient times, friction force has been investigated, often with the aim to reduce and avoid it, because of its tendency to contrast the motion and of the consequential phenomena considered as undesirable like heat production, power dissipation and wear.

In the automotive and in particular in the race field, the possibility to maximize the grip, driving in the same environmental conditions of the competitors, can represent a key factor to configure an optimal setup of the vehicle, designed in order to obtain the best performances under the expected loads and wheel angles, to choose the most suitable compound for each road and weather condition and to plan a proper driving strategy, able to make the tyre work under the desired conditions, predicted by means of a physical model.

The first attempt to formalize the relationship between the friction force and the main variables on which it is depending, after the studies about wheel invention carried out by Temistio (390 – 320 b.C.), dates back at the times of Leonardo da Vinci, who proposed in his unpublished handbooks a linear relationship between the contact force and the vertical load; after the experimental activity of G. Amontons [55], C. A. Coulomb theorized that for metals friction force was independent from contact area and directly proportional to the applied normal load by means of a coefficient [56], expressing for the first time the well known law:

$$\mu = \frac{\text{Friction force between two metal surfaces}}{\text{Applied normal load}} \quad (5.1)$$

Dependence on sliding velocity was not taken into account, but a first distinction between static and dynamic friction coefficient was proposed and analyzed. Bowden and Tabor [57][58] and Rabinowicz [59] introduced the theme of adhesion in polymers

contact, investigating the frictional behaviour of rubber and highlighting its strong dependence from loads, temperature and relative speed.

A generalized friction model was proposed by H. W. Kummer [60] during his activity in the field of tyre/road interaction; his model (Fig. 5.1) considered for the first time the resistant force as composed by three components: adhesion, deforming hysteresis and wear.

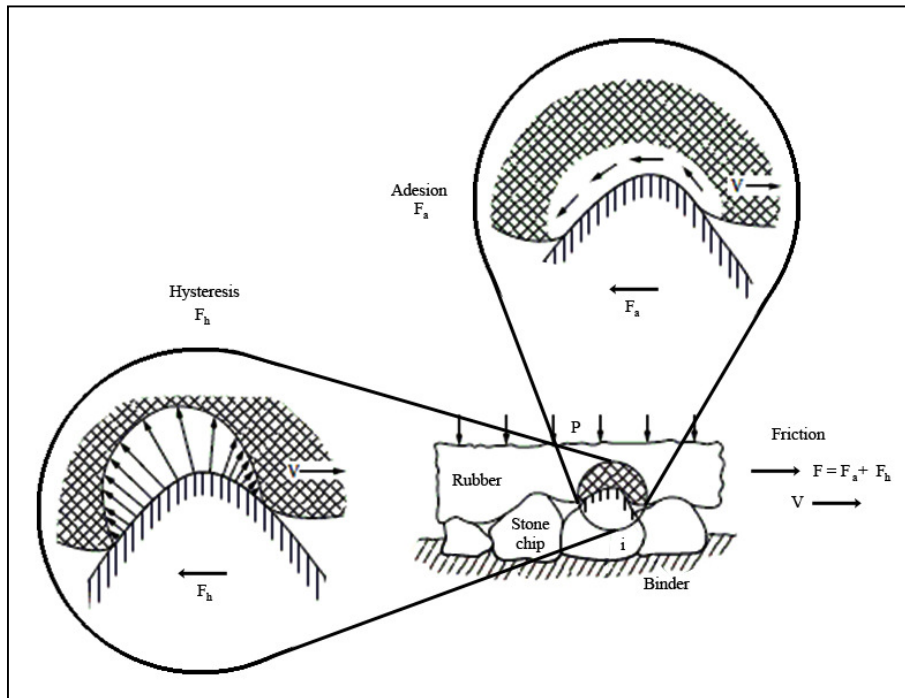


Fig. 5.1 - Kummer's model for rubber friction mechanisms.

In dry conditions, tyres friction forces take the following form:

$$F_T = F_{ADH} + F_{Hb} + F_C \quad (5.2)$$

where:  $F_T$  is the total frictional resistance developed between a sliding tyre and road,  $F_{ADH}$  is the frictional contribution due to Van der Waals' adhesion bonds between the two surfaces,  $F_{Hb}$  is the frictional contribution from bulk deformation hysteresis in the rubber, and  $F_C$  is the cohesion contribution linked with rubber wear.

Kummer postulated that  $F_{ADH}$  and  $F_{Hb}$  are not independent because adhesion is able to increase the extension of the contact area and consequently the zone in which the hysteretic deformations occur. The third contribution to the resistant forces is achieved because of the removal of rubber material by road asperities, but the contribution to friction due to this phenomenon is estimated around 2% on rough surfaces [33].

Thanks to Kummer and Savkoor's work [61], Moore [62] hypothesized that the different components were predominant on different scales: the macro-roughness affects the deformations related to hysteresis and the micro-roughness affects the intermolecular bonds characterizing adhesion. For this reason, the two aspects may conceptually be split and treated applying a sort of superposition principle (Fig. 5.2).

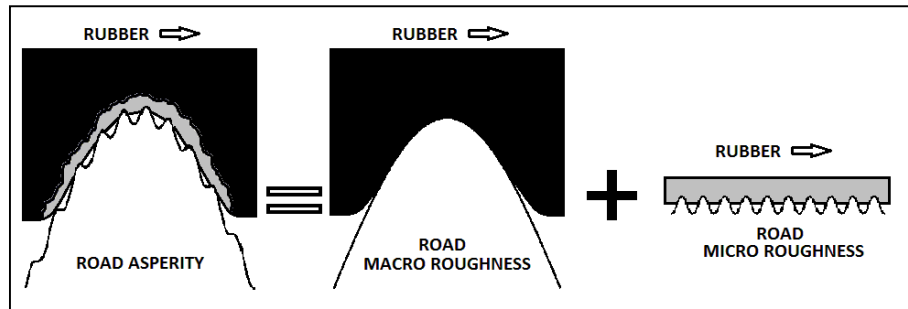


Fig. 5.1 - Influence of the roughness scales on the different friction mechanisms.

In more recent years, the cited theories concerning with friction modelling have been confirmed by further developments in the fields of tyre / road hysteretic and adhesive interaction analysis [63][64][65], of contact mechanics between rubber and rough surfaces [66][67] and of local heat transfer in frictional phenomena [68][69]. Typical methods to find out tyre grip are based on observers and identification procedures [70][71][72].

In this chapter, a tyre/road friction physical model, named Gr.E.T.A. (Grip Estimation for Tyre Analyses) Model, will be presented. The model, developed in collaboration with a motorsport racing team and a tyre manufacturing company, bases on the previous considerations, providing an effective calculation of the power dissipated by road asperities indented in tyre tread and taking into account the phenomena involved with adhesive friction, expressed by means of an original formulation (synthesizing some adherence models available in literature) whose parameters are identified thanks to dedicated experimental tests.

## 5.2 Model Definition And Basic Hypotheses

In order to model the complex interactions between tyre and asphalt at a microscopic level, it has been necessary to focus initially on the behaviour of an elementary volume of rubber in sliding contact with a limited portion of road.

	Range Size	
	Wavelength	R <sub>a</sub>
<b>Mega-</b>	50 – 500 mm	0.1 – 50 mm
<b>Macro-</b>	0.5 – 50 mm	0.1 – 20 mm
<b>Micro-</b>	0 – 0.5 mm	1 – 500 μm

Tab. 5.1 – Road texture scales dimensions [73].

Modelling asphalt, as commonly found in literature [74], as the sum of sinusoidal waves distributed in the space characterizing the different roughness scales (Tab. 5.1), tread elementary volume has been defined as a square-based parallelepiped. Its height is equal to tyre tread thickness and the base side to road macro-roughness wavelength  $\lambda_{\text{MACRO}}$  (Fig. 5.3).

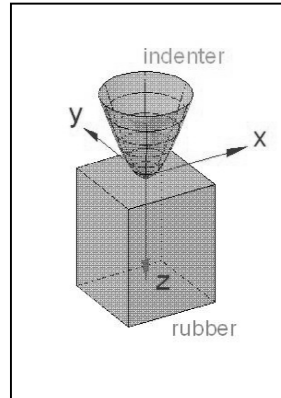


Fig. 5.2 - Elementary tread volume and coordinates system.

Wavelength parameters are connected with amplitude parameters [75], the most common to characterize surfaces topography; as a consequence, also the amplitude vertical characteristics of the surface will be described by macro and micro scale parameters.

The arithmetic average height parameter ( $R_a$ ), also known as the centre line average, is the most used roughness parameter for general quality control. It is defined as the average absolute deviation of the roughness irregularities from the mean line over one sampling length. This parameter is easy to define, easy to measure and gives a good general description of height variations. The mathematical definition and the numerical implementation of the arithmetic average height parameter are, respectively:

$$R_a = \frac{1}{L} \int_0^L |y(x)| dx \quad (5.3)$$

$$R_a = \frac{1}{n} \sum_{i=1}^n |y_i| \quad (5.4)$$

Wavelengths  $\lambda$  and roughness indices  $R_a$  characterizing soil profile have been estimated analysing data acquired experimentally by laser scan on different dry tracks and to reproduce the best-fitting sinusoidal waves corresponding to macro and micro profiles (Fig. 5.4).

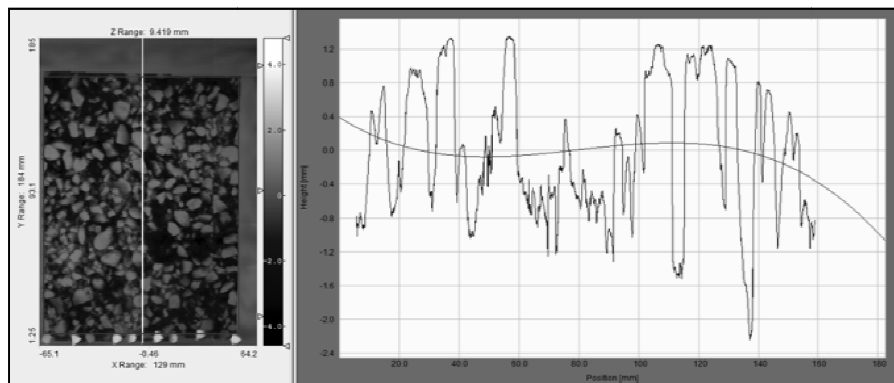


Fig. 5.3 - Road acquired profile and analysis of a 2D section of it.

The chosen Cartesian reference system, as shown in figure 5.3, has its origin in the centre of the upper parallelepiped face; x-axis is in the tread surface plane, oriented in the sliding direction of the indenter, z-axis is oriented in the direction of tread width, and y-axis is oriented in order to obtain a right handed coordinates system.

Tread rubber and road are considered as isotropic and homogeneous materials; moreover, road is modelled as perfectly rigid.

### 5.3 Material Characterization

Rubber employed in tyre treads is a hyperelastic, soft and virtually incompressible material (Poisson's ratio  $\nu_p = 0.5$ ), but it can usually be stretched more than 500%. Its molecular structure consists of long, linear flexible molecules interlinked into a 3D network. Chemical crosslinks are usually made by sulphur linkages coming out after a technological process, known as vulcanization [13]. The rubbery state of a polymer is determined by the so-called glassy transition temperature  $T_g$ . When the working temperature is above  $T_g$ , the polymer shows a rubbery behaviour. Otherwise, it is a glassy one [76].

The analysis of the response to deformation for a visco-elastic solid can be conveniently conducted referring to sinusoidal loads.

When an elastomeric material is subjected to an harmonic deformation

$$\varepsilon_1 = \varepsilon_1^0 \sin(\omega t) \quad (5.5)$$

where  $\varepsilon_1^0$  is the amplitude of the applied deformation and  $\omega$  is the angular frequency, the induced stress  $\sigma_1$  is harmonic too

$$\sigma_1 = \sigma_1^0 \sin(\omega t + \Delta) \quad (5.6)$$

with the same frequency but out of phase respect to deformation. The stress  $\sigma_1$  can be expressed as the sum of two contributions, one in phase with the imposed deformation and a second in quadrature phase

$$\sigma_1 = \varepsilon_1^0 (E' \sin(\omega t) + E'' \cos(\omega t)) \quad (5.7)$$

where  $E'$ , said storage modulus, is the elastic modulus part relative to the in phase response of the material and  $E''$ , called loss modulus, represents the elastic modulus of the part in quadrature phase. A very common index used to describe the dissipative attitudes of a compound is the loss angle tangent, defined as

$$\tan(\delta) = E'' / E' \quad (5.8)$$

The stiffness parameter adopted for visco-elastic materials in place of Young's modulus is the complex dynamic modulus

$$E = \sqrt{E'^2 + E''^2} \quad (5.9)$$

$E'$  and  $E''$  values and  $\tan(\delta)$  are strongly dependent on the temperature and on the frequency at which the rubber is stressed, as schematically represented in figure 5.5.

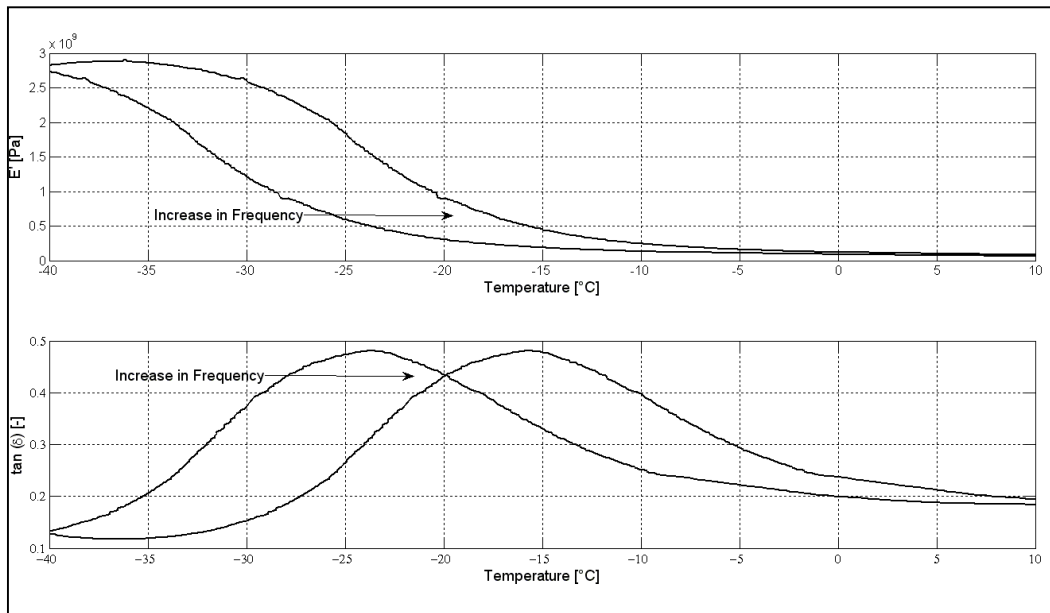


Fig. 5.4 -  $E'$  and  $\tan(\delta)$  relationship with frequency and temperature variations.

As regards the influence of temperature, the typical behaviour of polymers is characterized by a dynamic modulus decrement with increasing temperature, while the phase angle increases until it reaches a maximum before decreasing again.

Experimental tests have been initially carried out on common passenger tyre rubbers with the aim to acquire data useful to properly model the behaviour of SBR copolymers constituting tread: rubber specimens, properly cut and prepared, have been dynamically tested following DMA procedures [77][78][79] in a three point bending proof, in order to acquire storage modulus and  $\tan(\delta)$  data. Tests have been carried out at fixed frequency and displacement (1 Hz, 1%), making temperature increase at 1 °C per minute from -50 °C up to 100 °C.

The results of the  $E'$  characterization are shown in figure 5.6; as expected for the weakly crosslinked polymers employed in the tyres manufacturing, it has been possible to identify three areas: glassy region (low temperature, high storage modulus), transition region and rubbery region (high temperatures, low storage modulus). Figure 5.7 highlights, despite some irregularities, the expected  $\tan(\delta)$  trend, with an absolute maximum localized in the thermal transition zone.

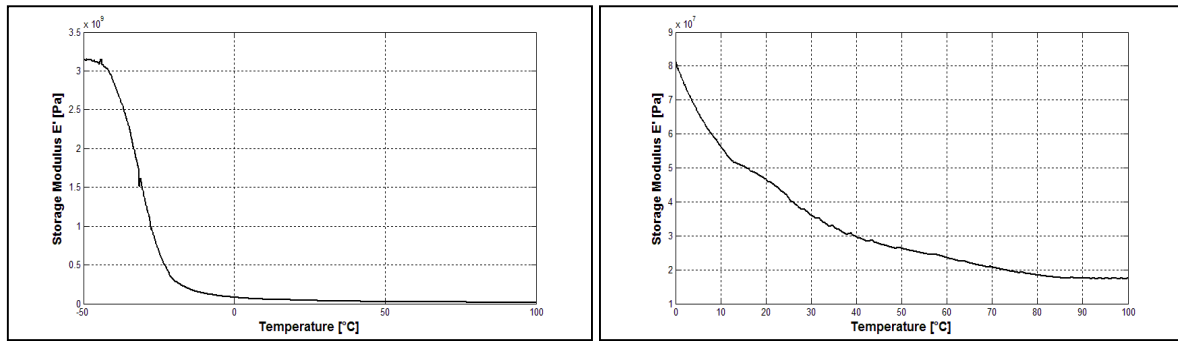


Fig. 5.6a - Passenger tyre  $E'$  thermal characterization data - Frequency = 1 Hz  
 Fig. 5.6b - Detail of the [0 – 100] °C zone.

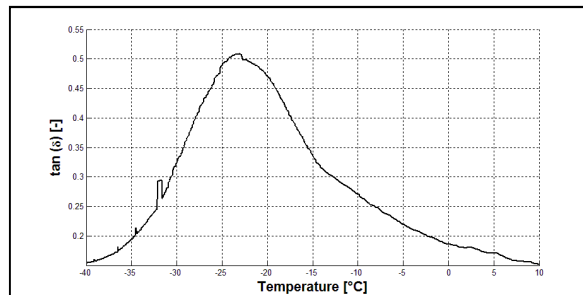


Fig. 5.7 - Passenger tyre  $\tan(\delta)$  thermal characterization data - Frequency = 1 Hz.

For common passenger tyres, glass transition temperature is often below 0 °C, so that usual working conditions are localized in the rubbery zone in order to provide optimal frictional performances. Sport and high-performance tyres, characterized by the employment of different rubber compounds and fillers, exhibit lower values of the dynamic modulus, that make the tread manifesting softer and highly wearable, a more hysteretic attitude and a definitely higher  $T_g$  and consequentially a higher thermal optimal working range.

When both the frequency and the temperature vary, it is possible to make use of the property whereby an appropriate shift operation is capable of combining the effect of them: the main element on which the temperature - frequency equivalence principle is based is that the values of the complex modulus components at any reference frequency and temperature ( $f_1, T_1$ ) are identical to the ones observable at any other frequency  $f_2$  at a properly shifted value of temperature  $\alpha(T_1)$ :

$$E(f_1, T_1) = E[f_2, \alpha(T_1)] \quad (5.10)$$

The most widely relationship used to describe the equivalence principle is the Williams-Landel-Ferry (WLF) transform [80]. For passenger tyre rubber it can be employed in a simplified way in order to determine the unknown equivalent temperature  $T^* = \alpha(T_1)$ :

$$\log\left(\frac{f_2}{f_1}\right) = \frac{T^* - T_1}{\Delta T} \quad (5.11)$$

in which a common  $\Delta T$  value, identifiable by means of DMA tests at different frequencies, is about 8 °C.

The physical meaning of the law is that rubber stressed at high frequency behaves like if the stress is applied at lower frequency but at the same time, at a colder working temperature. High frequency acts reducing the time between two consecutive stresses, not allowing the complete relax of the rubber, in the same way as a low working temperature would do.

A further behaviour of visco-elastic materials that has to be taken into account in contact mechanics with rigid indenters is the increasing trend that compression force shows respect to displacement in the first phase of indentation. Stressing a cylindrical specimen in a mono-axial compression test has allowed to investigate this effect, attributed to rubber dynamic modulus increasing and to contact area shape modifications, both responsible of the decrease of friction with contact pressure.

In figure 5.8, the global dynamic modulus  $E$ , adimensionalized respect to its value at a compression rate of 0.01, is plotted as a function of the compression rate itself, expressed as

$$\varepsilon = \frac{t_0 - t^*}{t_0} \quad (5.12)$$

in which  $t_0$  and  $t^*$  are, respectively, the initial thickness and the actual thickness of the specimen during the test.

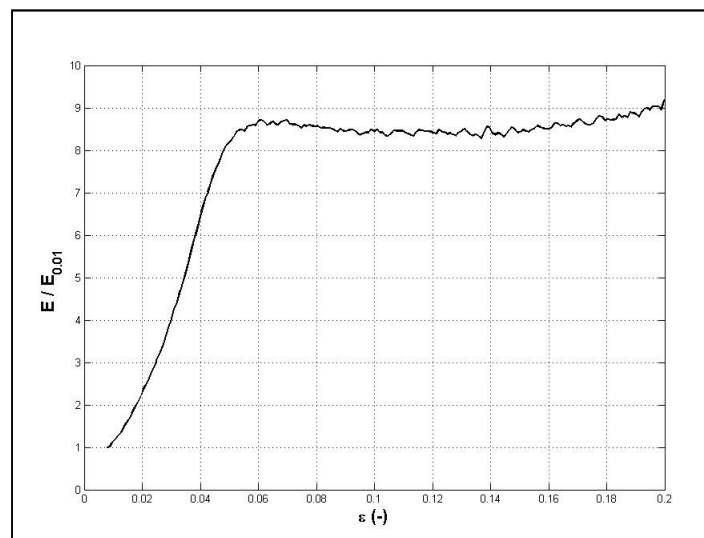


Fig. 5.8 - Passenger tyre tread hardening phenomenon observed by means of mono-axial compression test.

The experimental results highline that also for indentation levels largely smaller than the ones able to induce the typical hardening phenomenon [81] due to the compacting of the polymeric chains, the penetration of an asphalt asperity in a rubber layer has an influence in this last's characteristics, modifying the interaction between the two bodies; hypothesizing the penetration of an asperity 1 mm high in a 10 mm tyre tread, it is possible to observe a dynamic modulus value about 8.5 times higher than in unloaded conditions.

## **5.4 Adhesion**

### **5.4.1 Pin on Disk Tests**

#### **5.4.1.1 Introduction**

An experimental campaign has been planned and carried out with the aim to clarify the dependence of friction, and in particular of its adhesive component, on the main physical factors involved in the phenomenon.

In fact, especially in the automotive field, the estimation of the adherence between tyre and road is often performed by means of empirical calculations in which it is roughly distinguished among dry, wet or ice covered roads. More sophisticated theoretical models which take into account simultaneously road and rubber characteristics and operating conditions (load, temperature, sliding speed, ...) are hardly employable because of their complexity related, mainly, to the difficulty to measure with sufficient precision, the values of the microscopic and molecular variables involved in the model.

Therefore, it has been chosen to start from the development of a broad campaign of experimental tests aimed to characterize the local behaviour of a single piece of rubber. In such proofs different compounds, different countersurface profiles (characterized by various micro-roughness values) and different operating conditions have been adopted. In a second phase a critical analysis of the results has been carried out, with the aim to highlight trends and to identify the physical parameters that most influence the value of the local friction coefficient of the single rubber piece.

The goal of the experimental activity is the creation of a wide dataset, able to make the parameters identification of an analytical adhesive friction model possible. In what follows the test apparatus will be described, showing the main causes of uncertainty in the results provided by it and the experimentation results will be discussed, highlighting their dependence on the main characteristics of the rubber and of the road as well as on the operating conditions.

#### **5.4.1.2 Pin on Disk Experimental Test Bench**

Thanks to a tribological testing machine, friction relations with some typical parameters such as vertical load, sliding velocity and temperature have been investigated both in dry and in wet conditions.

The rotating disk of the tribometer has been covered with three different surfaces: glass, marble and 3M anti-slip tape; rubber specimens have been extracted from three slick slabs of different compounds, used for passenger automotive pneumatic tyres.

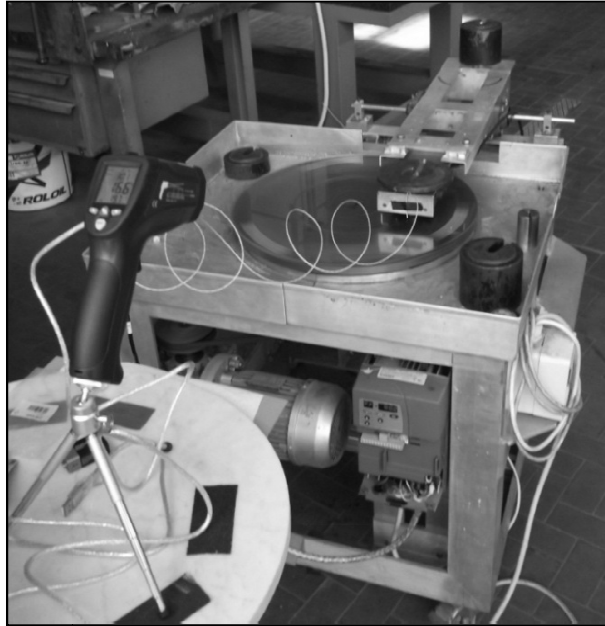


Figure 5.9 - The Pin on Disk tribometer.

Experiments were performed using a pin on disk machine (Fig. 5.9). This kind of tester is widely employed to measure friction and sliding wear properties of dry or lubricated surfaces of a variety of bulk materials and coatings. The elements of the machine are:

- an electric motor, driven by an inverter;
- a metal rotating disk, moved by the motor through a belt;
- a set of disks of different materials that can be fixed to the rotating disk;
- an arm on which a rubber specimen is housed;
- a load cell, interposed between the specimen and the arm, that allows the tangential force measurement;
- an incremental encoder, installed on the disk axis in order to measure its angular position and velocity;
- an optical pyrometer pointed on the disk surface in proximity of the contact exit edge, that provides an estimation of the temperature at the interface;
- a thermocouple located in the neighbourhood of the specimen, used to measure ambient temperature.

The arm is vertically approached to the rotating disk surface and through the application of calibrated weights, the normal force between specimen and disk can be varied. The rubber pins are cylinders of 14 mm diameter. The path they describe on the rotating disk is a 140 mm radius circumference.

In the experimental campaign, mainly aimed to investigate the adhesive and the micro hysteretic contributions to friction, the used disk materials are: glass ( $R_a < 0.03 \mu\text{m}$ ), marble ( $R_a = 0.1 \mu\text{m}$ ) and 3M tape ( $R_a = 27 \mu\text{m}$ ), chosen in order to simulate contact between rubber and different surfaces. Tests were performed both in dry and wet conditions.

As previously introduced, adhesion contribution to friction is directly connected with the actual extension of the contact surface. So, in order to highlight the adhesive friction contribution glass surface has been adopted, while 3M tape has been chosen in order to evaluate the micro-hysteretic contribution effects. Marble, characterized by

slightly wavy surface [82], offers the possibility to investigate the cross effect of both contributions.

#### 5.4.1.2 Results Analysis And Discussion

The results provided by the performed tests are affected by some degree of scattering, so a great attention should be posed in their interpretation. Scattering is mainly due to:

- local temperature: although temperature in the specimen neighbourhood is continuously monitored during the test, actual temperature in the contact zone can't be measured.
- wear: life of a specimen exhibits three characteristic stages. A new specimen presents a very smooth and hard surface providing low friction values on all partner surfaces. In a second stage the specimen surface is soft and "sticky", friction is higher, so this phase can be considered as the "useful life" of the specimen. In a third stage, the specimen surface either becomes hard again, or tends to break up; in both cases friction falls to very low values and the specimen must be replaced.
- extension of the contact patch: during the "useful life", wear continuously modifies the specimen surface, altering contact patch extension. To monitor this phenomenon, in several cases during the tests, the specimens have been marked with ink, so to be able to print their contact patch on graph paper. Under different known loads the specimens show, as expected, an increasing contact area with increasing load, with a clear tendency to saturation. In particular, under a 5 N load the contact area has been estimated to be equal to 70 mm<sup>2</sup> (pressure = 0.71 bar), employing the 45.5% of the available nominal area, equal to 154 mm<sup>2</sup>. Under a 10 N load the contact area has an extension of 100 mm<sup>2</sup> (pressure = 1 bar), that is the 65% of the available nominal area and, concerning with the 50 N load, real area is equal to 140 mm<sup>2</sup> (pressure = 3.5 bar), that is the 91% of the nominal one. During dynamical tests, even under the same vertical load, actual contact area, local pressure and friction can vary dramatically (Fig. 5.10): in general the greater the pressure the lower the friction [33].

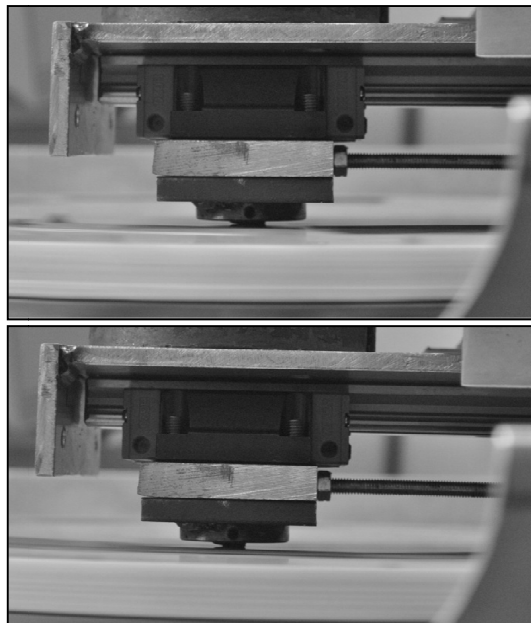


Fig. 5.10 - Specimen contact conditions during a test on marble.

- track conditions: clean or rubbery; in dependence of the track state friction may vary because of  $R_a$  variations; in particular, glass surface increases its micro-roughness from a starting value minor than  $0.03 \mu\text{m}$  to a value of about  $0.6 \mu\text{m}$ ; as concerns marble, its micro-roughness moves from an initial  $0.1 \mu\text{m}$  up to about  $1 \mu\text{m}$ ; paper roughness changes with an opposite tendency, showing a passivation phenomenon due to the filling of the valleys produced by rubber debris. Moreover, it has to be considered that rubber over rubber contact is different from the rubber over clean partner surface also for what concerns the intermolecular bonds formation.

- asset of the disk: due to unavoidable set up errors, the plane in which the contact takes place is not perfectly horizontal so causing little, one per revolution, vertical oscillations of the arm. The resulting inertia force makes the vertical load on the specimen not constant, causing oscillations also in the tangential force time history (Fig. 5.11). After compensation, the typical amplitude of such vertical oscillation is lower than  $0.05 \text{ mm}$  (which leads to a vertical force oscillation amplitude lower than  $5 \text{ N}$ ).

- water film thickness: during wet tests water film thickness can vary because of the difficulty to assure a constant fluid feed and for centrifugation effect occurring at high rotation speeds.

For the above reasons, the following comparisons refer to test conditions in which the causes of scattering are reasonably constant. Comparisons cannot be made among results relative to different test conditions.

Experiments have been conducted at constant speed, following a methodology named "step testing". The disk speed was regulated in order to realize in the contact zone the desired sliding velocity in the range  $0.1 - 2 \text{ m/s}$ . Once the disk steady state speed was reached, the loaded arm was slowly approached to the disk and the tangential force time history was recorded (Fig. 5.11). The kinetic friction coefficient was evaluated as the mean value of the ratio between tangential and vertical force in the time history steady state region. For each load and speed condition, tests were repeated several times in order to verify their repeatability. It is possible to notice that oscillations in acquired data (Fig. 5.11) can be linked with disk angular speed; step test, being performed at constant speed, shows results affected by constant frequency fluctuations. Such effects, noticeable also in the following discussed results, are correlated to the disk not perfectly flat surface and to the scattering causes previously listed.

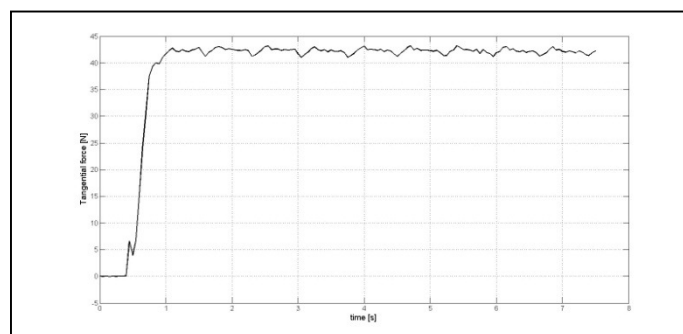


Fig. 5.11 - Step test on dry glass (vertical load  $F_z = 50 \text{ N}$ , relative speed  $V_s = 1.0 \text{ m/s}$ ).

During both the tests, especially in dry conditions, a temperature raising of about  $4^\circ\text{C}$  has been often observed in correspondence of the exit edge of the contact zone. Of

course in the contact zone the actual temperature will be increased of more than the value observed in the exit edge.

Since the measured temperature is only an index of the contact temperature and not the actual one, in all the tests performed the temperature has been monitored in order to verify its substantial constant value during the proof of the same kind.

The tests have been carried out employing three different rubber compounds, C1, C2 and C3, provided by a pneumatic tyres manufacturing company, interfaced with the three cited different materials: glass, marble and 3M tape. Preliminarily all compounds have been characterized by means of the cited Dynamic Mechanical Analysis (DMA) and Differential Scanning Calorimetry tests, carried out at 1 Hz frequency (Fig. 5.12a and 5.12b). Glass and marble have been scanned by means of a profilometer, while 3M surface has been analysed by means of a laser scan.

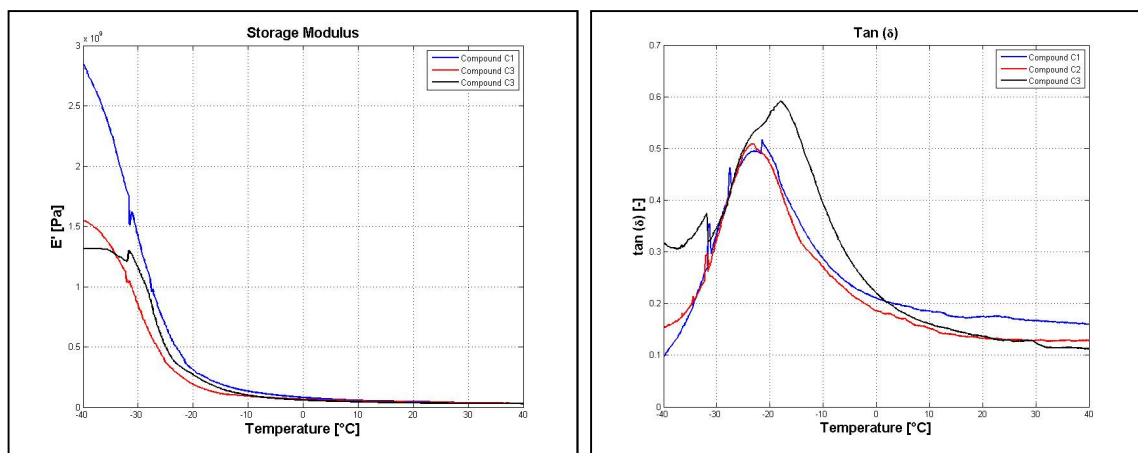


Fig. 5.12a - Storage modulus for compounds C1, C2 and C3.

Fig. 5.12b -  $\tan(\delta)$  for compounds C1, C2 and C3.

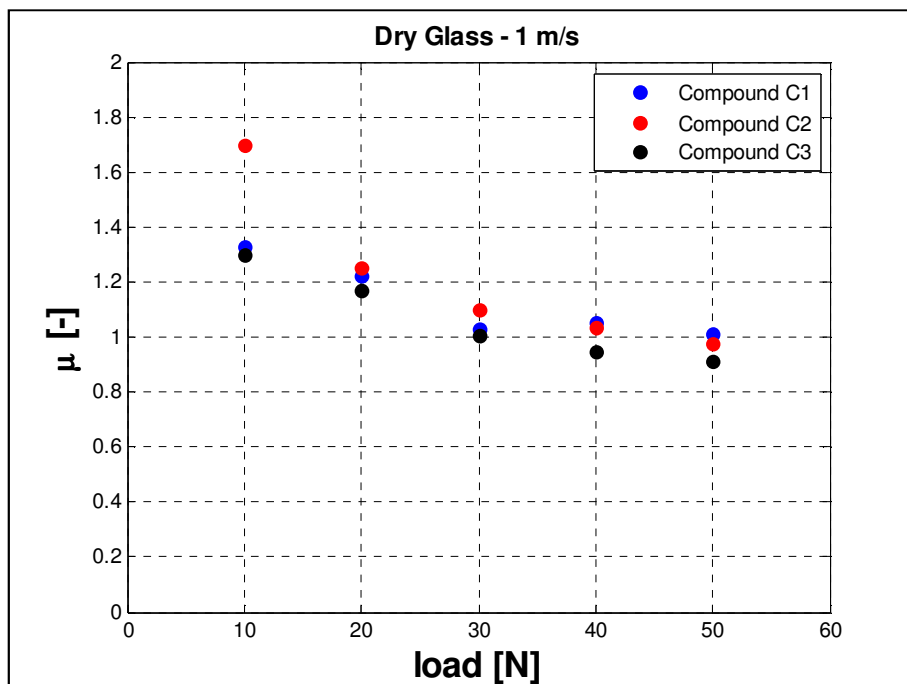


Fig. 5.13 - Friction coefficient vs load for the three compounds on dry glass ( $V_s = 1$  m/s).

In figure 5.13 it is reported the friction coefficient on dry glass as a function of the applied vertical load for the three different compounds (C1, C2 and C3).

From the above diagrams it is possible to notice how friction coefficient in dry conditions always decreases as load increases. This tendency could be explained taking into account that the contact pressure increases with load because the real contact area saturates and, as already stated, friction depends on contact pressure in an inverse way.

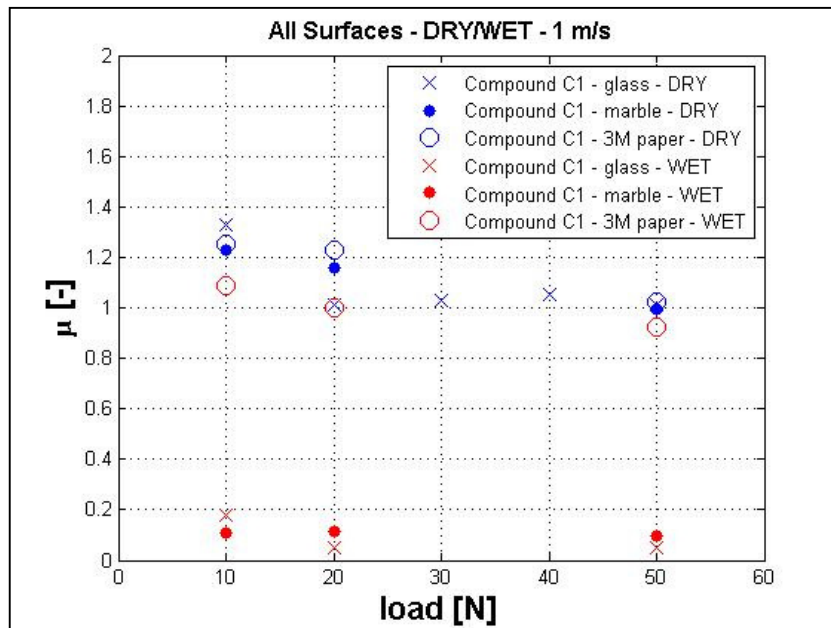


Fig. 5.14 - Friction coefficient vs load for compound C1 in dry and wet conditions ( $V_s = 1 \text{ m/s}$ ).

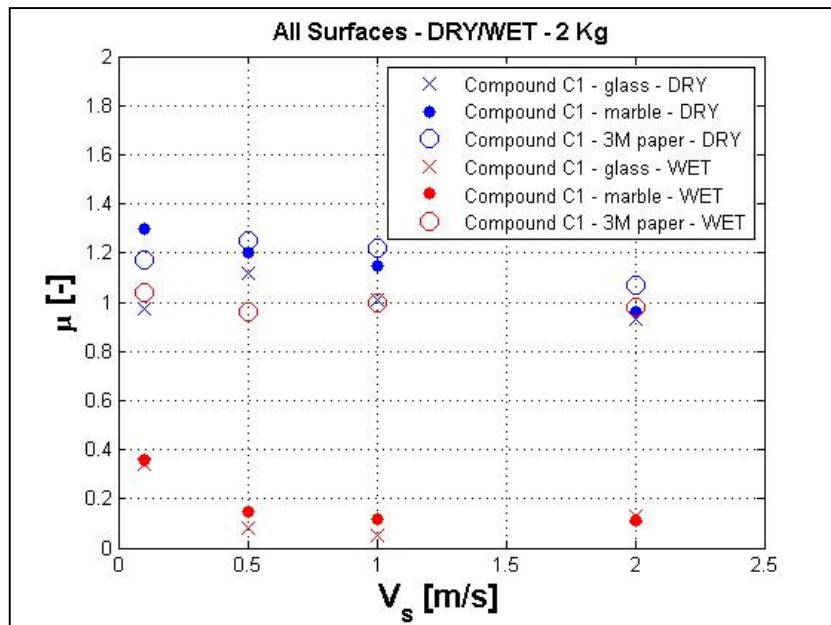


Fig. 5.15: Friction coefficient vs sliding velocity (step tests) for C1 compound on the three surfaces in dry and wet conditions ( $F_z = 20 \text{ N}$ ).

The friction coefficient between compound C1 and the three different surfaces (glass, marble and 3M tape) both in dry and in wet conditions is shown in figure 5.14 as a function of the applied load and in figure 5.15 as a function of the sliding velocity only for compound C1. As concerns wet contact, figure 5.14 and 5.15 allow to highlight the dissimilar covering of the micro-asperities operated by water on the different surfaces. While in dry conditions glass maximizes available contact area, in wet conditions it results easily covered by the water film, carrying consequently adhesion coefficient to a deep decrease. In wet conditions, when the load grows, the marble is almost constantly able to break the water film, thanks to its wavy profile. This explains the higher values of marble wet friction coefficient shown in figure 5.14 and 5.15 respect to glass ones. Increasing sliding velocity the specimens seem to float over water film and marble asperities lose their film-braking characteristics. The 3M tape, thanks to its high values of roughness, provides a clearer evidence of the cited film-braking phenomenon; as a consequence friction coefficients on this surface approach values near to the dry ones.

Moreover it is possible to see how friction coefficient in wet conditions always decreases as relative speed increases. Also this tendency was expected, in fact, as speed increases a boundary lubrication mechanism takes place.

In dry conditions the expected trend should be characterized by a peak at low speeds, followed by a marked decreasing tendency, but this is not always noticeable; it could be explained considering that, during a dry test, local contact temperature is non constant causing more scattered results than in wet conditions (almost isothermal because of the cooling effect assured by the water).

It is moreover possible to see how marble and glass, in wet conditions and at very low speed, show high values of the friction coefficient. At low speeds, in fact, no boundary lubrication mechanism takes place and the applied load is able to squeeze out the water interposed between rubber and micro rough surfaces allowing an almost dry contact of specimen on the countersurfaces. In dry conditions compound C1 exhibits a friction coefficient higher on marble than on glass; it is probably due to the fact that the loss of adhesion that marble wavy profile induces respect to the smoother glass surface is minor than the gain in micro-hysteresis generated by the cited wavy profile.

Figure 5.16 allows to examine the effects of rubber visco-elastic properties on friction. In particular, figure 5.16 shows a comparison between the compounds C1 and C3 in terms of step tests results concerning friction variation as a function of sliding speed on glass both in dry and in wet conditions.

In this figure it is possible to notice that dry friction coefficient for the pair C3-glass is always higher than the one for the pair C1-glass. The same happens for the low speed wet friction coefficient. At higher speed, in wet conditions, C1 and C3 compounds exhibit friction coefficients practically coincident.

This behaviour of the compounds in dry conditions could be explained considering that glass is a smooth surface on which the adhesion contribution is predominant, so in this case, as said, rubber storage modulus plays a key role. Figure 5.17 shows storage modulus curves of both compounds in the temperature range [-20, 20] °C. Applying WLF on glass surface, for which asperities wavelength is large enough to be considered into the metre order of magnitude, allows to consider the WLF output equivalent temperature close to ambient one. At common tyres working temperatures, compound C1 shows higher  $E'$  value, that identifies this compound as harder than C3 one. It explains the lower attitude of compound C1 to maximize contact area and, finally, the global lower value of friction coefficient. At low speed, it is possible to highlight how

compound C3 shows a wet friction coefficient on glass higher than the one of compound C1 in dry conditions.

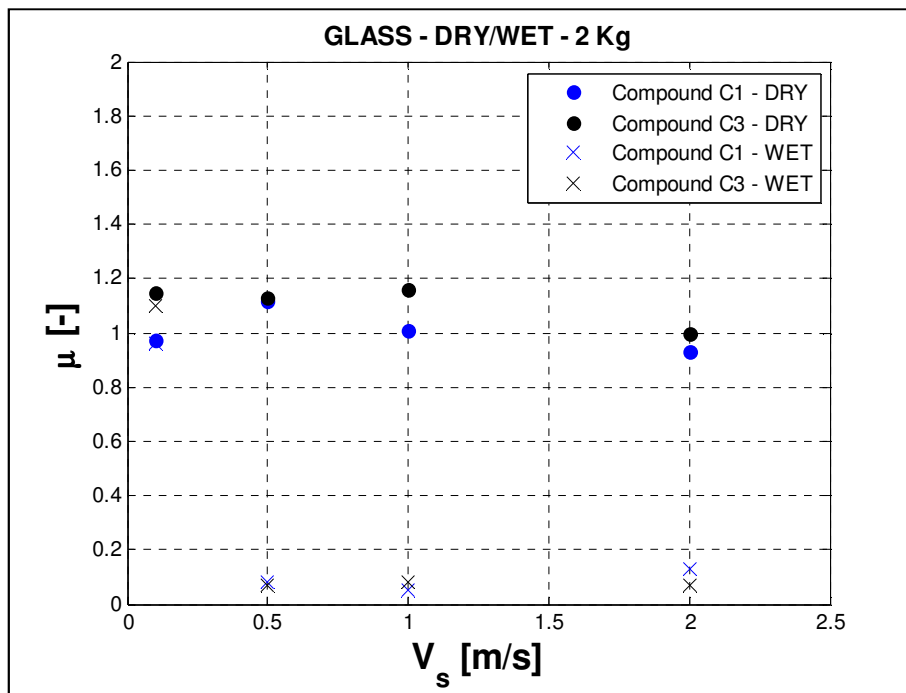


Figure 5.16 - Friction coefficient vs sliding velocity (step tests) for the three compounds on glass in dry and wet conditions ( $F_z = 20$  N).

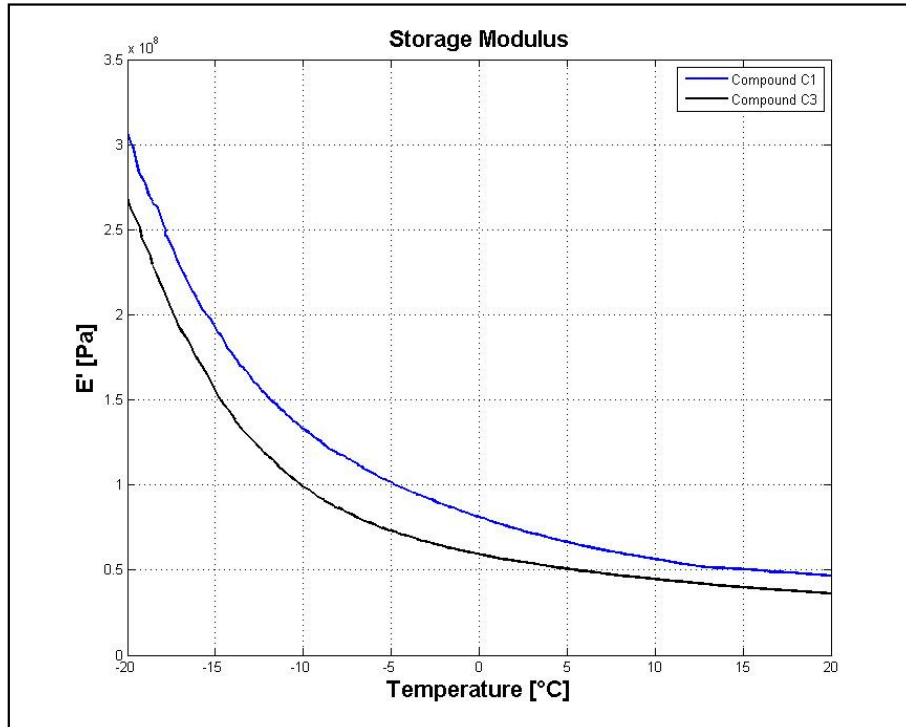


Figure 5.17 - Storage Modulus  $E'$  for compounds C1 and C3.

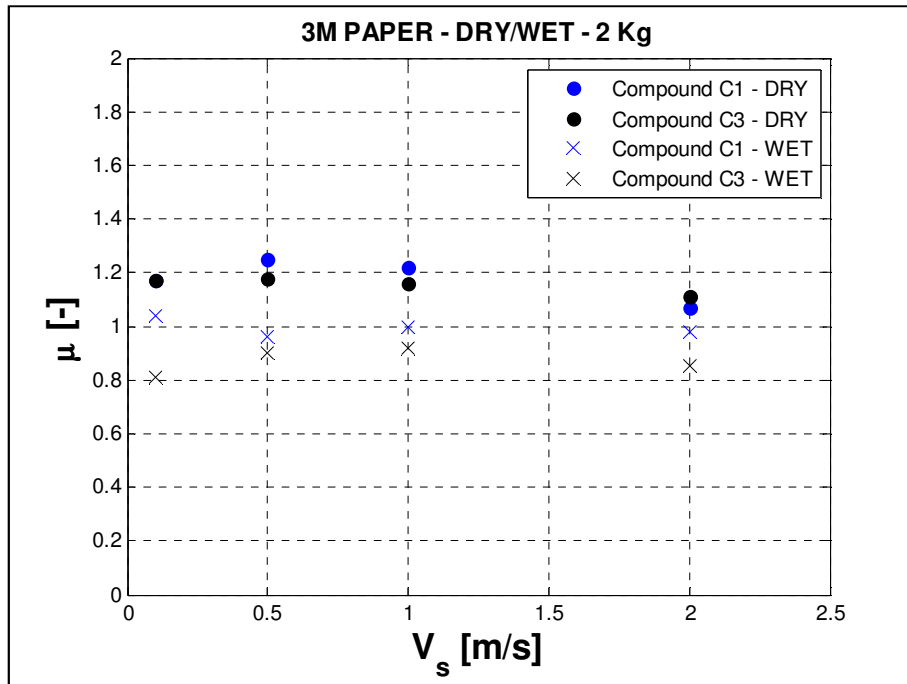


Figure 5.18 - Friction coefficient vs sliding velocity (step tests) for C1 and C3 compounds on 3M tape in dry and wet conditions ( $F_z = 20$  N).

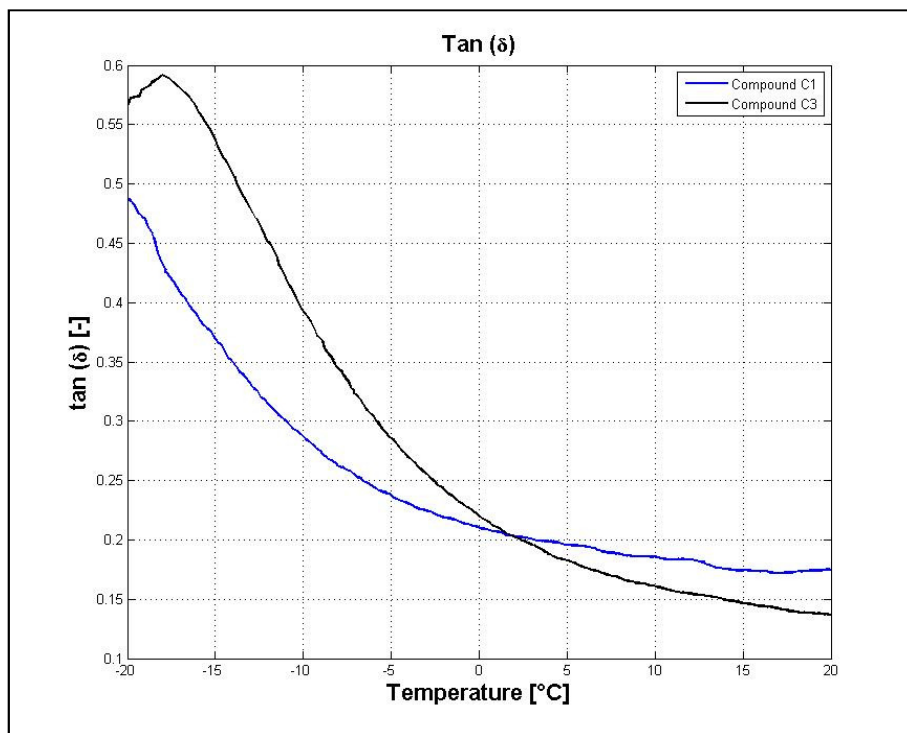


Figure 5.19 - Tan( $\delta$ ) curves for compounds C1 and C3.

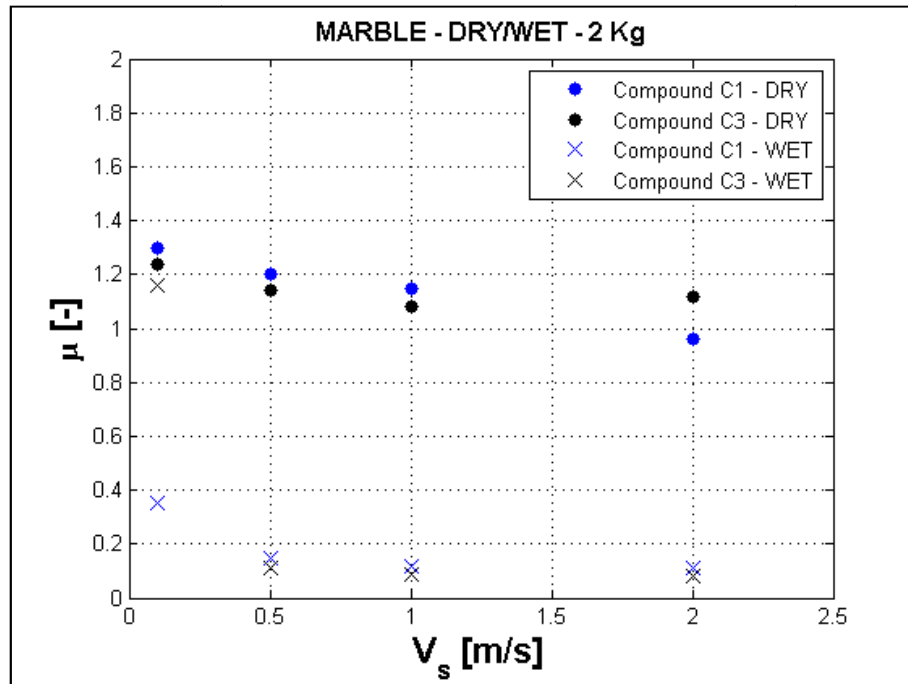


Figure 5.20 - Friction coefficient vs sliding velocity (step tests) for C1 and C3 compounds on marble in dry and wet conditions ( $F_z = 20$  N).

Figure 5.18 shows step tests results in terms of friction variation as a function of sliding speed on 3M tape both in dry and in wet conditions, comparing the two compounds C1 and C3.

It is possible to notice an intersection between the two curves: in dry conditions, at sliding speeds lower than the one corresponding to the intersection, compound C1 shows a friction coefficient higher than C3; after the intersection, the compounds invert their reciprocal friction attitude. This behaviour is in good agreement with the  $\tan(\delta)$  curves trends showed in figure 5.19; calculating from equation (5.11) WLF output temperature variation over 3M surface for a sliding speed of 1m/s:

$$\Delta T = 8 * (\log_{10}(V_s / \lambda)) = 8 * (\log_{10}(1 / 0.00005)) \approx 34.4^\circ C \quad (5.13)$$

Roughly speaking, starting from an average working temperature estimated in about  $35^\circ C$  (i.e. measured ambient temperature =  $25^\circ C$  + estimated temperature increase in the contact zone and in dry condition =  $10^\circ C$ ), the final output temperature will be close to  $0^\circ C$ , and then in the neighbourhood of the thermal range in which the trends show the crossing.

As regards marble behaviour (Fig. 5.20), characterized by a slightly rough surface, the contemporary superposition of adhesion and hysteresis mixes viscoelastic effects, increasing the difference between the compounds at high  $V_s$ , at which compound C1 results low-performing both from  $E'$  and from  $\tan(\delta)$  point of view. Low marble micro-roughness, finally, is not as able as 3M paper to break water film, but produces wet friction results better than the ones generated by almost totally flat glass surface.

### 5.4.2 Adhesion Model

Adhesive friction, regarded as being the primary contributor when a rubber block slides over a smooth unlubricated surface, is usually pictured as being due to molecular bonds between the rubber chains and the molecules of the track.

For this reason a satisfying modelling of such friction mechanism cannot exclude the knowledge of the complex phenomena concerning chemistry of polymers and molecular physics. With the aim to reproduce the functionalities between adhesive friction and the main variables influencing it (i.e. sliding velocity  $V_s$ , contact pressure  $p$  and temperature  $T$ ), a model which takes into account both the approach of Le Gal and Klüppel [83] and the one of Momozono and Nakamura [84] has been adopted:

$$\mu_{ADH} = \frac{F_{ADH}}{F_N} = \frac{\tau_s}{p} \frac{A_C}{A_0} \quad (5.14)$$

in which, from Le Gal's model,

$$\tau_s = \tau_{s,0} \left( 1 + \frac{E_\infty / E_0}{\left( 1 + \left( \frac{v_c}{V_s} \right) \right)^n} \right) \quad (5.15)$$

and, from Momozono's model, the ratio of the real actual contact area  $A_c$  to the apparent contact area  $A_0$  is approximated by

$$\frac{A_C}{A_0} = \frac{2}{\sqrt{m_2 \pi}} \frac{F_N}{A_0 E} = \frac{2}{\sqrt{m_2 \pi}} \frac{p}{E} \quad (5.16)$$

Thanks to the experimental campaign illustrated in the previous paragraphs, performed using a pin on disk machine and discussed also in [36][37], it has been possible to identify the parameters of Le Gal's model most difficult to define, i.e. the interfacial shear strength  $\tau_{s,0}$ , the critical velocity  $v_c$  and the viscoelastic dissipation parameter  $n$ .

The adhesion variations with sliding velocity are explicit in the model, while the thermal effect is modelled by means of the variation induced by temperature in rubber dynamic modulus  $E$ . Glassy region modulus  $E_\infty$  and rubbery region modulus  $E_0$  have been identified by means of the visco-elastic characterization tests;  $m_2$  is the second profile moment of the probability distribution function of the track (equivalent to the rms slope), has been computed elaborating road data in accordance with the ASME B46.1.

It is relevant to highlight that frequency effect acting on rubber for sliding phenomenon in the field of adhesive friction estimation is taken into account considering the only micro roughness profile, as a consequence of the superposition principle previously described. Adhesion expression is actually able to model frictional interactions arising at micro-roughness level; identified parameters values take into

account of micro-hysteretic effects and indentation phenomena highlighted in the above cited experimental tests.

### 5.5 Hysteresis Model

The modelling of the hysteresis starts from the expression of the power dissipated by a rubber block that slides with speed  $V_s$  under a vertical load  $F_z$  over a generic macro-rough surface. Because of the complexity of the real track surface, each elementary volume of the deformed compound block is subjected to a local stress/strain field (variable with the time) resulting in a dissipated power, due to the visco-elastic behaviour of the polymers.

In general, considering the volume  $V_{TOT}$  of the elementary tread element, it is possible to express the dissipated power  $W_{diss}$  at time  $t$  as:

$$W_{diss}(t) = \int_{V_{TOT}} w(x, y, z, t) dV = \int_{V_{TOT}} \left( \sigma_1(x, y, z, t) \frac{d\varepsilon_1}{dt}(x, y, z, t) \right) dV \quad (5.17)$$

in which  $w(x, y, z, t)$  represents the dissipated power in each point of the deformed elementary volume at time  $t$ .

Hypothesizing the  $V_s$  constant in the sliding over a single asperity, each stress/strain cycle can be considered as performed in a period equal to

$$T_0 = \frac{\lambda_{MACRO}}{V_s} \quad (5.18)$$

The average value of dissipated power must be thus evaluated over such this time period:

$$w(x, y, z) = \frac{1}{T_0} \int_0^{T_0} w(x, y, z, t) dt \quad (5.19)$$

In the same time period, considering  $V_s$  and  $F_N$  as constant, the global power dissipated in the elementary volume, can be expressed as:

$$W_{diss} = F_T V_s = \mu F_N V_s = \mu p A_0 V_s \quad (5.20)$$

in which  $p$  represents the average contact pressure in the nominal elementary area  $A_0$ , equal to  $(\lambda_{MACRO})^2$ . In this way, the balance between global and local dissipated powers is:

$$\mu p A_0 V_s = \int_{V_{TOT}} \left( \frac{1}{T_0} \int_0^{T_0} \sigma_1(x, y, z, t) \frac{d\varepsilon_1}{dt}(x, y, z, t) dt \right) dV \quad (5.21)$$

For [85], it can be written:

$$\frac{1}{T_0} \int_{T_0}^{T_0} \sigma_1(x, y, z, t) \frac{d\varepsilon_1(x, y, z, t)}{dt} dt = \frac{1}{2} \alpha \varepsilon_1^2 E \tan(\delta) = \frac{1}{2} 2\pi \frac{1}{T_0} \frac{\sigma_1^2}{E} \tan(\delta) = \pi \frac{V_s}{\lambda_{MACRO}} \frac{\sigma_1^2}{E} \tan(\delta) \quad (5.22)$$

allowing to formulate the final hysteretic friction expression:

$$\mu = \pi \frac{\tan(\delta)}{\lambda_{MACRO} E} \frac{\int_{V_{TOT}} \sigma_1^2 dV}{pA_0} \quad (5.23)$$

In order to estimate this friction coefficient, knowing polymer characteristics, road wavelength and input variables, it is necessary to provide the stress  $\sigma_1^2$  in each point of the discretized elementary tread volume, and, in particular, of the stress components along x, y and z directions. Although many authors have proposed formulations able to estimate stress distributions and contact area extension [86][87], a multi-dimensional approach did not result able to satisfy the real-time requirements and the low computational loads that the applications for which the model has been developed need. Thanks to the studies of Y. A. Kuznetsov [88][89][90], it is possible to calculate the stress state induced in a rubber elastic body by a periodic sinusoidal perfectly rigid indenter in sliding contact with it.

Once determined the radius of curvature  $R_s$  of the road sinusoidal indenter at the apex

$$R_s = \frac{1}{\left( \left( \frac{2\pi}{\lambda_{MACRO}} \right)^2 (R_{aMACRO}) \right)} \quad (5.24)$$

it is possible to estimate by means of Kuznetsov formula, the half-length  $N$  of the contact area (Fig. 5.21) as a function of the radius  $R_s$ , of the average contact pressure  $p$  in the nominal area  $A_0$ , of the rubber dynamic modulus  $E$  calculated taking into account of the working conditions acting on the examined elementary volume and of the macro asperity wavelength:

$$N = \frac{l}{\pi} \sin^{-1} \left( \frac{\pi}{l} \sqrt{\frac{4pR_s(1-\nu^2)}{\pi E}} \right) \quad (5.25)$$

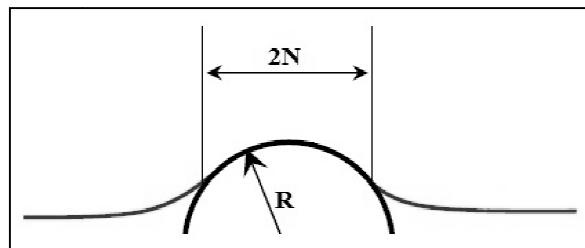


Fig. 5.21 - Detail of the contact between sinusoidal asperity apex and tyre tread.

Kuznetsov's method for planar stress calculation can be used to determine the three-dimensional field starting from the vertical planes  $xz$  (with sliding velocity) and  $yz$  (without sliding velocity) shown in figure 5.22 and 5.23, localized under asperity apex. The model does not need the direction of the sliding velocity on each asperity as an input because the orientation of the elementary volume adapts automatically to it, considering  $x$  axis parallel to  $V_s$ . In this way the only cinematic input is the modulus of the sliding velocity and it is taken into account by means of the frequency effect that it has on rubber for WLF law and on adhesion for the functionality discussed in the respective submodel.

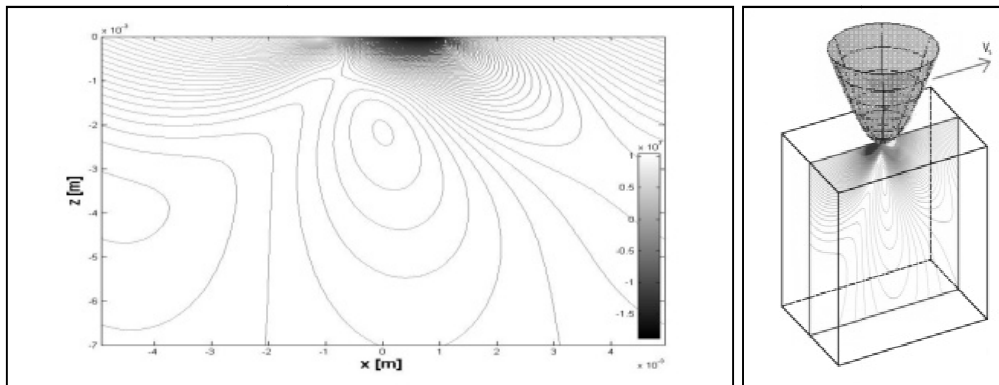


Fig. 5.22a -  $\sigma_{1x}$  distribution in the  $xz$  plane, localized as shown in figure 5.22b, under a pressure of 125 KPa.

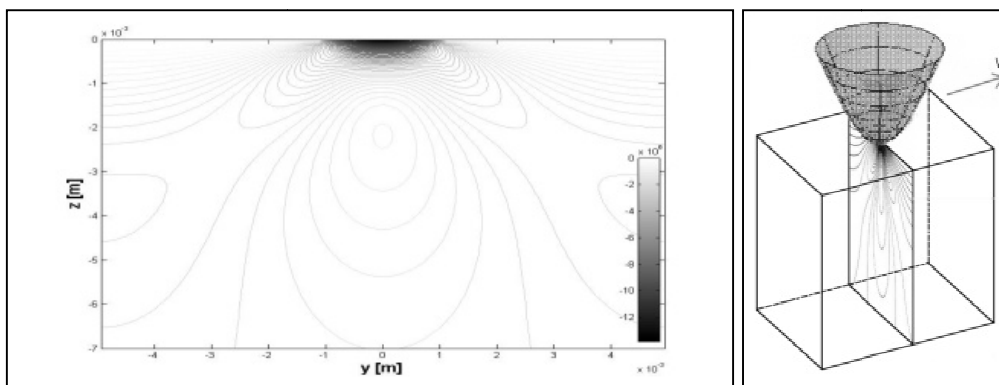


Fig. 5.23a -  $\sigma_{1y}$  distribution in the  $yz$  plane, localized as shown in figure 5.23b, under a pressure of 125 KPa.

The strong relationship between adhesive and hysteretic friction is taken into account by means of the Kuznetsov's parameter  $K$ , that is supposed to be equal to the adhesive friction coefficient. In figure 5.24 the effect of adhesion on the stress profile is shown: the increase of the adhesive component causes a progressive asymmetrisation of the stress field in the direction of the sliding.

Applying Kuznetsov equations in the plane  $xz$ , it is possible to calculate the stress components  $\sigma_{1x}$  and  $\sigma_{1z}$  generated by the sliding indenter, noticing in figure 5.22a the compressive tangential stress localized before the indenter and the traction state behind this last, due to the presence of the adhesive contribution. Because of the self-orientation of the elementary volume, it is possible to state that in the plane  $yz$  sliding velocity components are absent: it means that applying Kuznetsov's equations in this

plane, imposing K equal to zero, the perfectly symmetric tangential stress so obtained can be considered as an estimation of the stress component  $\sigma_{1y}$ .

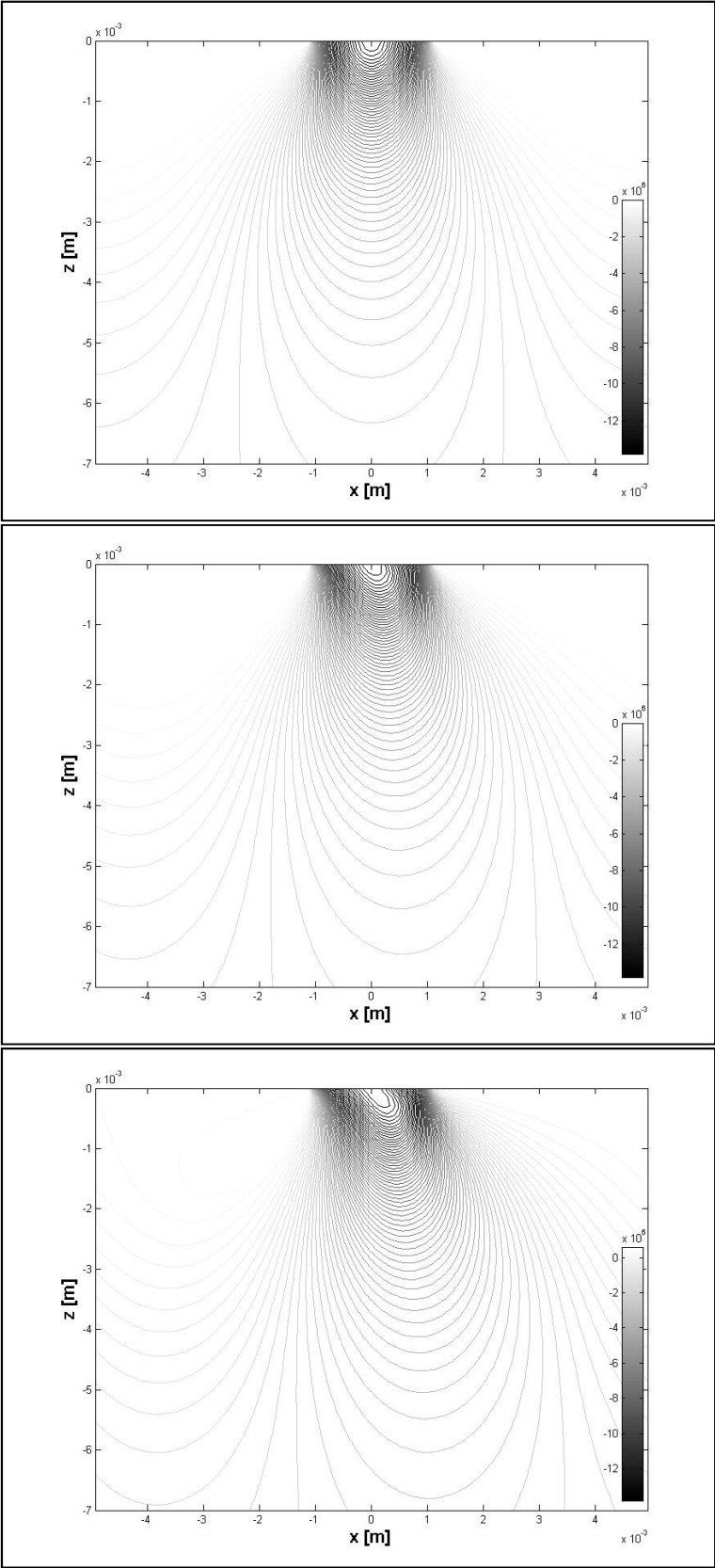


Fig. 5.24 -  $\sigma_{1z}$  in the xz plane for adhesion coefficient (Kuznetsov's parameter K) equal to 0, 0.5 and 1 under a pressure of 125 KPa and a sliding velocity of 1 m/s directed from left to right.

With the aim to extend the bi-dimensional results to the whole three-dimensional elementary volume (Fig. 5.25), the planar components have been scaled, reducing stress entity at increasing distance from asperity apex, by means of a quadratic function identified on the basis of proper tests carried out with a commercial FEM solver (Fig. 5.26). The tests, characterized by high computational loads, confirmed the goodness of the stress fields calculated much more easily with Kuznetsov's equations, that, once implemented, represent an optimal solution for the needs of a real time physical model.

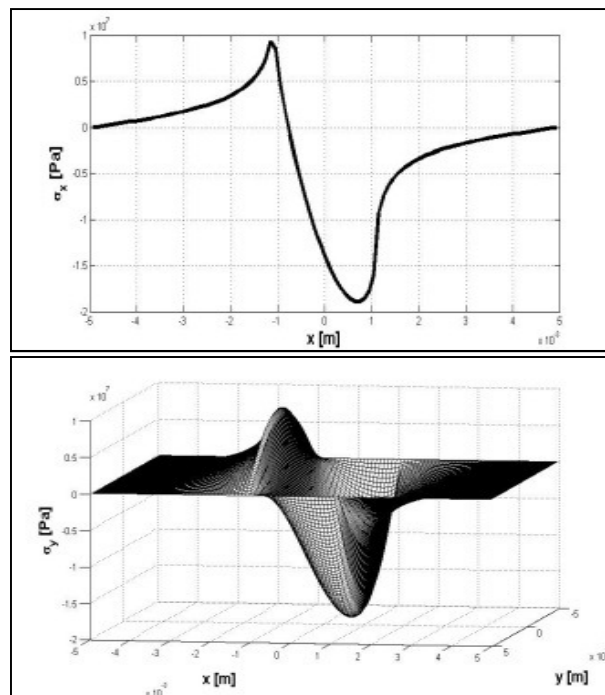


Fig. 5.25a -  $\sigma_{1x}$  stress in the xz plane for K=1 under a pressure of 125 KPa and a sliding velocity of 1 m/s directed from left to right.  
Fig. 5.25b - Extension of  $\sigma_{1x}$  to the whole 3D elementary volume.

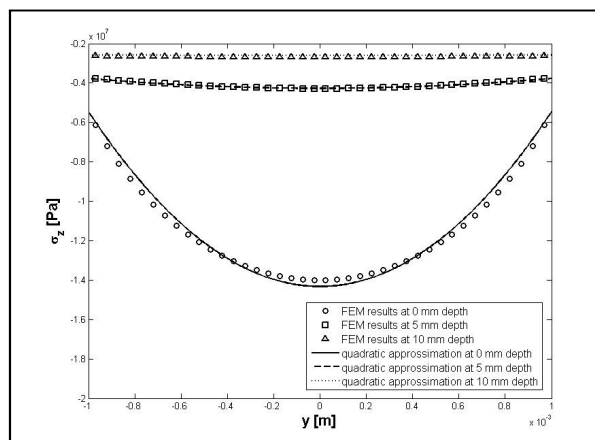


Fig. 5.26 -  $\sigma_{1z}$  stress resulted from FEM simulations along y direction compared with the quadratic function chosen to extend the planar stress field in the 3D tread volume.

Information coming from finite elements analysis allowed, moreover, to neglect the stress components  $\tau_{xy}$ ,  $\tau_{xz}$  and  $\tau_{yz}$ , because their contribution to power dissipation is about one order of magnitude lower than the one relative to components  $\sigma$ . Finally, indentation tests confirmed the contact zone extension provided by Kuznetsov by means of the parameter N.

The knowledge of the described stress components allows to calculate the numerical integral extended to the elementary tread volume of equation 5.23. At this aim, the volume has been discretized in 200 nodes along x and y and 50 along z; this number represents an optimal trade off between the stability of the results and the computation performances.

Further developments will regard the possibility to express explicitly the micro-hysteretic dissipations, taking into account the indentation phenomena involving micro-roughness, replicating the same procedure employed for the macro-roughness.

## 5.6 Results And Validation

The connection of the presented grip model with both an interaction model [21][51] - able to provide for each steptime the contact pressure and the sliding velocity at which each tread element interacts with the corresponding asperity - and with a thermal model [chapter 4] - whose output is tread temperature in the same steptime, supposed to be uniform in the neighbourhood of the contact area with a single road asperity - gives the possibility to estimate friction arising at tyre/road interface as the sum of the adhesive contribution (equation (5.14)) and of the hysteretic one (equation (5.23)).

As shown in figures 5.27, 5.28 and 5.29, the model is able to give a coherent response to input variations; in particular, in figure 5.27 is reported a 3D plot obtained for a passenger GT tyre, whose compound has been fully characterized, sliding at different  $V_s$  and  $p$  over a road profile, employed also for the analyses discussed in the following, described by macro and micro sinusoids having  $\lambda_{\text{MACRO}} = 9.9$  mm,  $R_{a \text{ MACRO}} = 0.8$  mm,  $\lambda_{\text{MICRO}} = \lambda_{\text{MACRO}}/100$  and  $R_{a \text{ MICRO}} = R_{a \text{ MACRO}}/100$ , chosen basing on a similarity conception introduced by Persson [53].

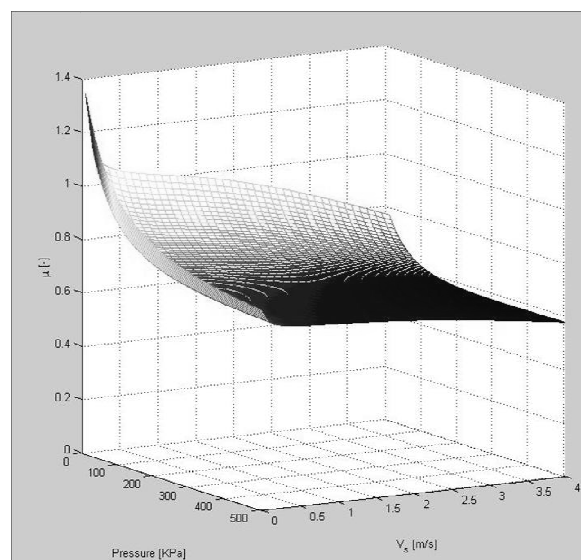


Fig. 5.27 - 3D plot reporting friction coefficient for a passenger GT tyre as a function of sliding velocity  $V_s$  and contact pressure  $p$ , at a tread average temperature of 25 °C.

Figures 5.28a and 5.28b highlight friction dependence on temperature and on rubber Storage Modulus. As expected for polymers, SBR is highly sensitive to working temperature, confirming that the selection of the proper thermal range in which the compound will work is the main key factor for the grip performances maximization. A variation of 30°C has a drastic effect on friction of such kind of tyres; different tyre models, characterized by different design and compounds might have an optimal working range centred on other temperatures: lower, for common passenger tyres, in order to ensure safety in the widest range of weather conditions, or higher, for racing tyres operating under high tangential loads and able to reach high levels of friction and wear. For what concerns the effect of a variation of the storage modulus, the response of the model reproduces the expected physical behaviour, describing the decrease of the frictional attitude of the tyre consequently to an increase in  $E'$  value, that generates a lower indentation level and a less adhesive interaction.

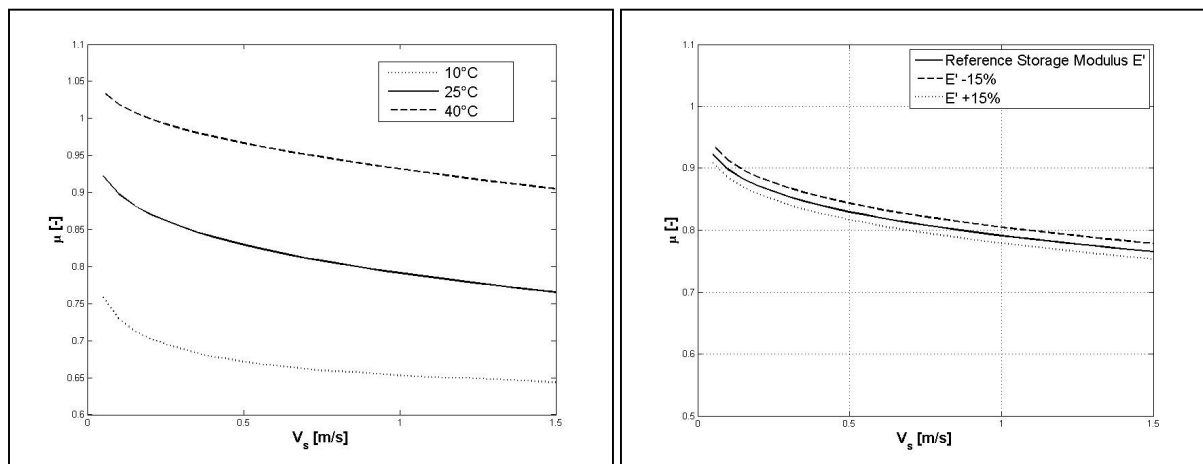


Fig. 5.28a - Passenger GT tyre friction coefficient as a function of sliding velocity  $V_s$  for different tread Temperatures, under a pressure of 300 kPa.

Fig. 5.28b - Influence of Storage Modulus at 25 °C and 300 kPa.

Figure 5.29 allows an analysis of the effect that a variation in road roughness has on friction and in particular on its two components; as noticeable in the plot and as expectable from the analytical modelling, a decrease in  $R_a$  index (triangle marker) is responsible of an increase of the adhesion (no-line curves), due to the fact that a smoother micro profile allows an optimization of the available contact area, in which a greater number of intermolecular bonds can be created. On the other side, roughness decrease is responsible for a lower indentation degree, for a consequential lower dissipated power and finally for a decrease of the hysteretic friction component. The differences in rubber structure make a compound more or less capable to maximize adhesion rather than hysteresis; the analyzed tyre, for its structure and compound, has shown a high dependence of adhesion from roughness, with the final result that global friction manifested an increasing trend with decreasing roughness. A different tyre, characterized by different  $E'$  and  $E''$  moduli, could have shown opposite tendencies due to a major indentation attitude.

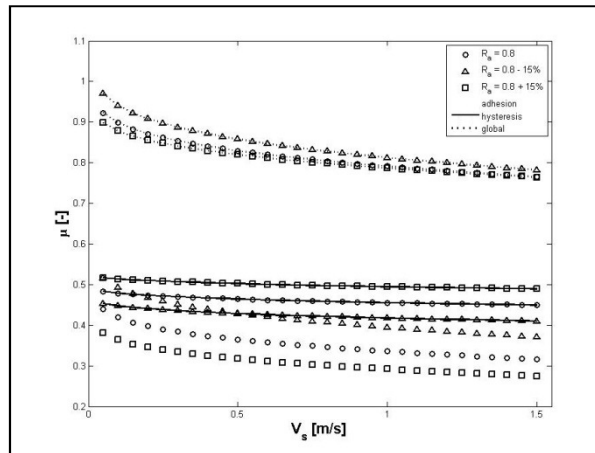


Fig. 5.29 - Passenger GT tyre friction components as a function of sliding velocity  $V_s$  for different roughness indices, at 25 °C and under a pressure of 300 kPa.

An experimental activity has provided a comparisons between model simulations results and friction tests carried out with the described pin on disk tribometer (Fig. 5.9).

In the experimental campaign, aimed to investigate hysteretic contribution to friction, the disk has been covered with 3M anti-slip tape ( $R_a = 27 \mu\text{m}$ ) and its surface has been kept wet during the contact by means of a thin water film.

The role played by water is to avoid the adhesive interaction between rubber and 3M tape, depurating global friction from this contribution. In this way road asperities, able to break the water film, reach the specimens surface and indent it, isolating the pure hysteretic contribution.

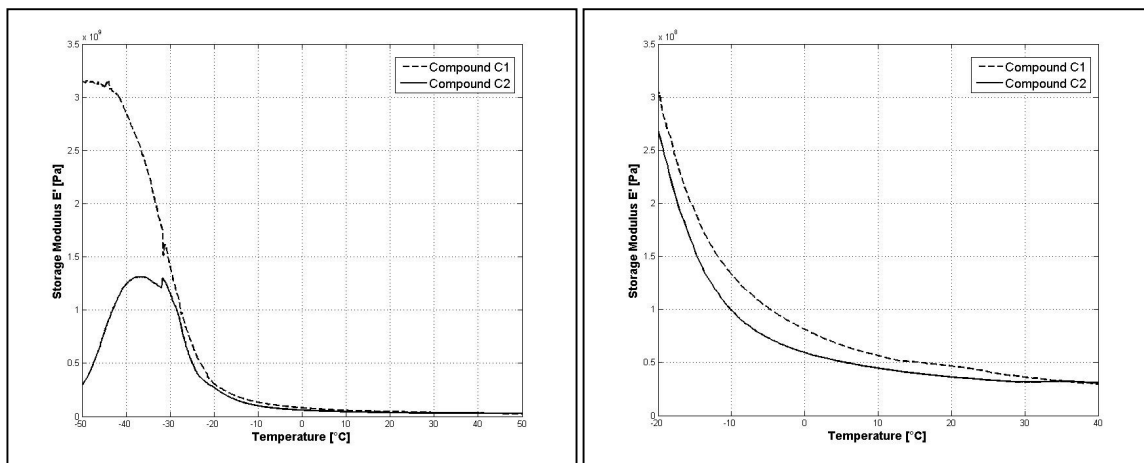


Figure 5.30a - Passenger tyre  $E'$  thermal characterization data - Frequency 1 Hz.

Figure 5.30b - Detail in the tyre thermal working range.

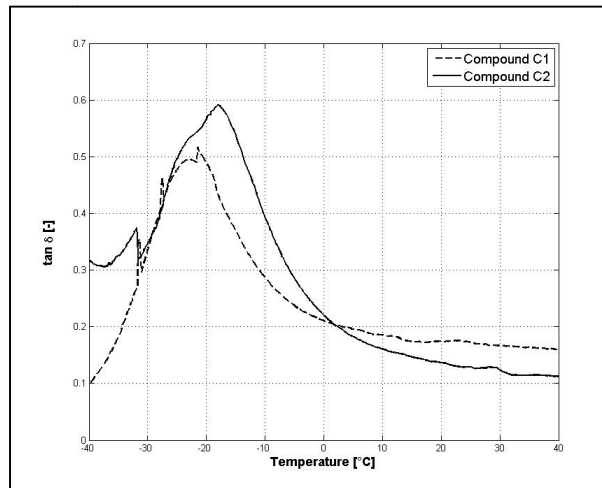
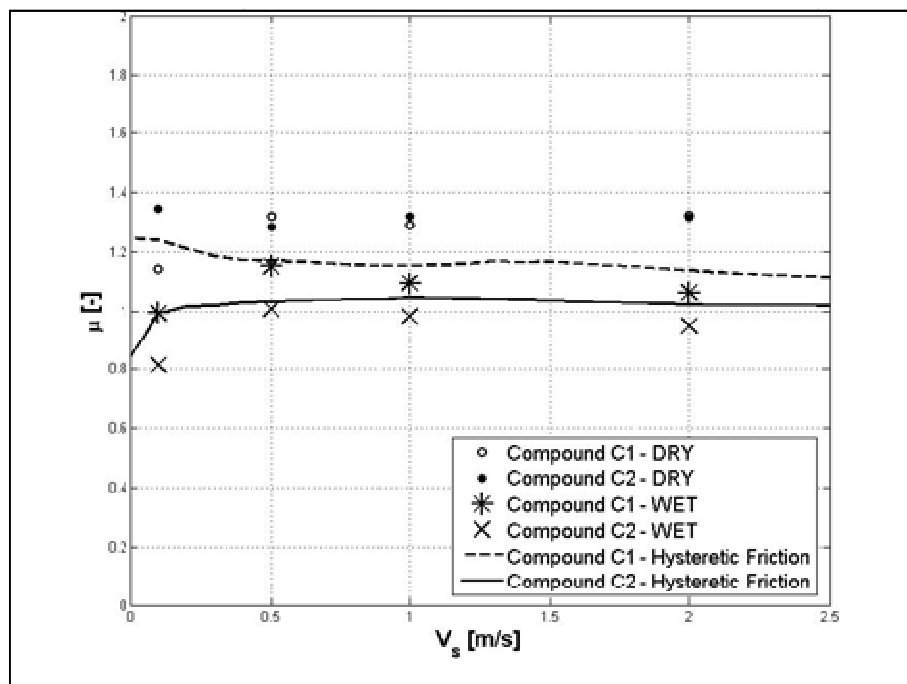


Figure 5.31 - Passenger tyre  $\tan(\delta)$  thermal characterization data - Frequency 1 Hz.

The specimens employed in the tests have been extracted from two slabs made up of two different compounds (C1 and C2) and characterized by means of DMA procedures, obtaining  $E'$  (Fig. 5.30) and  $\tan(\delta)$  (Fig. 5.31) curves as a function of temperature. Hysteresis model outputs have been compared with the experimental points highlighting a good correspondence for both compounds; in figure 5.32 some results of the validation campaign are shown.



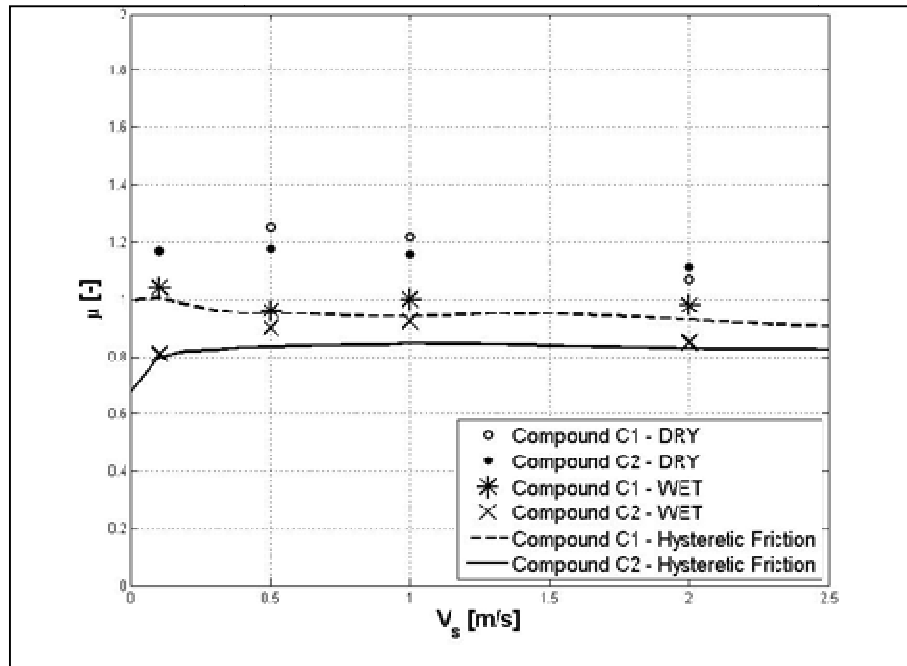


Figure 5.32a - Estimated Hysteretic Friction compared with experimental points for 3M tape at 40 °C - Vertical Load 1 kg.  
Figure 5.32b - Vertical Load 2 kg.

The figures report as points the mean value of the friction coefficient for the two compounds in both dry and wet conditions. The applied load is constant (1 kg, 2 kg) and the sliding velocity assumes the values 0.05, 0.5, 1, and 2 m/s. Hysteretic friction trend provided by the model under the same operating conditions (i.e. applied load, surface roughness, rubber characteristics) is plotted as a function of  $V_s$  in order to highlight the good accordance with the experimental results. As said above, differences between dry and wet experimental results can be attributed to the substantial reduction of adhesive component of friction in wet conditions.

## 6. Tyre Models Integration

### 6.1 Introduction

Models, procedures and methodologies discussed in the previous chapters are able to describe and analyse different aspects of the phenomena concerning with tyre/road interaction, but their cooperation can constitute an even more powerful instrument to extend the comprehension of such complex theme.

In the following paragraphs different possibilities to make the models cooperate will be described, highlighting the main features of each combination and discussing its results in detail. A general overview of the developed models and procedures is reported in figure 6.1, in which it is possible to observe the connections that link the models, providing different solutions of employment.

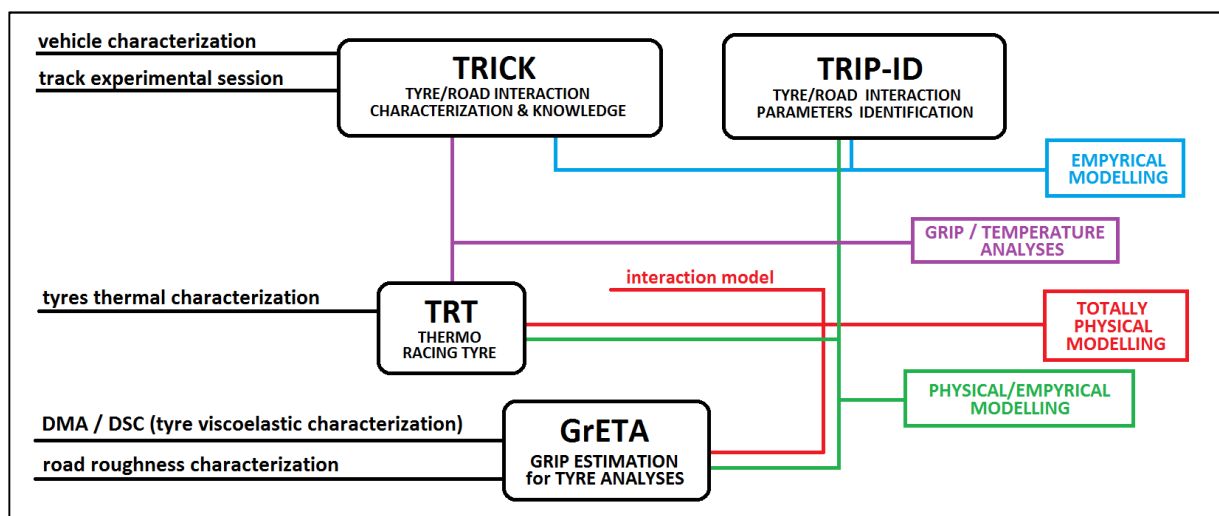


Fig. 6.1 - Models Integration Solutions.

### 6.2 TRICK & TRIP-ID

TRICK (chapter 2) and TRIP-ID (chapter 3) have been developed with the initial aim to increase the confidence that car-makers can feel respect to the Magic Formula adoption in virtual drive modelling and in vehicle dynamics models employed for predictive performance analyses. One of the main advantages of the tool is the possibility to validate Pacejka coefficients provided by tyre-makers or even do without their contribution, identifying coefficients after a proper vehicle characterization and a specific track session.

The weak points of the initial MF parameters set identified with bench procedures by tyre company, highlighted by data analysis, are the followings:

- Too high grip performances in longitudinal and lateral interaction;
- Too low cornering stiffness in front tyres;
- Lower than real attitude to allow to the driver to bring back the vehicle to a stability condition after the adherence limit crossing;
- Absence of grip and stiffness variations due to thermal effects.

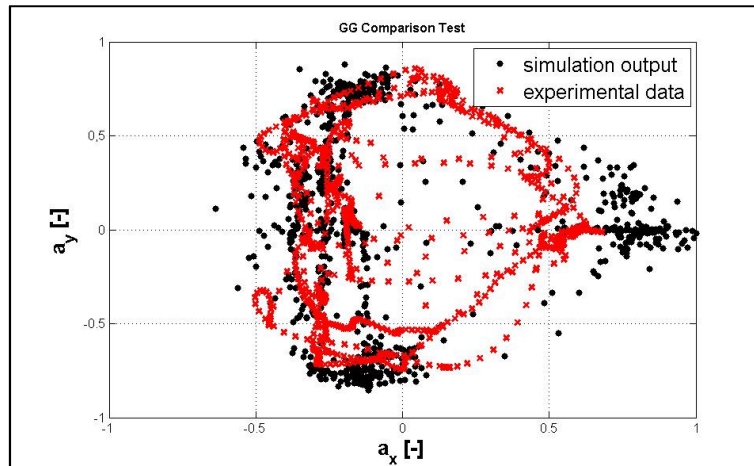


Fig. 6.2 - G-G diagram realized both with experimental data and with results of a simulation performed with starting MF tyre parameters set.

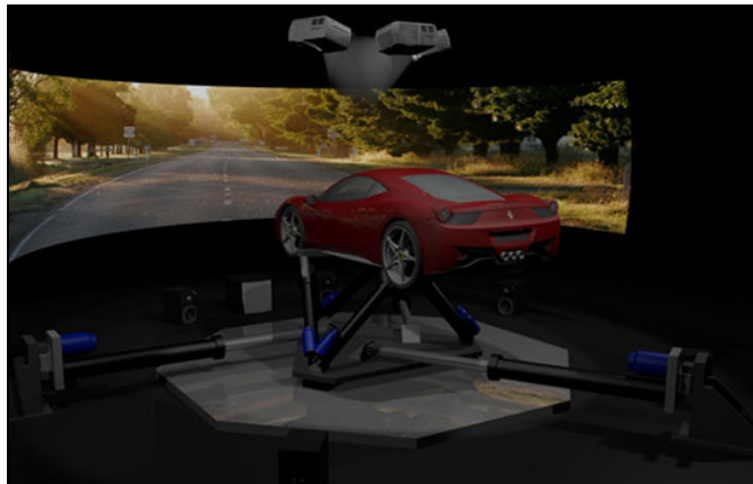


Fig. 6.3 - A 3D render depicting the driving simulation system recently developed by Ferrari S.p.A..

In figure 6.2 a G-G diagram, a classical and simple instrument employed to evaluate global vehicle performances [9] is plotted (again in nondimensional form, for the already cited industrial confidentiality agreements), comparing on a reference track lap the measured vehicle accelerations with accelerations exported as an output from a commercial highly validated vehicle simulation model<sup>13</sup> employed in virtual driving

<sup>13</sup> Ferrari has installed a motion platform named DiM (Driver in Motion) designed by VI-grade and engineered and manufactured by Saginomiya. The vehicle model is used to calculate the real-time response to the driver's inputs; the vehicle motions are processed and transformed into feasible platform motions by VI-MotionCueing; actuator movement is eventually calculated on the fly by platform controller.

The 9DOF platform consists of a small-size hexapod mounted on top of a planar frame moving on a very smooth sliding surface by means of an efficient and innovative system based on air pads and magnetic pads. The hexapod has been designed to produce consistent pitch/roll rotations and Z translations, as well as small X/Y translations and Yaw rotation. The consistent X, Y and Yaw movements required to generate the feeling of vehicle accelerations on the driver are instead generated by the base tripod. The cueing strategy harmonizes the system motion extending the motion envelope and separating low and high frequency contributions, which makes this type of motion platform suitable for both vehicle dynamics and ride studies (source: <http://www.vehicledynamicsinternational.com>).

simulation environment (Fig. 6.3) that adopted for the specific session the tyre MF parameters set provided by the tyre maker. In this last model the vehicle has been fully characterized from geometrical and constructive point of view, components mass has been carefully weighted, suspensions and steering chain have been modelled by means of KnC elasto-kinematic curves and control systems act in the same way of the real vehicle ones thanks to HIL or SIL implementation techniques; so, the system differs from the real vehicle mainly for tyre modelling, and the described activities focus on its evaluation.

High grip levels reached by bench tested tyres are often due to the fact that testing countersurface is abrasive paper (or rough material surfaces characterized by low macro-roughness), that is able to maximize contact patch effective area providing an interface surely better than the one that contact with real road allows.

The consequence of the grip overestimation is an improvement of the simulated vehicle performances respect to the real one, highlighted in figures 6.4 and 6.5 in terms of vehicle speed and lateral acceleration acquired in a lap sector. The correspondence between the compared data in each plot is not optimal as concerns time synchronization and manoeuvres reproduction because in both cases the vehicle has been driven by a human driver, obviously not able to perform the lap in the same identical way.

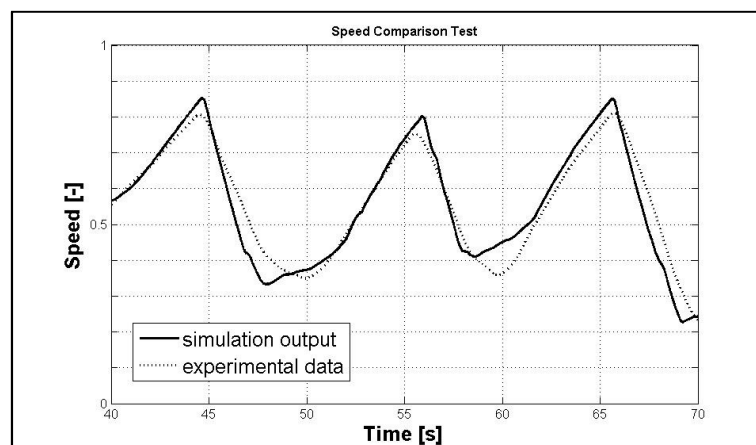


Fig. 6.4 - Detail of a lap speed profile comparison between experimental data and results of a simulation performed with starting MF tyre parameters set.

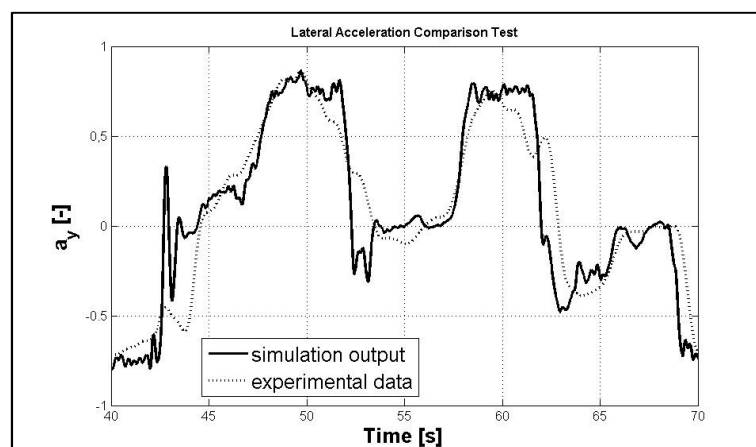


Fig. 6.5- Detail of a lap lateral acceleration profile comparison between experimental data and results of a simulation performed with starting MF tyre parameters set.

The employment of abrasive paper and of severe testing cycles causes, in addition to grip overestimation (and consequently to it), a continuous and massive heat generation at contact interface, that increases tyre temperature; as well known, one of the main effects that temperature has on tyres is stiffness variation [1][76] (increasing temperature causes decreasing stiffness), particularly evident in front tyres, commonly thinner, narrow and less thermally inert. Figure 6.6 focuses on these considerations, highlighting the unsatisfying results obtained as concerns front slip angles employing the starting tyres parameters set; the unbalances caused by slip angles misestimations act on the whole vehicle under/oversteering tendency [91], reported in figure 6.7 by means of the understeer gradient index [10].

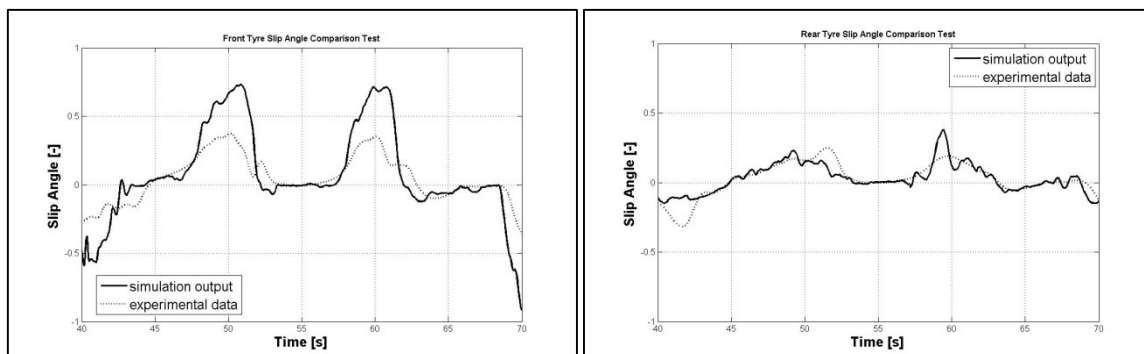


Fig. 6.6 - Detail of the front (left image) and rear (right image) tyre slip angles, both from experimental data and from outputs of a simulation performed with starting MF tyre parameters set.

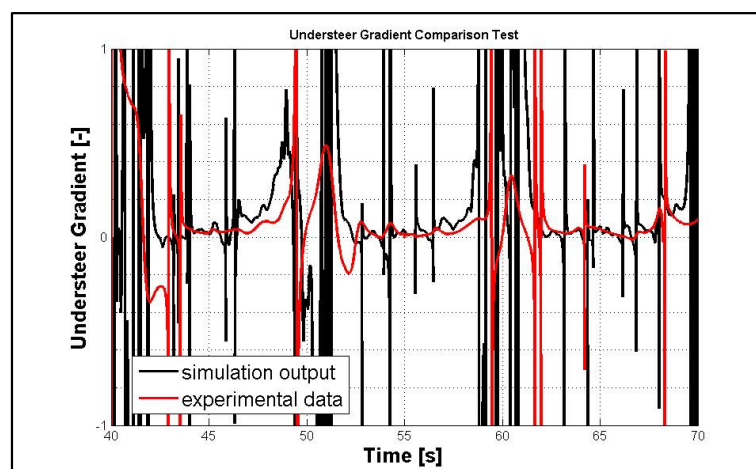
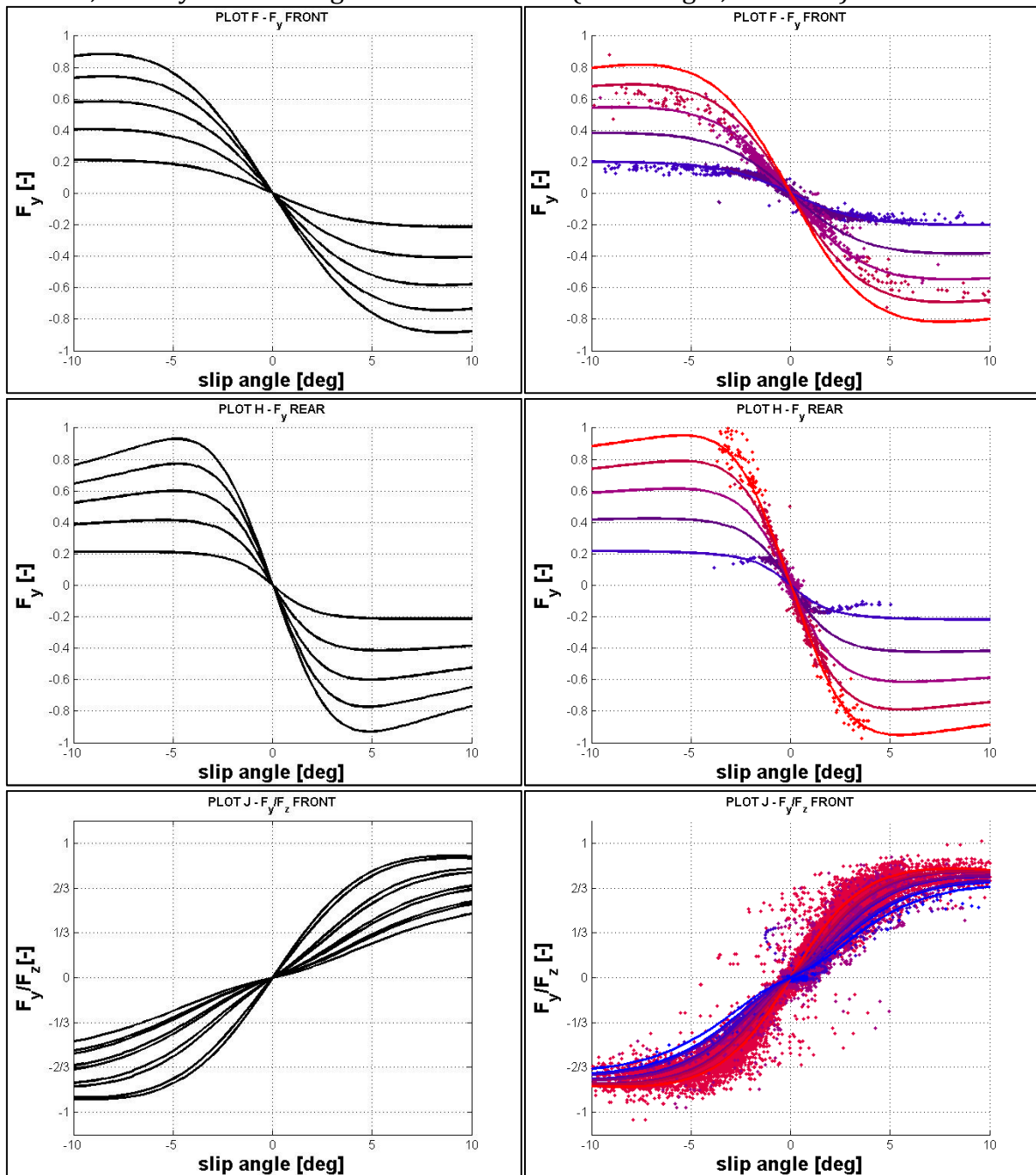


Fig. 6.7 - Detail of the understeer gradient calculated both with experimental data and with outputs of a simulation performed with starting MF tyre parameters set.

The identification of the optimal parameters set performed by means of TRIP-ID procedure allows also to solve the vehicle driveability problems observed at simulator linked with the shape of the tyre starting set; the cited lower than real attitude to allow to the driver to bring back the vehicle to a stability condition after the adherence limit crossing is due to a double reason: an excessively "peaky" trend of lateral interaction curves and a too sharp decrease of cornering force in combined interaction at increasing values of slip ratio. The improvement that the characterized tyres have represented as concerns the cited effects can be observed in figures 6.8, that compare starting set pure

and combined lateral interaction curves (on the left, in black) with the optimal identified set ones, already shown in figures 3.10 and 3.12 (on the right, coloured).



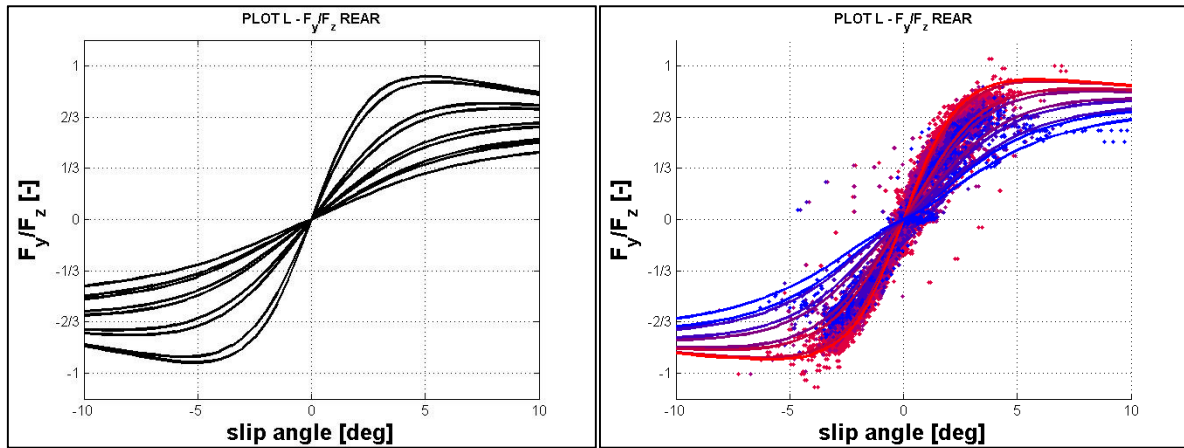


Fig. 6.8 - PLOT F left: starting set, front tyre, pure lateral interaction. -  
 PLOT F right: identified final set, front tyre, pure lateral interaction (Fig. 3.10). -  
 PLOT H left: starting set, rear tyre, pure lateral interaction. -  
 PLOT H right: identified final set, rear tyre, pure lateral interaction (Fig. 3.10). -  
 PLOT J left: starting set, front tyre, combined lateral grip. -  
 PLOT J right: identified final set, front tyre, combined lateral grip (Fig. 3.12). -  
 PLOT L left: starting set, rear tyre, combined lateral grip. -  
 PLOT L right: identified final set, rear tyre, combined lateral grip (Fig. 3.12).

It can be noticed that data collected during experimental session described in chapter 2 are able to provide information useful to modify properly the starting set, obtaining an identified set that results in good agreement with the drivers' requests (as analyzed referring to figure 6.8) and with the objective data already shown acquired equipping the real vehicle with measurement instruments; figures from 6.9 to 6.12 show the results of the simulations performed employing the new tyres set, comparing them with the ones relative to the starting set, plotted in figures from 6.2 to 6.6 and reported in small size on the left.

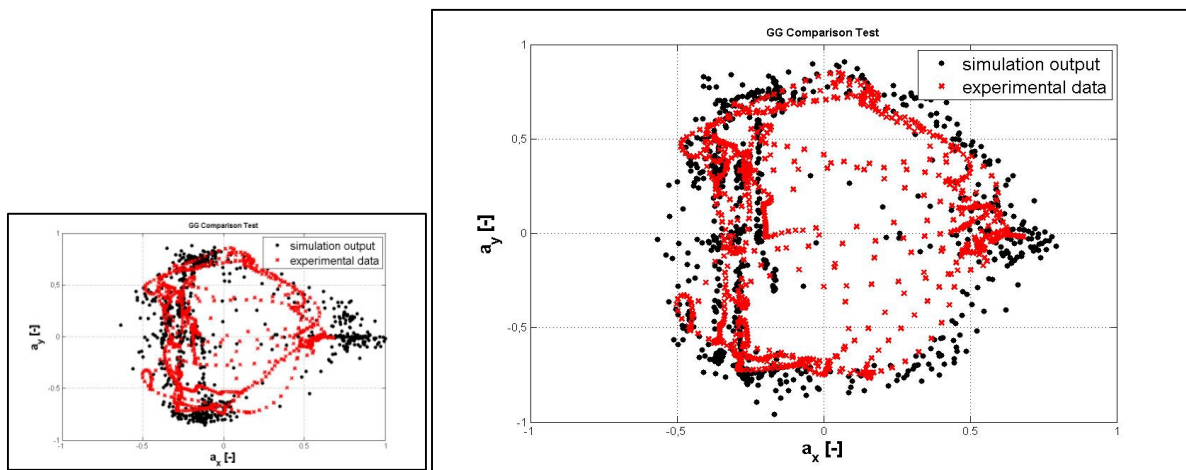


Fig. 6.9 - On the left, figure 6.2 in reduced size, reported for the sake of comparison; on the right, G-G diagram realized both with experimental data and with results of a simulation performed with the final identified MF tyre parameters set.

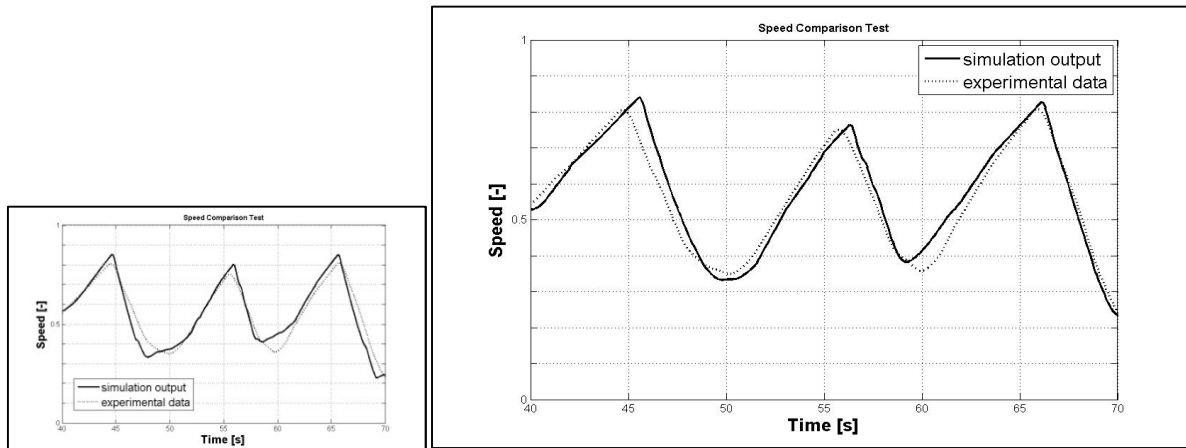


Fig. 6.10 - On the left, figure 6.4 in reduced size, reported for the sake of comparison; on the right, detail of the speed comparison between experimental data and results of a simulation performed with final identified MF tyre parameters set.

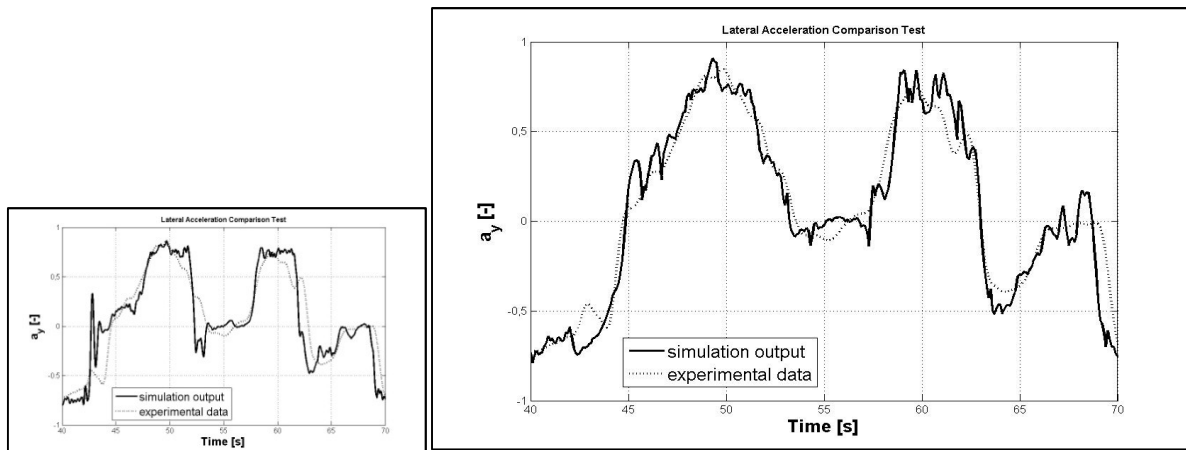


Fig. 6.11 - On the left, figure 6.5 in reduced size, reported for the sake of comparison; on the right, detail of the lateral acceleration comparison between experimental data and results of a simulation performed with final identified MF tyre parameters set.

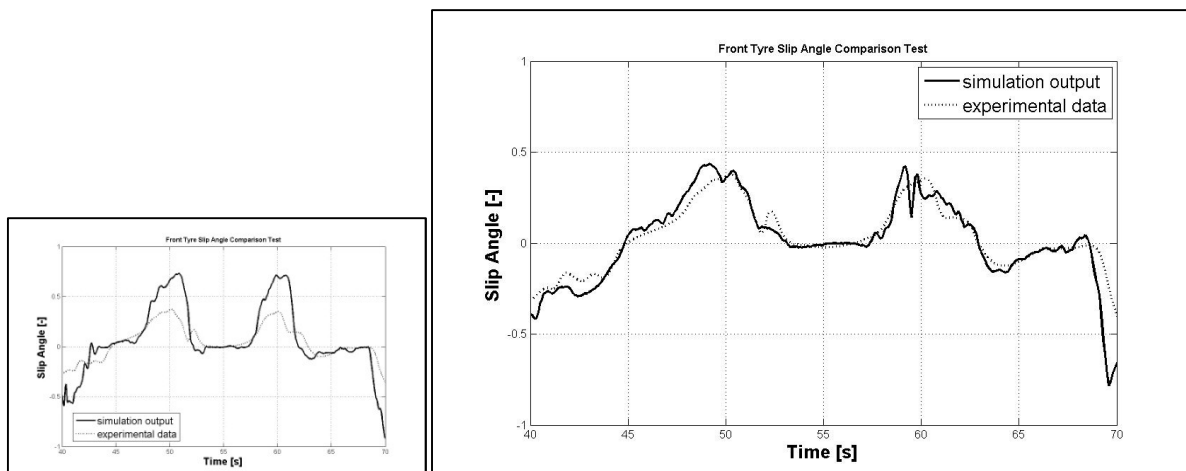


Fig. 6.12 - On the left, the first image of figure 6.6 in reduced size, reported for the sake of comparison; on the right, detail of the front tyre slip angle comparison between experimental data and results of a simulation performed with final identified MF tyre parameters set.

### 6.3 TRICK & TRT

TRICK (chapter 2) and TRT (chapter 4) have been successfully employed together, constituting an instrument able to provide tyre thermal analyses, useful to identify the range of temperature in which grip performances are maximized, allowing to define optimal tyres and vehicle setup. TRT characterization has been moreover a fundamental stage in the development of a tyre interaction model that takes into account frictional and thermodynamic phenomena observable during tyre working; in particular, test results relative to a GT sport vehicle will be reported in the following.

The test procedures adopted to characterize tyres, obtaining data useful to initialize properly the models, can be schematically divided in two main subcategories, destructive and non-destructive; to the first one belong:

- meridian plane section analysis

This kind of test consists in the observation and measurement of the thickness of the different layers constituting the meridian section; in figure 6.13 it is possible to distinguish tread layer, characterized by an evident and deep pattern, bulk layer, in which steel cord plies are clearly observable and inner liner, very thin and impermeable.

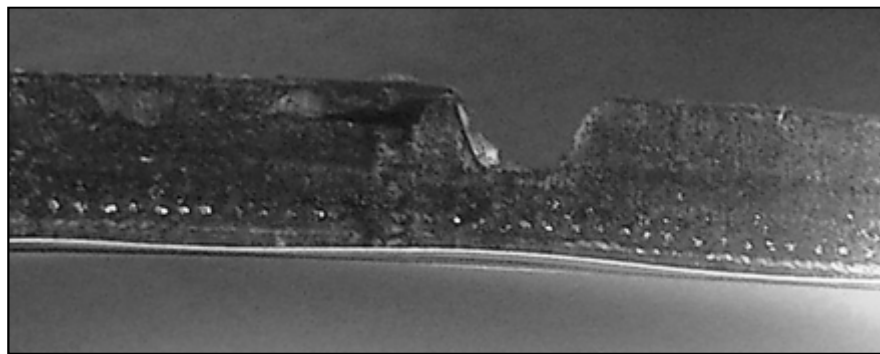


Fig. 6.13 - Detail of a tyre section cut along the meridian plane.  
Tread, plies and inner liner are distinguishable;  
a paper sheet, positioned for testing reasons, is visible at bottom surface.

- thermal conductivity and specific heat measurements

As described in chapter 4, tyre layers need to be characterized from thermodynamic point of view, focusing in particular on conductivity and specific heat measurements. Standard test procedure is carried out employing an Stabilite 2017 argon-krypton laser (Fig. 6.14a) that is pointed on the whole tyre or on specimens of each layer, emitting a beam of given power. Knowing specimen thickness and measuring temperature of the two surfaces by means of two thermographic cameras (a Phoenix by Flir, figure 6.14b and a Ti-45 by Fluke, figure 6.14c), it is possible to provide an effective estimation of the desired parameters, validated thanks to the comparison with tests carried out with a COND1 device, following certified procedures [92].

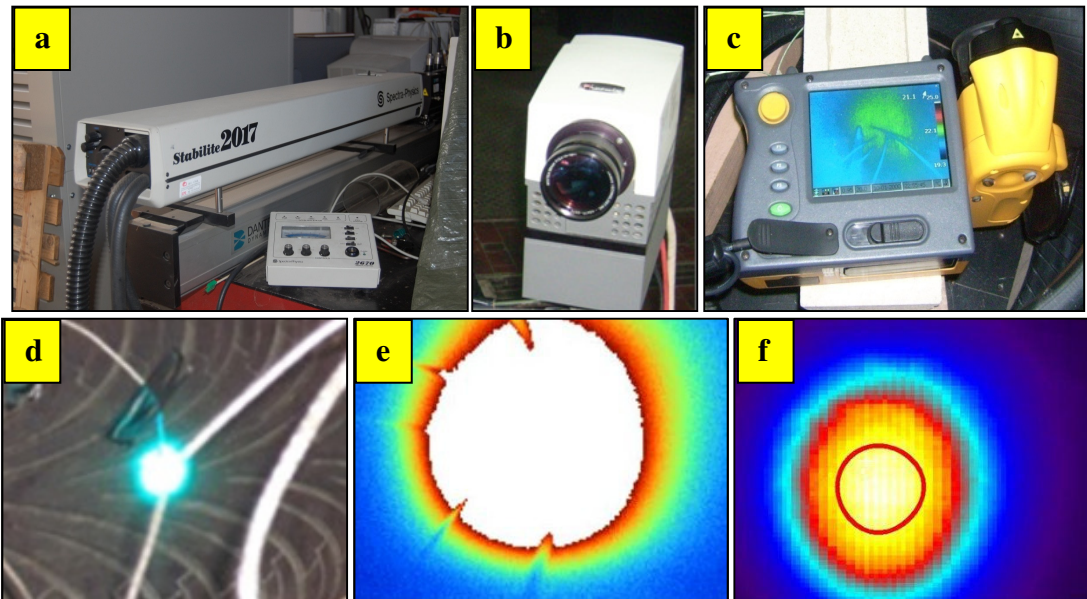


Fig. 6.14 - a: Stabilite 2017 argon-krypton laser. - b: Phoenix thermographic camera. - c: Ti-45 thermographic camera. - d: the laser spot on the tyre external surface. - e: a thermographic camera image of the laser spot on the tyre external surface. - f: a thermographic camera image of the laser spot on the tyre internal surface.

- DMA viscoelastic characterization

DMA has been described in paragraph 5.3.

Tests carried out on GT sport tyres have highlighted interesting aspects, in particular comparing results with common passenger tyres ones. Figure 6.15 shows that, as expected, sport tyres are characterized by lower storage modulus values in their optimal thermal working range (35 °C and over), that mean higher attitude to adhesion and to adapt to road asperities, optimising contact area, at the price of a lower wear resistance; passenger tyres are more stable and able to offer good adhesion levels also at very low temperatures, being adapt to the widest possible range of working conditions. Figure 6.16 reports in a clear plot the plausible reason of the so called "feeling the grip" phenomenon; GT tyres, differently from passenger ones, are characterized by a well distinct relative maximum at about 42 °C and by higher values of  $\tan(\delta)$  at the usual employment temperatures.

Remembering that DMA test has been carried out at 1Hz frequency, definitely different from common tread stress frequencies, a quick calculation, hypothesizing an average road macro-roughness wavelength equal to 0.01 m and an average sliding speed of 5m/s, allows to estimate the real tyre temperature at which the  $\tan(\delta)$  maximum can be experienced by the driver. Re-applying equation 5.13, it is possible to obtain:

$$\Delta T = 8 * (\log_{10}(Vs / \lambda)) = 8 * (\log_{10}(5 / 0.01)) \approx 21.6^{\circ}\text{C} \quad (6.1)$$

that, added to the starting 42 °C, gives a temperature of 63.6 °C, absolutely in accordance with the experimental value shown in the further analyses presented in the following.

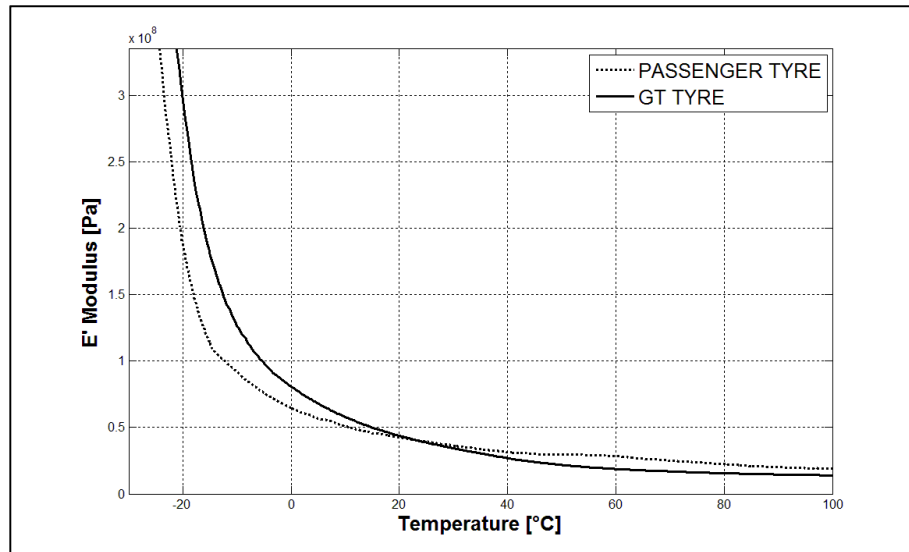


Fig. 6.15 - A comparison of storage modulus ( $E'$ ) between a common passenger tyre and a GT sport one.

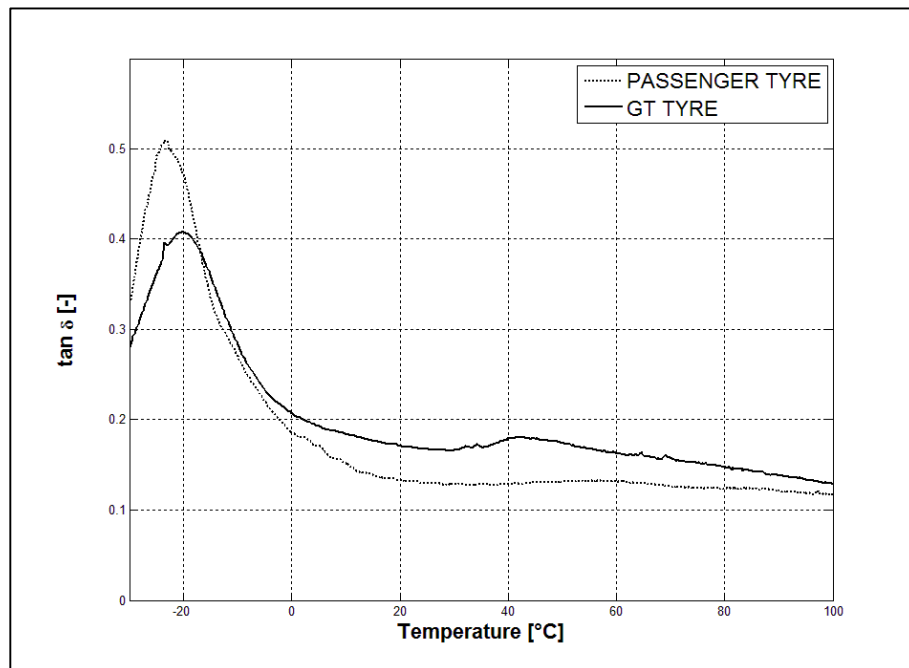


Fig. 6.16 - A comparison of  $\tan(\delta)$  between a common passenger tyre and a GT sport one.

- indentation test  
Described in paragraph 5.3.
- adhesion test  
Described in paragraph 5.4

The applied non-destructive testing procedures are:

- contact patch analysis

The test bench described in 4.4.4 has been employed to apply static vertical load on tested tyres, analysing contact patch extension and pressure distribution. It has been possible interposing pressure sensitive Prescale sheets between tyre

and flat steel countersurface, planning tests at different load, inflating pressure and camber angle. In figure 6.17 the results of a generic testing session on a 235x35 front tyre are reported and figure 6.18 summarizes the results of the 0-camber session, providing data analogous to the ones described in figures 4.11 and 4.12.

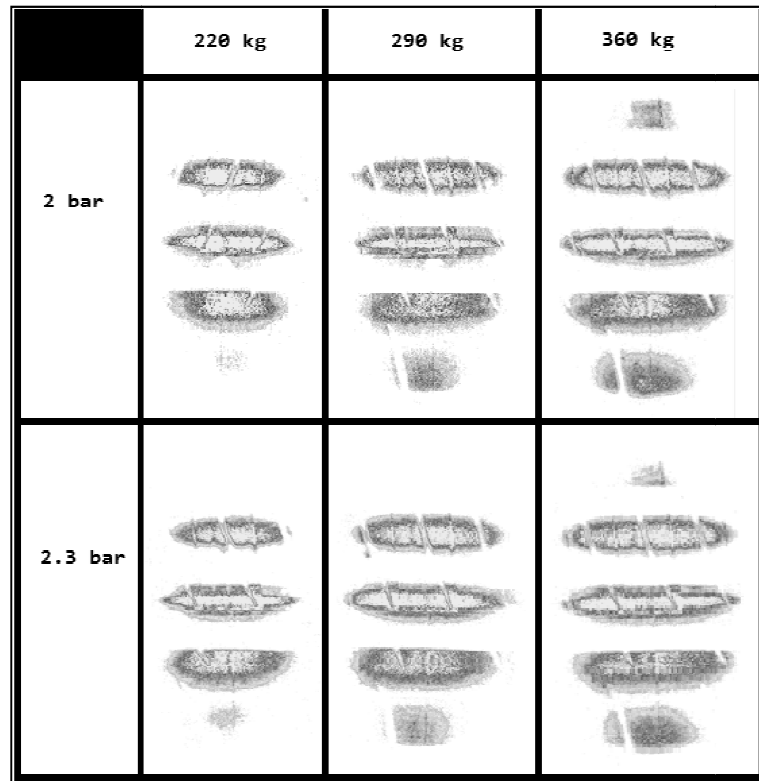


Fig. 6.17 - Scans of a GT tyre contact patch under different testing conditions at null camber angle. It is noticeable that at increasing load contact area increases, progressively inserting shoulders in the interaction zone; at high inflating pressure the central rib is more extended, while decreasing pressure the tyre tends to overload shoulders (Fig. 4.24).

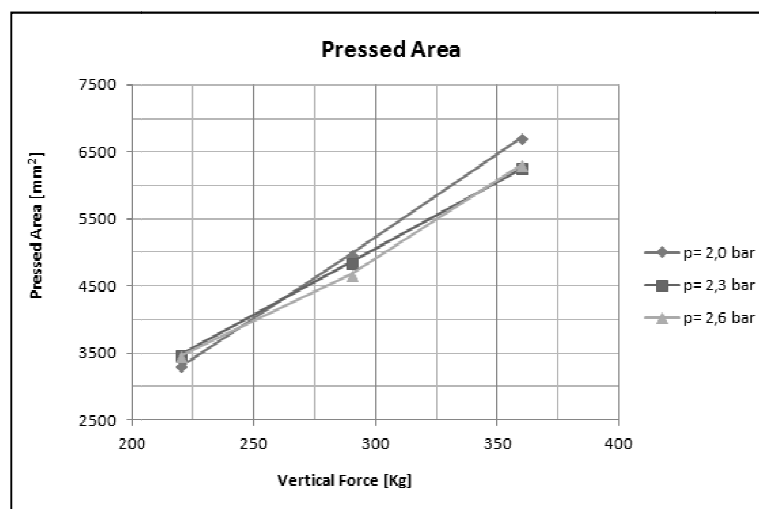


Fig. 6.18 - A diagram reporting contact patch area as a function of vertical force and inflating pressure, summarizing results highlighted in figure 6.17.

- SEL tests

Described in paragraph 4.4.5.

- track thermal tests

Specific thermal test session have been carried out following the procedure reported in table 2.3, developed with the aim to collect tyre data at different thermal conditions. In order to acquire tyre temperature, vehicle has been equipped with infrared sensors installed in the wheelhouses (Figure 6.19) and pointing on tread surface, whose signals have been acquired by Dewesoft hardware. Each tyre tread has been interested by two different measurements, particularly useful for front tyres, that, steering, could be characterized by discontinuous temperature profiles. In order to reduce such inconvenient, front sensors have been installed in correspondence of wheel centre, as shown in figure 6.20.

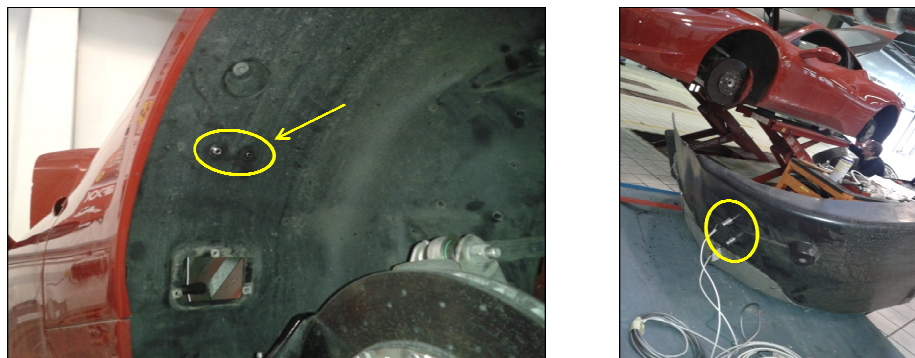


Fig. 6.19 - Infrared thermal sensors installation and localization inside vehicle wheelhouses.

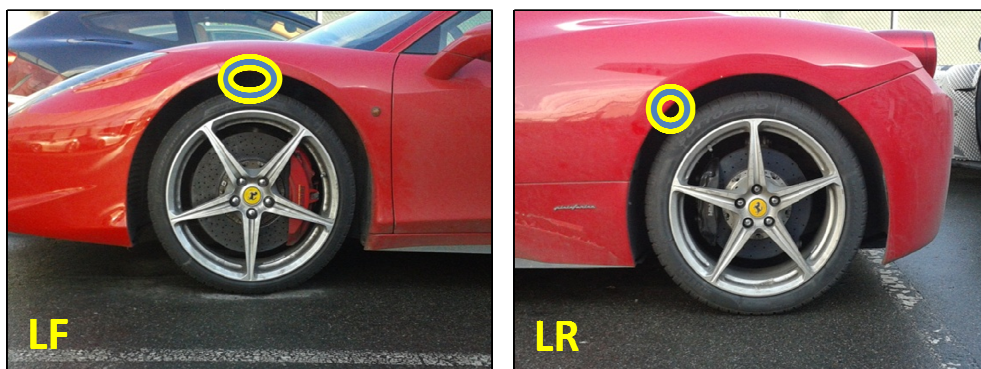


Fig. 6.20 - Position of thermal sensors at front and rear axles.

After having carried out a track experimental session (table 2.3), acquiring data useful to be processed by TRICK procedure, a "virtual telemetry" DATA matrix (table 2.1) has been generated.

Speed, slip, camber and force channels have been used as an input for TRT, whose results have been compared with measured surface temperatures (figure 6.21), obtaining good correspondence with available data and, very usefully for the grip analysis discussed in the following, an estimation of tyre bulk temperature.

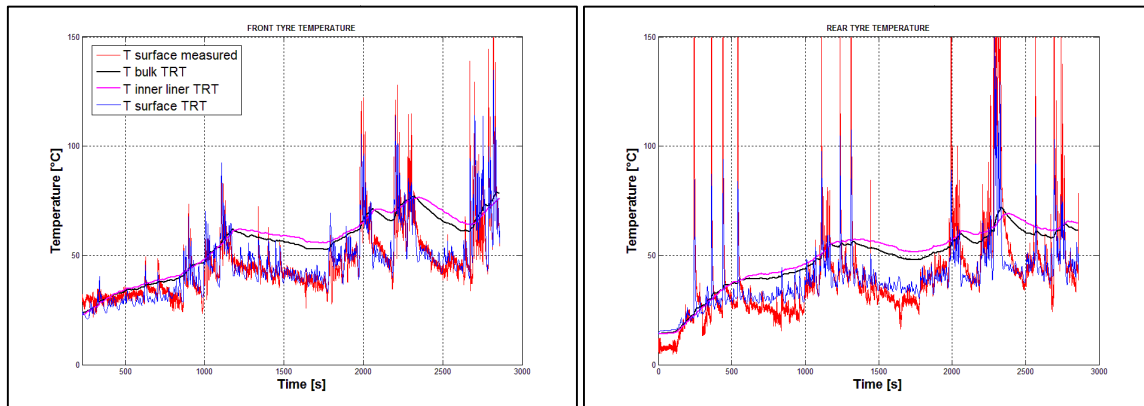


Fig. 6.21 - TRT results evaluation for front and rear tyres.

Common analyses concerning the relationship between tyre friction coefficient and temperature are based on the only thermal data experimentally available, id est tyre external (and in few cases, internal) surface temperature, measured with a great variety of methodologies. A typical correlation between lateral grip and measured temperature appears like the one shown in figure 6.22, from which very few information can be deduced.

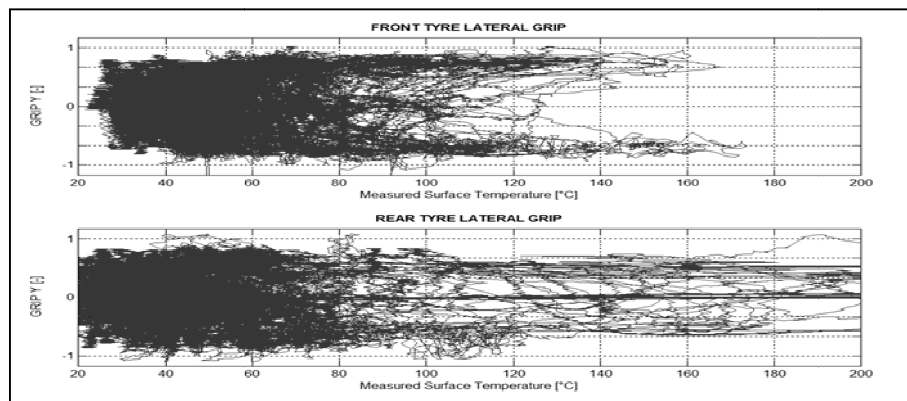


Fig. 6.22 - Front and rear lateral grip reported as a function of tyre measured surface temperature.

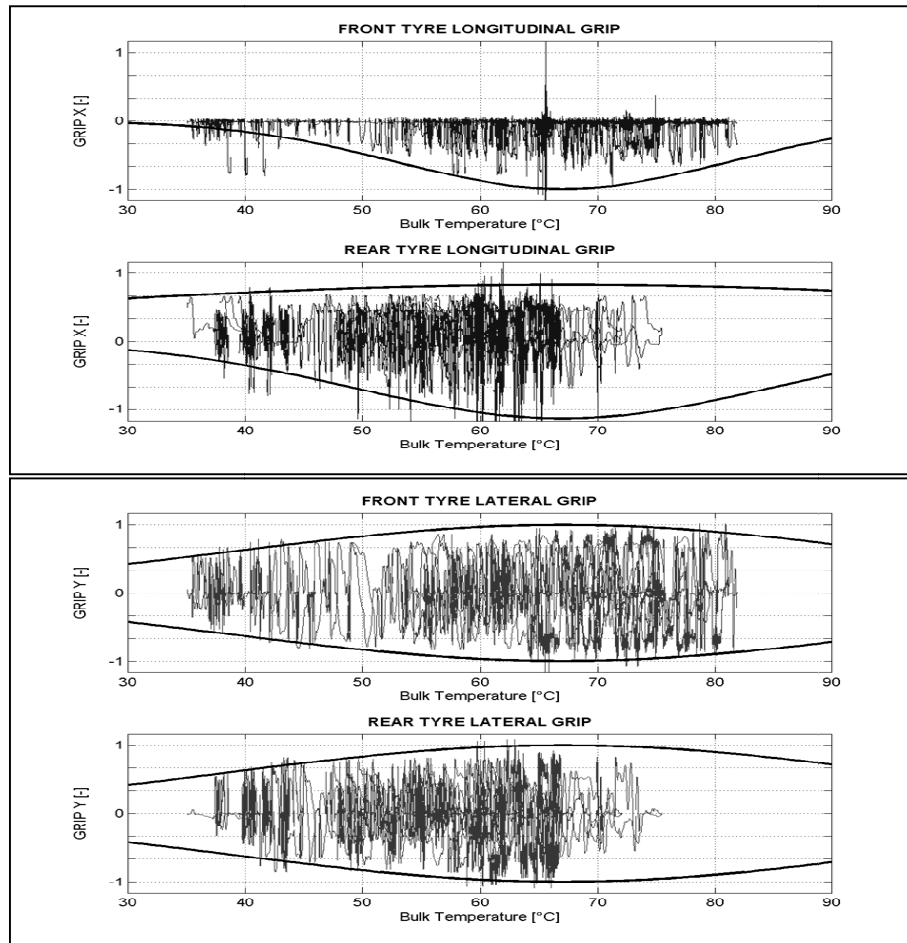


Fig. 6.23 - Front and rear grip reported as a function of tyre bulk temperature estimated by means of TRT. Bell shape curves have been drawn to highlight the trends.

Thanks to the availability of bulk temperature, it is possible to provide much more useful correlations, as the ones reported in figure 6.23, from which optimal thermal range can be identified. The reason for which bulk temperature offers better results can be attributed to the fact that surface temperature varies with very fast dynamics, not able to modify in a so short time polymers characteristics in order to have a response on the whole tyre frictional behaviour. Bulk temperature, on the other side, can be considered as the tread core temperature, more reluctant to fast variations and directly connected with rubber viscoelastic states. As a further validation of the described procedure, it can be noticed that temperature optimal value is in good agreement with the theoretical result provided in equation 6.1, confirming that thermal model can be employed as a predictive instrument to investigate on performance optimization strategies and that, on the other side, a proper knowledge of polymer characteristics can be a useful starting point to a better comprehension of tyre interaction dynamics.

#### 6.4 TRIP-ID - TRT - GrETA

Thermal and grip model can usefully cooperate, employing TRT output as an input for GrETA, that can be so used to introduce in Pacejka interaction model the dependence from temperature, tyre working variables, road roughness and compound characteristics.

The advantages coming from the interaction of these models can be summarized in the following three points, currently already exploited, but further application possibilities are clearly available:

- Prediction of tyre behaviour on different tracks of a racing championship, each one characterized by different road roughness (earlier measured) and weather conditions.
- Performance evaluation at compound characteristics variation, that allows to establish a dialog channel with tyre makers, leading tyre construction and compound development to the achievement of a common aim.
- Definition of optimal vehicle setup, in terms of wheel characteristic angles, load balance and tyre inflating pressure, and of driving strategies able to reach optimal grip/thermodynamic conditions.

Being not available local velocity and pressure distribution, GrETA is supposed to work in this case basing on global variables, measured on track or calculated in simulation; longitudinal and lateral friction estimated values are considered as sort of normalized scaling factors for longitudinal and lateral interaction forces coming as an output from Pacejka formulation. Figures 6.24 and 6.25 show the differences between forces data from telemetry and from Pacejka model, whose input are measured slip, load and camber values. In a first case the calculated forces are reported as scaled by a coulomb friction model, always constantly equal to one except for static value (it means considering standard Pacejka output, with no further processing); in a second case forces are processed with GrETA friction scaling factors, taking into account phenomena neglected in the first case. It can be noticed that grip model employment produces better results, in particular as concerns longitudinal interaction in traction phase, thermally stressful for high performance tyres and able to generate heat for friction power mechanism that induces not negligible effects in tyre/road interaction modelling.

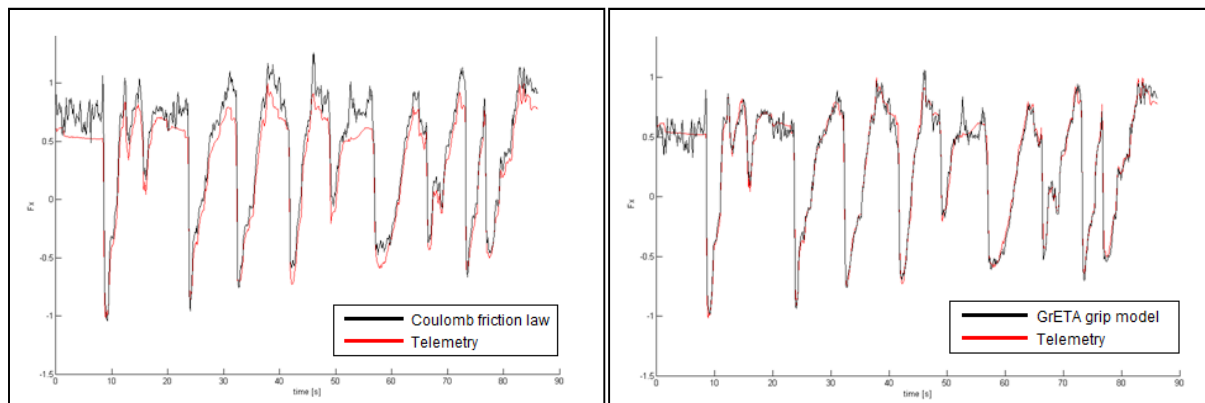


Fig. 6.24 - Comparison between longitudinal tyre forces modelled by MF with a coulomb friction law and with GrETA friction model.

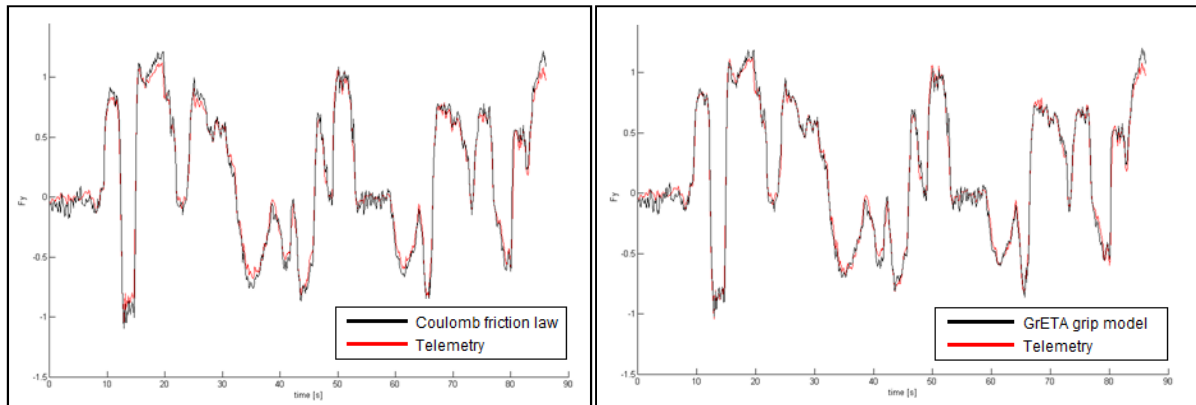


Fig. 6.25 - Comparison between lateral tyre forces modelled by MF with a coulomb friction law and with GrETA friction model.

### 6.5 TRT - GrETA - Physical Interaction Model

As clear from previous paragraph, and as well known from vehicle dynamics experience, Pacejka model is not the most flexible and detailed method to describe tyre/road interaction local phenomena, but represents a very robust and intuitive solution to obtain the hardly achievable aim to model tyre tangential forces.

For this reason, further developments of the activities discussed in the present work will focus on the realization of a fully physical interaction model that, starting from the knowledge acquired about the topic by the vehicle dynamics research group [21][51], will be able to interact deeply with the other developed models, creating an analytic and predictive instrument employed in a wide range of automotive applications.

## **Conclusions and Further Developments**

In the presented thesis the author's PhD path has been described, from the initial phase of aim definition of the activities to the final development of an analysis and modelling multi-tool instrument, passing through the multitude of themes that concern with tyre/road interaction and, more generally, with vehicle dynamics.

The target, fixed in collaboration with a motorsport racing team, with a high performance vehicle manufacturing company and with a tyre research and development technical centre, evolved progressively, finally becoming the development of a procedure able to estimate tyre interaction characteristics, reproducing them in simulation environments taking into account the fundamental friction and thermal phenomena concerning with tyre/road interaction.

A first tool, called TRICK, has been developed with the aim to process data acquired from experimental test sessions, estimating tyre interaction forces and slip indices. Once characterised the vehicle, filtering and sensors output correction techniques have been employed on the available data, creating a robust procedure able to generate as an output a "virtual telemetry" and, following a specifically defined track driving routine, to provide tyre interaction experimental curves.

TRICK virtual telemetry can be employed as an input for the second tool, TRIP-ID, developed with the aim to identify the parameters of a Pacejka Magic Formula tyre model. The advantage of this kind of procedure is the possibility to simulate the behaviour of a tyre without the bench characterizations provided by tyre makers, with the further benefit to reproduce the real interactions with road and the phenomena involved with it, commonly neglected in bench data.

Among such phenomena, one of the most important is surely the effect that temperature induces on tyre performances, especially in racing applications. For this reason a specific model, called TRT, has been realised and characterised by means of proper thermodynamic tests, becoming a fundamental instrument for the simulation of a tyre behaviour as close to reality as possible. One of the most useful features provided by the model is the prediction of the so called "bulk temperature", recognized as directly linked with the tyre frictional performances.

With the aim to analyse and understand the complex phenomena concerning with local contact between viscoelastic materials and rough surfaces, GrETA grip model has been developed. The main advantage to which the employment of the grip model conducts is constituted by the possibility to predict the variations induced by different tread compounds or soils on vehicle dynamics, leading to the definition of a setup able to optimise performances as a function of tyre the working conditions.

The described models and procedures can cooperate, generating a many-sided and powerful instrument of analysis and simulation; the main features of the available employment solutions can be summarised as follows:

- full geometric, thermodynamic, viscoelastic and structural characterization of tyres on which the analyses are focused;
- estimation of the tyre interaction characteristic curves from experimental outdoor test data;
- definition of a standard track driving procedure that employs tyres in multiple dynamic and thermal conditions;

- identification of Pacejka Magic Formula tyre models parameters on the basis of the estimated tyre interaction characteristic curves;
- estimation of surface, bulk and inner liner tyre temperatures for variable working conditions and real-time reproduction of tyre thermodynamic behaviour in simulation applications;
- correlation of tyre thermal conditions with friction phenomena observable at the interface with road;
- prediction of tyre frictional behaviour at tread compound and soil roughness variations;
- modelling of tyre interaction by means of MF innovative formulations able to take into account grip and thermodynamic effects on vehicle dynamics;
- definition of the optimal wheels and vehicle setup in order to provide the maximum possible performances improvement.

A further step in the field of tyre/road interaction modelling and analysis could be represented by the development of a fully physical contact and interaction model, able to cooperate with the presented ones, constituting an ideal instrument for the prediction and the simulation of the real tyre dynamics.

## **References**

- [1] Gent A. N., Walter J. D., *The Pneumatic Tire*, University of Akron, National Highway Traffic Safety Administration (NHTSA), 2005.
- [2] Wong J. Y., *Theory of ground vehicles*, John Wiley and sons, 2001.
- [3] Reimpell J., Stoll H., Betzler J. W., *The Automotive Chassis: engineering principles*, SAE International, 2002.
- [4] Blundell M. V., Harty D., *The Multibody Systems Approach to Vehicle Dynamics*, Butterworth-Heinemann, 2004.
- [5] Katz J., *Race Car Aerodynamics*, BentleyPublishers, 1995.
- [6] Happian-Smith J., *An Introduction to Modern Design Vehicle*, Butterworth-Heinemann, 2002.
- [7] VV. AA., *Vehicle Dynamics Stability and Control*, SAE International, 2011.
- [8] Guiggiani M., *The Science of Vehicle Dynamics*, Springer, 2014.
- [9] Milliken W. F., Milliken D. L., *Race Car Vehicle Dynamics*, SAE International, 1995.
- [10] Gillespie T. D., *Fundamentals of Vehicle Dynamics*, SAE, 1992.
- [11] Wright P., *Formula 1 Technology*, SAE, 2001.
- [12] Pacejka H. B., *Tyre and Vehicle Dynamics*, Butterworth-Heinemann, 2006.
- [13] Mark J. E., Erman B., Eirich F. R., *The Science and Technology of Rubber*, Elsevier, 2005.
- [14] Gent A. N., *Engineering with Rubber*, Hanser, 2000.
- [15] Heisler H., *Advanced Vehicle Technology*, Butterworth-Heinemann, 2002.
- [16] Sperling L. H., *Introduction to Physical Polymer Science*, Wiley, 2006.
- [17] Loudon B., *Non Pneumatic Tyre Assembly*, US Patent US8091596B2 January 10, 2012.
- [18] European Tyre and Rim Technical Organisation, *Standards Manual*, 2014.
- [19] ISO8855:2011, *Road vehicles - Vehicle Dynamics and Road-Holding Ability - Vocabulary*, 1992.
- [20] Guiggiani M., *Dinamica del Veicolo*, Città Studi, 2007.
- [21] Capone G., Giordano D., Russo M., Terzo M., Timpone F., *Ph.An.Ty.M.H.A.: a Physical Analytical Tyre Model for Handling Analysis - the Normal Interaction*, Vehicle System Dynamics, Vol. 47, N. 1, pp. 15-27, 2009.
- [22] Mancosu F., Sangalli R., Cheli F., Braghin F., *Mathematical-Physical 3d Tire Model for Handling/Comfort Optimization on a Vehicle: Comparison with Experimental Results*, Tire Science and Technology, Vol. 28, N. 4, pp. 210-232, 2000.
- [23] Deur J., Ivanović V., Troulis M., Miano C., Hrovat D., Asgari J., *Extensions of The Lugre Tyre Friction Model Related to Variable Slip Speed along the Contact Patch Length*, Vehicle System Dynamics, Vol. 43, Supplement 1, 2005.
- [24] DELFT-TYRE, *Tyre Models Users Manual*, TNO Automotive, 2002.

- [25] Bevely D. M., Daily R., Travis W., *Estimation of Critical Tire Parameters Using GPS Based Sideslip Measurements*, Proc. SAE Dynamics, Stability, and Controls Conf., Novi, USA, pp. 87-94, 2006.
- [26] Baffet G., Charara A., Lechner D., *Estimation of Tire-Road Forces and Vehicle Sideslip Angle*, Advances in Robotics, Automation and Control, I-Tech, pp. 472, 2008.
- [27] Milanese M., Regruto D., Fortina A., *Direct Virtual Sensor (DVS) Design in Vehicle Sideslip Angle Estimation*, Proc. 2007 American Control Conference, New York City, USA, 2007.
- [28] Oppenheim A. V., Schaffer R. W., *Discrete-Time Signal Processing*, Prentice-Hall, pp.284-28, 1989.
- [29] Chatterjee S., Hadi A. S., *Influential Observations, High Leverage Points, and Outliers in Linear Regression*, Statistical Science, Vol. 1, pp. 379-416, 1986.
- [30] Pacejka H. B., Bakker E., *The Magic Formula Tyre Model*, Proc. 1st international colloquium on tyre models for vehicle dynamics analysis, Amsterdam/Lisse, 1993.
- [31] Byrd R. H., Gilbert J. C., Nocedal J., *A Trust Region Method Based on Interior Point Techniques for Nonlinear Programming*, Mathematical Programming, Vol. 89, N. 1, pp. 149-185, 2000.
- [32] Waltz R. A., Morales J. L., Nocedal J., Orban D., *An Interior Algorithm for Nonlinear Optimization that Combines Line Search and Trust Region Steps*, Mathematical Programming, Vol. 107, N. 3, pp. 391-408, 2006.
- [33] Horigan Smith R., *Analyzing Friction in the Design of Rubber Products*, CRC Press, 2008.
- [34] Farroni F., Rocca E., Timpone F., *A Full Scale Test Rig to Characterize Pneumatic Tyre Mechanical Behaviour*, International Review of Mechanical Engineering (I.R.E.M.E.), Vol. 7, N. 5, pp. 841-847, 2013.
- [35] Castagnetti D., Dragoni E., Scirè Mammano G., *Elastostatic Contact Model of Rubber-Coated Truck Wheels Loaded to the Ground*, Proc. Inst. Mech. Eng. Part L, Vol. 222, pp. 245-257, 2008.
- [36] Farroni F., Rocca E., Russo R., Savino S., Timpone F., *Experimental Investigations about Adhesion Component of Friction Coefficient Dependence on Road Roughness, Contact Pressure, Slide Velocity and Dry/Wet Conditions*, Proc. 14th mini Conference on vehicle system dynamics, identification and anomalies (VSDIA), 2012.
- [37] Farroni F., Russo M., Russo R., Timpone F., *Tyre-Road Interaction: Experimental Investigations about the Friction Coefficient Dependence on Contact Pressure, Road Roughness, Slide Velocity and Temperature*, Proc. ASME 11th Biennial Conference On Engineering Systems Design And Analysis (ESDA), 2012.
- [38] Park H. C., Youn I. S. K., Song T. S., Kim N. J., *Analysis of Temperature Distribution in a Rolling Tire Due to Strain Energy Dissipation*, Tire Science And Technology, Vol. 25, pp. 214-228., 1997.
- [39] Lin Y. J., Hwang S. J., *Temperature Prediction of Rolling Tires by Computer Simulation*, Mathematics and Computers in Simulation, Vol. 67, pp. 235-249, 2004.

- [40] De Rosa R., Di Stazio F., Giordano D., Russo M., Terzo M., *Thermo Tyre: Tyre Temperature Distribution During Handling Maneuvers*, Vehicle System Dynamics, Vol. 46, pp. 831-844, 2008.
- [41] Allouis C., Amoresano A., Giordano D., Russo M., Timpone F., *Measurement of the Thermal Diffusivity of a Tyre Compound By Mean of Infrared Optical Technique*, International Review of Mechanical Engineering (I.R.E.M.E.), Vol. 6, pp. 1104-1108, 2012.
- [42] Kreith F., Manglik R. M., Bohn M. S., *Principles of Heat Transfer.*, Brooks/Cole, 2010.
- [43] Johnson K. L., *Contact Mechanics*, Cambridge University Press, 1985.
- [44] Agrawal R., Saxena N. S., Mathew G., Thomas S., Sharma K. B., *Effective Thermal Conductivity of Three-Phase Styrene Butadiene Composites*, Journal of Applied Polymer Science, Vol. 76, pp. 1799-1803, 2000.
- [45] Dashora P., *A Study of Variation of Thermal Conductivity of Elastomers with temperature*, Physica Scripta, Vol. 49, pp. 611-614, 1994.
- [46] Chadbourn B. A., Luoma J. A., Newcomb D. E., Voller V. R., *Consideration of Hot-Mix Asphalt Thermal Properties during Compaction*, ASTM STP 1299, 1996.
- [47] Browne A. L., Wickliffe L. E., *Parametric Study of Convective Heat Transfer Coefficients at the Tire Surface*, Tire Science and Technology, Vol. 8, pp. 37-67, 1980.
- [48] Karniadakis G. E. M., *Numerical Simulation of Forced Convection Heat Transfer from a Cylinder in Crossflow*, International Journal of Heat and Mass Transfer, Vol. 31, pp. 107-118, 1988.
- [49] van der Steen R., *Tyre/Road Friction Modeling*, Ph.D. Thesis, Eindhoven University of Technology, 2007.
- [50] Cossalter V., Doria A., Lot R., Ruffo N., Salvador M., *Dynamic Properties of Motorcycle and Scooter Tires: Measurement and Comparison*, Vehicle System Dynamics, Vol. 39, N. 5, pp.329-352, 2003.
- [51] Calabrese F., Farroni F., Timpone F., *A Flexible Ring Tyre Model for Normal Interaction*, International Review on Modelling and Simulations (I.RE.MO.S.), Vol. 6, N. 4, 2013.
- [52] Russo R., Terzo M., Timpone F., *Software-in-the-Loop Development and Validation of a Cornering Brake Control Logic*, Vehicle System Dynamics, Vol. 45, pp.149-163, 2007.
- [53] Persson B. N. J., Tartaglino U., Albohr O., *On the Nature of Surface Roughness with Application to Contact Mechanics, Sealing, Rubber Friction and Adhesion*, J Phys: Condensed Matter, Vol. 17, pp. R1-R62, 2005.
- [54] Maurice J. P., Savkoor A. R., *Influence of Flexibility Properties and Friction Laws on Tyre Behaviour*, Vehicle System Dynamics, Vol 37, pp. 107-124, 2002.
- [55] Amontons G., *De la Resistance Cause dans les Machines*, Histoire de l'Academie Royale des Sciences avec les Mémoires de Mathematique et de Physique, pp. 12-206, 1699.

- [56] Coulomb C. A., *Premier Mémoire sur l'Electricité et le Magnétisme*, Histoire de l'Académie des Sciences, pp. 569–577, 1785.
- [57] Bowden F. P., Tabor D., *The Friction and Lubrication of Solids*, Oxford Clarendon Press, 2001.
- [58] Bowden F. P., Tabor D., *The Adhesion of Solids in the Structure and Properties of Solid Surfaces*, The University of Chicago Press, 1953.
- [59] Rabinowicz E., *Friction and Wear of Materials*, J. Wiley & Sons, 1995.
- [60] Kummer H. W., *Unified Theory of Rubber and Tire Friction*, Engineering Research Bulletin B-94, 1966.
- [61] Savkoor A. R., *On the Friction of Rubber*, Wear, Vol. 8, pp. 157-244, 1965.
- [62] Moore D. F., *The Friction and Lubrication of Elastomers*, Pergamon Press, 1972.
- [63] Heinrich G., Kluppel M., *Rubber Friction, Tread Deformation and Tire Traction*, Wear, Vol. 265, pp. 1052-1060, 2008.
- [64] Tuononen A. J., *Digital Image Correlation to Analyse Stick-Slip Behaviour of Tyre Tread Block*, Vol. 69, pp. 7.-76, 2014.
- [65] Tonazzi D., Massi F., Culla A., *Instability Scenarios between Elastic Media under Frictional Contact*, Mechanical Systems and Signal Processing, Vol. 40, pp. 754-766, 2013.
- [66] Wallaschek J., Wies B., *Tyre Tread-Block Friction: Modelling, Simulation and Experimental Validation*, Vehicle System Dynamics, Vol. 51, pp. 1017-1026, 2013.
- [67] Carbone G., Putignano C., *A Novel Methodology to Predict Sliding and Rolling Friction of Viscoelastic Materials: Theory and Experiments*, Journal of the Mechanics and Physics of Solids, Vol. 61, pp. 1822–1834, 2013.
- [68] Yokota K., Higuchi E., Kitagawa M., *Estimation of Tire Temperature Distribution and Rolling Resistance under Running Conditions Including Environmental Factors*, SAE Technical Paper 2012-01-0796, 2012.
- [69] Persson B. N. J., Lorenz B., Volokitin A. I., *Heat Transfer between Elastic Solids with Randomly Rough Surfaces*, Eur. Phys. J., Vol. 31, 2010.
- [70] Li L., Song J., Li H. Z., *Comprehensive Prediction Method of Road Friction for Vehicle Dynamics Control*, Proc. IMechE Part D: J. Automobile Engineering, Vol. 223, 2009.
- [71] Patel N., Edwards C. Spurgeon S. K., *Tyre-Road Friction Estimation - A Comparative Study*, Proc. IMechE Part D: J. Automobile Engineering, Vol. 222, 2008.
- [72] Savaresi S. M., Tanelli M., *Identification of Tyre-Road Friction Conditions, Active Braking Control Systems Design for Vehicles Advances in Industrial Control*, Springer, 2010.
- [73] American Association of State Highway and Transportation Officials, *Guide for Pavement Friction*, 2008.
- [74] Chunyan Y., *Role of Surface Roughness in Tribology: from Atomic to Macroscopic Scale*, Jülich Forschungszentrums GmbH, 2008.
- [75] Gadelmawla E. S., Koura M. M., *Roughness Parameters*, Journal of Material Processing Technology, Vol. 123, 2002.

- [76] Ferry J. D., *Viscoelastic Properties of Polymers*, Wiley, 1980.
- [77] Gabbott P., *Principles and Applications of Thermal Analysis*, Blackwell Publishing, 2008.
- [78] Lorenz B., Pyckhout-Hintzen W., Persson B. N. J., *Master Curve of Viscoelastic Solid: Using Causality to Determine the Optimal Shifting Procedure, and to Test the Accuracy of Measured Data*, *Polymer*, Vol. 55, N. 2, pp. 565–571, 2014.
- [79] *Dynamic Mechanical Properties of Passenger and Light Truck Tire Treads*, National Highway Traffic Safety Administration (NHTSA), 2010.
- [80] Williams M. L., Landel R. F., Ferry J. D., *The Temperature Dependence of Relaxation Mechanisms in Amorphous Polymers and Other Glass-forming Liquids*, *Journal of the American Chemical Society*, Vol. 77, 1955.
- [81] Paterson M. S., *Effect of Pressure on Young's Modulus and the Glass Transition in Rubbers*, *Journal of Applied Physics*, Vol. 35, 1964.
- [82] Avdelidisa N. P., Delegouc E. T., Almond D. P., Moropoulou A., *Surface Roughness Evaluation of Marble by 3d Laser Profilometry and Pulsed Thermography*, *NDT&E International*, Vol. 37, pp. 571–575, 2004.
- [83] Le Gal A., Kluppel M., *Investigation and Modelling of Rubber Stationary Friction on Rough Surfaces*, *Journal of Physics: Condensed Matter*, Vol. 20, 2008.
- [84] Momozono S., Nakamura K., Kyogoku K., *Theoretical Model for Adhesive Friction Between Elastomers and Rough Solid Surfaces*, *The Journal of Chemical Physics*, Vol. 132, 2010.
- [85] Etienne S., David L., *Introduction à la Physique des Polymères*, DUNOD, 2012.
- [86] Feng G., Qu S., Huang Y., *An Analytical Expression for the Stress Field Around an Elastoplastic Indentation Contact*, *Alma Materialia*, Vol. 55, 2007.
- [87] Bhushan B., *Contact Mechanics of Rough Surfaces in Tribology*, *Appl Mech Rev*, Vol. 149, 1996.
- [88] Kuznetsov Y. A., Gorokhovskiy G. A., *Stress Distribution in a Polymeric Material Subjected to the Action of a Rough-Surface Indenter*, *Wear*, Vol. 51, 1978.
- [89] Kuznetsov Y. A., Gorokhovskiy G. A., *Distribution of Mechanical Energy Supplied to the Contact Area by a Periodic Sinusoidal Indenter*, *Wear*, Vol. 62, 1980.
- [90] Kuznetsov Y. A., Gorokhovskiy G. A., *Effect of Tangential Load on The Stressed State of Rubbing Rough Bodies*, *Wear*, Vol. 73, 1981.
- [91] Farroni F., Russo M., Russo R., Terzo M., Timpone F., *A Combined Use of Phase Plane and Handling Diagram Method to Study the Influence of Tyre and Vehicle Characteristics on Stability*, *Vehicle System Dynamics*, Vol. 51, N. 8, pp. 1265-1285, 2013.
- [92] Buonanno G., Carotenuto A., Giovinco G., Massarotti N., *Experimental and Theoretical Modeling of the Effective Thermal Conductivity of Rough Steel Spheroid Packed Beds*, *Journal of Heat Transfer*, Vol. 125, N. 4, pp. 693-702, 2003.